In vivo imaging of the dynamic interactions of acute leukaemias with the bone marrow microenvironment

Delfim Diogo Ferreira Duarte

Department of Life Sciences
Imperial College London
Supervised by Dr. Cristina Lo Celso

A thesis submitted for the degree of
Doctor of Philosophy
2018

À Di

Aos meus Pais

We shall not cease from exploration
And the end of all our exploring
Will be to arrive where we started
And know the place for the first time.

T. S. Elliot

Declaration of Originality

The data presented in this thesis is my own work, generated in Dr. Cristina Lo Celso's laboratory, at Imperial College London. When data was generated by or in collaboration with others, I acknowledge it within the thesis and here:

- Dr. Olufolake Akinduro contributed to the generation of MLL-AF9 AML cell batches (Chapter 2) and to the IVM of the calvarium of Col2.3-GFP mice infiltrated with mTomato^{+} AML (Chapter 3).
- Dr. Edwin Hawkins generated the Notch1-driven T-ALL cell batches (Chapter 2) and together with me, performed part of the IVM studies of mice transplanted with Notch1-driven T-ALL cells (Chapter 4).
- Dr. Catriona McLean (Alfred Hospital, Melbourne, Australia) stained the human trephine biopsies provided by Drs. Andrew Wei (Alfred Hospital) and Louise Purton (St. Vincent's Institute of Medical Research, Melbourne, Australia). Lenny Straszkowski (St. Vincent's Institute of Medical Research) contributed to the analysis of these samples (Chapter 3).
- Isabella Y. Kong (The Walter and Eliza Hall Institute of Medical Research, Melbourne, Australia) performed RNA sequencing experiments and Gene Set Enrichment Analysis (Chapter 2, 3 and 5).
- Drs. Katia De Filippo and Leo M. Carlin (National Heart and Lung Institute, Imperial College London) performed together with me ELISA studies and IVM of the spleen (Chapter 3).
- Dr. Ken Duffy (Hamilton Institute, Maynooth University) applied the statistical test in MATLAB used in Figure 3.29F (Chapter 3).
- Dr. Ricky W. Johnstone (Peter MacCallum Cancer Centre, Melbourne, Australia) provided the TEL-JAK2 T-ALL cells (Chapter 4).
- Drs. Diana Passaro and Dominique Bonnet (The Francis Crick Institute, London, UK) transplanted NOD/SCID/γ (NSG) mice with primary human T-ALL samples obtained by Dr. John Gribben (Barts Cancer Institute, London, UK) (Chapter 4).

Copyright Declaration

Abstract

Adult haematopoietic stem cells (HSC) reside in the bone marrow (BM) microenvironment, or niche, where they are regulated by several cell types including osteoblasts, endothelial cells and Nestin-expressing perivascular cells, and by niche-derived signals, such as CXCL12. In parallel, leukaemia growth and chemoresistance have been proposed to be dependent on an analogous malignant microenvironment.

Using a murine model of MLL-AF9 driven acute myeloid leukaemia (AML), I show that AML outcompetes non-malignant haematopoiesis by gradual elimination of stroma cells, endosteal endothelium and osteoblastic cells. I further demonstrate that blood vessels in AML-burdened mice are more cell-permeable and likely contribute to loss of haematopoietic cells. The rescue of the endosteal vascular microenvironment in AML rescues HSC loss and improves chemotherapy efficacy (Chapter 3).

To address the reverse question, i.e. whether the microenvironment influences disease progression, I studied a mouse model of T-cell acute lymphoblastic leukaemia (T-ALL) driven by constitutively active Notch1. Our group had previously shown that T-ALL progression is independent from particular niches. Here, I show that chemoresistant T-ALL cells are also niche-independent and highly motile, maintaining very transient interactions with surrounding microenvironments (Chapter 4).

Studying the *in vivo* behaviour of Notch-1 T-ALL and MLL-AF9 cells in parallel, I observed that chemoresistant AML cells, in contrast with T-ALL, are less migratory than naïve ones. I also show that AMD3100, an antagonist of CXCR4 (the receptor of CXCL12), inhibits the migration of treatment-naïve and chemoresistant T-ALL cell migration. In contrast, AML cell behaviour remains unaltered after CXCR4 inhibition, likely because of disease-specific, more complex interactions with the BM microenvironment (Chapter 5).

These results support the importance of cell-intrinsic and overall tissue influence rather than stroma-specific signals supporting chemoresistant T-ALL. Additionally I show that therapies targeting the endosteal vasculature could potentially improve existing AML therapeutic regimes. The different nature of leukaemia-microenvirnment interactions for the two diseases is further demonstrated by the observation that CXCR4 inhibition affects T-ALL but not AML cell migration within the BM space.

Contents

Acknowledgments

I would like to thank my supervisor Cristina Lo Celso for all the support, guidance and infectious enthusiasm and for providing the perfect *microenvironment*. I also want to thank my friend Chaz, who goes by the official name of Edwin Hawkins, for being a brilliant teacher and a great mentor.

I thank my project advisors Nadia Guerra and Holger Auner for their input and critical discussions. I also acknowledge all the members from the Lo Celso lab involved in this project. In particular, I thank Nicola Ruivo for her support and friendship, Folake Akinduro for her early work on MLL-AF9 and Heather Ang, Myriam Haltalli and Chiara Pirillo for being fantastic friends and for providing fantastic food and sweets. I also thank Reema Khorshed, Dina Pospori, Sara Gonzalez and Alba Meira for scientific discussions and contributions. Thank you Hugh, Tom, Yiran, Nahide, Joana and Sam. My lab neighbours in the Brady and Guerra groups made Imperial an enjoyable and stimulating place to work in.

I am truly grateful to Debbi Keller and Steve Rothery (Imperial College FILM facility) and Nick Sergent (Carl Zeiss) for support with microscopy, Savvas Piperelis, Edgar Ibarguen, Wendy Steel, Helen Goyal and Cathy Godfrey (Imperial College CBS facility) for help with animal care, Catherine Simpson, Jane Srivastava and Jessica Rowley for support with flow cytometry and Arwa Kocache (Imperial College Healthcare NHS Trust) for supplying cytarabine and doxorubicin.

There were fundamental collaborations, through which I met fantastic people and learned enormously. I thank Mohammad Jafarnejad, Samira Jamalian, Dimitrios Athanasiou, and James E Moore Jr (Department of Bioengineering, Imperial College), Katia De Filippo and Leo Carlin (NHLI, Imperial College), Ken Duffy and Tom Weber (Hamilton Institute, Maynooth University), Lenny Straszkowski and Louise Purton (St Vincent's Institute of Medical Research), Isabella Kong (WEHI), Andrew Wei (Alfred Hospital, Melbourne), Diana Passaro and Dominique Bonet (The Francis Crick Institute), Saoirse Amarteifio and Gunnar Pruessner (Department of Mathematics, Imperial College), Saravana K Ramasamy, Anjali P Kusumbe and Ralf Adams (Max Planck Institute for Molecular Biomedicine, Munster) and Alexander Medvinsky (University of Edinburgh).

Thanks to my GABBA friends Elsa, Raquel and Rita, Portugal always felt close by. Thank you to my long time friends Manel, Teresinha, Filipa and Incio for always listening to my stories and updates. My time in London was very special thanks to Vivek, Mark and Marion who illuminated me with their brightness and friendship. I was blessed to be part of the Circle of Trust with my buddies Ana Luisa, Andrea and Joram. I also want to thank Dr. Rita Negrão and Prof. Raquel Soares for introducing me to research and Drs. José Mário Mariz, Sérgio Chacim and Nuno Sousa of IPO-Porto for the opportunity of pursuing this PhD during my residency. I am grateful to Paula, little Octavia and their lovely family for always making me feel at home. A special thank you to my parents in law Judite, António and to Pipinho for the support and friendship during these years away from home.

Obrigado aos meus pais Delfim e Silvina por sempre me apoiarem e por me terem dado todas as ferramentas para me tornar um cidadão do mundo.

Obrigado à minha querida Di por ser simultaneamente o meu porto de abrigo e o meu destino.

I finally thank FCT and GABBA for the funding and for supporting the development of young Portuguese scientists abroad.

List of Figures

List of Tables

Abbreviations

Abbreviation	Meaning
2D	Two-dimensional
3D	Three-dimensional
3DISCO	3D imaging of solvent-cleared organs
4D	Four-dimensional
7-AAD	7-Amino-Actinomycin
AML	Acute myeloid leukaemia
ANG	Angiogenin
ANGPT1	Angiopoietin 1
Ara-C	Cytarabine
BM	Bone marrow
BSA	Bovine serum albumin
c-Kit	Stem cell growth factor receptor
CAR	CXCL12 abundant reticular
CFP	Cyan fluorescent protein
CFU-S	Colony forming unit-spleen
CLEM	Correlative light and electron microscopy
CLPs	Common lymphoid progenitors
CML	Chronic myeloid leukaemia
CMPs	Common myeloid progenitors
CNS	Central nervous system
CTLs	Cytotoxic T cells
CUBIC	Clear, Unobstructed Brain/Body Imaging Cocktails and Computational analysis
CXCL12	C-X-C motif chemokine 12
DAPI	4,6-diamidino-2-phenylindole
DFO	Deferoxamine
DMEM	Dulbecco's Modified Eagle Medium
Doxo	Doxorubicin
Dp	Diaphysis

DVA	Dexamethasone, vincristine and l-asparaginase treatment
EC	Endothelial cell
ECM	Extracellular matrix
EDTA	Ethylenediaminetetraacetic acid solution
Emcn	Endomucin
EMT	Epithelial-to-mesenchymal transition
EVISC	*Ex vivo* imaging of stem cells
FAB	French-American-British
FACS	Fluorescence-activated cell sorting
FBS	Fetal Bovine Serum
FDR	False detection rate
FMO	Fluorescence-minus-one
GaAsP	Gallium arsenide phosphide detector
GEO	Gene Expression Omnibus
GFP	Green fluorescent protein
GM-CSF	Granulocyte-macrophage colony-stimulating factor
GMPs	Granulocyte-monocyte progenitors
GSEA	Gene set enrichment analysis
HBSS	Hank's Balanced Salt Solution
Hif-1α	Hypoxia-inducible factor 1α
HSCs	Haematopoietic stem cells
HSPCs	Haematopoietic stem and progenitor cells
I.V.	Intravenous
ICAM-1	Intercellular adhesion molecule-1
ICN	Intracellular Notch1
IRES	Internal ribosome entry site
IVM	Intravital microscopy
L-GMPs	Leukaemic GMPs
LepR	Leptin receptor
Lin	Lineage
LKS	Lin^-, c-Kit^+, Sca-1^+
LSC	Leukaemic stem cells
LSCM	Laser scanning confocal microscopy

LT-HSCs	Long-term haematopoietic stem cells
M-CSF	Macrophage colony-stimulating factor
MDS	Multidimensional scaling
MEPs	Megakaryocyte-erythrocyte progenitors
MLL	Mixed leukaemia lineage
MMPs	Metalloproteinases
MP	Multiphoton microscopy
Mp	Metaphysis
MPPs	Multipotent progenitors
MRD	Minimal residual disease
MSC	Mesenchymal stem cells
MSCV	Murine Stem Cell Virus
NDD	Non-descanned detector
NOD .	Non-obese diabetic background
NSG	NOD-SCID-Il2r$\gamma^{-/-}$
OCT	Cutting temperature compound
OPN	Osteopontin
PBS	Phosphate Buffered Saline
PMT	Photomultiplier tube
Qdots	Quantom dots
ROI	Region of interest
ROS	Reactive oxygen species
Sca-1	Stem cell antigen
SCF	Stem cell factor
SCID	Severe combined immunodeficiency
SD	Standard deviation
SDF1	Stromal cell-derived factor 1
SEM	Standard error of the mean
SHG	Second harmonic generation
SLAM	Signalling lymphocyte activation molecule
ST-HSCs	Short-term haematopoietic stem cells
T-ALL	T-cell acute lymphoblastic leukaemia
TDE	2,2′ -thiodiethanol

TNF	Tumour necrosis factor
TPO	thrombopoietin
TPO	Thrombopoietin
TUNEL	TdT-mediated dUTP nick end labelling
VEGF	Vascular endothelial growth factor
WHO	World Health Organization
YFP	Yellow fluorescent protein

List of Published Material

Papers A, B, C, D and E were published during my PhD studies. Paper A and B are related to Chapter 1; papers C and D are related to Chapter 3; paper E is related to Chapter 4.

(A) D. Duarte, C. Lo Celso. Chapter Four - Imaging the Hematopoietic Stem Cell Niche. Editor(s): Dominique Bonnet, In **Advances in Stem Cells and their Niches**, Elsevier, Volume 1, 2017, Pages 59-83, ISSN 2468-5097, ISBN 9780128113752, https://doi.org/10.1016/bs.asn.2017.01.002. (book chapter).

(B) Duarte D*, Hawkins ED*, Lo Celso C. The interplay of leukemia cells and the bone marrow microenvironment. **Blood**. 2018. *In press.* doi: https://doi.org/10.1182/blood-2017-12-784132. (*co-first authors).

(C) Duarte D, Hawkins ED, Akinduro O, Ang H, De Filippo K, Kong IY, Haltalli M, Ruivo N, Straszkowski L, Vervoort SJ, McLean C, Weber TS, Khorshed R, Pirillo C, Wei A, Ramasamy SK, Kusumbe AP, Duffy K, Adams RH, Purton LE, Carlin LM, Lo Celso C. Inhibition of Endosteal Vascular Niche Remodeling Rescues Hematopoietic Stem Cell Loss in AML. **Cell Stem Cell**. 2018 Jan 4;22(1):64-77.e6. doi:10.1016/j.stem.2017.11.006.

(D) Akinduro O*, Weber TS*, Ang H, Haltalli MLR, Ruivo N, Duarte D, Rashidi NM, Hawkins ED, Duffy KR, Lo Celso C. Proliferation dynamics of acute myeloid leukaemia and haematopoietic progenitors competing for bone marrow space. **Nat Commun**. 2018 Feb 6;9(1):519. doi: 10.1038/s41467-017-02376-5. (*co-first authors).

(E) Hawkins ED*, Duarte D*, Akinduro O, Khorshed RA, Passaro D, Nowicka M, Straszkowski L, Scott MK, Rothery S, Ruivo N, Foster K, Waibel M, Johnstone RW, Harrison SJ, Westerman DA, Quach H, Gribben J, Robinson MD, Purton LE, Bonnet D, Lo Celso C. T-cell acute leukaemia exhibits dynamic interactions with bone marrow microenvironments. **Nature**. 2016 Oct 27;538(7626):518-522. doi: 10.1038/nature19801. (*co-first authors).

Chapter 1

Introduction

Acute leukaemia is cancer of white blood cells, characterised by aggressive behaviour and poor response to therapy. Acute myeloid leukaemia (AML) and T-cell acute lymphoblastic leukaemia (T-ALL) are large groups of acute leukaemias from the myeloid and lymphoid lineages, respectively. Leukaemia patients often present with cytopenias resulting from disruption of normal blood cell production (haematopoiesis) (Hoffbrand et al., 2010) and have reduced bone mass (Wilson and Ness, 2013). It has been speculated that quiescent leukaemia initiating cells reside in nurturing bone marrow (BM) niches that favour their expansion and survival in protective microenvironments where they evade chemotherapy and drive subsequent relapse of disease (Ishikawa et al., 2007; Lane et al., 2009). It has also been hypothesised that leukaemia cells can indirectly disrupt haematopoiesis by altering the structure of BM microenvironments (Colmone et al., 2008), or by targeting haematopoietic cells themselves (Miraki-Moud et al., 2013), thus, blocking these processes has been suggested as a therapeutic mechanism. Therefore, the aim of my project is to investigate the interactions of T-ALL and AML with BM microenvironments to develop better therapies to target leukaemia, including chemoresistant leukaemic cells, and restore normal haematopoiesis.

1.1 - Haematopoiesis

Adult haematopoiesis occurs primarily in the BM, where haematopoietic stem cells (HSCs) reside. The haematopoietic system is a structured hierarchy of blood cells, where all differentiated progeny are downstream of the HSC. Through asymmetric division, HSCs can self-renew thereby maintaining a long-lived pool of stem cells as well as differentiated progenitors. These differentiated progenitors give rise to lineage-restricted blood cells that

play significant physiological roles in immune surveillance, oxygen transport, tissue repair and clotting (Hoffbrand et al., 2010).

According to the classical model of haematopoiesis (Kondo et al., 2003) (Figure 1.1), HSCs with long-term reconstitution potential (LT-HSCs) progressively give rise to HSCs with short-term reconstitution potential (ST-HSCs) and multipotent progenitors (MPPs). MPPs do not self-renew and branch into lymphoid and myeloid lineages, by differentiating into common lymphoid progenitors (CLPs) (Kondo et al., 1997) and common myeloid progenitors (CMPs) (Akashi et al., 2000). CLPs generate single-lineage progenitors that give rise to lymphoid cells (T cells, B cells, NK cells, and innate lymphoid cells). CMPs branch into granulocyte-monocyte progenitors (GMPs) (that generate macrophages and granulocytes, such as neutrophils, basophils and eosinophils) and into megakaryocyte-erythrocyte progenitors (MEPs) (that generate megakaryocytes and erythrocytes). Dendritic cells can be generated either from CLPs or CMPs (Manz et al., 2001). Recently, this classical model was disputed. Multipotent HSCs are in fact lineage-biased (Beerman et al., 2010; Muller-Sieburg et al., 2012; Sanjuan-Pla et al., 2013). Furthermore, studies analysing differentiation at the single cell level (Paul et al., 2015; Perie et al., 2015) have shown that the majority of phenotypically defined MPPs and CMPs are not truly multipotent but in fact already committed to a single lineage. In this work, I have focused on HSCs and how they are affected by extrinsic interactions, namely the BM microenvironment and leukaemic cells.

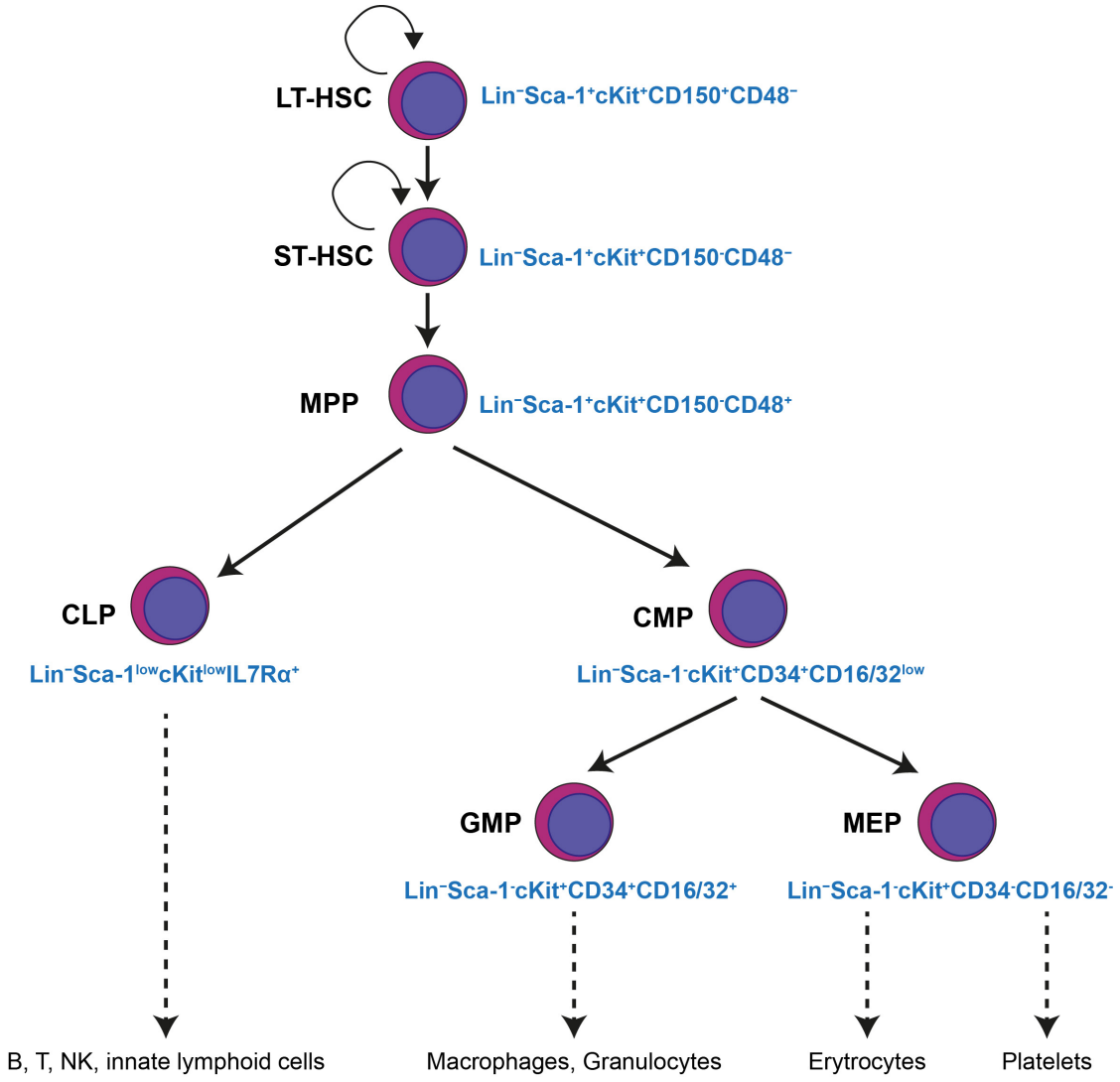

Figure 1.1 – Classic model of haematopoiesis. Using cell surface markers (*in blue)*, it is possible to separate groups of haematopoietic cells with different self-renewal and multipotency properties. Lin: Lineage.

1.1.1 – Haematopoietic stem cells

The concept of a single blood stem cell with multilineage potential was initially proposed by Maximow (Maximov, 1909). This was in opposition to the popular view that stem cells were lineage-restricted. However, formal *in vivo* experimental evidence of a multipotent HSC was only presented in studies by Till and McCulloch during the 1960s (Becker et al., 1963; Till and Mc, 1961). They showed that haematopoietic cells transplanted into lethally irradiated mice gave rise to macroscopic splenic colonies, proportional to the number of cells injected (Till and Mc, 1961). The cell capable of generating these colonies was designated colony forming unit-spleen, CFU-S. Till and McCulloch also demonstrated that these colonies were originated from single multipotent cells, by showing that the colonies were clonal (assessed by X-ray induced chromosomal lineage tracking) and contained haematopoietic cells from multiple lineages (Becker et al., 1963). It was however later demonstrated that CFU-S were not able to generate lymphoid lineages (Paige et al., 1981) and that they had a limited repopulating capacity, particularly under stress (Lajtha and Schofield, 1971; Siminovitch et al., 1964). This led Schofield to hypothesize the existence of an HSC niche within the BM, essential for inducing true stem cell activity (Schofield, 1978). This is discussed in more detail below.

The introduction of competition assays led to the understanding that HSCs could be distinguished based on their long-term versus short-term repopulation capacity (Harrison, 1980). The existence of LT-HSCs with multilineage potential was definitely established by later studies where the use of irradiation was circumvented and cells could be tracked by the expression of inserted genes (Dick et al., 1985; Keller et al., 1985; Lemischka et al., 1986). Thus, the classic definition of HSCs relies on functional assays (i.e. the long-term capacity of regenerating the whole haematopoietic tissue, assessed by serial transplantation), and the true stem cell can only be identified retrospectively, at which time the HSC does no longer exist to be assayed and visualized. This obstacle is partially circumvented by using phenotypic markers that can easily identify haematopoietic cell populations that are more or less enriched in HSCs. The definition of such markers using flow cytometry was pioneered by the group of Irving Weissman using the mouse as a model (Spangrude et al., 1988) and later refined by others (Bryder et al., 2006). In mice, haematopoietic progenitors are classically identified based on their lack of markers associated with blood cell lineage commitment (lineage negative, Lin^-). This population is further enriched for progenitors based on the expression of stem cell antigen (Sca-1) and stem cell growth factor receptor (c-Kit). The Lin^-, $c\text{-}Kit^+$, Sca-

1^+ (LKS) fraction can be additionally split according to the expression of the members of the signalling lymphocyte activation molecule (SLAM) family, CD48 and CD150 (Figure 1.2). This top-down strategy is commonly applied to identify a LKS $CD48^-CD150^+$ population that is highly enriched in HSCs (estimated frequency of 1 functional HSC in 2.1 cells) (Kiel et al., 2005). Using the same marker combination, subpopulations of HSC progeny can also be identified (short-term HSCs – ST-HSCs, multipotent progenitors – MPPs, haematopoietic progenitors – HPCs) (Figure 1.2). Thus, the mouse provides a robust system for accurately tracking the early haematopoietic stem and progenitor cells.

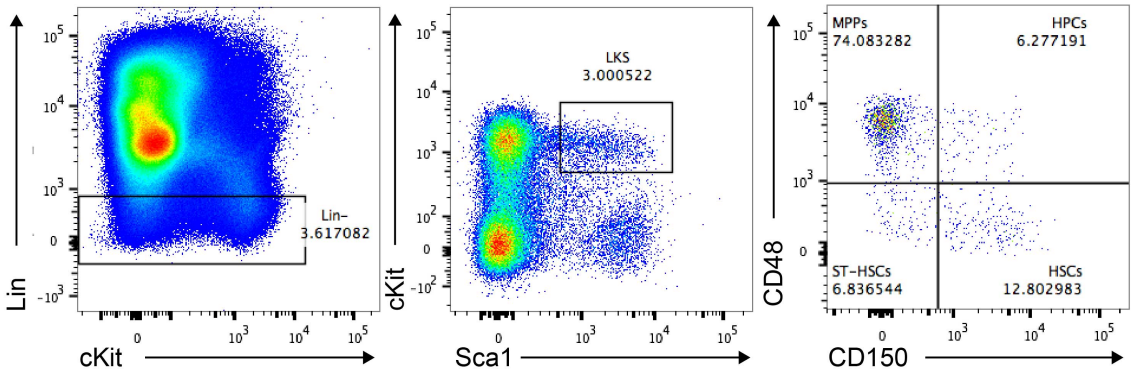

Figure 1.2 – HSCs identification by flow cytometry. Gating strategy used to identify healthy $Lineage^-$ cells (left), Lin- $c\text{-}Kit^+$ $Sca\text{-}1^+$ (LKS) progenitors (middles) and LKS $CD48^-$ $CD150^+$ haematopoietic stem cell (HSCs, right).

More recently, transgenic mouse lines in which expression of reporter genes was driven by genes that are highly enriched in HSCs were developed. Two particular genes recently identified through gene expression screenings of HSCs were α-catulin (Acar et al., 2015) and Hoxb5 (Chen et al., 2016a). According to these studies, limiting dilution assays showed a frequency of HSCs with multi-lineage capacity of 1 in 6.7 α-catulin-GFP^+ cells and 1 in 2.1 Hoxb5-tri-$mCherry^{hi}$ cells. Such mice are very promising to prospectively identify resident adult HSCs that can be easily imaged. Other reporters marking candidate HSCs include Fgd5 (Gazit et al., 2014), Hoxb4 (Hills et al., 2011) and Tie2 (Ito et al., 2016). In most cases, however, either other cells express the same marker, making the identification of comparatively very rare HSCs more complex, or not all HSCs express the marker, raising the question whether there might be functional (and anatomical) differences between labelled and unlabelled HSCs.

Human HSCs with self-renewal and multilineage capacity exist at an estimated frequency of 1 in 10^6 BM cells. Similarly to the mouse system, it is possible to enrich for stem cell activity by selecting a population using cell surface markers by flow cytometry. The most widely accepted phenotype of human HSCs is $CD34^+CD38^-Thy1^+CD45RA^-$. Recently, Notta et al subdivided this population in a $CD49f^+$ HSC fraction with long-term engraftment potential and a $CD49f^-$ fraction of MPP cells (Notta et al., 2011). Phenotypic HSCs can be therefore isolated from human cord blood or adult BM and transplanted into mice that lack certain immune cells or immune cell functions and therefore do not reject human cells.

1.2 – Acute myeloid leukaemia

AML is a leukaemia of blood cells from the myeloid lineage. Its incidence increases with age, affecting 2-3 children and 15 older adults out of 100,000 every year (Hoffbrand et al., 2010). The prognosis for AML patients is poor, with an average 5-year survival of 25%, mainly due to relapse and high morbidity associated with treatment. Just 35 to 40% of patients younger than 60 years old and only 5-15% of patients older that 60 years old are cured (Dohner et al., 2010).

Currently, the categorization of AML follows the World Health Organization (WHO) classification, which takes into account clinical, cytogenetic, molecular and morphological features (Swerdlow et al., 2008). The WHO system allows for the classification of entities that have distinct treatment and prognosis (e.g. acute promyelocytic leukaemia with t(15;17)(q22;q12); PML-RARA). Despite AML being a heterogeneous group of biologically distinct diseases, there are common features and shared physiopathology worth discussing.

1.2.1 – Clonal evolution of AML

AML, similarly to other cancer types, is a clonal disease originating from a single cell of the corresponding tissue, the haematopoietic system. It has been proposed that leukaemia is propagated and maintained by leukaemic stem cells (LSC), which have an HSC-like phenotype (Lapidot et al., 1994). According to the current model, clonally expanded pre-LSCs acquire additional mutations that are key for their transformation and for the development of AML (Grove and Vassiliou, 2014). These mutations enable three fundamental properties for cancer cells: block in differentiation, self-renewal and

uncontrolled proliferation (Hanahan and Weinberg, 2011). The resultant leukaemic cell mass is the result of clonal evolution and is organized in a complex architecture where dominant clones co-exist with minor subclones. This complexity is illustrated by genomic analyses of leukaemic samples showing that AML relapse can be driven by either the dominant clone or by minor subclones, upon acquisition of new mutations during chemotherapy (Ding et al., 2012a). Multiple clones and not just the founding one need therefore to be targeted to eradicate the disease. Nevertheless, a specific cell feature, self-renewal, seems to be key for therapy resistance of leukaemic cells. Regardless of their genomic diversity, both rare LSCs and the more abundant phenotypically committed leukaemic cells that have a "stem-like" transcriptional signature are responsible for initiating disease relapse in AML (Shlush et al., 2017).

1.2.2 – Leukaemic Stem Cell

Given the therapeutic implications of specifically targeting LSCs, it is important to correctly define this biologically distinct group of cells. Using primary human AML samples xenotransplanted into immunodeficient mice, the group of John Dick first proposed that hierarchically organized leukaemia cells are descendent of very rare LSCs (as few as 1 in 10^7) (Bonnet and Dick, 1997; Lapidot et al., 1994). It has been however pointed out that fundamental leukaemia-microenvironment interactions are not replicated in the xenotransplantation setting (Kelly et al., 2007), which would mask higher frequencies of LSCs. Consistently, a recent study using humanized ossicles that replicate the human BM microenvironment has provided much higher frequencies of AML LSCs (as few as 1 in 100 cells) (Reinisch et al., 2016). In line with this idea, studies using syngeneic leukaemia mouse models have calculated higher LSCs frequencies (of 20 to 30%) (Kelly et al., 2007; Somervaille and Cleary, 2006). Moreover, in a mouse model of mixed leukaemia lineage (MLL)-rearranged AML (MLL-AF9), it has been shown that leukaemia has a broad hierarchical organization and that LSCs can be found in all leukaemic cell fractions (including Lin^+) (Somervaille and Cleary, 2006). Another study, using a similar MLL-AF9 model has found however that LSCs are infrequent (1 in 150) and phenotypically similar to GMPs (leukaemic GMPs, L-GMPs) (Krivtsov et al., 2006). These discrepancies are probably explained by differences in the disease models studied, the type of assay used to calculate LSCs frequency (e.g. limiting dilution vs. colony formation), and the study of mouse vs.

human AML. Nevertheless, all of these studies highlight that LSCs: (1) have the ability to self-renew (i.e. asymmetrically divide to generate one daughter LSCs and one more differentiated leukaemic daughter cell or symmetrically divide to generate two daughter LSCs), (2) generate bulk leukaemic cells organized in a hierarchy, (3) have higher resistance to anti-proliferative chemotherapy, (4) exist in several phenotypically-defined groups of cells, (4) have unique interactions with BM stroma that influence their homing and proliferation. Given the important conceptual framework that these "cancer stem cells" provide to understand oncogenesis, they were also investigated and identified in other types of cancer, importantly in solid tumours (Al-Hajj et al., 2003; Singh et al., 2004).

It should be highlighted that LSC is not the same as the cell of origin for leukaemia (Clarke et al., 2006). Although LSCs might arise from mutations in HSCs (Bonnet and Dick, 1997; Passegue et al., 2004), they can also result from more differentiated cells. For example, committed progenitors can gain self-renewal properties, as shown for CMPs transformed with the fusion proteins MLL-ENL (Cozzio et al., 2003) and MOZ-TIF2 (Huntly et al., 2004) and for GMPs transformed with MLL-AF9 (Krivtsov et al., 2006).

The similarities between LSCs and HSCs, specifically kinetics studies showing a self-renewing population generating a fast cycling fraction (Dick, 2008), put forward the idea that LSCs reside in a leukaemic niche that support their maintenance and chemotherapy evasion (Lane et al., 2009).

1.2.3 – MLL-AF9 Acute Myeloid Leukaemia

MLL-rearranged leukaemias are particularly aggressive diseases, associated with trisomy 21 in paediatric patients and with therapy-related adult leukaemia that comprehend 5 to 10% of the total cases of AML (Munoz et al., 2003). The MLL-AF9 fusion results from the chromosomal translocation t(9;11)(p22;q23) and is the most common subtype of MLL-rearranged leukaemias in adults (Krivtsov and Armstrong, 2007). The MLL-AF9 fusion is typically associated with myelo-monoblastic AML and classified as the French-American-British (FAB) M4 or M5 subtype (Swansbury et al., 1998). As discussed above, using a retrovirally expressing system, it was shown that MLL-AF9 can drive the transformation of GMPs, which as a result acquire a self-renewal transcriptional signature. It was also shown that expression of the MLL-AF9 oncogene in LKS (Krivtsov et al., 2013) and CLP cell populations (Chen et al., 2008) led to a more aggressive leukaemia. This highlights the

importance of the baseline expression programs in different cells of origin. The study by Stavropoulou and colleagues uses an elegant model of doxycycline-inducible MLL-AF9 leukaemia to explore the question of cell-of-origin in AML (Stavropoulou et al., 2016). Consistently with the findings of (Krivtsov et al., 2006), when MLL-AF9 expression is induced in LT-HSCs, the resulting AML is more aggressive and chemoresistant, compared with induction in GMPs. Interestingly, HSC-initiated AML is enriched in genes involved in epithelial-to-mesenchymal transition (EMT) (Stavropoulou et al., 2016). These programs are often studied in solid tumours and are associated with migration, invasion and metastasis, which remain poorly explored in leukaemia. Importantly, the MLL-AF9 AML syngeneic mouse model provides a well-established system to study several aspects of aggressive AML, including interaction with the BM microenvironment (Hanoun et al., 2014) and with non-malignant haematopoiesis and HSCs (Cheng et al., 2015).

1.2.4 – AML treatment

AML treatment typically includes an induction phase and a consolidation phase.

The goal of induction therapy is to establish remission. It consists of continuous intravenous (I.V.) infusion of cytarabine during 7 days and I.V. anthracyclin on days 1, 2 and 3 (popularly known as the 7+3 regimen) (Dohner et al., 2015). Cytarabine (Ara-C) is an anti-metabolite that inhibits DNA synthesis (Shelton et al., 2016). Anthracyclins include drugs such as idarubicin, daunorobicin and doxorubicin (Doxo) that inhibit topoisomerase II and lead to DNA breaks. New drugs are being actively sought to improve induction therapy. Despite conflicting results in clinical trials, it seems that the addition of gemtuzumab ozogamicin, an anti-CD33 monoclonal antibody, might be beneficial (Hills et al., 2014).

Postremission therapy is needed to eliminate surviving leukaemic cells and avoid relapse. The consolidation therapy in patients younger than 60 years old normally includes intensive chemotherapy with high-dose cytarabine and allogeneic haematopoietic-cell transplantation (Dohner et al., 2015). Transplantation is the most effective therapy due to the graft-versus-leukaemia effect. Patients older than 60 years benefit more from intermediate-dose cytarabine and non-myeloblative or reduced-intensity conditioning haematopoietic-cell transplantation (Dohner et al., 2015).

1.2.5 - Loss of healthy haematopoiesis in AML

In AML, non-malignant haematopoiesis is progressively lost and patients develop life-threatening cytopenias of all blood lineages, including thrombocytopenia, anaemia and neutropenia. As a consequence, patients with AML often present clinically with bleeding, fatigue and recurrent infections. It is therefore important to understand how non-malignant haematopoietic cells are lost and HSC function is disrupted. From a clinical point of view, trying to understand how healthy haematopoiesis is disrupted is an even more evident problem in the elderly, who are commonly not fit to receive high-dose chemotherapy and HSC transplantation.

The loss of HSCs and of rapidly cycling MPPs (responsible for the maintenance of adult steady-state haematopoiesis) are the likely key elements that justify the loss of healthy haematopoiesis observed in AML. Yet, the mechanisms underlying their loss remain poorly understood. It has been proposed that the simple expansion and occupation of BM space by leukaemic cells with consequent displacement of non-malignant haematopoietic cells, justifies the decay of haematopoiesis. However, a poor correlation between BM leukaemic infiltration (AML blast counts in the BM) and peripheral blood cytopenias has been reported (Rauch et al., 2016). Interestingly, the expression of the thrombopoietin (TPO) receptor c-MPL by AML blasts appears to correlate well with both neutropenia and thrombocytopenia (Rauch et al., 2016). In this case, the scavenging of TPO (an important cytokine for the maintenance of megakaryocytes and HSCs) was the proposed mechanism (Rauch et al., 2016). It should be highlighted that a model for "space occupation" cannot be discarded as the loss of erythropoiesis could not be explained and the analysis of the half-life of different blood cells, the analysis of specific haematopoietic BM populations (e.g. HSCs, progenitors, differentiated cells) and the study of transendothelial trafficking were not addressed in this report. Using a xenograft model of AML, it has been proposed that the differentiation of HSCs to progenitors is disrupted (Miraki-Moud et al., 2013). Importantly, quiescent HSCs surviving in the infiltrated marrow engraft well upon transplantation. Although several primary samples of AML were tested, a drawback of this study is the limited interactions between human AML cells and mouse microenvironments and haematopoietic cells (Miraki-Moud et al., 2013). Consistent with this hypothesis, Chen et al used the murine MLL-AF9 AML model to propose that leukaemic blasts induce the quiescence of HSCs through the expression of Egr3, an inhibitor of proliferation (Cheng et al., 2015).

It remains to be elucidated whether and how the AML-induced remodelling of the BM microenvironment directly contributes to the loss of non-malignant haematopoiesis *in vivo.*

1.3 – T-cell acute lymphoblastic leukaemia

T-ALL is a disease characterized by uncontrolled clonal proliferation of immature lymphoid cells. T-ALL prevalence is highest among children between 3 and 5 years old and it comprises 10 to 15% of all paediatric and 20 to 25% of all adult acute leukaemias (Belver and Ferrando, 2016; Hunger and Mullighan, 2015). Despite cure rates in excess of 80%, approximately 25% of T-ALL paediatric patients develop relapsed disease that is often refractory to the initial therapies and has an extremely poor prognosis (Pui et al., 2008). Furthermore, only 40% of adult T-ALL patients reach complete remission and long-term survival is very rare (Fielding et al., 2007). Notably, the failure to eliminate minimal residual disease (MRD) in the BM during early phases of initial disease treatment identifies T-ALL patients at a very high risk of disease relapse (Szczepanski, 2007).

1.3.1 - Genetic alterations in T-ALL

Leukaemogenesis in T-ALL is the result of accumulating genetic somatic alterations that change homeostatic cellular processes (e.g. apoptosis, differentiation) essential for normal T-cell development. These alterations include aneuploidy, mutations, deletions and chromosome structural changes that produce chimeric fusion proteins or change gene expression (Hunger and Mullighan, 2015).

Chromosomal translocations and rearrangements are early events (pre-leukaemic) (Wiemels et al., 1999), maintained in relapse (Mullighan et al., 2008) and that are able to generate T-ALL in disease models. The fusion protein TEL(ETV6)-JAK2 exemplifies this group of genetic alterations. It results from the chromosomal translocation t(9;12)(p24;p13), is present in cases of T-ALL, B-cell ALL and chronic myeloid leukaemia (CML) and is able to drive transformation of haematopoietic cell lines (Lacronique et al., 2000; Lacronique et al., 1997; Peeters et al., 1997; Schwaller et al., 1998). TEL-JAK2 transgenic mice (Carron et al., 2000) and mice reconstituted with TEL-JAK2 transduced marrow cells (Schwaller et al., 1998) develop T-ALL, demonstrating the oncogenic potential of JAK/STAT pathway

overactivation. Furthermore, activating JAK mutations have been identified in T-ALL patients (Jeong et al., 2008) and were associated with poor prognosis (Flex et al., 2008).

Mutations are another important class of genetic alterations in T-ALL. Gain-of-function mutations that lead to NOTCH1 overactivation are detectable in more than 60% of human T-ALL cases (Weng et al., 2004). Interestingly, Notch1 is a transmembrane receptor necessary for T-cell commitment in the thymus (Radtke et al., 1999), demonstrating that interference with key haematopoietic programs can drive leukaemogenesis. Mutations in NOTCH1 normally cooperate with additional transformative steps to generate frank T-ALL, as illustrated in animal models (Chen et al., 2007; Li et al., 2008; Pear et al., 1996). When the activated form intracellular Notch1 (ICN) is overexpressed in BM cells (Li et al., 2008) and transplanted, mice develop a disease that resembles Notch1-driven T-ALL both genetically and phenotypically (Sanda et al., 2010). It is therefore possible to model clinically relevant forms of T-ALL.

1.3.2 – T-ALL treatment

Similarly to AML, the therapeutic strategy in T-ALL includes an induction phase and consolidation treatment.

Induction therapy normally includes the administration of a glucocorticoid (prednisone or dexamethasone), vincristine, asparaginase, optional anthracycline, including intrathecal chemotherapy administration to target central nervous system (CNS) disease (Pui et al., 2008). Glucocorticoid drugs act through binding to the glucocorticoid receptor, which in turn translocates into the nucleus, regulating gene expression and inducing leukaemic cell apoptosis (Schmidt et al., 2004). Vincristine targets microtubules, causes mitotic arrest and induces cell death (Kothari et al., 2016). Asparaginase has also a strong anti-leukaemic effect (Broome, 1963) because it converts the non-essential amino acid asparagine to aspartic acid (Broome, 1981). T-ALL cells, however, are not able to synthesize asparagine and are therefore susceptible to asparagine depletion mediated by asparaginase. The three-drug combination can be used but the four-drug regimen is preferred for all adult ALL patients and children with T-ALL (Pui et al., 2008). The dosing window in this combination treatment is very narrow and small increases in dexamethasone or asparaginase doses can result in toxicity and death. The goal of this regimen is to induce remission by killing the majority of

leukaemic cells. However, cure can only be achieved if it is followed by a consolidation phase (Hunger and Mullighan, 2015).

Consolidation therapy aims to eradicate surviving T-ALL cells. It varies according to the patient's risk classification and the protocol adopted but it normally consists on repeated administrations of methotrexate (Hunger and Mullighan, 2015). Methotrexate is an anti-folate that belongs to the same compound family of aminopterin, used by Sidney Farber to treat and induce the first-ever remissions in ALL (Farber and Diamond, 1948). This is followed by a long (up to 30 months) continuation therapy with the anti-metabolites mercaptopurine (or thioguanine) and methotrexate (Hunger and Mullighan, 2015).

1.4 – Bone marrow microenvironments

Adult haematopoiesis occurs primarily in the BM, where HSC function is most efficient, however we do not fully understand how the anatomy of bone regulates the function of the haematopoietic system. In 1978, Schofield proposed that cellular microenvironments in the BM are associated with and critical to maintain tissue-fixed HSCs (Schofield, 1978). According to this hypothesis, after division, HSCs are retained in an anatomically and functionally defined niche, while progenitors are spatially dislodged and differentiate (Figure 1.3). This is known as the stem cell niche hypothesis and it was believed that a specific cell type or a limited number of cell types instructed the quiescence of HSCs. Formal experimental evidence for the existence of a stem cell niche only came years later, after studies in *Drosophila* confirmed the critical role of local signals (Xie and Spradling, 1998) and niche sites (Xie and Spradling, 2000) in the maintenance of stem cells (germ line stem cells). It has also been demonstrated that niches define the fate of stem cells in other tissues, such as the epidermis (Rompolas et al., 2012) and intestinal epithelium (Ritsma et al., 2014b). The establishment of *in vitro* haematopoietic cultures using stromal cells isolated from the BM (Dexter et al., 1977) suggested the existence of a supporting stromal microenvironment *in vivo*. Later studies proposed that either a BM endosteal (Zhang et al., 2003) or a vascular / perivascular niche (Kiel et al., 2005) support HSCs. Yet, we now understand better the complexity of these microenvironments and it is unlikely that a single niche area or cell type is the master regulator of HSC quiescence, although its location appears to be consistently perivascular (Morrison and Scadden, 2014). Furthermore, recent data suggest that niches,

instead of directing cell fate, play their role purely as maintenance stations for self-renewing HSCs (Baryawno et al., 2017).

To comprehend the BM microenvironment it is therefore fundamental to study the spatial organization of HSCs and the interactions with their neighbours. This obviates the importance of microscopy to directly visualize the niche.

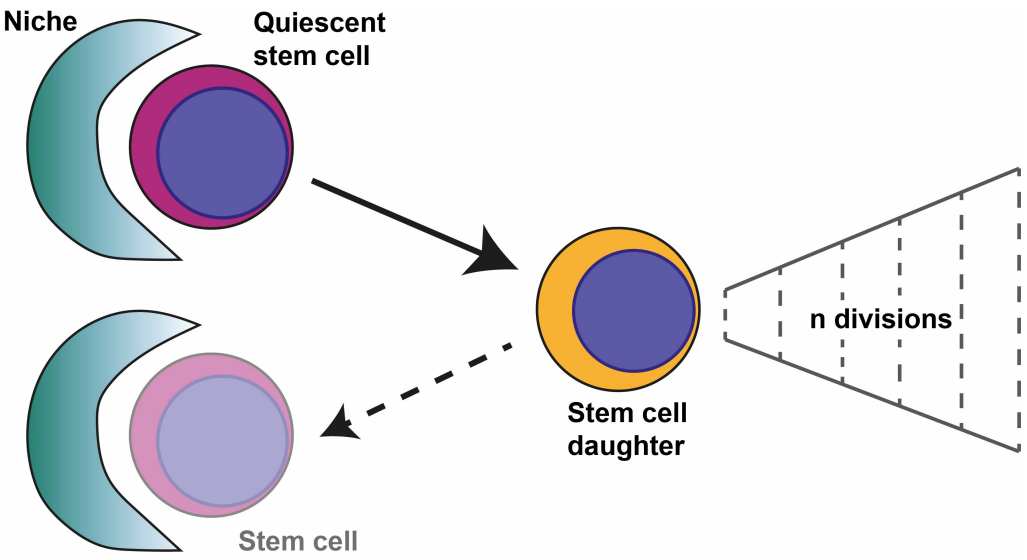

Figure 1.3 – HSC niche model. Quiescent HSCs reside in spatially defined niches in the BM. Upon mobilization from the niches, cells divide and differentiate. Upon re-localization to the niche area, stem cell activity is re-established. Adapted from (Schofield, 1978).

1.4.1 - Visualization of bone marrow niches

1.4.1.1 – Murine bone marrow niches

Several chemical signals (e.g. stem cell factor, SCF) produced by haematopoietic and stromal cells are involved in the maintenance of HSCs. Megakaryocytes, macrophages and regulatory T cells have been described to be associated with HSCs. Several mesenchymal cells have been shown one by one to be able to affect HSC numbers and function: bone-forming osteoblasts and their progenitors, endothelial cells, C-X-C motif chemokine 12 (CXCL12) abundant reticular (CAR) cells, leptin receptor (LepR)-expressing stromal cells and Nestin-expressing mesenchymal stem cells (MSC) (Morrison and Scadden, 2014). Through the use of genetically modified mouse models, it has been possible to study phenotypic HSCs (see 1.1.1) and to visualize and manipulate specific niche cells and factors produced by them. For example, the Cre-Lox system allows deletion of target genes in specific cells, either constitutively or following induction at specific times. This strategy and the many transgenic mouse lines used in HSC research are reviewed in (Joseph et al., 2013). Because the loxP cassettes are normally inserted in the Rosa26 locus, it is possible to cross them with other Rosa26 strains expressing fluorescent proteins, such as GFP, and in this way image a large number of reporter mice. There are, however, strains that are particularly popular in HSC niche studies. To image mature osteoblasts, the Col2.3-GFP strain is often used (Figure 1.4). These mice express enhanced GFP under the control of a 2.3 kb region of the rat or mouse procollagen type 1 alpha 1 (Col1a1) promoter (Calvi et al., 2001). Alternatively, osteoblast progenitors can be visualized using Osx1-CreGFP mice, where the transgene is expressed under the regulation of the osterix promoter (Rodda and McMahon, 2006), albeit in fewer cells than highlighted by immunostaining for the transcription factor osterix. Nestin-expressing perivascular mesenchymal stem/progenitor cells can be identified using the Nestin-GFP mouse, where the expression of the intermediate filament Nestin drives GFP (Mignone et al., 2004) (Figure 1.4), and CXCL12-expressing cells, primarily perivascular, can be visualized using the CXCL12-GFP (Sugiyama et al., 2006) or CXCL12-DsRed knock-in mice (Ding and Morrison, 2013). Endothelial cells can be studied through the use of endothelial-specific promoters, such as Flk1 and VE-Cadherin reporter mice. Yet, most of the studies label these cells using antibodies specific for vascular markers such as CD31, VE-Cadherin, laminin and endomucin. Such antibodies can be either applied to sections or intravenously injected in the live animal to perform intravital microscopy (IVM)

or *ex vivo* whole mounts analyses. Alternatives that provide excellent discrimination of endothelial cells include Dil-labelled acetylated low-density lipoprotein (Dil-Ac-LDL) (Kunisaki et al., 2013) and fluorescently conjugated *Griffonia simplicifolia* isolectin B4 (Lassailly et al., 2013). In IVM studies, blood vessels are often identified through the use of intravascular dyes, such as fluorescently tagged bovine serum albumin (BSA) or dextrans with various molecular weights (Figure 1.4). To increase the number of colours analysed, far red and near infrared Quantom dots (Qdots), such as Qdot 655 and Qdot 800, can also be used (Lo Celso et al., 2009). Importantly, immune labelling is not restricted to endothelial cells and can be applied to other putative niche cells, such as angiopoietin-1 expressing stromal cells (Zhou et al., 2015) and to many of the classical niche cells, such as osteoblasts marked by anti-osteopontin antibodies (Calvi et al., 2003). Finally, nonlinear optical microscopy, specifically second harmonic generation (SHG) signal allows to image collagen 1 fibres that compose the bone itself (Figure 1.4) (Zipfel et al., 2003). Although these strategies are often used in isolation, the combination of reporter mice, antibodies and SHG signals makes possible the simultaneous imaging of different BM microenvironmental components either in sections or in live imaging (Figure 1.4).

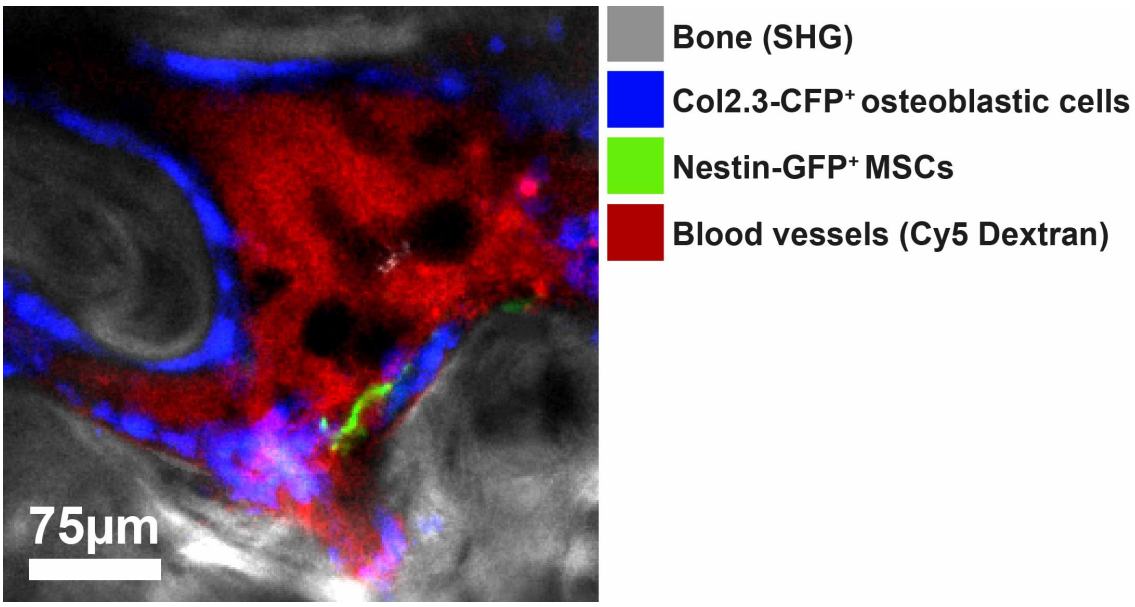

Figure 1.4 – IVM of the calvarium BM of a Col2.3-CFP/Nestin-GFP mouse. Using a combination of reporter mouse lines, vascular dyes and imaging techniques, it is possible to simultaneously visualize key elements of the HSC microenvironment.

1.4.1.1 – Human bone marrow niches

In contrast to the mouse, the BM niche for human HSCs remains less well studied. This is in part justified by the difficult access to human samples and by our poor understanding of the human haematopoietic hierarchy. However, the main restraints for the exploration of the human HSC microenvironment are the experimental limitations associated with the manipulation of human HSCs and human BM tissue. In this regard, the group of John Dick pioneered the study of human haematopoiesis by xenotransplanting human HSCs into immunodeficient mice (Doulatov et al., 2012). Among the strains of immunodeficient mice available today, one of the most used is the NOD-SCID-Il2rγ$^{-/-}$ (NSG) line (Shultz et al., 2005). These mice have a defective V(D)J recombination and accompanying deficiency of mature B and T cells due to the severe combined immunodeficiency (SCID) mutation, a deficiency of Natural Killer (NK) cells due to the lack of Il-2Rγ and a phagocytic tolerance due to the presence of cross-reactive signal regulatory protein α (SIRPα) of the non-obese diabetic background (NOD). Future studies focusing on the imaging of human haematopoietic niches will benefit from recently developed mouse strains. Exciting examples are the NSGW41 mice, capable of sustaining human erythro-megakaryopoiesis (Rahmig et al., 2016) and the next-generation humanized mice containing knock-in alleles that express human genes, such as TPO (Theocharides et al., 2016). The latter are important because they mimic the human microenvironment in the recipient mouse BM and are able to support both benign and malignant haematopoiesis. One example of such strain is the MIS$^{(KI)}$TRG containing knock-ins for five human genes: macrophage colony-stimulating factor (M-CSF), IL-3, granulocyte-macrophage colony-stimulating factor (GM-CSF), TPO and SIRPα (Das et al., 2016). More recently, several groups have developed humanized niche xenograft models by subcutaneously implanting human MSCs and different types of scaffolds into immunodeficient mice (Abarrategi et al., 2017; Antonelli et al., 2016; Reinisch et al., 2016). These humanized environments engraft well both human haematopoietic stem and progenitor cells (HSPCs) and leukaemias and are good alternatives to xenotransplantation alone. The use of humanized ossicles and the transplantation of immunodeficient mice coupled with the analysis of human biopsies and *in vitro* assays, allow for the study of the human HSC microenvironment.

1.4.2 – Intravital microscopy of the BM

As described in section 1.4.1, the BM cellular environment is best visualized through microscopy. The microscope, which literally permits "to see" (-scope) what is "small" (micro), increases both resolution and contrast to resolve images invisible to the naked eye. Good examples of landmark discoveries in biology made possible by the microscope include the observation of bacteria and other microorganisms by Leewenhoeck (Leewenhoeck), the observation of phagocytosis by Metchnikoff (Tauber, 2003) and the description of structures of the central nervous system by Ramon y Cajal (Cajal, 1911).

1.4.2.1 – Laser scanning confocal microscopy

Different microscopy approaches are available and result from theoretical and technical advances combined with the development of dyes, fluorochromes, model organisms and sample preparation methods (see section 1.4.1). While wide-field microscopy is appropriate for thin specimens (e.g. two-dimensional (2D) cell cultures and very thin tissue sections), it lacks depth discrimination. It illuminates the sample in its entire width and depth, and is therefore not suitable to image thick or highly scattering samples, such as bone. Alternatively, laser scanning confocal microscopy (LSCM) is able to obtain good quality three-dimensional (3D) information of living specimens.

In LSCM, different laser lines (chosen according to the excitation wavelength of the fluorophores of interest) emit light. This light is tilted in the direction of the sample by different mirrors and is focused onto the sample by the objective lens. A fluorescent sample that is illuminated will emit an emission light that will travel the same beam path (of the laser light) backwards. A beam splitter splits the excitation from the emission light that eventually encounters the pinhole. The pinhole allows for the elimination of out-of-focus signal. The size of the pinhole can be adjusted to achieve the best compromise between light collection and optical sectioning. The light finally reaches photomultiplier tube (PMT) detectors that amplify and convert the photon into electrical signal, which is recognized and displayed by the computer. In summary, LSCM acquires a series of optical sections, by rejecting the light from out-of-focus z planes, and is therefore ideal for thick specimens. It has been often used for imaging tissue sections and for IVM.

1.4.2.2 – Multiphoton microscopy

LSCM is limited to the tissue surface and for depths over 100 μm there is increased light scattering, which limits the contrast and signal strength. Imaging of deeper planes is better achieved by multiphoton microscopy (MP) (Denk et al., 1990). MP, or more specifically two-photon microscopy can image the tissue at depths ranging from 150 μm, such as in the calvarium (Lo Celso et al., 2009) to 500 μm deep in soft tissues like the lymph nodes (Halin et al., 2005).

In two-photon microscopy, the excitation of the fluorophore is achieved through the near-simultaneous absorption of two photons. This is different from LSCM, which uses higher energy one-photon excitation. In two-photon excitation, the emitted photons have lower energy and higher wavelength (about twice of the equivalent wavelength in one-photon excitation). In MP microscopy, a femtosecond laser emitting a high flux of photons is used to increase the probability of absorption of two photons at the 'same' time and in the same location. Since a very restricted area is excited, there is no out-of-focus illumination and, therefore, no need for a pinhole. Because MP microscopy uses near infrared light (typically 700-1100 nm), it allows not only deeper fluorescence excitation but also less phototoxicity and photobleaching, in comparison to LSCM (Helmchen and Denk, 2005). 2-photon excitation also allows better 3D resolution, photolytic release of caged molecules, SHG signal detection to observe bone collagen without any specific staining/manipulation, and the excitation of near-infrared Qdots, which increases the range of signals generated.

Due to their ability to excite fluorescence in deep tissues, LSCM and particularly MP microscopy have been used in time-lapse mode either alone or in combination to perform IVM and capture biological processes in four dimensions (4D). The use of IVM has contributed to significant discoveries in stem cell biology in several fields of study (Brown and Greco, 2014). For example, non-invasive IVM was used to show how the stem cell niche in the hair follicles of the skin is structurally and functionally compartmentalized (Rompolas et al., 2012). Also, MP live imaging combined with a chronically implanted abdominal imaging window was used to demonstrate how intestinal stem cells compete with each other for clonal dominance and are organized in relation to niche cells (Ritsma et al., 2014a). IVM studies have also revolutionized the fields of neuroscience, cancer, immunology and pulmonology (Ellenbroek and van Rheenen, 2014; Helmchen and Denk, 2005; Presson et al., 2014; Sumen et al., 2004).

1.4.2.3 – Intravital microscopy of the HSC niche

As discussed, IVM is able to capture the dynamics and complexities of biological processes, particularly in situations where the environmental context is pivotal. One such example is the immunological synapse formation between cytotoxic T cells (CTLs) and target cells. In this regard, the active killing of tumour cells by CTLs *in vitro* takes about 5 min (Stinchcombe et al., 2001). In striking contrast, *in vivo* imaging showed CTL killing of peptide-pulsed B cells in the lymph node and of tumour cells in the tumour microenvironment taking up to 25 min and 6 hours, respectively (Breart et al., 2008; Mempel et al., 2006). Another example that illustrates the importance of intravital imaging is the migration of tumour cells, as nicely reviewed by Condeelis and Segall (Condeelis and Segall, 2003). They describe how the *in vivo* speed of migrating breast adenocarcinoma cells is greater than 3 μm/min, which is 10 times superior compared to recordings of these cells migrating in 2D plates and 30 times higher compared to migration in 3D matrices. Altogether, these observations are very informative because they tell us that only IVM can correctly capture dynamic events that are important in the study of HSCs and the interactions with their niches. These are: the influence of the tissue microenvironment (i.e. the study of HSCs in the BM), the timescale of biological processes (for example, how long does it take for an HSC to divide and differentiate) and the cell behaviour (for example, whether the cell is immotile or migratory, how is it moving and at what speed).

Early attempts at performing live imaging of the BM were made by McCuskey, McClugage and colleagues in 1971 (McClugage et al., 1971; McCuskey et al., 1971). In these studies, a metallic chamber was transversely inserted in the tibias of rabbits and coupled with a conventional wide-field microscope. Notably, chronic imaging was possible and the same areas could be revisited. The images obtained were obviously low resolution and low contrast and the BM cells and structures were identified solely based on their morphology. Nevertheless, the authors were able to draw important conclusions from functional manipulation of the haematopoietic system. For example, they observed that blood vessels could support bone regeneration through a vascular network that was primarily venular in nature. They also concluded that arterioles and capillaries supported haematopoiesis, which was stimulated by bleeding and erythropoietin administration. It is remarkable that in more

recent years, much more refined studies have confirmed the central role of BM blood vessels in bone formation (Kusumbe et al., 2014) and haematopoiesis (Kobayashi et al., 2010).

In 2009, several imaging studies aimed to visualize the dynamics of phenotypically purified HSCs in their natural BM environment (Kohler et al., 2009; Lo Celso et al., 2009; Xie et al., 2009). In one of this studies, Xie et al. developed a method called *ex vivo* imaging of stem cells (EVISC), consisting in imaging of sagittally sectioned tibias and femurs of mice, previously transplanted with phenotypic HSCs (Xie et al., 2009). While using the long bones, the imaging was done in a severally damaged tissue, which leads to the severe damage of, for example, blood vessels and BM innervation, both shown to be fundamental in HSCs regulation (Mendez-Ferrer et al., 2008). Nevertheless, this study suggested that the endosteal area is converted into a stimulatory environment that promotes HSC expansion after irradiation. At the same time, Lo Celso et al. performed IVM of single engrafting HSCs by focusing on the BM contained in the frontal bones of the mouse skull (calvarium) and obtained 3D measurements indicating that engrafting HSCs selectively localize in proximity of osteoblastic cells and endosteal vessels, while their progeny are more distal (Lo Celso et al., 2009). Multiple groups have developed new methods that allow for the *in vivo* imaging of the long bones. Köhler et al. thinned the tibeal compact bone to reveal differential positioning and activity of young and aged HSCs (Kohler et al., 2009). Lewandowski et al. used a miniaturised endoscope to capture what remains the only live imaging of central marrow in the femur, albeit achieved with an invasive imaging technique (Lewandowski et al., 2010). Very recently, Pitt and colleagues used 2-photon live imaging of shaved tibias to enquire about the interaction between T-ALL cells and CXCL12-producing stromal cells in the BM (Pitt et al., 2015). Chronic imaging of long bones has been achieved through the development of imaging windows analogous to others used in the brain and abdomen. These imaging windows have been applied to both the thinned femur (Chen et al., 2016b) and the thinned tibia (Kim et al., 2016). Although real-time imaging of the femur and tibia has the advantage of studying stem and progenitor cell behaviour in bones that sustain the majority of the adult mouse steady-state haematopoiesis, it also presents significant problems that limit their present utility. One of these is the skeletal shaving required to make the marrow space underlying the bone optically accessible. A bone thinning of around 200 μm is done with a micro drill, can easily lead to tissue disruption and bleeding, and is bound to trigger a repair response that will likely affect at least some stroma cells in the BM. Another pitfall of the method is that it maintains a bias towards the recording of events occurring next to the

endosteum. Finally, the image resolution obtained with IVM of long bones is often lower in comparison to that of calvarium imaging.

Calvarium BM imaging was pioneered by the von Andrian group, using epifluorescence microscopy (Mazo et al., 1998). One of the main advantages of this method is that because the bone plate is very thin, shaving is not required. Therefore, the BM can be imaged non-invasively and without altering tissue architecture. Recent refinements have shown that further higher quality in the imaging can be achieved after laser-mediated osteotomy of the calvarium (Turcotte et al., 2014). Here the laser is expected to cause less damage than the conventional drills used on the long bones, however this approach would not be easily implemented to shave those much thicker areas. One of the concerns often raised with the use of the calvarium for the study of HSCs and their niches is how its BM compares with well-described compartments in long bones. This has been disputed by Lo Celso and colleagues and by Lassailly and colleagues, who demonstrated that while the calvarium is a flat bone resulting from intramembranous ossification, it is as representative as the femur and the tibia in the study of haematopoiesis (Lassailly et al., 2013; Lo Celso et al., 2009).

Building on the original work by Mazo and co-workers, IVM of the calvarium was also used to image platelet formation from megakaryocytes (Junt et al., 2007), T cells (Cavanagh et al., 2005), B cells (Cariappa et al., 2005) and dendritic cells (Sapoznikov et al., 2008). This technique was later expanded by the groups of David Scadden, Charles Lin and us to obtain images of the BM with higher resolution (Lo Celso et al., 2009; Sipkins et al., 2005). Through the combination of LSCM with MP microscopy, Lo Celso et al. were able to increase the number of components analysed and reported the first *in vivo* measurement of transplanted HSCs localisation in relation to the osteoblastic and vascular niche compartments (Lo Celso et al., 2009). Recently, our group developed a protocol that enables long time-lapsing and repeated cycles of imaging and recovery using a calvarial window and high-precision mouse holder (Scott et al., 2014). Using this approach, it was possible to uncover the *in vivo* migratory pattern of some HSCs (Rashidi et al., 2014). In contract to stationary steady state, infection-exposed HSCs are motile and engage with larger surrounding BM niches within the first 24 hours from injection (Rashidi et al., 2014). Using this technological platform we have also recently uncovered the migratory behaviour of niche-agnostic T-ALL cells throughout disease progression (Hawkins et al., 2016). Dominique Bonnet and colleagues have recently adapted the IVM setup used to image the mouse calvarium (Lo Celso et al., 2009) to visualize human HSCs transplanted into NSG

mice. Foster et al showed that while haematopoietic progenitor cells remain motile after homing to the BM, HSCs are only transiently migratory until complete arrest next to hypothetical niche areas (Foster et al., 2015). This confirms previous observations with transplanted mouse HSCs (Rashidi et al., 2014) and suggests that long-lasting engagement with the niche is important for haematopoietic reconstitution (Lapidot et al., 2005). These data suggest that HSCs require long-lived interactions with surrounding microenvironments.

1.4.3 – Osteoblasts and the endosteal niche

Studies describing an endosteal-biased spatial distribution of progenitor cells in the BM first suggested the importance of bone in the regulation of haematopoiesis and the existence of an endosteal niche (Lord et al., 1975). Phenotypically-defined HSCs are enriched in the trabecular area, or metaphysis (Nombela-Arrieta et al., 2013) and transplanted HSCs localize very close to the endosteum (Lo Celso et al., 2009). Guezguez, Bhatia and co-workers performed elegant immunofluorescence imaging of bone sections from human BM biopsies and from immunodeficient mice transplanted with human $CD34^+$ cells and showed that human HSCs are preferentially located in the trabecular bone (Guezguez et al., 2013). The authors nicely compared the whole-tissue distribution of stem *versus* progenitor cells and concluded that HSCs were more concentrated in endosteal areas. In these regions, osteoblasts line the bone and are a key cell type. Osteoblasts derive from MSC differentiation and are responsible for synthesizing and depositing components of the bone matrix. Once osteoblasts become included in the matrix, they are designated osteocytes. Consistently with the observed spatial distribution of HSCs, it was first proposed that osteoblasts were a principal niche component. Human osteoblasts were shown to produce haematopoietic growth factors, such as G-CSF and to support primitive haematopoietic cells *in vitro* (Taichman and Emerson, 1994). The first *in vivo* demonstration of a HSC niche was achieved years later through the demonstration of HSC expansion following the expansion of osteoblasts (Calvi et al., 2003; Zhang et al., 2003). Furthermore, quiescent HSCs were shown to be directly in contact with osteoblasts (Arai et al., 2004) and enriched in the endosteum (Wilson et al., 2004; Zhang et al., 2003). The direct role of osteoblasts was however put into question. *In vivo* deletion of osteoblasts (Visnjic et al., 2004) consistently led to reduction in the number of HSCs but only after the reduction of more committed haematopoietic progenitors. The specific deletion of the HSC maintenance factors SCF (Ding et al., 2012b) and CXCL12 (also

known as stromal cell-derived factor 1, SDF1) (Ding and Morrison, 2013; Greenbaum et al., 2013) in osteoblasts did not led to a decrease of HSC numbers. Moreover, the precise nature of a N-Cahderin^{+} HSC fraction that establishes homophilic interactions and engages with N-Cadherin-expressing osteoblasts (Zhang et al., 2003) has been put into question (Kiel et al., 2009; Li and Zon, 2010). Altogether, these data suggest that osteoblasts might be indirect, rather than direct, regulators of HSCs (Morrison and Scadden, 2014).

1.4.4 – Blood vessels and the vascular niche

The bone-lining endosteum and bone-rich metaphysis are highly vascularized and a strict niche categorization based on stromal composition might be artificial, as nicely illustrated by the preferential localisation of transplanted HSCs to endosteal blood vessels (Ellis et al., 2011). The interdependency between bone and vasculature is well demonstrated by a specific type of endosteal and metaphyseal endothelium expressing high levels of both CD31 and endomucin (Emcn) (type H endothelium), shown to couple angiogenesis to osteogenesis (Kusumbe et al., 2014).

Despite the consensus for the existence of a perivascular niche in adult haematopoiesis (Morrison and Scadden, 2014), there is controversy regarding the exact nature of blood vessels that neighbour HSCs, i.e. whether these are sinusoids or arterioles. Furthermore, we are only now starting to appreciate the heterogeneity of the BM vasculature (Kusumbe et al., 2014) and more specific endothelial cell (EC) transgenic mouse lines (as opposed to the pan-endothelial Tie2-Cre, for example) are expected to illuminate the field in the future. Nevertheless, advanced imaging of the BM has suggested that HSCs are non-randomly distributed and locate close to blood vessels and perivascular stromal cells (discussed below). The use of SLAM markers in immunofluorescence allowed the identification of steady state phenotypically defined populations enriched for HSC. Using this strategy, Kiel et al found Lin^{-}CD41^{-}CD48^{-}CD150^{+} HSCs localizing adjacently to sinusoids (Kiel et al., 2005). Importantly, immunofluorescence studies can be approached with same type of analysis used for flow cytometry, but to obtain refined spatial information. Laser scanning cytometry takes this concept further and merges LSCM with an automated flow cytometry-like acquisition (Harnett, 2007). While traditional immunofluorescence imaging focuses on specific fields of view, laser scanning cytometry expands the image acquisition to much larger areas, thereby decreasing biases inherent to subjective area selection. Using this technology, Nombela-

Arrieta and colleagues were able to show that phenotypic HSPCs preferentially localized next to endosteal blood vessels, although hypoxic HSPCs were found throughout the BM cavity (Nombela-Arrieta et al., 2013).

In recent years, several groups have perfected imaging of thick BM sections (over 300 μm thickness). Typically, the bone of interest is either cryosectioned from both sides or cut in half and stained (Acar et al., 2015; Kunisaki et al., 2013). Alternatively, BM plugs are obtained through flushing with a syringe (Acar et al., 2015; Chen et al., 2016a). In this way, it is possible to optically section the sample and 3D reconstruct what is often called a BM whole-mount. Bones used for whole-mount preparation include the sternum (Kunisaki et al., 2013), femur (Nombela-Arrieta et al., 2013) and tibia (Acar et al., 2015; Chen et al., 2016a). This technique can be accompanied by tissue clearing, initially developed for and popularized in neuroscience studies (Chung et al., 2013). The clearing process makes deeper areas optically accessible but can significantly alter tissue morphology and intrinsic fluorescence and requires long troubleshooting for the selection of the best method. Clearing strategies used for the bone to visualize HSCs include modified Murray's clear (Acar et al., 2015; Becker et al., 2013), 3DISCO (3D imaging of solvent-cleared organs) (Acar et al., 2015; Erturk et al., 2012), CUBIC (Clear, Unobstructed Brain/Body Imaging Cocktails and Computational analysis) (Chen et al., 2016a; Susaki et al., 2014) and TDE (2,2′-thiodiethanol) clearing (Coutu et al., 2018). Kunisaki and colleagues were able to show that in sternum whole-mounts, dormant $Lin^-CD41^-CD48^-CD150^+$ HSCs located near arterioles, which are surrounded by other important stromal cells, such as $Nestin^+$ MSCs and sympathetic nerve fibres (Kunisaki et al., 2013). This observation was opposed by a study from Acar et al (Acar et al., 2015). In this report, the authors used optically cleared tibias to perform deep imaging of the BM and showed that non-dividing α-catulin-GFP^+ HSCs did not have a specific spatial patterning in relation to arterioles. Interestingly, Chen et al using Hoxb5 as an HSC reporter and cleared BM plugs of the tibia, propose that in fact LT-HSCs are virtually all next to VE-$Cadherin^+$ blood vessels (Chen et al., 2016a). Several reasons can explain the differences between the reports, including the different bones analysed (tibia vs. sternum) and the different methods used to identify HSCs (phenotypic $Lin^-CD41^-CD48^-CD150^+$ HSCs vs. α-$catulin^+$ HSCs vs. $Hoxb5^+$ HSCs) (see section 1.1.1).

The manipulation of ECs and angiocrine factors also favours the vascular niche hypothesis. Conditional deletion of VEGFR2 and inhibition of VEGFR2 signalling prevented regeneration of sinusoidal blood vessels, engraftment of HSPCs and haematopoietic recovery

post-irradiation (Hooper et al., 2009). Interestingly, endothelial-cell specific deletion of VEGFR2 disrupted spherical endothelial structures termed haemospheres located in the periphery of the BM cavity and found to be associated with phenotypic HSCs and clonal haematopoietic expansion (Wang et al., 2013). The central role of blood vessels in HSC regulation is highlighted by the fact that ECs produce critical HSC maintenance factors, such as SCF and vascular endothelial growth factor (VEGF). Indeed, cultured ECs are able to maintain self-renewal of HSCs *in vitro*, through the production of angiocrine growth factors and Notch ligands (Butler et al., 2010). Recently, it was shown that Notch signalling in endosteal blood vessels is essential for the *in vivo* expansion of HSCs and that these specialized type H vascular microenvironments are lost during aging (Kusumbe et al., 2016). The *in vivo* deletion of key HSC maintenance factors in different BM cell populations by Sean Morrison's group has further suggested that endothelial cells and perivascular stromal cells (discussed below) are the main niches for HSCs. The specific deletion of SCF (Ding et al., 2012b) and CXCL12 (Ding and Morrison, 2013) in ECs (Tie2-Cre) depleted HSCs *in vivo*. Moreover, a recently described HSC niche factor, pleiotrophin (Himburg et al., 2010) is expressed in sinusoidal ECs (Himburg et al., 2012). The *in vivo* deletion of pleiotrophin led to a loss of both HSC self-renewal and retention in the BM (Himburg et al., 2012).

Using LSCM of the skull's frontal bones, Sipkins et al showed preferential localisation of HSPCs and leukaemia cells to specific BM endothelial microdomains expressing high levels of E-selectin and CXCL12, which facilitates homing by binding to CXCR4 (Sipkins et al., 2005). Live imaging of the calvarium has also recently contributed to the functional assessment of BM areas and blood vessels. Spencer and colleagues used two-photon phosphorescence lifetime microscopy to directly measure the local oxygen tension in the BM of live mice (Spencer et al., 2014). Unexpectedly, they found that the perisinusoidal zone was more hypoxic when compared to the endosteal part that is preferentially irrigated by arterioles lined by $Nestin^{+}$ cells. Another study by Itkin et al. also used IVM of the calvarium to question how different population of BM blood vessels regulate haematopoiesis (Itkin et al., 2016). According to their study, sinusoids are more permeable to reactive oxygen species (ROS) that in turn induce HSPCs to migrate and differentiate. In contrast arterial vessels are less permeable and therefore maintain HSCs in a less activated state. In a recent study by Tamplin, Durrand and colleagues (Tamplin et al., 2015), confocal live imaging and correlative light and electron microscopy (CLEM) of zebrafish was performed to visualize previously unseen dynamics of the perivascular niche. The authors showed endothelial cells

wrapping around single HSCs and mesenchymal stromal cells engaging with stem and progenitors cells and directing their divisions.

1.4.5 – Mesenchymal stem cells and the perivascular niche

MSCs are a heterogeneous group of stromal cells with self-renewing capacity and able to differentiate into adipocytes, chondrocytes, osteoblasts and other stromal cells. In the BM, MSCs are reticular cells mainly found in the perivascular space that participate in the regulation of HSCs as part of the so-called perivascular niche. Alternatively, the term mesenchymal *stromal* cell is often used to designate other perivascular stromal cells (e.g. pericytes) that are not MSCs but that belong to the mesenchymal lineage and play a role in HSC maintenance. Several markers (e.g. Nestin (Nes), NG2, LepR, CD146) are used to define MSCs with different phenotypes, that are in fact often partially or totally overlapping populations. The use of different Cre and reporter mouse lines to mark MSCs also contributes to the confusion about the exact identity of these niche cells. For example, Nes-Cre and LepR-Cre mark both the targeted cells and all their progeny; NG2-Cre and Nes-GFP marked cells are nearly overlapping, however Nes-GFP and NG2-Red less so (Kunisaki et al., 2013). Around 90% of the cells marked by LepR-Cre and 80% of the cells marked by NG2-Cre are CAR cells (Asada et al., 2017). Nevertheless, it is consensual that MSCs directly regulate HSC maintenance.

Using CXCL12-GFP knock-in mice, Sugiyama and colleagues identified perivascular (and frequently, perisinusoidal) CAR cells spatially associated with phenotypic HSCs (Sugiyama et al., 2006). Upon depletion of CAR cells, HSCs were reduced in numbers albeit being more quiescent (Omatsu et al., 2010). It was later shown that the selective deletion of CXCL12 from Prx1-cre-expressing mesenchymal cells led to a loss of HSCs and HSC activity (Greenbaum et al., 2013). Histological analysis revealed the association of human HSCs with human perivascular $CD146^+$ MSCs (Sacchetti et al., 2007). This study also showed that $CD146^+$ MSCs express the important niche factor angiopoietin-1. Mendez-Ferrer and colleagues showed that HSCs are in the vicinity of and regulated by $Nestin^+$ MSCs (Mendez-Ferrer et al., 2010). Later, it was shown that human fetal $PDGFR\alpha^+$ $CD51^+$ cells expressing Nestin represent a subset of $CD146^+$ MSCs that are enriched for HSC activity (Pinho et al., 2013). Nestin-expressing cells from Nes-GFP mice were further sub-classified based on the level of GFP expression: a $Nes\text{-}GFP^{bright}$ fraction surrounding arterioles and

overlapping with the pericyte marker NG2 and a Nes-GFP^{dim} fraction surrounding sinusoids (Kunisaki et al., 2013). Importantly, periarteriolar NG2^{+} MSCs were shown to be in close contact with quiescent HSCs (Kunisaki et al., 2013). Alternatively, Ding et al. showed that the important HSC niche factor SCF was highly expressed by LepR-Cre-expressing perivascular cells (Ding et al., 2012b). When SCF was selectively deleted in LepR^{+} stromal cells, HSCs were depleted from the BM (Ding et al., 2012b). Deletion of CXCL12 in the same LepR^{+} population led to a mobilization of HSCs and progenitors from the BM to the peripheral blood (Ding and Morrison, 2013). In an attempt to resolve the discrepancies between these different reports, Asada and colleagues recently showed that Nes-GFP^{+} MSCs are fundamental sources of both SCF and CXCL12 and that the deletion of either factor in these cells reduces HSC cell numbers (Asada et al., 2017). Alternatively, the selective deletion of CXCL12, but not SCF, in periarteriolar NG2^{+} MSCs and the specific deletion of SCF, but not CXCL12, in perisinusoidal LepR^{+} stromal cells cause a reduction in HSC numbers (Asada et al., 2017). This study highlights the heterogeneous niche factor contribution from different stroma niche cells.

1.4.6 – Other BM microenvironments

In addition to the classical microenvironmental compartments discussed above, additional cell types in the BM are integrated in the HSC niche. Adrenergic sympathetic neurons are intimately associated with Nestin^{+} MSCs, secrete noradrenaline and regulate the circadian release of HSCs and expression of niche factors (Mendez-Ferrer et al., 2008). Fat-enriched yellow marrow has been classically associated with decreased haematopoietic activity and adipocytes were shown to be negative regulators of HSCs (Naveiras et al., 2009). BM glial non-myelinating Schwann cells that wrap autonomic nerves produce the niche factor TGF-β, associate with and maintain quiescent HSCs (Yamazaki et al., 2011). Osteoclasts were shown to promote the endosteal niche formation and the mobilization of haematopoietic progenitors from the BM (Kollet et al., 2006; Mansour et al., 2012). T regulatory (T_{reg}) cells provide immune privilege to the endosteal HSC microenvironment (Fujisaki et al., 2011). Megakaryocytes are also associated with quiescent HSCs and their deletion causes HSCs to enter cell cycle (Bruns et al., 2014; Zhao et al., 2014).

It is also important to identify the factors that regulate HSCs in a cell extrinsic manner and that are secreted by anatomically or phenotypically defined niches. Fundamental niche

factors differently secreted by endothelial cells and perivascular stromal cells include CXCL12 (Asada et al., 2017; Ding and Morrison, 2013; Greenbaum et al., 2013; Omatsu et al., 2010; Sugiyama et al., 2006), SCF (Asada et al., 2017; Ding et al., 2012b) and VEGF-A (Hooper et al., 2009), which were discussed in sections 1.4.4 and 1.4.5. One of the first recognized factors shown to induce the quiescence of Tie2-expressing HSCs *in vivo* was endosteal-born angiopoietin 1 (ANGPT1) (Arai et al., 2004). Another factor highly secreted by osteoblasts is osteopontin (OPN). OPN knock-out mice have an increased HSC pool size (Stier et al., 2005). Furthermore, OPN regulates the homing and quiescence of HSCs (Nilsson et al., 2005). Recently, the RNase angiogenin (ANG) was shown to simultaneously promote HSC quiescence and myeloid progenitor proliferation through differential regulation of RNA processing (Goncalves et al., 2016).

1.5 – Leukaemia-microenvironment crosstalk

It has been speculated that leukaemia cells highjack (Ishikawa et al., 2007; Lane et al., 2009), and destroy (Colmone et al., 2008) HSC-supportive microenvironments potentially shifting the equilibrium of microenvironments from a state that supports steady state haematopoiesis in favour of conditions that instead lead to accelerated expansion of leukemic cells or even to leukaemogenesis and development of chemoresistance. Thus, understanding the role of microenvironments in leukaemia initiation, progression and development of chemoresistance (Figure 1.5) is critical for development of novel therapeutic interventions.

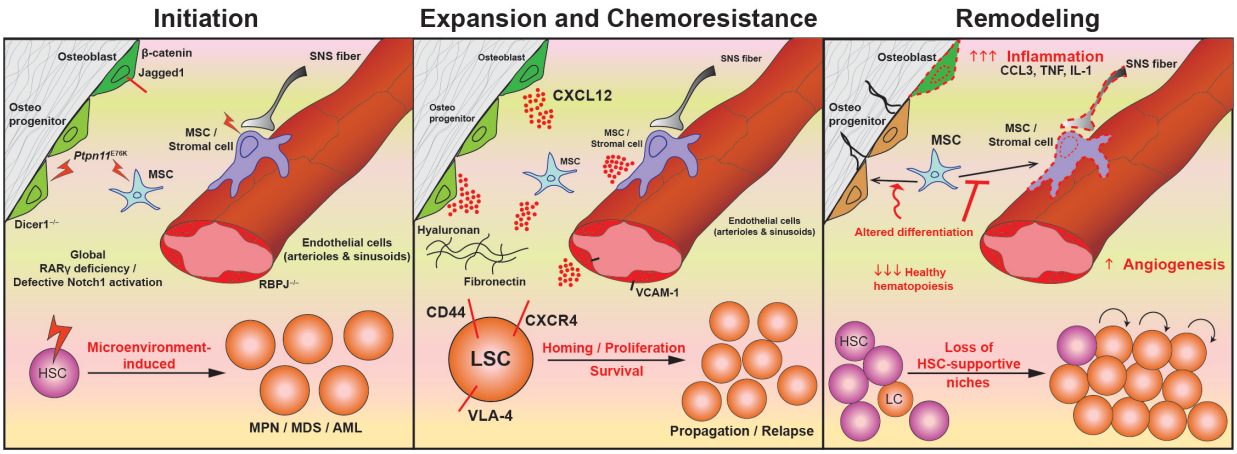

Figure 1.5 – The crosstalk between leukaemic cells and the microenvironment. Several studies suggest a causative role of the BM microenvironment in leukaemogenesis (**Initiation**). Additionally, LSC co-opt existing strategies normally used by HSCs to interact with the microenvironment and proliferate and survive (**Expansion and Chemoresistance**). LSC use adhesion molecules (CD44 and VLA-4) to bind the extracellular matrix and stroma cells and through CXCR4 they bind the abundantly secreted CXCL12. Leukaemia also shapes the microenvironment (**Remodelling**) by creating a pro-inflammatory milieu, impairing MSC differentiation and destroying key HSC-supportive niches. Adapted from (Duarte et al., 2018b).

1.5.1 – Leukaemia initiation

It has been suggested that an altered BM niche can promote leukaemogenesis. Clinically, this is best illustrated by donor cell leukaemia (Wiseman, 2011), where leukaemia originates from engrafted donor cells after allogeneic HSC transplantation (although drug-induced effects are hard to exclude). In mouse models, onset pre-leukaemic myeloproliferative-like disease has been observed after manipulation of the microenvironment. Specifically, after loss of retinoic acid receptor gamma in non-haematopoietic cells (Walkley et al., 2007) and defective Notch signalling (either endothelial-specific (Wang et al., 2014) or global (Kim et al., 2008)) and after targeted expression of *Ptpn11* activating mutations in MSCs and osteoprogenitors (mutation of a positive regulator of RAS signalling found in Noonan syndrome) (Dong et al., 2016). Furthermore, a condition similar to myelodysplastic syndrome with sporadic AML/myeloid sarcoma development was observed after specific deletion of the endoribonuclease *Dicer1* in osteprogenitors (Raaijmakers et al., 2010). In these mice, mutated osteoprogenitors expressed lower levels of *Sbds*, the gene mutated in Shwachman-Bodian-Diamond Syndrome (a condition characterized by BM failure, and occasional myelodysplastic syndrome development and secondary AML). Interestingly, deletion of *Sbds* in osteprogenitors mimicked the phenotype observed in *Dicer* loss. Additionally, targeted overexpression of β-catenin in osteoblasts was shown to induce transformation of HSCs and promote AML development (Kode et al., 2014). This is mediated by the downstream overexpression of the Notch ligand Jagged-1 in osteoblasts that promote the transformation of haematopoietic progenitors. Although these data support the view that the microenvironment has a key role in causing or promoting the growth of cancer cells harbouring cell intrinsic changes, it is still uncertain whether these changes in the microenvironment are alone causative of human leukaemias (Sanchez-Aguilera and Mendez-Ferrer, 2017).

1.5.2 – Leukaemia propagation and development of chemoresistance

There is an increasingly popular view that cancer follows a Darwinian-like evolution, in which microenvironmental changes, often induced by the malignant cells themselves, contribute to the selection and expansion of better-adapted malignant clones (DeGregori, 2017). It is not clear whether the microenvironment facilitates the propagation of pre-leukaemic clones. Clonal haematopoiesis is a recently described entity in which clonally expanded hematopoietic cells harbouring somatic mutations are found in persons with no history of haematological malignancy (Genovese et al., 2014; Jaiswal et al., 2014; McKerrell et al., 2015; Xie et al., 2014). It is present in more than 10% of individuals over 70 years old and it is associated with increased all-cause mortality and with a 10-fold higher incidence of hematologic cancer (Genovese et al., 2014; Jaiswal et al., 2014). The methyltransferase *DNMT3A* is the most commonly mutated gene in clonal haematopoiesis (Genovese et al., 2014; Jaiswal et al., 2014; Xie et al., 2014) and is commonly mutated in leukaemia (reviewed in (Brunetti et al., 2017)). Consistently, *Dnmt3a*-null HSCs have increased self-renewal capacity and expand preferentially in competitive transplantation assays (Challen et al., 2011). Moreover, $DNMT3A^{mut}$ pre-leukaemic HSCs were shown to outcompete wild-type HSCs and to survive in AML patients in remission (Shlush et al., 2014). There is evidence that an aged BM microenvironment favours the expansion of single dominant HSPCs clones (Vas et al., 2012). Whether the competitive fitness of $DNMT3A^{mut}$ pre-leukaemic cells is purely driven by cell intrinsic mechanisms or whether the microenvironment is also taking part is currently unexplored. As described above, AML is hierarchically organized and descendant of rare LSCs (Bonnet and Dick, 1997; Lapidot et al., 1994). It is believed that LSCs hijack HSC niches that in turn support the expansion, survival and relapse of leukaemia (Ishikawa et al., 2007; Lane et al., 2009).

Numerous studies explored the influence of the CXCR4/CXCL12 pathway in the regulation of leukaemia-stroma interactions. These interactions support leukaemia cells that express high levels of CXCR4 and bind the chemokine CXCL12 (also known as SDF-1α), secreted by multiple BM stromal cells. Using genetic models and CXCR4 antagonists (e.g. AMD3100/plerixafor), it was shown that CXCL12 promotes the homing, residence and survival of leukaemic cells in the BM (Nervi et al., 2009; Pitt et al., 2015; Tavor et al., 2004; Zeng et al., 2009). These studies provided the rationale for clinical trials (proved safe in AML (Uy et al., 2012)) and for the development of new CXCR4 antagonists, with prolonged half-life and higher potency (Abraham et al., 2017). It is however not well understood how

short-acting CXCL12 gradients control leukaemic cell behaviours (e.g. cell migration) within the marrow tissue. In addition to CXCR4, there are other molecules expressed by leukaemic cells and shown to be very important in their adhesion to and survival in the BM microenvironment. Chemoresistance is enhanced in leukaemic cells expressing the integrin VLA-4, which binds fibronectin (Matsunaga et al., 2003) and VCAM-1 (Jacamo et al., 2014) expressed by the BM stroma. Another key adhesion molecule in leukaemia is the glycoprotein CD44, which binds hyaluronic acid in the extracellular matrix. LSCs in both CML (Krause et al., 2006) and AML (Jin et al., 2006) require CD44 to home and engraft efficiently.

More recently, our group challenged the view that all leukaemic cells depend on particular niches. Using IVM, we tracked T-ALL cells in real time at different disease stages (Hawkins et al., 2016). The *in vivo* imaging of whole BM tissue revealed that seeding T-ALL cells are stochastically distributed in relation to Col2.3^{+} osteoblasts, Nestin^{+} MSCs and blood vessels. Contrarily to the popular view that leukaemic cells are immotile, we observed that T-ALL cells are continuously migratory.

1.5.3 – Bone marrow remodelling

The decay of HSC-supportive niches supports the view that leukaemic cells outcompete HSCs (Boyd et al., 2014) by re-shaping the BM microenvironment. This is well illustrated by the destruction of BM microenvironments induced by xenotransplanted ALL cell lines (Colmone et al., 2008; Duan et al., 2014). Importantly, the leukaemia-driven remodelling can promote the loss of bone homeostasis and healthy haematopoiesis and also lead to the expansion and survival of the leukaemia itself. For example, precursor B ALL cells were shown to secrete CCL3, recruit Nestin^{+} MSCs from sinusoidal niches and promote their transition into α-SMA^{+} cells (through TGF-β) to form chemo-protective islands (Duan et al., 2014).

The BM microenvironment re-shaping was well characterized in a model of CML by the modification of MSCs differentiation into aberrant osteoblasts that promote leukaemia growth and neglect the maintenance of normal haematopoiesis (Schepers et al., 2013). Similarly, in a model of MLL-AF9 AML, sympathetic neuropathy ensues and limits the differentiation of Nestin^{+} MSCs into NG2^{+} periarteriolar cells that normally support HSCs (Hanoun et al., 2014). In *JAK2*^{V617F}-induced myeloproliferative neoplasia (MPN), HSC-

supporting Nestin$^+$ MSCs are critically reduced. Interestingly, the specific depletion of Nestin$^+$ MSCs causes expansion of hematopoietic progenitors and an MPN-like phenotype, highlighting the interplay between niche and leukaemic cells (Arranz et al., 2014). In MPN patients and MPN mice there is also a loss of sympathetic nerve fibers and nonmyelinating Schwann cells next to Nestin$^+$ cells (Arranz et al., 2014). This remodelling is mediated by IL-1β and can be partially reverted by pharmacological treatment (Arranz et al., 2014).

The factors driving the remodelling of the BM microenvironment in leukaemia are not well understood but inflammation (an hallmark of cancer (Hanahan and Weinberg, 2011)) appears to be a key player. The pro-inflammatory environment is driven by different cytokines, depending on the model used and leukaemia type studied, and include: tumour necrosis factor (TNF) (Mead et al., 2017; Wang et al., 2014), IL-1β (Arranz et al., 2014; Schepers et al., 2013) and CCL3 (Duan et al., 2014; Schepers et al., 2013). Other recently described factors mediating the leukaemia-induced remodelling of the microenvironment are leukaemia-derived exosomes that transport microRNAs (Kumar et al., 2017). Exosomes are small extracellular vesicles emerging as key players in cell-cell communication in cancer (Skog et al., 2008).

It should be highlighted that, although there is some redundancy, different types of leukaemia might interact differently with the microenvironment (Krause et al., 2013). LSCs in AML (Lapidot et al., 1994) and CML (Sirard et al., 1996) are well characterised and have previously been suggested to have an altered dependency on the endosteal niche, and specifically osteoblastic cells after parathyroid hormone treatment (Krause et al., 2013). In this context, the expansion of osteoblastic cells promotes the propagation of MLL-AF9 driven AML while it halts BCR-ABL CML-like disease (Krause et al., 2013).

The understanding of how leukaemic cells co-opt and disrupt HSC niches will help designing new therapies that target the microenvironment to restore healthy haematopoiesis, improve HSC transplantation and limit disease relapse. The combination of therapies that target cell-intrinsic mechanisms with new CXCR4 antagonists (Abraham et al., 2017; Pitt et al., 2015), small molecules targeting cell adhesion (Jin et al., 2006; Krause et al., 2006) and anti-inflammatory therapies (Mead et al., 2017) has the potential to improve disease outcomes in leukaemia. Furthermore, changes of the BM stroma from leukaemic patients may be used as prognostic factors (Kim et al., 2015) and help guide treatments in the future.

1.6 - Project aim and research questions

My aim is to understand the interaction between T-ALL and AML cells and the surrounding BM microenvironment. I will focus on three questions:

1) Does AML remodel the HSC vascular niche? **(Chapter 3)**

2) Is T-ALL chemoresistance dependent on specific BM niches? **(Chapter 4)**

3) What is the *in vivo* effect of chemotherapy and CXCR4 antagonism on T-ALL and AML migratory cell behaviour? **(Chapter 5)**

I will approach these problems using a combination of flow cytometry, IVM and immunofluorescence.

Chapter 2

Materials and Methods

2.1 – Reagents

Reagent	Component	Source	Catalogue
TAE buffer	40 mM Tris	Sigma	0000000107 08976001
	20 mM Acetic Acid	Sigma	71251
	1 mM Ethylenediaminetetraacetic acid solution (EDTA) pH 8.0	Sigma	E9884
FACS buffer	Dulbecco's Phosphate Buffered Saline (PBS)	Sigma	D8537
	2% Fetal Bovine Serum (FBS) heat inactivated	Life technologies	10500-064
Red Cell Lysis Buffer	0.001 g/ml Potassium bicarbonate	Sigma	60339
	0.008 g/ml Ammonium chloride	Sigma	A9434
	20mM EDTA	Sigma	3690
	5% (v/v) FBS	Life technologies	10500-064
	Milli-Q© water		
Collagenase solution	0.25% (w/v) Collagenase, Type I, powder	Gibco	17018029
	Hank's Balanced Salt Solution (HBSS)	Gibco	14175-053

Reagent	Component	Source	Catalogue
D10+ Medium	Dulbecco's Modified Eagle Medium (DMEM)	Sigma	D6429
	2% FBS heat inactivated	Life technologies	10500-064
	1% L-Glutamine	PAA Laboratories	M11-004
	1% Penicillin / Streptomycin	PAA Laboratories	P11-010
Transduction Medium	DMEM	Sigma	D6429
	10% FBS heat inactivated	Life technologies	10500-064
	50 μM (1:1000 of stock) 2-Mercaptoethanol	ThermoFisher	21985023
	1% MEM Non-essential Amino Acid Solution	Sigma	M7145
	Cytokines added just before platting of cells:		
	Recombinant Human IL-6 (10 ng/ml)	Peprotech	200-06
	Recombinant Murine IL-3 (10 ng/ml)	Peprotech	213-13-10
	Recombinant Murine SCF (20 ng/ml)	Peprotech	250-03
LKS medium	StemSpan™ Serum Free Expansion Medium	STEMCELL Technologies	9650
	50 ng/ml Recombinant Murine SCF	Peprotech	250-03
	10 ng/ml Recombinant Human IL-6	Peprotech	200-06
	10 ng/ml Recombinant Murine TPO	Peprotech	315-14
	20 ng/ml Recombinant Murine Flt-3 ligand	Peprotech	250-31L
Periodate-lysine-paraformaldehyde fixative (PLP)	0.075 M L-Lysine monohydrochloride	Sigma	L5626
	1% paraformaldehyde (PFA)	Sigma	P6148
	0.01 M Sodium-M-Periodate	Sigma	71859
	0.1 M Na_2HPO_4 'Dibasic' solution	Sigma	71640
	0.1 M NaH_2PO_4 'Monobasic' solution	Sigma	71507
	0.1 M Phosphate Buffer		
	* 3 parts of Dibasic and 1 part of Monobasic		

Table 2.1 – Reagents used and their specific components.

2.2 – Mice

2.2.1 - Ethics

All animal work was in accordance with the animal ethics committee at Imperial College London, UK and UK Home Office regulations (ASPA 1986). The work described here was done under the project licenses 70/7061 and 70/8403. I performed regulated procedures after accreditation by the Society of Biology (IMP/14/163) and after obtaining a personal license (I612F6C83).

2.2.2 – Animal lines

Flk1-GFP mice were a gift from Alexander Medvinsky (University of Edinburgh) (Xu et al., 2010), PU1-YFP mice were a gift from Claus Nerlov (University of Oxford) (Kirstetter et al., 2006), Col2.3-GFP (Hawkins et al., 2016) and Col2.3-CFP (Paic et al., 2009) were a gift from David Rowe (University of Connecticut Health Center); Fbxw7$^{lox/lox}$ Cdh5(PAC)-CreERT2$^{T/+}$ mice were a gift from Ralf Adams (Max Planck Münster) and Anjali Kusumbe (University of Oxford) (Kusumbe et al., 2014). C57Bl6 mice were from Charles River and Harlan UK Ltd; Nestin-GFP were a gift from Simon Mendez-Ferrer (Mignone et al., 2004) and mT/mG (Muzumdar et al., 2007) were purchased from Jackson Laboratories (Stock No: 007576; ME, USA). All mice were bred and housed at Imperial College London. For fluorescence-activated cell sorting (FACS) experiments 6-8 weeks old female WT mice were used. For imaging experiments, male and female Col2.3-GFP, Nestin-GFP, Col2.3-CFP/Flk1-GFP and Col2.3-CFP/Nestin-GFP mice >8 weeks old were used. NOD/SCID/γ (NSG) mice were a gift from Dominique Bonnet (The Francis Crick Institute) (Hawkins et al., 2016) and were bred and maintained at the London Research Institute, Cancer Research UK.

2.2.3 – Genotyping

Flk1-GFP and Nestin-GFP mice were genotyped by mounting an ear snip in a slide and analysing the presence of GFP signal emitted by blood vessels or reticular cells under the microscope. PU1-YFP and mT/mG mice were genotyped by analysing the YFP and mTomato signals by flow cytometry in peripheral blood cells obtained by tail bleeds. Col2.3-GFP and Col2.3-CFP mice were genotyped by analysing the presence of GFP and CFP signals emitted by bones of newborn pups with ‘GFP goggles’ (Model GFsP-0; BLS Ltd., HU), which have a blue light source and appropriate filters. Fbxw7$^{lox/lox}$ Cdh5(PAC)-

CreERT2$^{T/+}$ mice were either already genotyped or genotyped by polymerase chain reaction (PCR). To obtain genomic DNA, ear snips were digested in 45 µl lysis buffer (50 mM KCl, 10 mM Tris-HCl pH 9.0 and 0.1% Triton X-100) with 5 µl proteinase K at 60˚C for 2 hours, shaking at 850rpm. Then, 150 µl of nuclease-free water was added and sample was incubated at 95ºC for 30 minutes. The samples were then centrifuged at 19,314 x *g* for 2 minutes at room temperature and the supernatant transferred to a new 1.5 ml Eppendorf tube. A PCR reaction was set by mixing 12.5µl of dNTP, polymerase and $MgCl_2$-containing GoTaq G2 Green Master Mix (Promega, Cat. # M7822), 1 µM forward primer, 1 µM reverse primer, 9.5µl of nuclease-free water and 1µl of DNA. For Fbxw7 primers, the following thermal cycling was used: (1) 94°C for 2:00 min; (2) 94°C for 0:45 min; (3) 60°C for 0:45 min; (4) 72°C for 1:00 min; (5) go to step 2) 34 cycles; (6) 72°C for 5:00min; (7) 4°C forever. For Cre primers, the following thermal cycling was used: (1) 94°C for 0:30 min; (2) 70°C for 0:30 min; (3) 72°C for 1:00 min; (4) go to step 1) 34 cycles; (5) 72°C for 10:00min; (6) 4°C forever. The PCR reactions were analysed on a 1.5% agarose gel (1.5g agarose in 100ml 1x TAE buffer).

Primer	**Sequence (5'-3')**
FBXW7_lox (forward)	CAGTCGAGTGAAGTACAACTCTGG
FBXW7_lox (reverse)	GCATATTCTAGAGGAGGGTATCGG
Cdh5_Cre (forward)	GCCTGCATTACCGGTCGATGCAACGA
Cdh5_Cre (reverse)	GTGGCAGATGGCGCGGCAACACCATT

Table 2.2 – Primers used for genotyping.

2.3 – Flow cytometry

2.3.1 – Bone marrow cell isolation

For haematopoietic and leukaemic cell analysis, bones were gently crushed with mortar and pestle, suspended in FACS buffer and filtered through a 40μm strainer, centrifuged at 500 x *g* for 5 minutes at 4ºC, resuspended in red cell lysis buffer and washed in FACS buffer, centrifuged at 500 x *g* for 5 minutes at 4ºC, resuspended in FACS buffer and stained. For stroma analysis, tibias and femurs were minced with scissors and gently crushed with mortar and pestle, transferred to a 50 ml Falcon© tube and resuspended in 3 ml of collagenase solution, incubated at 37ºC for 30 minutes with 110rpm agitation, washed in FACS buffer, filtered through a 100 μm strainer and stained.

2.3.2 – Cell staining and acquisition

Cells were stained in FACS buffer for 20 minutes at room temperature, washed in FACS buffer, centrifuged at 500 x *g* for 5 minutes at 4ºC and resuspended in adequate volume of FACS buffer before acquisition. All primary antibodies were used at 1:200 dilution, apart from anti-CD34 (1:50) and anti-CD150, anti-CD127, anti-endomucin and anti-CXCR4 (1:100). All secondary antibodies were used at 1:1000 dilution. The following fluorochrome-conjugated or biotinylated primary antibodies specific to mouse were used:

Antibody	Clone	Source	Catalogue
Biotin anti-mouse CD3e	145-2C11	BioLegend	100304
Biotin anti-mouse CD4	GK1.5	BioLegend	100404
Biotin anti-mouse CD8a	53-6.7	BioLegend	100704
Biotin anti-mouse Ter119	TER119	BioLegend	116204
APC/Cy7 anti-mouse Ter-119	TER119	BioLegend	116223
APC/Cy7 anti-mouse CD45	30-F11	BioLegend	103116
Biotin anti-mouse/human CD45R/B220	RA3-6B2	BioLegend	103204
APC anti-mouse Ly6G	1A8	BioLegend	127613
Biotin anti-mouse Ly-6G/Ly-6C (Gr-1)	RB6-8C5	BioLegend	108404
Biotin anti-mouse CD11b	M1/70	BioLegend	101204
APC/Cy7 anti-mouse/human CD11b	M1/70	BioLegend	101226

Antibody	Clone	Source	Catalogue
APC anti-mouse/human CD11b	M1/70	BioLegend	101212
PE/Cy7 anti-mouse/human CD11b	M1/70	BioLegend	101216
APC anti-mouse CD117 (c-Kit)	2B8	BioLegend	101212
APC/Cy7 anti-mouse CD117 (c-Kit)	2B8	BioLegend	105826
PerCP/Cy5.5 anti-mouse Ly6a/E (Sca-1)	D7	BioLegend	108124
Anti-Mouse CD34 eFluor ® 660	RAM34	eBioscience	50-0341-82
APC anti-mouse CD34	HM34	BioLegend	128612
PE-Cy7 anti-mouse CD16/32	93	BioLegend	101318
Anti-mouse CD127 APC efluor780	A7R34	eBioscience	47-1271-82
BV650 anti-mouse CD150 (SLAM)	TC15-12F12.2	BioLegend	115931
PE/Cy7 anti-mouse CD48	HM48-1	BioLegend	103424
Biotin anti-mouse CD31	MEC13.3	BioLegend	102504
PE/Cy7 anti-mouse CD31	MEC13.3	BioLegend	102524
Anti-Mouse Endomucin eFluor® 660	V.7C7	eBioscience	50-5851-82
PE/Cy5 anti-mouse CD11c	N418	BioLegend	117316
FITC anti-mouse CD71	R17217	BioLegend	113806
Anti-Human/Mouse CD44 APC	IM7	eBioscience	17-0441-81
Anti-Mouse CD184 (CXCR4) APC	2B11	eBioscience	17-9991-82
Anti-Mouse CD184 (CXCR4) PE	2B11	eBioscience	12-9991-81
Anti-Mouse CD184 (CXCR4) Alexa Fluor® 488	2B11	eBioscience	53-9991-80
PE-conjugated mouse anti-human CD45	HI30	eBioscience	12-0459-42
APC Mouse Anti-Human CD7	M-T701	BD Biosciences	561604
APC-Cy7 Mouse Anti-Human CD4	RPA-T4	BD Biosciences	557871
PE-Cy7 Mouse Anti-Human CD8a	RPA-T8	eBioscience	25-0088-42
PE/Cy7 Streptavidin		eBioscience	405206
Streptavidin Pacific Orange		Invitrogen	S32365

Table 2.3 – Antibodies used in FACS.

The biotin-conjugated lineage cocktail included the following antibodies: anti-CD8, CD4, CD8, Ter119, B220, Gr-1 and CD11b mixed in equal amounts. Live and dead cells were distinguished using 4,6-diamidino-2-phenylindole (DAPI) (NucBlue® Fixed Cell ReadyProbes® Reagent; Invitrogen, Cat. # R37606). Single colour controls were always prepared and fluorescence-minus-one (FMO) controls were prepared when appropriate.

To detect nucleic acids, the cell-permeant SYTO® 17 Red Fluorescent Nucleic Acid Stain (Invitrogen, Cat. # S7579) was used.

Calibrite Beads (BD Calibrite 3 Beads Unlabeled, FITC, PE, and PerCP Beads; BD Biosciences, Cat. # 340486) were used to determine absolute cell counts, as previously described (Hawkins et al., 2007). Briefly, single-colour calibrite beads were suspended in PBS at a concentration of 1 x 10^6 beads/ml and resuspended using a 10 ml pipette to guarantee an homogenous distribution of beads; then, a specific volume of beads (e.g. 100 µl containing 100,000 beads) was added to the sample to be acquired (beads should represent 1 to 10% of the total number of mononuclear cells contained in the sample); final absolute cell numbers are back-calculated using the numbers of acquired beads and acquired cells.

For cell cycle analysis, BM from T-ALL infiltrated untreated and treated mice and human T-ALL xenotransplanted mice was harvested, fixed and permeabilised with BD Cytofix/Cytoperm (BD Biosciences; Cat. # 554722) and Perm/Wash Buffer (BD Biosciences; Cat. # 554723) and stained with DAPI (Invitrogen) and FITC mouse anti-Ki-67 set (BD Biosciences; Cat. # 556026), according to the manufacturer's instructions.

To detect apoptotic cells, Annexin V (BD Pharmingen™ Annexin V APC; BD Biosciences, Cat. # 550474) was used. Annexin V is a calcium-dependent protein that binds the negatively charged phospholipid phosphatidylserine (PS), which is translocated to the outer leaflet of the plasma membrane in apoptotic cells. By combining Annexin V with a cell-impermeable vital dye, such as propidium iodide (PI), 7-Amino-Actinomycin (7-AAD) or DAPI it is possible to identify live (Annexin V^- / $DAPI^-$), early apoptotic (Annexin V^+ / $DAPI^-$) and dead cells (Annexin V^+ / $DAPI^+$) (Figure 2.1). The cells of interest (1 x 10^5 cells) are resuspended in 100 µl of 1x Annexin V binding buffer and 5 µl of Annexin V are added. The solution is gently vortexed and incubated for 15 minutes in the dark. 400 µl of 1x Annexin V binding buffer (BD Biosciences; Cat. # 556454) are added and the sample analysed within 1 hour. 5 µl of DAPI are added just before acquisition and the sample analysed.

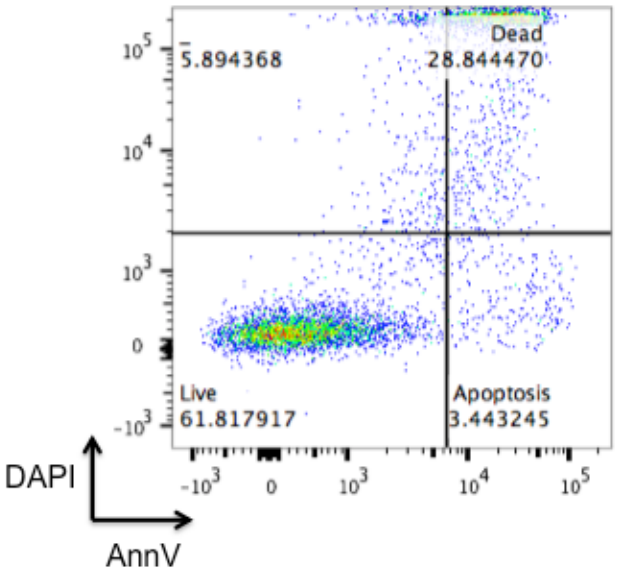

Figure 2.1 – Annexin V and DAPI staining of BM cells. Live (Annexin V^- / $DAPI^-$), early apoptotic (Annexin V^+ / $DAPI^-$) and dead cells (Annexin V^+ / $DAPI^+$) can be identified by flow cytometry.

Cells were analysed with a LSR Fortessa, sort-purified using a FACSAria III (BD Biosciences) and data were analysed with FlowJo (Tree Star). The gating strategy used for the normal and malignant AML haematopoietic cells is shown below (Figure 2.2).

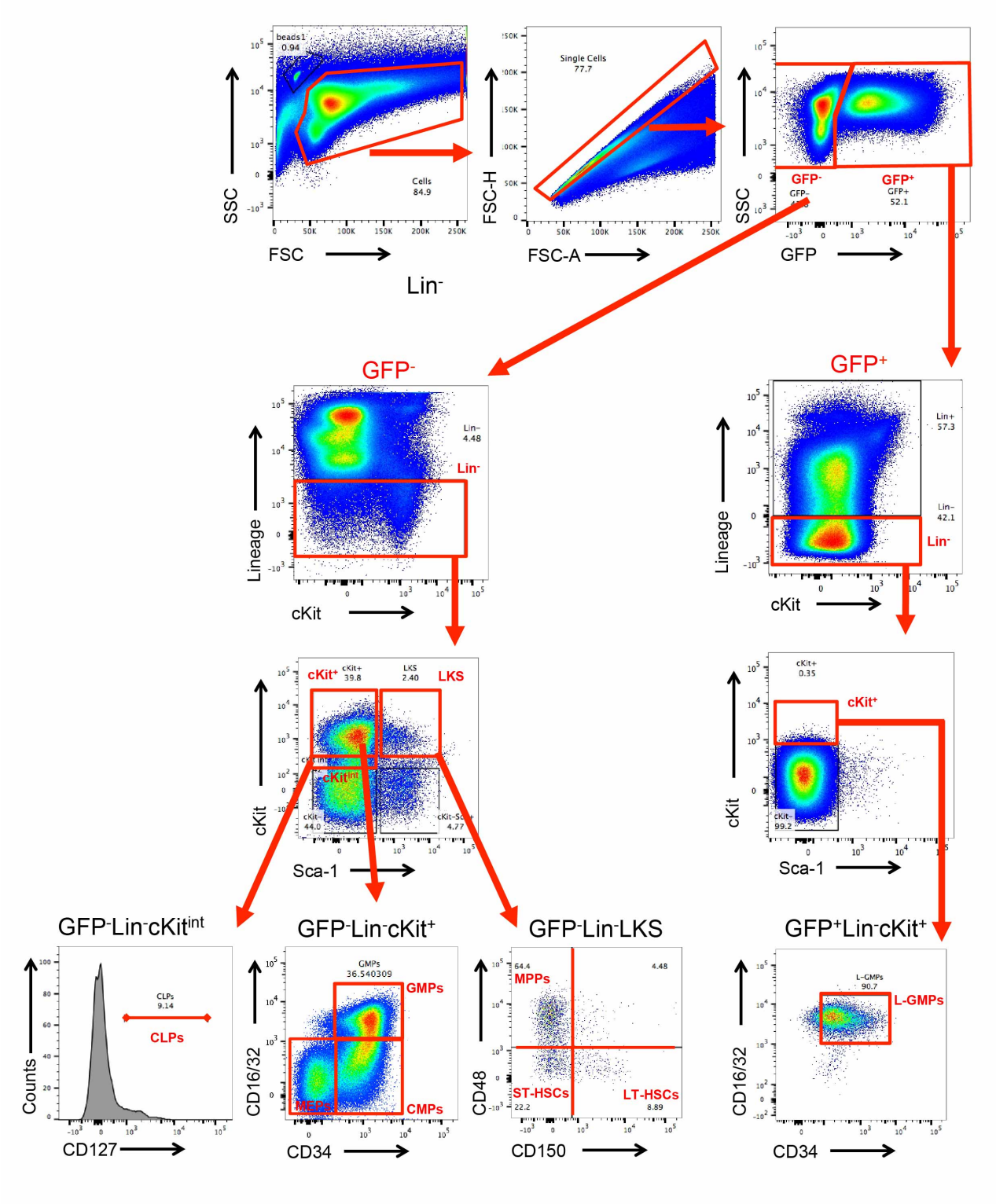

Figure 2.2 – FACS gating strategy used to identify HSCs, progenitors and Leukaemic (L)-GMPs. Representative plots from day 20 post-transplantation of MLL-AF9 AML blasts in non-irradiated recipient mice.

2.4 – Lineage depletion

Tibias, femurs, ileac bones, vertebrae and sternum were harvested from donor mice and cells isolated as described above (2.3.1). Whole BM cells were labelled with a cocktail of biotinylated lineage antibodies (CD3, CD4, CD8, Ter119, B220, Gr-1, CD11b). Then cells were resuspended in 1 ml of PBS and incubated with 30 µl of streptavidin magnetic Microbeads (Miltenyi Biotech; Cat. # 130-048-101) for 30 minutes at 4ºC. In the meantime, LD columns (Miltenyi Biotech; Cat. # 130-042-901) were equilibrated with PBS (3 ml/column). 2 ml PBS were added to the tubes containing the cells and transferred to the LD columns. A lineage depleted BM sample (Figure 2.3) was collected in 15 ml Falcon© tubes using the MACS® Column Technology (Miltenyi Biotech). The sample was then stained with appropriate antibodies, as described in 2.3.2.

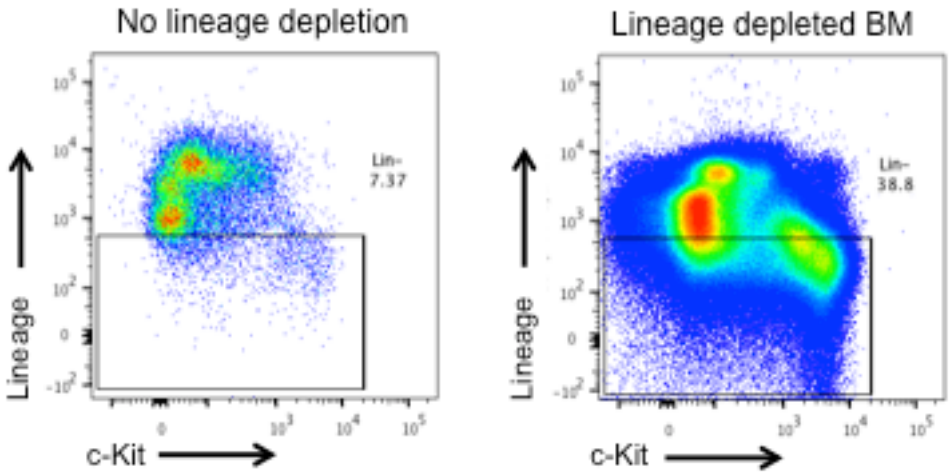

Figure 2.3 – BM lineage depletion. Flow cytometry analysis of the same BM sample without (left) and with (right) lineage depletion.

2.5 – c-Kit enrichment

For detection of apoptotic HSCs, c-Kit enrichment was performed using anti-CD117 magnetic microbeads (Miltenyi Biotech; Cat. # 130-091-224) as described in 2.4 MS columns (Miltenyi Biotech; Cat. # 130-042-201) were used instead of LD columns. The flow-throw was discarded and the c-Kit^{+} cells retained in the column collected by adding FACS buffer and pushing them out of the column with the provided plunger. c-Kit enriched BM cells (Figure 2.4) from healthy control and leukaemia burdened animals were then stained with Annexin V (APC, BD) and DAPI as described in 2.3.2.

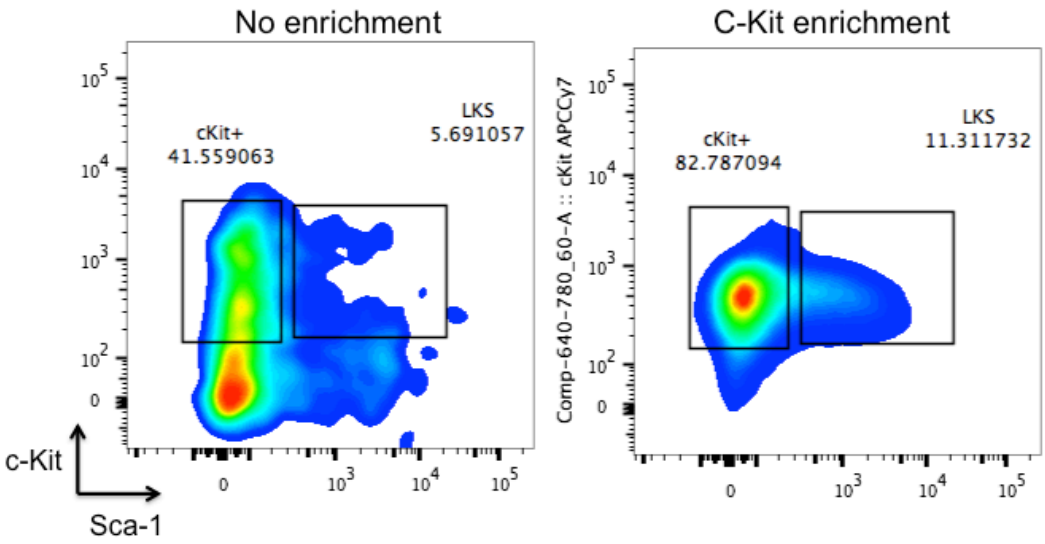

Figure 2.4 – BM c-Kit enrichment. Flow cytometry analysis of the same BM sample before (left) and after (right) c-Kit enrichment.

2.6 – AML experimental model

I generated AML blasts using an adapted version of the methods described in (Krivtsov et al., 2006).

2.6.1 – Plasmid preparation

The retroviral expression vector pMSCV-MLL-AF9-IRES-GFP was previously generated (Somervaille and Cleary, 2006), contained ampicillin resistance genes and was a gift from Steve Lane (QIMR Barhofer, Brisbane). DNA was isolated from transformed competent *E. coli* cells using the HiSpeed® Plasmid Maxi Kit (Qiagen; Cat. # 12663) according to the manufacturer's protocol and eluted in nuclease-free water.

2.6.2 – Transfection

The LinXE cell line was a gift from Hugh Brady (Imperial College London) (Dunne et al., 2010; Hannon et al., 1999) and was used to produce retrovirus batches. LinXE cells were maintained in $D10^+$ medium supplemented with 15 μM hygromycin to select for expression of retroviral packaging genes, at 37˚C and 5% CO_2. For transfection, LinXE cells were plated out in 10 cm cell culture dishes in $D10^+$ medium without hygromycin at 37˚C and 5% CO_2 for 2 days. When plates were 60 to 80% confluent, the $D10^+$ medium was changed 3 to 4 hours prior to transfection. At this point, the calcium phosphate transfection kit (Invitrogen; Cat. # K278001) was used. For each transfection, I mixed 61 μl of 2 M CaCl2, 10-20 μg DNA and RNase-free H_20 (tube A, 500μl) with 500 μl HBS (tube B). The reagents were gently mixed for 1 to 2 minutes and incubated for 30 minutes at room temperature. The solution was then dropwise and evenly added to LinXE cells and incubated overnight at 37˚C and 5% CO_2. On the following day, the presence of precipitate was confirmed under the microscope and 16 to 20 hours post-transfection, the $D10^+$ medium was replaced.

2.6.3 – Transduction

I used the retronectin-bound virus infection method (Chono et al., 2001) for transduction of GMPs. On the day of transfection medium replacement, 6-well non-tissue culture plates (BD Biosciences; cat. # 351146) were coated with retronectin - RetroNectin® Recombinant Human Fibronectin Fragment (Takara; Cat. # T100B) (2ml/well of 15μg/ml retronectin in PBS) and incubated overnight at 4ºC. On the following day, wild type, mTomato and PU.1-YFP fluorescent BM cells were harvested as described above (see section 2.3.1) from C57/B6

wild type, mT/mG or PU.1-YFP mice. After lineage depletion (see section 2.4), GMPs were FACS-sorted onto transduction medium. In the meantime, retronectin was removed from the 6-well plates and the plates were blocked with 2% BSA (Sigma; Cat. # A7030) in PBS (2 ml/well) for 30 minutes and washed with PBS. The retrovirus was isolated from transfected LinXE cells by collecting the supernatant and filtering it through a 0.45 μm filter using a 20 ml syringe. A small amount of LinXEs was harvested and the transfection efficiency was evaluated by FACS (GFP^+ cells). 5 to 6 ml of the collected viral supernatant were added to each well of the 6-well plate. The plate was then centrifuged at 2,000 x *g* for 1 hour at 37ºC and incubated for 4 hours at 37ºC and 5% CO_2. The viral supernatant was removed and the plates washed with PBS. Sorted GMPs were counted with a haemocytometer, plated in the 6-well plate (1-2 x 10^6 GMPs/well) in transduction medium (3 ml/well) and incubated for about 60 hours at 37ºC and 5% CO_2. GMPs were than harvested and the transduction efficiency determined by FACS (GFP^+ cells).

2.6.4 – Transplants

25,000 to 100,000 MLL-AF9 transduced GMPs were transplanted into sub-lethally irradiated (irradiation with two doses of 3 Gy separated by 3 hours) primary recipient mice. 8 to 10 weeks post transplantation, recipient mice developed leukaemia characterized by multi-organ infiltration of leukaemic blasts (>90% infiltration). GFP^+ cells were then harvested from BM and spleen and stored in liquid N_2. Blasts from each primary recipient were labelled as a separate batch. Primary blasts from different mice were thawed, suspended in PBS and 100,000 viable cells were transplanted through tail vein injection into secondary, non-conditioned recipient mice. In some instances secondary blasts were used. Progressive blast expansion was observed from day 8-10 and full BM infiltration was typically reached between day 20 and 28, depending on the primary blasts analysed. This was accompanied by infiltration of the spleen, typically delayed compared to BM infiltration. Mice were monitored daily for signs of leukaemia onset or other signs of ill health and disease progression was monitored through sampling of peripheral blood. Mice were euthanized when any one or a combination of the following signs were observed: hunched posture, laboured breathing, weight loss, enlarged lymph nodes and/or spleen.

2.7 – T-ALL experimental model

2.7.1 – Notch1-driven T-ALL model

The Notch1 T-ALL blasts used were generated by Edwin Hawkins as described in (Aster et al., 2000). Briefly, foetal liver cells where harvested from wild-type embryonic day 14.5 (E14.5) embryos and transduced with MigR1 plasmids containing DsRed with NotchICNΔRamΔP. 1 x 10^6 $DsRed^+$ foetal liver cells were transplanted into primary lethally irradiated recipient mice (two doses of 5.5 Gy administered greater than three hours apart). Recipient mice were maintained on baytril treated water to prevent infection for >6 weeks post transplantation. Mice were euthanized upon onset of signs of leukaemia (typically, primary disease at 6 to 25 weeks). $DsRed^+$ cells were isolated from BM, spleen and lymph nodes. Cells from each primary recipient were labelled as a separate batch.

2.7.2 – TEL-JAK2-driven T-ALL model

The TEL-JAK2 T-ALL cells used were a gift from Ricky Johnstone (The Peter MacCallum Cancer Centre, Melbourne) and shipped from Australia. TEL-JAK2 T-ALL cells were from spleen of Ubiquitin-GFP/6:Eμ-TEL-JAK2 transgenic mice (Carron et al., 2000).

2.7.3 - Transplants

T-ALL cells were thawed and suspended in RPMI containing 10% FBS in a 15 ml Falcon© tube. Cells were then spun down at 500 x *g* for 5 minutes, at 4ºC, resuspended in 5 ml of RPMI with 10% FBS and slowly layered (pipette controller set at 'gravity') in a new 15 ml Falcon© tube containing 5 ml of Ficoll™. The sample was centrifuged at 1,625 x *g* for 20 minutes at 4ºC (with 0 acceleration and 0 break). After centrifugation, the top layer was discarded and T-ALL cells were isolated from the buffy coat (containing mononuclear cells), transferred to a new Falcon© tube and resuspended in RPMI medium. Cells were then spun down at 1,463 x *g* for 5 minutes at 4ºC, counted with a haemocytometer (viable cells identified by Trypan blue dye exclusion) and washed with PBS alone to remove any remaining serum. After centrifugation at 1,463 x *g*_for 5 min at 4ºC, T-ALL cells were suspended in adequate volumes for injection.

For imaging and flow cytometry experiments, I injected 10,000-50,000 primary (occasionally secondary) live Notch1 $DsRed^+$ T-ALL blasts into sub-lethally irradiated (irradiation with two doses of 3 Gy separated by 3 hours) secondary, and in some cases, tertiary recipients. In specific cases, 50,000 secondary blasts were injected into non-irradiated

tertiary recipients. 200,000 live TEL-JAK2 GFP^+ T-ALL blasts were injected into non-irradiated recipients. Mice were monitored daily for signs of leukaemia onset or other signs of ill health and disease progression was monitored through sampling of peripheral blood. Mice were euthanized when any one or a combination of the following signs were observed: hunched posture, laboured breathing, weight loss, enlarged lymph nodes and/or spleen.

2.8 – Human T-ALL xenografts

Xenografts were prepared by Diana Passaro (CRUK LRI, London). Briefly, primary human T-ALL samples were obtained from the Barts Hospital (London, UK) after informed consent via a protocol approved by the East London Research Ethics Committee and carried out in accordance with the principles of the Helsinki declaration. Primary cells were immunophenotyped, and $CD45^+/CD7^+/CD4^{-/low}/CD8^{-/low}$ cells sorted and infused I.V. in non-conditioned Osterix-CreGFP/NOD/SCID/γ recipient mice. Primary xenograft transplantation was assessed via peripheral blood sampling and/or BM aspiration. BM and spleen-derived primary xenografts were infused I.V. in non-conditioned NOD/SCID/γ secondary recipient mice for therapy experiments. I performed intravital imaging as described below (see section 2.16). Human T-ALL cells were labelled by injecting 10 μg of PE-conjugated human CD45 antibody (clone HI30, Biolegend; Cat. # 304058) 15-30 minutes prior to the imaging session. PE Mouse IgG1, κ Isotype Control Antibody (Biolegend; Cat. # 400112) was also used.

2.9 - Drug administration

To model chemoresistance, drugs commonly administered in the treatment regimens of T-ALL and AML patients were used in our mouse models.

Mice burdened with T-ALL were treated daily, for 3 days, with I.V. 15 mg/kg dexamethasone sodium phosphate (Stratech Scientific; Cat. # S4028) alone, 0.15 mg/kg vincristine (Sigma; Cat. # V8879) alone or with combination of I.V. 15 mg/kg dexamethasone sodium phosphate, 0.15 mg/kg vincristine and 1,000 IU/kg l-asparaginase (medac; obtained from the Imperial College Healthcare NHS Trust Pharmacy). NSG mice xenotransplanted with human T-ALL cells were treated with daily I.V. injections of 15 mg/kg dexamethasone for 14 days upon full infiltration as confirmed by tibeal aspiration (treatment regimen adapted from (Chiu et al., 2010)).

Induction chemotherapy for AML was administered when BM infiltration was over 50% by injecting 100 mg/kg cytarabine (Ara-C; Stratech Scientific; Cat. # S1208-SEL) I.V. for 5 days and 3 mg/kg doxorubicin (Doxo; Stratech Scientific; Cat. # S1648-SEL) for 3 days. Ara-C was co-delivered with Doxo on days 1 to 3 and alone on days 4 and 5, similarly to induction chemotherapy used in AML patients (Wunderlich et al., 2013). Both Ara-C and Doxo were purchased from Stratech Scientific or obtained from the Imperial College Healthcare NHS Trust.

For DFO treatment, daily 100 mg/kg deferoxamine mesylate (DFO; Sigma; Cat. # D9533) was administered I.P. from day 8 until day 22 post-transplantation of AML blasts, at which time mice were sacrificed and their BM analysed. Control mice were injected I.P. with 100 µl of PBS.

For CXCR4 inhibition experiments, mice were I.V. injected with 4mg/kg AMD3100 octahydrochloride hydrate (Sigma; Cat. # A5602).

For EC-specific deletion of Fbxw7, tamoxifen (500µl/mouse I.P.; Sigma; Cat. # T5648) was given daily to $Fbxw7^{lox/lox}$ Cdh5(PAC)-$CreERT2^{T/+}$ ($Fbxw7^{i\Delta EC}$) mice and to control $Fbxw7^{lox/lox}$ and WT mice. In experiments where relapse and survival were analysed, tamoxifen was given daily between day 10 and 20 post-transplantation, at which point chemotherapy was initiated. Blinding was followed for the tamoxifen studies.

2.10 – Bone marrow chimeras

To generate chimeras, whole BM cells were obtained from femurs and tibias of wild-type or mT/mG donor mice, diluted in PBS and transplanted intravenously into lethally irradiated (two doses of 5.5 Gy separated by 3 hours) mT/mG, Col2.3-CFP or Flk1-GFP recipient mice at a dose of 1.5 x 10^6 cells/mouse. Mice were kept on baytril-treated water for five weeks following transplantation. >95% chimerism was confirmed after 8 weeks and at that point mice were injected with AML cells and used for intravital imaging experiments.

2.11 - HSC transplantation and homing analysis

A BM lineage-depleted sample (see section 2.4) was stained and sorted for phenotypic HSCs, defined as $lineage^-c\text{-}Kit^+Sca\text{-}1^+CD48^-CD150^+$ cells. HSCs were centrifuged at 500 x *g* for 5 minutes at 4ºC, suspended in PBS and incubated with Vybrant® 1,1'-dioctadecyl-3,3,3'-

tetramethylindodicarbocyanine perchlorate (DiD) (ThermoFisher Scientific; Cat. # v22887) (0.5 µl DiD / 100 µl PBS) for 10 minutes, at 37ºC. After washing with PBS, 5,000 to 12,000 DiD-labelled HSCs were transplanted per mouse via tail vein injection. Control and leukaemic recipient mice had been previously lethally irradiated (two irradiations of 5.5 Gy, 3 hours apart). Two days after transplantation, recipient mice were sacrificed and femurs, tibias and the spleen harvested, BM cells obtained and stained for HSCs. $DiD^{+}DAPI^{-}c\text{-}Kit^{+}Sca\text{-}1^{+}CD48^{-}CD150^{+}$ cells were detected by flow cytometry.

2.12 - LKS culture and DFO in vitro treatment

Lineage depletion was performed as described above (see). Live ($DAPI^{-}$) $lineage^{-}c\text{-}Kit^{+}Sca\text{-}1^{+}$ (LKS) cells were sorted and plated at a density of 15,000 cells per well in a 48-well plate. Cells were maintained in StemSpan™ media (Stem Cell Technologies) supplemented 50 ng/ml SCF, 10 ng/ml IL-6, 10 ng/ml TPO and 20 ng/ml Flt3l (all from Peprotech). LKS cells were incubated with 0.5 µM, 5 µM, 50 µM and 500 µM DFO. After two days, cells were harvested, stained and the number and frequency of $DAPI^{-}c\text{-}Kit^{+}Sca\text{-}1^{+}CD48^{-}CD150^{+}$ HSCs analysed by flow cytometry.

2.13 - Quantitative real-time polymerase chain reaction (qRT-PCR)

Flk1-GFP mice were transplanted with primary $mTomato^{+}$ AML cells. Upon full infiltration, tibias and femurs were harvested and metaphysis and diaphysis separated using scissors. Endosteal $Flk1^{+}$ endothelial cells were isolated by crushing the metaphysis and sorting $DAPI^{-}GFP^{+}mTomato^{-}$ cells. Central $Flk1^{+}$ endothelial cells were isolated by flushing the diaphysis and sorting $DAPI^{-}GFP^{+}mTomato^{-}$ cells. Control endosteal and central $Flk1^{+}$ endothelial cells were obtained in an identical manner from age- and sex-matched Flk1-GFP mice. RNA was isolated using the NucleoSpin© RNA XS kit (Fischer Scientific; Cat. # 12723580) and treated with DNase I, according to manufacturer's instructions. First strand synthesis was performed using the SuperScript® IV First-Strand Synthesis System (Invitrogen; Cat. # 18091050), according to the manufacturer's instructions. The obtained cDNA was then treated with 1 µL *E. coli* RNase H at 37°C for 20 minutes to remove remaining RNA and mixed with 2x LightCycler® 480 SYBR Green I Master mix (Roche; Cat. # 04707516001) and primers (Table 2.4), according to the manufacturer's instructions.

The DNA samples were set in technical triplicates and the qRT-PCR was performed using a Light Cycler 480 with standard cycling conditions. The relative copy numbers ($2^{-\Delta Ct}$) were calculated from the Ct values obtained using the Light Cycler 480 software and normalized to GAPDH.

Gene	Primer	Sequence (5'-3')
GAPDH	F	TGTGTCCGTCGTGGATCTGA
	R	CCTGCTTCACCACCTTCTTGA
Cxcl12	F	CGCCAAGGTCGTCGCCG
	R	TTGGCTCTGGCGATGTGGC
VCAM1	F	GACCTGTTCCAGCGAGGGTCTA
	R	CTTCCATCCTCATAGCAATTAAGGTG
Angpt1	F	CTCGTCAGACATTCATCATCCAG
	R	CACCTTCTTTAGTGCAAAGGCT
Opn	F	TCCCTCGATGTCATCCCTGTTG
	R	GGCACTCTCCTGGCTCTCTTTG
SCF	F	CCCTGAAGACTCGGGCCTA
	R	CAATTACAAGCGAAATGAGAGCC
Ang	F	AGCGAATGGAAGCCCTTACA
	R	CTCATCGAAGTGGACAGGCA
VEGFA	F	CAGAGCGGAGAAAGCATTTGT
	R	CGCGAGTCTGTGTTTTTGCA

Table 2.4 – Primers used in qRT-PCR.

2.14 - RNA sequencing and analysis

Mice were transplanted with primary AML cells from 3 different donors (batch_1_BM_mTmG, batch_3_BM_mTmG and batch_19_spleen_mTmG). Upon full infiltration, tibias and femurs were harvested and metaphysis and diaphysis separated using scissors. Endosteal AML cells were isolated by crushing the metaphysis and sorting $DAPI^{-}$ $GFP^{+}mTomato^{+}$ cells. Central AML cells were isolated by flushing the diaphysis and sorting

DAPI$^-$GFP$^+$mTomato$^+$ cells. The control population, GMPs, was sorted from whole BM of age- and sex-matched wild-type mice. Total RNA was extracted using RNeasy® Mini Kit (Qiagen, Hilden, Germany; Cat. # 74104) according to the manufacturer's instructions. The extracted RNA was shipped to the Walter and Eliza Institute of Medical Research (WEHI, Melbourne) where it was processed by Isabella Y. Kong. Briefly, extracted RNA was analysed on the Agilent 4200 Tapestation prior to library preparation. High quality RNA with RIN values greater than 9 was used for downstream application. 3'mRNA-sequencing libraries were prepared from 100ng of total RNA using the QuantSeq 3' mRNA-Seq Library Prep Kit (Lexogen) according to the manufacturer's instructions and sequenced on a NextSeq 500 (Illumina). The single-end 75bp were demultiplexed using CASAVAv1.8.2 and Cutadapt (v1.9) was used for read trimming. The trimmed reads were subsequently mapped to the mouse genome (mm10) using HISAT2. FeatureCounts was used for read counting (Liao et al., 2014) after which differential gene expression analysis was performed using Voom-LIMMA packages (Law et al., 2014). GSEA2-2.2.2 was used for Gene set enrichment analysis (GSEA) (Liberzon et al., 2015; Subramanian et al., 2005). RNAseq data are accessible on the Gene Expression Omnibus (GEO) repository, with accession number GSE105159. Data for RNA-seq for T-ALL samples shown in Chapter 5 were generated by the Hawkins group as described in (Waibel et al., 2017) and can be accessed through GEO with the accession numbers GSE102757.

2.15 - Enzyme-linked immunosorbent assay (ELISA)

To obtain BM supernatants, tibias and femurs were harvested from control and AML-burdened mice. With scissors, the metaphysis and diaphysis of long bones were separated. To obtain *flushed BM supernatant,* 70µl of PBS were flushed through each diaphysis, collected and reflushed; then, cells were excluded by centrifugation at 400g for 5min; the supernatant was collected and any remaining cells excluded by centrifugation at 500g for 5min. To obtain *crushed BM supernatant*, the metaphyses were gently crushed in 150µl of PBS, and the supernatant isolated by centrifugation as described above. Serum was prepared by collecting blood through cardiac puncture after terminal anaesthesia with pentobarbital; blood was then left at 4ºC for 3 hours or more to allow clot formation and centrifuged at 12,000g for 10min at 4ºC; the supernatant (serum) was then transferred to a new eppendorf tube. BM supernatants and serum were stored at -20ºC until used for ELISA. Samples were diluted

1:10 and DuoSet ELISAs (R&D Systems) were performed according to the manufacturer's instructions. The kits used were: Mouse VEGF DuoSet ELISA (Cat. # DY493), Mouse TNF-alpha DuoSet ELISA (Cat. # DY410) and Mouse CXCL2/MIP-2 DuoSet ELISA (Cat. # DY452).

2.16 - Intravital microscopy

IVM was performed using a Zeiss LSM 780 upright confocal/two-photon hybrid microscope equipped with Argon (458, 488 and 514 nm), a diode-pumped solid-state 561 nm laser and a Helium-Neon 633 nm, a tunable infrared multiphoton laser (Spectraphysics Mai Tai DeepSee 690-1020 nm), 4 non-descanned detectors (NDD) and an internal spectral detector array. In some cases a Leica SP5 was used instead. The SP5 was fitted with the following lasers: Argon, 546 nm, 633 nm and a tunable infrared multiphoton laser (Spectraphysics Mai Tai 690-1020). Signal was visualized with a Leica HCX IRAPO L ×25 water immersion lens (0.95 N.A) and a Zeiss W Plan-Apochromat ×20 DIC water immersion lens (1.0 N.A). Live imaging of the calvarium BM was done as described in (Hawkins et al., 2016). Anaesthesia was induced and maintained with isoflurane in medical O_2 (4% isoflurane in 4 L/min O_2 for induction and 1-2% isoflurane in 1 L/min O_2 for maintenance), throughout the procedure. Minimally invasive surgery was performed to remove the skin and subcutaneous tissue on top of the frontal bones, as shown in (Scott et al., 2014). A custom-made imaging window (headpiece, (Scott et al., 2014)) was then attached with Diamond Carve Dental Cement (Associated Dental Products; Cat. # SUN527). The dental cement was prepared by mixing 3 spoons of powder with 2 drops of liquid. After attaching the headpiece, the cement solidified and the mouse was transferred to the microscope automatic stage and placed on top of a heat pad. The mouse temperature was monitored with a rectal probe equipped with a thermal sensor. A lubricant eye ointment was applied to prevent eye dryness and corneal injury. For repeated imaging, protective intrasite gel (Smith & Nephew; Cat. # 7308) was applied to the imaging window to preserve the bone integrity and prevent scar formation. The window was bandaged, and mice were allowed to recover from anaesthesia. Owing to the lock-and-key mechanism of the imaging window (Scott et al., 2014), mice could then be re-anaesthetized and accurately repositioned on the microscope stage and the same BM areas re-imaged. After each imaging, analgesia was provided by oral buprenorphine mixed in raspberry jelly at a dose of 0.8 mg/kg.

The spleens of live mice were imaged under general, terminal anaesthesia. Anaesthesia was induced and maintained with isoflurane in medical O_2 (4% isoflurane in 4L/min O_2 for induction and 1-2% isoflurane in 1 L/min O_2 for maintenance), throughout the procedure. Mice were placed in the right lateral decubitus position and a small section of hair was removed from the left flank. A 5-8 mm abdominal incision on the left flank above the spleen was used to expose the surface of the spleen, which was mechanically stabilized with a gentle vacuum using a coverslip vacuum chamber similar to that used in (Headley et al., 2016). A drop of water was placed on top of the chamber coverslip and the spleen was imaged using a long working distance W Plan-Apochromat ×20 DIC water immersion lens (1.0 N.A.).

Blood vessels were labelled with either 80 µl of 8 mg/ml 500kD Cy5-Dextran (Nanocs, MA, Cat. # DX500-S5-1) or 50 µl of 40 mg/ml 150 kD TRITC-dextran (TdB Consultancy, SE; Cat. # TD150). SHG signal was excited at 860-880 nm and detected with external detectors. CFP signal was excited at 870 nm or 458 nm and detected using external or internal detectors; GFP signal: excitation at 880 nm or 488 nm, external or internal detectors; YFP signal: excitation at 488 nm or 514 nm, internal detectors. mTomato/DsRed and Cy5 signals were respectively excited at 561nm and 633 nm and detected using internal detectors. To simultaneously detect SHG, CFP, mTomato, YFP and Cy5 signals in chimeras, lambda acquisition and online fingerprinting were used and the signal collected using an internal 32-channel gallium arsenide phosphide (GaAsP) array detector. The reference spectra of each fluorophore were acquired in different BM areas of the same mouse, using areas containing a single fluorophore. Large three dimensional ‘tile scans’ of the entire BM cavity space were acquired by stitching adjacent, high-resolution z-stack images (Figure 2.5).

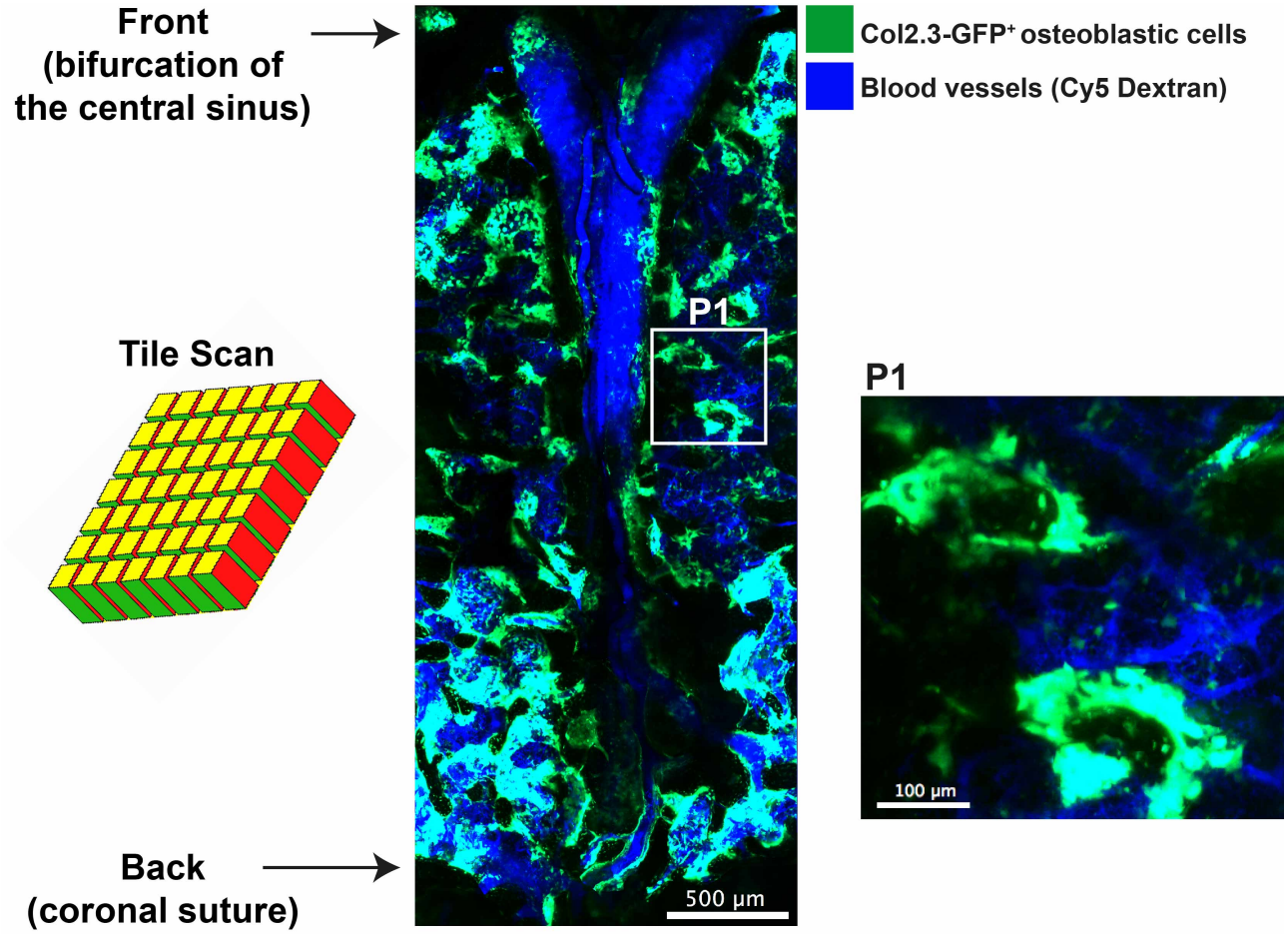

Figure 2.5 – Intravital imaging of the mouse calvarium bone marrow. Individual 3D stacks are acquired and stitched together to build a 3D 'Tile Scan' that permits whole tissue visualization of the calvarium BM with single cell resolution (P1). BM blood vessels are highlighted by Cy5 Dextran I.V. injected in the tail vein. A central sinus runs in the middle line and bifurcates in the anterior margin of the calvarium BM space. A network of sinusoids and arterioles irrigates the BM tissue, as shown in P1. Col2.3-GFP^{+} osteoblastic cells are at the interface between the bone and the tissue.

2.17 - Immunofluorescence of undecalcified long bone sections

Tibias, femurs and hips were harvested and fixed overnight in PLP fixative, at 4ºC. The bones were then washed with 0.1 M phosphate buffer, immersed in sucrose 10% for 1 hour, followed by sucrose 20% for 1 hour and followed by sucrose 30% for 48 hours for cryoprotection, frozen in optimal cutting temperature (OCT) compound (TissueTek) and kept at -80ºC. Sections were obtained using a cryostat (Leica) and the Cryojane tape transfer system (Leica). Slides were either kept at 4ºC and used within the following week or stored at -80ºC. For staining, slides were re-hydrated in PBS, permeabilised in 0.1% Triton X-100, blocked in 5% goat serum and incubated with primary antibodies overnight, at 4°C. After washing in PBS, slides were incubated with secondary antibodies, counter-stained with DAPI, washed in 0.1% Triton X-100 and mounted with Prolong Diamond antifade (Life Technologies; Cat. # P36961). TdT-mediated dUTP nick end labelling (TUNEL) labelling was performed to detect apoptotic cells, according to the manufacturer's instructions (DeadEnd Colorimetric TUNEL System, Promega; Cat. # G7130). The antibodies used are listed in Table 2.5. Images were obtained using a Zeiss LSM 780 upright confocal/two-photon combined microscope (see section 2.16) and analysed using FIJI/ImageJ.

Antibody	Clone	Dilution	Source	Catalogue ID
Rat Anti-Mouse Endomucin antibody	V.7C7	1:100	Santa-Cruz	sc-65495
Rabbit Anti-Laminin	Polyclonal	1:50	Sigma	L9393
Rabbit anti-GFP	Polyclonal	1:500	Abcam	ab6556
Rabbit Anti-CXCL12 alpha	Polyclonal	1:100	eBioscience	14-7992-83
Purified Rabbit Polyclonal Isotype Ctrl	Polyclonal	1:100	Biolegend	910801
Rabbit anti-Cleaved Caspase-3 (Asp175)	5A1E	1:100	Cell Signaling Tecnhology	9664
Alexa Fluor® 647 mouse anti-human Ki-67	B56	1:50	BD Biosciences	558615
PE-conjugated mouse anti-human CD45	HI30	1:100	eBioscience	12-0459-42
Goat anti-Rabbit IgG (H+L) Alexa Fluor® 488	Polyclonal	1:400	Life Technologies	A-11034
Goat anti-Rat IgG (H+L) Alexa Fluor 633	Polyclonal	1:400	Life Technologies	A-21094

Table 2.5 – Antibodies used for immunofluorescence.

2.18 - Human trephine biopsies

Human trephine biopsies were obtained by Andrew Wei and Louise Purton from patients after informed consent had been obtained, under full ethical approval by the Alfred Hospital, the Peter MacCallum Cancer Centre Human Research Ethics Committee, and St. Vincent's Hospital Melbourne. Information about control and AML samples is provided below. De-waxed human trephine biopsy sections were stained with vWF antibody (Anti-Human Factor VIII-Related Antigen, Ready-to-Use, DAKO; Cat. # N1505), counterstained and mounted for viewing by Catriona McLean. Representative areas of each section were captured and analysed by me and Lenny Straszkowski. The samples used are listed in Table 2.6.

Control

#	**Diagnosis**
1	Primary CNS lymphoma
2	Diffusive large B-cell lymphoma
3	Mantle cell lymphoma
4	Non-hodgkin lymphoma
5	Non-hodgkin lymphoma
6	Non-hodgkin lymphoma

AML

#	**WHO classification**	**Cytogenetics**	**Blasts**
1	Acute monoblastic and monocytic leukaemia	t(10;11)	94%
2	Therapy-related acute myeloid leukaemia	t(9;11)	88%
3	Acute promyelocytic leukaemia	t(15;17)	83%

Table 2.6 – Diagnosis of control and AML trephine biopsy samples.

2.19 - Image quantification

ZEN black (Zeiss, Germany) software was used to stich three-dimensional BM and spleen tile scans. FIJI/Image J was used to visualize and process raw data. Simulated data was prepared using a customized FIJI macro to create, and overlay z-stack images on original tile scan data. Using the internal random number algorithm, spheres matching the size of T-ALL cells (11-15 μm) were placed at random x,y,z co-ordinates. Automated cell segmentation, and volume measurements were performed in Definiens (Definiens Developer 64, Germany) using local heterogeneity segmentation (Khorshed et al., 2015) to isolate Col2.3-GFP$^+$, Nes-GFP$^+$ Flk1-GFP$^+$, and mTomato$^+$ AML cells. Distance measurements were done in Definiens through a combination of seed detection algorithm and morphological growing and shrinking operations to detect leukaemia cells. Vessel-bone colocalization was analysed using Imaris (Bitplane, Switzerland). After creating a surface for Flk1-GFP$^+$ signal and a surface for bone (SHG) signal from half tile scans, the Imaris XTension "Surface surface colocalization" was used.

Cell tracking was performed manually using the FIJI plugin MTrackJ or semi-automatically using Imaris. For accuracy in cell tracking data, any displacement in the Z plane caused by movement artifacts (e.g. breeding) was corrected by applying 4D data protocols implemented in FIJI (Preibisch et al., 2010) that allow for the registration of the acquired time-lapses. Imaris was used to detect the leukaemia cells and create either "spots" or "surfaces"; semi-automatic cell tracking was done using built-in algorithms that were manually supervised. Data, including track mean speed and cell coordinates were exported for further analysis. Cell counting was performed manually using the FIJI plugin Cell Counter and cells enumerated in the ROI manager.

Vessels oscillation was quantified in FIJI. After registration, maximum projections of 3D movies were produced. In each movie, 2 regions of interest (ROI) were selected and combined in a single object. After clearing the outside of ROIs, a Gaussian filter and a bleach correction were applied and the vessel movement automatically tracked using the plugin TrackMate.

Endosteal vessels were quantified in immunofluorescence sections by dividing the length of blood vessels (marked with laminin and endomucin) in contact with the bone surface (SHG signal) by the total length of the endosteal surface. Metaphyseal and diaphyseal vessels were quantified by thresholding the vascular signal in the metaphysis and diaphysis and

quantifying the area occupied by blood vessels. Microvascular density was quantified manually counting blood vessels and dividing the obtained counts by the total area.

2.20 - Statistical analysis

Raw data was visualized and processed using Microsoft Excel, MATLAB and GraphPad Prism (GraphPad Software Inc.). Group means were compared using the unpaired Student's T test. For multiple comparisons, one-way ANOVA with post-hoc Tukey test or Bonferroni correction were used.

An exact one-tailed permutation test was implemented in MATLAB for the time-course data in Figure 3.29F by Ken Duffy (Hamilton Institute, Maynooth University). The statistic used was the sum across days of the difference between the mean infiltration in the Cre^- and Cre^+ cohorts.

For all data, differences were considered significant whenever $p<0.05$. * $p<0.05$; ** $p<0.01$; *** $p<0.001$; **** $p<0.0001$. Specific statistical parameters (e.g. number of animals used) can be found in the figure legends.

Chapter 3

Acute myeloid leukaemia selectively remodels the bone marrow endosteal vascular niche

3.1 - Introduction

HSCs reside in the BM, where they receive survival and differentiation signals from several cell types, including endothelial and multiple lineages of perivascular mesenchymal cells (Morrison and Scadden, 2014). Similarly, cancer growth and chemoresistance have been hypothesized to be dependent on a malignant microenvironment that is highly vascularized (Duan et al., 2014; Pitt et al., 2015). This relationship is well illustrated in epithelial cancers, where increased angiogenesis supports growth and metastasis (Quail and Joyce, 2013).

AML is an aggressive leukaemia with poor prognosis (Dohner et al., 2015). Thus, there is an unmet clinical need for more effective therapies, especially since the mainstay of treatment has not changed significantly in the last 30 years (Dohner et al., 2015). To develop more selective and better-tolerated therapies it is critical that we understand how AML cells grow, outcompete healthy haematopoiesis, and eventually generate an environment supportive of chemoresistant leukaemia stem cells. Alterations in BM innervation and stroma have been described in late stages of disease (Hanoun et al., 2014). However, the dynamic process leading to this stage is unknown, and its dissection promises to uncover new therapeutic targets. There are reports of VEGF secretion by AML cells (Fiedler et al., 1997) and of increased BM microvasculature density in patients (Aguayo et al., 2000; Hussong et al., 2000; Padro et al., 2000) and, more recently, murine models (Hanoun et al., 2014) at advanced stages of disease. However, clinical trials investigating anti-angiogenic therapy in AML patients have been disappointing (Fiedler et al., 2003; Ossenkoppele et al., 2012; Zahiragic et al., 2007). Thus, questions remain about the effect of AML growth on BM

vasculature, whether vascular remodelling may be beneficial for the disease, and whether BM vessels may be a valuable therapeutic target.

I hypothesized that AML-induced BM vascular remodelling may be more complex than simple induction of angiogenesis, and that progressive, nuanced changes could shape the ecological competition between leukaemia and healthy haematopoiesis. A spatio-temporal understanding of these changes may point to novel candidate interventions that could restore BM normal ecology, including HSC function, and in turn make AML cells more susceptible to chemotherapy.

3.2 – AML model establishment

To study the effects of AML growth on BM vasculature and HSCs as disease propagates through the tissue, I used the well-established MLL-AF9-driven murine model of AML, which recapitulates phenotypic and pathological features of human MLL-rearranged AML (Krivtsov et al., 2006; Somervaille and Cleary, 2006). To generate leukaemia cells detectable by IVM, I harvested myeloid progenitor cells from donor mice that expressed high levels of fluorescent proteins (FP), transduced them with a retroviral vector encoding the oncogene and GFP, and injected them into sub-lethally irradiated recipients. With this approach, multiple batches of GFP^+ FP^+ primary blasts (Figure 3.1A) were generated. Experiments were repeated using blasts from different primary recipients to ensure identification of consistent features of AML growth and to discount any possible primary donor-specific phenotype. To achieve reliable disease progression while minimizing the number of blasts injected, 100,000 primary AML blasts were transplanted by tail vein injection into non-irradiated secondary recipients. This strategy was critical as potential myelo-ablative conditioning regimens that could favour AML progression and cause haematopoietic and stromal damage were avoided. In all secondary recipients, progressive blast expansion was observed from day 8-10 post-transplantation with full BM infiltration typically reached between day 20 and 28, with the variation depending on the source of the primary blasts analysed. This leukaemic engraftment was accompanied by infiltration of the spleen, typically delayed compared to BM infiltration (Figure 3.1A). Blasts could be detected by flow cytometry in BM, spleen and peripheral blood. In each mouse, healthy haematopoiesis was progressively lost with AML expansion (Figure 3.1B). The loss of normal haematopoietic cells in the BM translated in peripheral cytopenias at advanced disease stages.

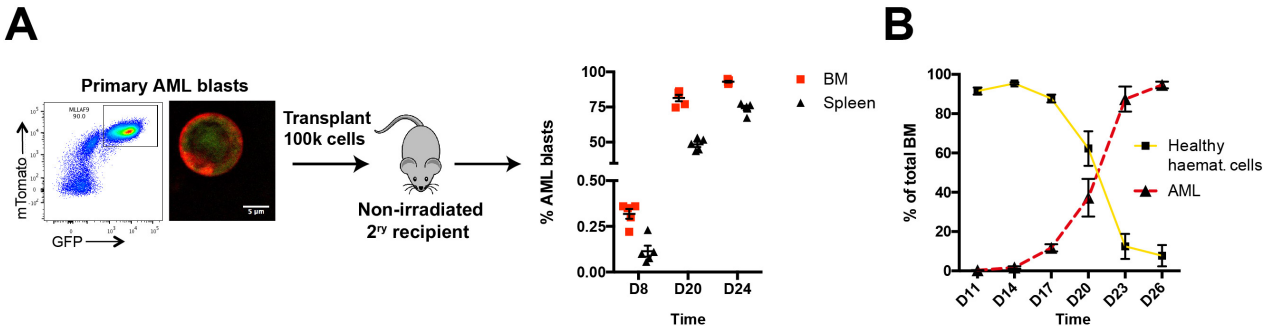

Figure 3.1 – MLL-AF9 driven experimental AML model. (A) 100,000 primary mTomato (or YFP or non-labelled) and GFP double positive AML cells are transplanted into non-irradiated secondary recipients, where they progressively infiltrate BM and spleen (n=5 mice analysed per time-point). **(B)** AML blasts infiltrate and outcompete non-malignant, healthy BM cells over time. Data shown are from 5 leukaemic per time-point from 2 independent cohorts. Error bars: mean ± S.D. Adapted from (Duarte et al., 2018a).

3.3 - Characterization of AML subsets during disease progression

AML is a heterogeneous disease with different phenotypic subtypes hypothesized to contribute to disease development and relapse. To better characterise this model, I therefore asked whether the proportions of these subsets changed during the development of leukaemia. To assess this, and following the hypothesis that AML is organized in a hierarchical way, I used a flow cytometry gating strategy similar to that applied to characterise normal haematopoiesis (Figure 2.2). The blasts were all $CD11b^+$ and contained varying proportions of cells expressing progenitor markers such as c-Kit, CD34 and CD16/32 (Figure 2.2). I observed significant heterogeneity in populations of AML subsets, with a decrease in frequency of differentiated Lin^+ cells at full infiltration (Figure 3.2A). The absolute number of L-GMPs increased in the BM, particularly at late timepoints (25-fold) (Figure 3.2B).

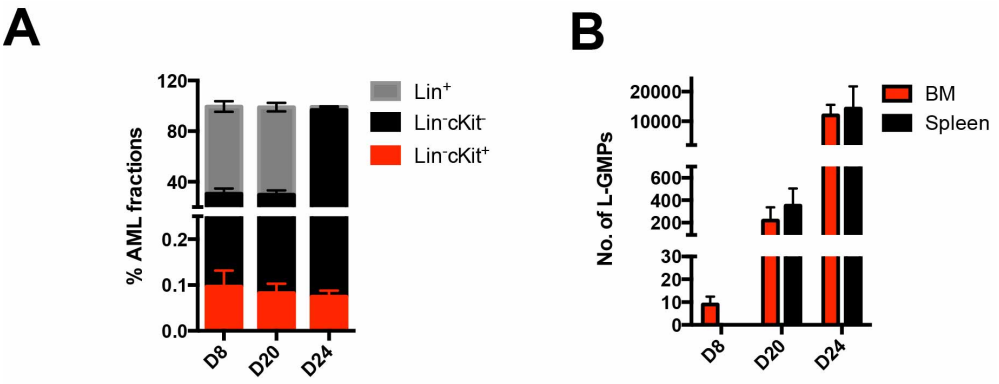

Figure 3.2 – AML subsets over time. (A) Proportions of AML fractions and **(B)** absolute numbers of L-GMPs in BM and spleen during disease progression. Data obtained from 5 leukaemic and 3 control mice per time-point from 2 cohorts. Error bars: mean ± SEM.

As discussed above, there is a debate about the frequency of LSCs, and more importantly, about the relative abundance of LSCs in the different phenotypically-defined AML fractions (Dick, 2008; Kelly et al., 2007). It is currently accepted that, in AML, disease-causing populations are organized according to a similar hierarchy as normal haematopoiesis and are descendent of LSCs (Bonnet and Dick, 1997; Lapidot et al., 1994) (Figure 3.3A). In the MLL-AF9 AML model, L-GMPs were shown to be highly enriched for LSCs. As we observed a significant enrichment for L-GMPs over time, and expansion of a stem-like population is normally not expected, I hypothesized a different hierarchy may exist in our disease model, whereby L-GMP could arise from downstream, differentiated blasts (Figure 3.3B).

To test this, I functionally tested 4 populations sorted at day 24 post-transplantation: L-GMPs, $CD34^-$, c-$Kit^{dim/-}$ and Lin^+ (Figure 3.3C). To prevent an overestimation of L-GMPs, I considered only cells that expressed very high levels of CD34 for both their analysis and isolation. Recipient mice developed leukaemia and were euthanized by approximately day 30, with the exception of mice injected with Lin^+ cells, as they developed disease at a faster rate (Figure 3.3D). All the groups presented with BM infiltration and peripheral disease, as demonstrated by spleen enlargement (Figure 3.3E). All AML fractions were generated in all the groups and the observed proportion of Lin^-c-Kit^+ cells was higher when compared to the previous experiment (Figure 3.3F and 3.3C). I also detected L-GMPs in all 4 groups of recipients (Figure 3.3G). Interestingly, the Lin^+ group had higher numbers of L-GMPs in the spleen than the BM. Altogether, this suggests that even Lin^+ cells, which are classically viewed as terminally differentiated AML cells, are able to generate less differentiated cells, including L-GMPs. Altogether, these data suggest that transplantable AML cells able to generate disease exist at a high frequency in several AML fractions, not just L-GMPs. This is consistent with (Somervaille and Cleary, 2006).

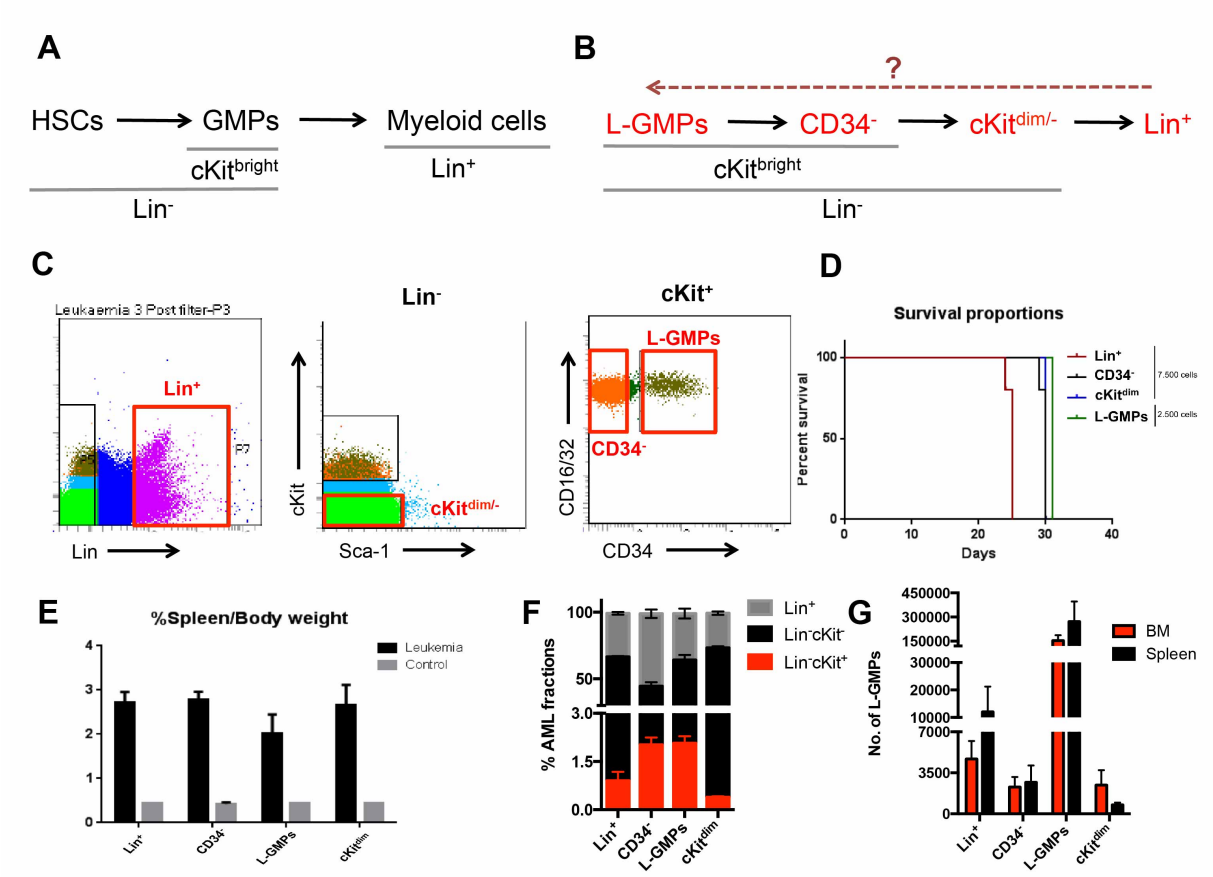

Figure 3.3 – L-GMPs are generated from downstream populations. (A) Simplified schematic of haematopoiesis leading to formation of myeloid cells **(B)** Organization of AML hierarchy (black arrows) and alternative view (dashed red arrow). **(C)** Gating strategy used to sort different AML populations (red) at day 24 post-transplantation. **(D)** Survival curves, **(E)** spleen weight and representative spleen appearance from mice injected with cells defined in (C). **(F)** Proportions of AML fractions and **(G)** absolute numbers of L-GMPs in BM and spleen at the time of multi-organ infiltration when the cell populations indicated on the X axis were injected in non-irradiated recipient mice. Data obtained from 5 leukaemic and 2 control mice per time-point from 1 cohort. Error bars: mean ± SEM.

3.4 – Multi-modal imaging of AML and the microenvironment

AML cells, vasculature, and haematopoietic cells were visualized by IVM performed on mouse calvarium BM (Figure 3.4), which has been shown to be representative of long bones marrow in terms of stroma composition and ability to support functional HSCs, and their homing and engraftment (Lassailly et al., 2013; Lo Celso et al., 2009). This approach is minimally invasive, and uniquely allows longitudinal observation of cellular dynamics (including cell migration, proliferation and death) taking place within the tissue over the course of hours or days.

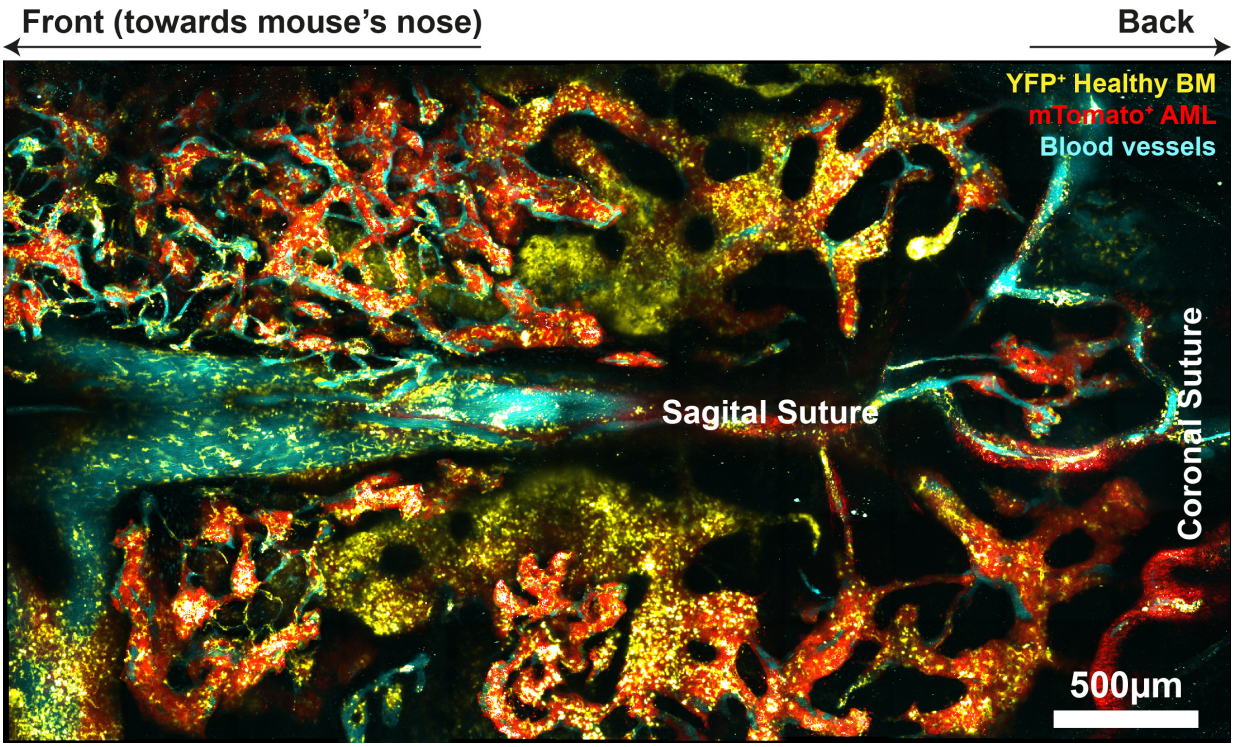

Figure 3.4 – Intravital imaging of the AML-microenvironment crosstalk. Maximum projection of IVM tile scan image showing AML cells (mTomato$^+$; red) interacting with non-malignant haematopoietic cells (YFP$^+$; yellow) and the vascular microenvironment (Cy5 dextran$^+$ blood vessels; cyan). Adapted from (Duarte et al., 2018a).

This approach has been essential to uncover previously unappreciated biological processes such as the ability of HSCs exposed to acute infection to engage wider than normal BM niches (Rashidi et al., 2014), the continuous migratory behaviour of individual T-ALL cells at different disease stages, and the rapid remodelling of osteoblastic cells induced by T-ALL (Hawkins et al., 2016). In particular, tile scan images of the entire BM space contained within the calvarium provide a comprehensive, three-dimensional, single-cell resolution overview of the overall organization of the tissue and are therefore ideal to uncover complex remodelling processes that are still poorly understood.

Furthermore, using a multi-modal imaging approach (Figure 3.5), AML blasts were detectable not only in the calvarium, but also in the spleen by IVM and in long bone sections by immunofluorescence imaging and flow cytometry, thereby allowing evaluation of *in vivo* cell dynamics and BM structural changes occurring during AML growth.

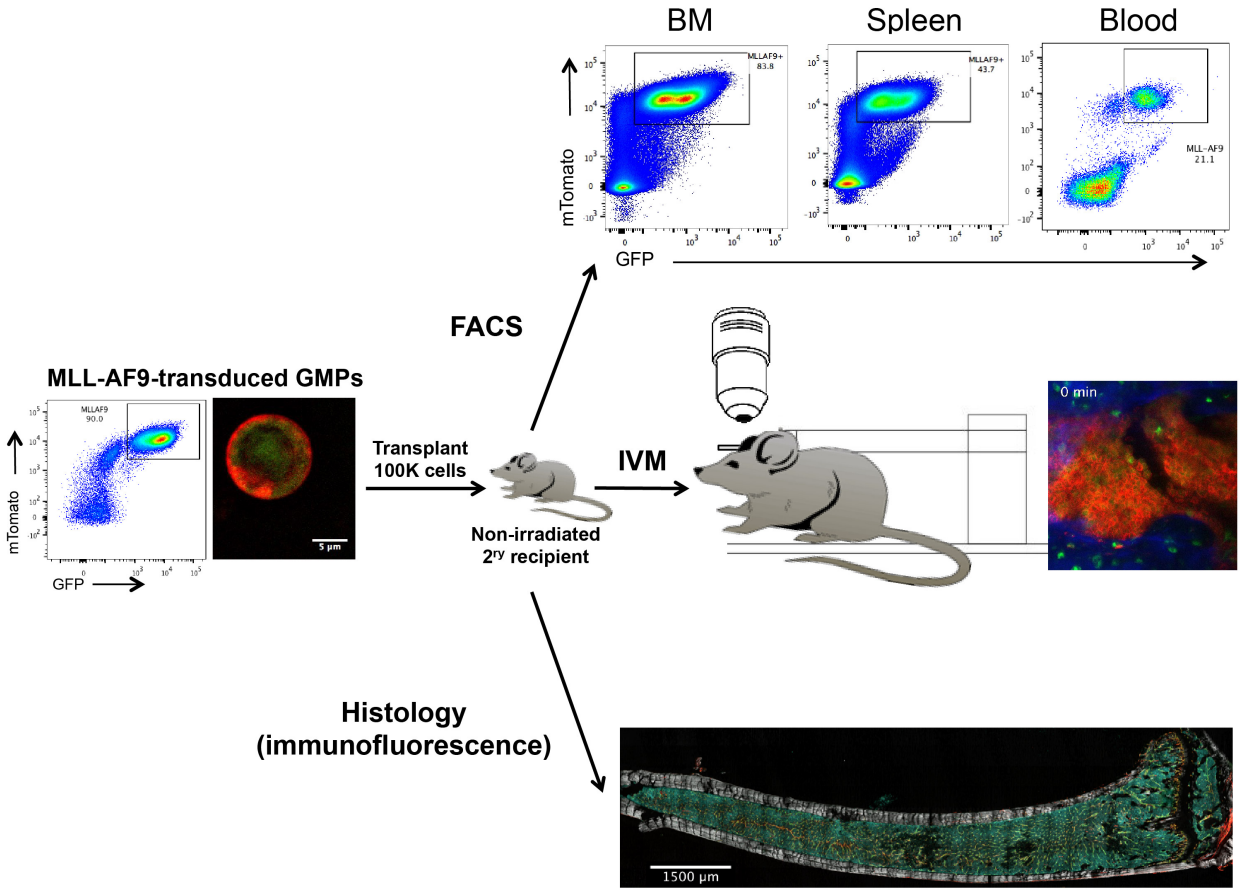

Figure 3.5 – Multimodal imaging of AML. MLL-AF9 blasts (left) were transplanted into non-irradiated secondary recipients (centre) and disease in BM, spleen and peripheral blood was detected by flow cytometry (right, top). IVM of the calvarium was performed to evaluate interaction of leukaemia with BM niches (right, middle) and immunofluorescence of bone sections allowed analysis of additional stromal populations (right, bottom).

3.5 - AML is associated with remodelling of bone marrow blood vessels

To identify progressive changes of blood vessels during AML progression *in situ*, I performed IVM of Flk1-GFP transgenic mice, in which $CD45^{-}Ter119^{-}CD31^{+}$ phenotypic ECs express GFP (Figure 3.6A) and can be visualized lining BM blood vessels labelled with Cy5-Dextran (Figure 3.6B). I observed multiple, significant changes in Flk-1 GFP^{+} blood vessels in mice burdened with AML (Figure 3.6C and D). Importantly, no significant differences in the total volume of BM blood vessels could be detected (Figure 3.6C).

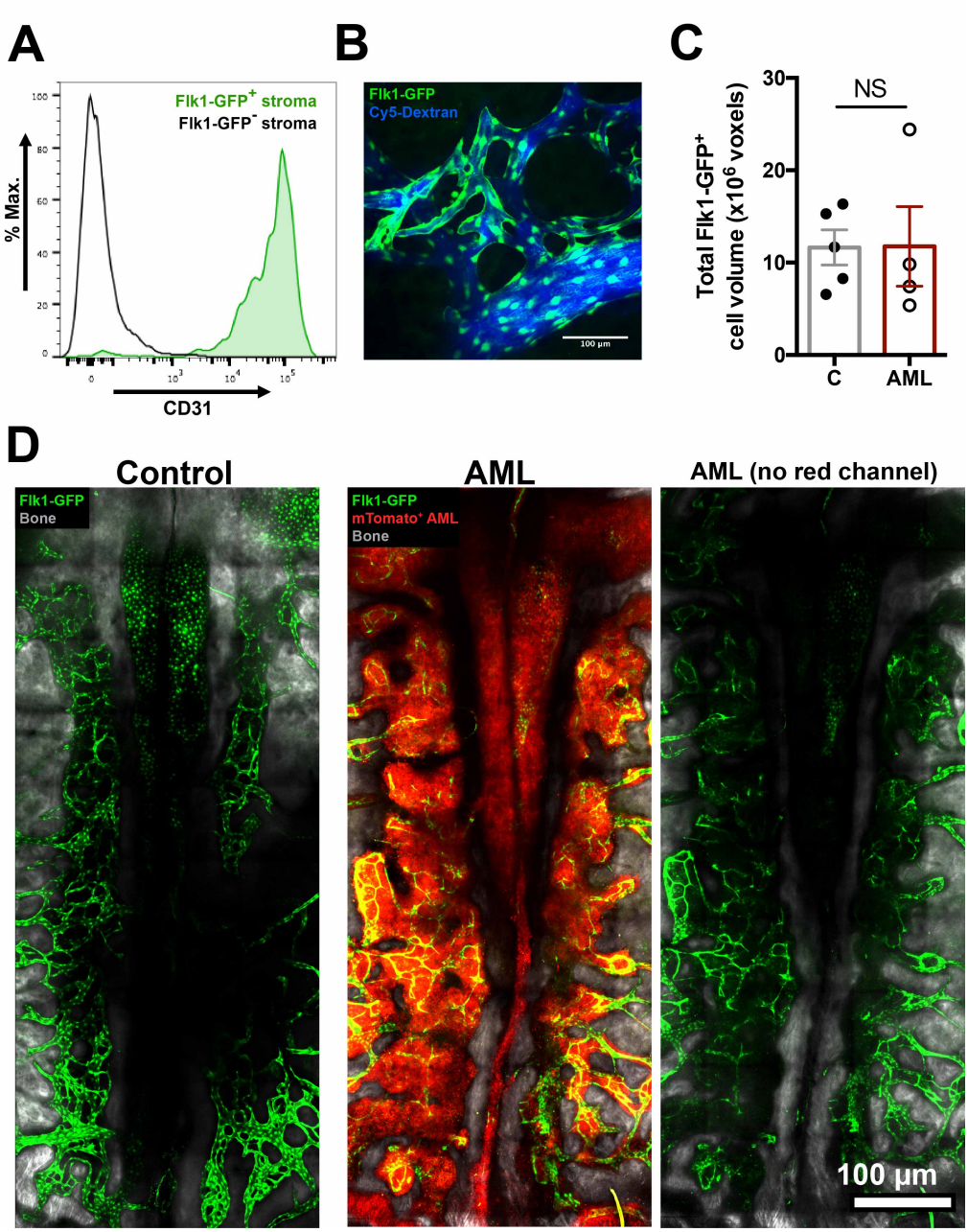

Figure 3.6 – Intravital imaging of Flk1-GFP mice. (A) Flk1-GFP$^+$ stromal cells (green) express high levels of CD31. **(B)** Representative maximum projection of a calvarial area showing Flk1-GFP+ ECs lining blood vessels highlighted by Cy-5 Dextran. Green: Flk1-GFP$^+$ cells; Blue: Cy-5 Dextran. **(C)** Total Flk1-GFP$^+$ cell volume from acquired tile scans. **(D)** Representative tile scans of control and leukaemic Flk1-GFP mice. Green: Flk1-GFP$^+$ cells (maximum projection); Grey: bone collagen SHG (median projection); Red: mTomato$^+$ leukaemia cells. Data are from 5 control and 4 AML mice. Adapted from (Duarte et al., 2018a).

Firstly, most vessels were narrower than those in control mice (Figure 3.7A). Secondly, they were characteristically further from the endosteal bone surface (Figure 3.7B and C). Imaging of partially infiltrated mice was consistent with the findings of (Herault et al., 2017) in revealing that AML cells clustered in patches of highly infiltrated areas, while the remaining BM space contained only sparse AML cells (Figure 3.7D). Blood vessels in highly infiltrated areas appeared unusually barbed and presented dynamic subcellular protrusions towards the parenchyma (Figure 3.7D, right panels).

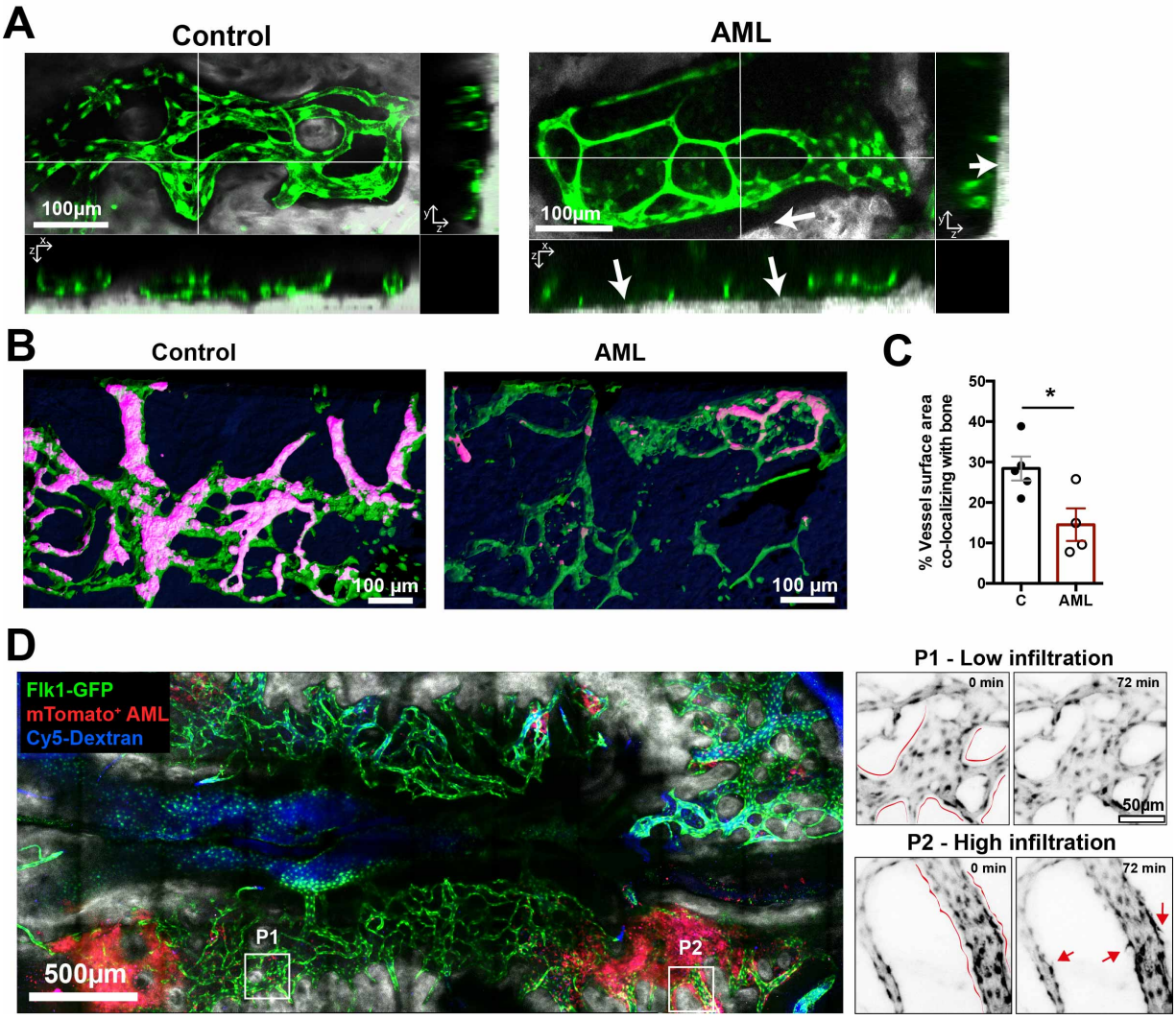

Figure 3.7 - Intravital imaging of the bone marrow reveals blood vessel remodelling in AML. **(A)** Representative projections and respective orthogonal views of Flk1-GFP$^+$ vessels (green) in the BM, showing vessels from leukaemic mice have reduced diameter and increased distance from bone (arrows). Grey: bone collagen SHG. **(B)** Representative 3D renderings of the surface of Flk1-GFP$^+$ vessels (green) with the areas co-localizing with bone highlighted in pink. Dark blue in the background is bone. **(C)** The contact area between vessels and bone is significantly reduced in AML-infiltrated BM. Data in (B-E) are from 5 control and 4 AML mice. **(D)** Representative tile scan of a Flk1-GFP mouse partially infiltrated with mTomato$^+$ AML cells (red). Time-lapse imaging shows steady and smooth vascular contours (red lines) in lightly infiltrated areas (P1). Instead, vessels in heavily infiltrated areas (P2) have irregular contours (red lines) and show active and inefficient sprouting (red arrows) over time. Adapted from (Duarte et al., 2018a).

High-resolution time-lapse recording of blood vessels at late stages of AML revealed sequential formation and retraction of sprouts (Figure 3.8A and Supplementary Video 3A), similar to those described in response to strong angiogenic stimuli (Gerhardt et al., 2003; Jakobsson et al., 2010). However, this sprouting process was never efficient and I could not detect formation of any steady lateral branches. This is consistent with the increased levels of VEGF-A detected in mice infiltrated with AML (Figure 3.8B).

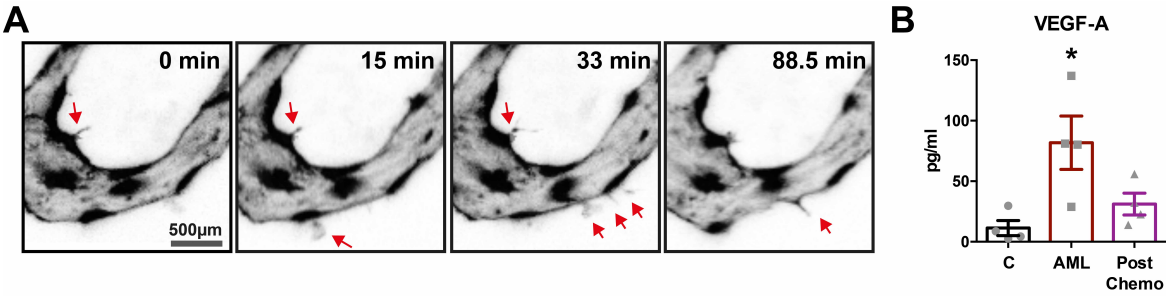

Figure 3.8 – Inefficient angiogenesis in AML-burdened areas. (A) Selected frames from representative time-lapse data from a heavily infiltrated area showing rapid vascular sprout formation (red arrows) and regression (full time-lapse: Movie S1). **(B)** VEGF-A levels in serum of control mice (C), mice with AML (AML) and mice with AML treated with combined cytarabine and doxorubicin (Post Chemo). n: 4 mice per group. Error bars: mean ± SEM. Adapted from (Duarte et al., 2018a).

I also occasionally observed vascular damage caused by EC breakage into small fragments (Figure 3.9A and Supplementary Video 3B). Consistent with this observation, I observed abundant 1 to 4μm-sized cellular debris of endothelial origin (GFP^+) in the vascular lumen of AML-burdened mice (Figure 3.9B and C, and Supplementary Video 3C). These debris particles maintained expression of phenotypic endothelial markers, including high levels of CD31 and endomucin (Figure 3.9D), and contained nucleic acids within an intact membrane (Figure 3.9E).

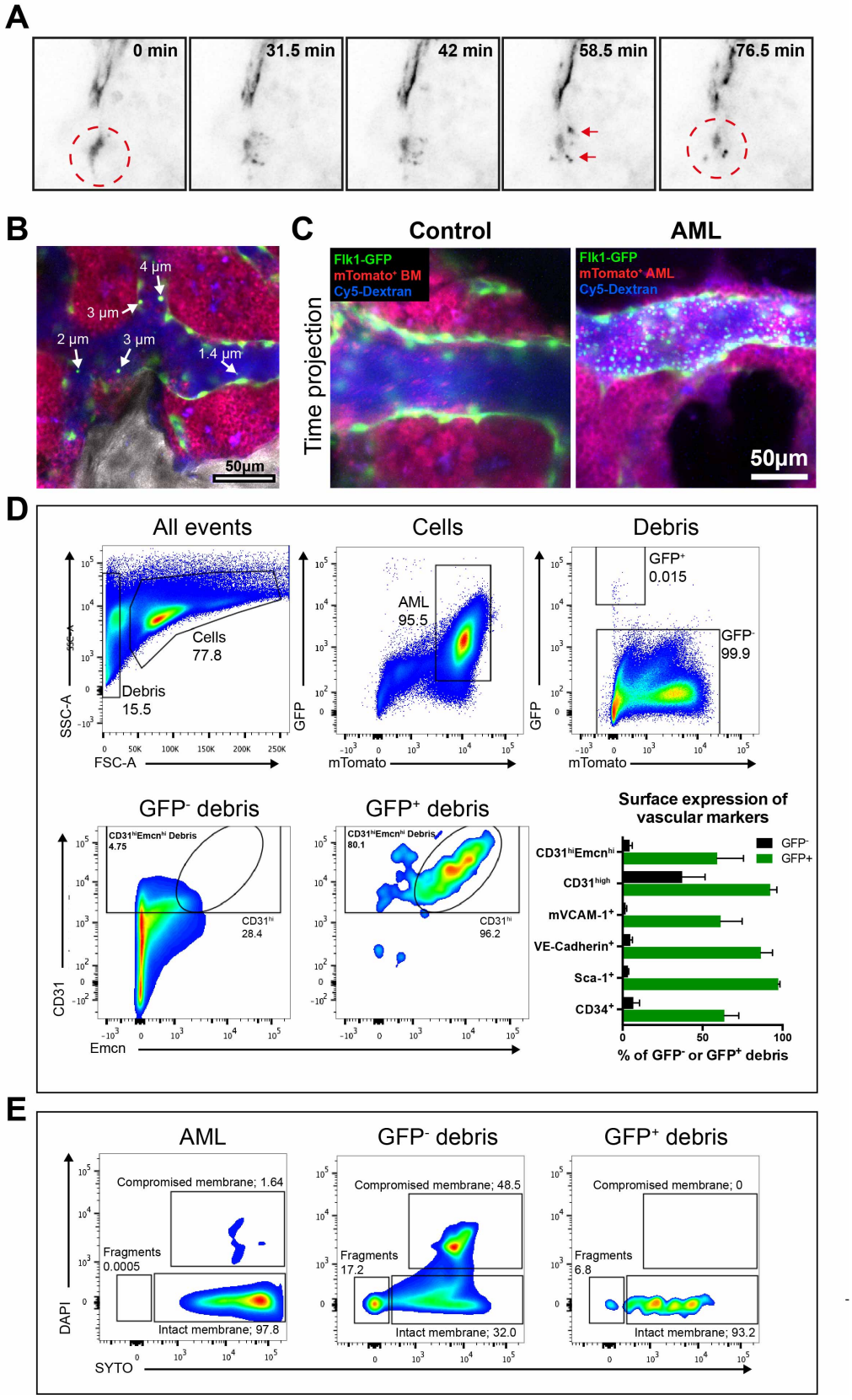

Figure 3.9 – Cellular debris is released from Flk1-GFP$^+$ endothelial cells in AML-burdened mice. (A) Selected time points from representative time-lapse data from a heavily infiltrated area showing rapid vascular collapse **(B, C)** GFP$^+$ extracellular vesicles are found in circulation in

leukaemia-burdened Flk1-GFP mice (A: single 2D frame; B: time projection of Supplementary Video 3C). **(D)** Gating strategy used to identify GFP^+ debris ("GFP^+ debris"), expressing high levels of vascular markers, as assessed by flow cytometry of the BM. **(E)** GFP^+ debris is positive for the cell-permeable SYTO and negative for the cell-impermeable DAPI dyes, suggesting that they are membrane-layered particles, carrying variable levels of nucleic acids. Data representative of 3-4 leukaemic mice. Adapted from (Duarte et al., 2018a).

3.6 - Endosteal vessels are specifically lost in mice with AML

Prompted by these initial observations, I performed in-depth analysis of blood vessels in the endosteal areas of long bones using immunofluorescence of whole, undecalcified long bone sections from healthy and diseased mice (Figure 3.10A). This approach allowed me to simultaneously investigate AML-mediated changes in the vasculature of different BM areas: the central marrow diaphysis, the bone-lining endosteum, and the trabecular metaphysis. I was able to detect a significant decrease of vessels in the endosteum and metaphysis over time (Figures 3.10B and C). The endosteal vessels were significantly, and progressively, lost at both intermediate (40-50% BM infiltration) and advanced (>80% BM infiltration) disease stages (Figure 3.10C). Notably, vessel loss was specific to these areas, and not observed in the diaphysis region, where vessels were either maintained or transiently increased (Figures 3.10B and C).

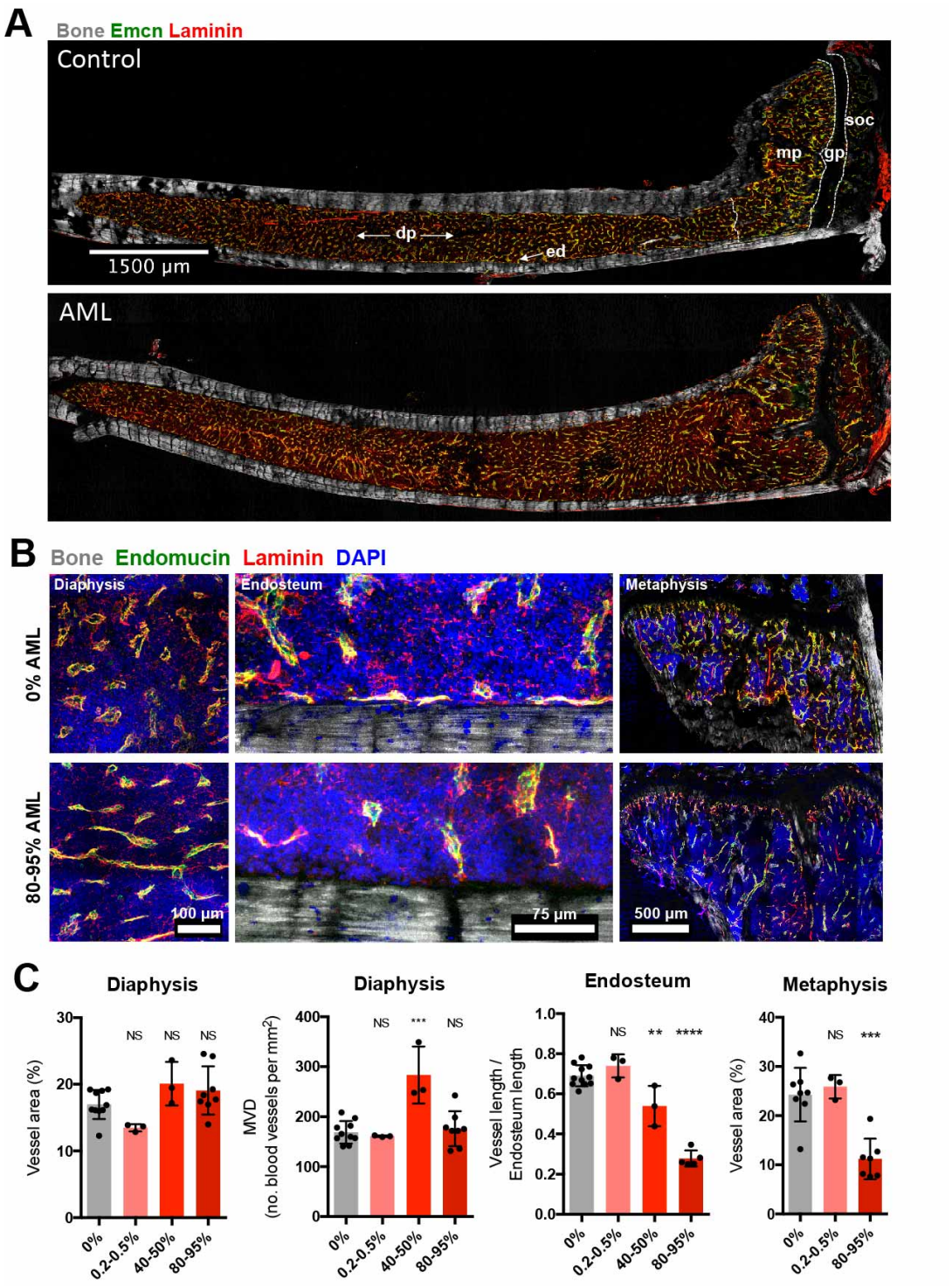

Figure 3.10 – Endosteal and metaphyseal vessels are decreased in AML. (A) Representative maximum intensity projection of a tile scan of 20µm thick sections of undecalcified tibias from wild-type control (top) and fully infiltrated (bottom) mice. Vessels are labelled by laminin and endomucin (Emcn) immunostaining. dp: diaphysis; ed: endosteum; mp: metaphysis; gp: growth plate; soc: second ossification centre. **(B)** Representative maximum intensity projections comparing vascular staining in the diaphysis, endosteum and metaphysis of control (top row) and fully infiltrated (bottom row) mice. Grey: bone collagen SHG; green: endomucin^{+} vessels; red: laminin^{+} vessels and extracellular matrix;

blue: DAPI. **(C)** Quantification of blood vessels in diaphysis, endosteum and metaphysis at different stages of AML progression. Data obtained from 11 mice with 0% infiltration (control), 3 mice with 0.2-0.5% infiltration, 3 mice with 40-50% infiltration and 5-10 mice with 80-95% infiltration from 2 independent cohorts. Error bars: mean ± SD. Adapted from (Duarte et al., 2018a).

The relevance of these observations in humans was confirmed by additional histological analysis of BM trephine biopsies from AML patients with >80% infiltration, obtained through collaboration with the groups of Prof. Louise Purton (Peter MacCallum Cancer Centre, Melbourne, Australia) and Dr. Andrew Wei (Department of Haematology, Alfred Hospital, Melbourne, Australia). We were able to confirm that endosteal vessels were decreased in AML samples (Figure 3.11A and B).

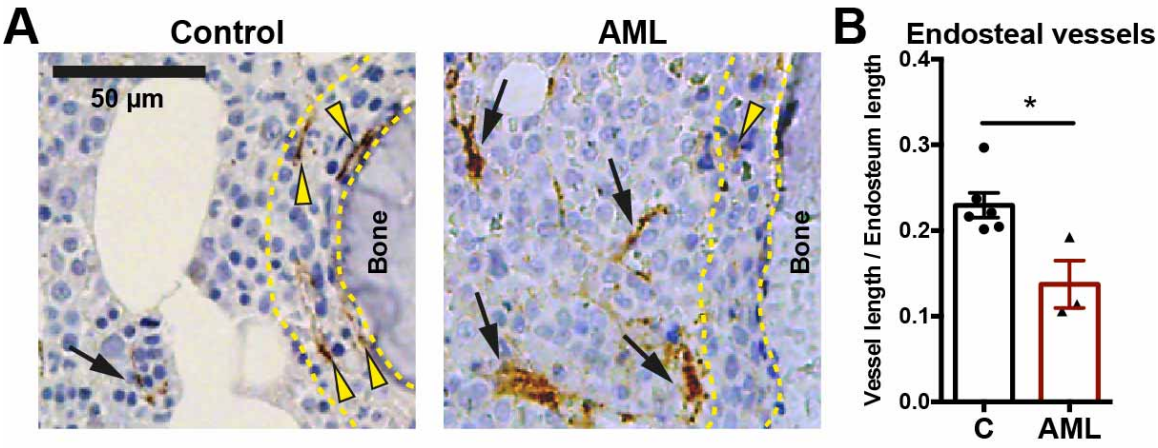

Figure 3.11 – Endosteal vessels are decreased in AML patients. (A) Representative images of BM trephine biopsies from control and AML patients stained with anti-von Willebrand factor antibody to mark blood vessels (brown). Yellow dotted lines delineate endosteal area within 20µm from the bone. Yellow arrowheads point at endosteal vessels, black arrowheads at central marrow vessels. **(B)** Endosteal vessels are decreased in AML patients. Data obtained from 6 control and 3 AML patients. Error bars: mean ± SEM. Adapted from (Duarte et al., 2018a).

Additionally, I questioned whether the loss of endosteal endothelium was specific of AML or rather a general consequence of cancer invasion in the BM. Using a murine model of Notch1-driven T-ALL, I was able to observe that in this setting endosteal vessels were maintained (Figure 3.12A and B), suggesting that the vascular remodelling I observed is specific to AML. These findings pointed to a specific depletion of the functionally unique endosteal endothelium, recently shown to regulate osteogenesis (Kusumbe et al., 2014) and to maintain HSCs (Itkin et al., 2016; Kusumbe et al., 2016).

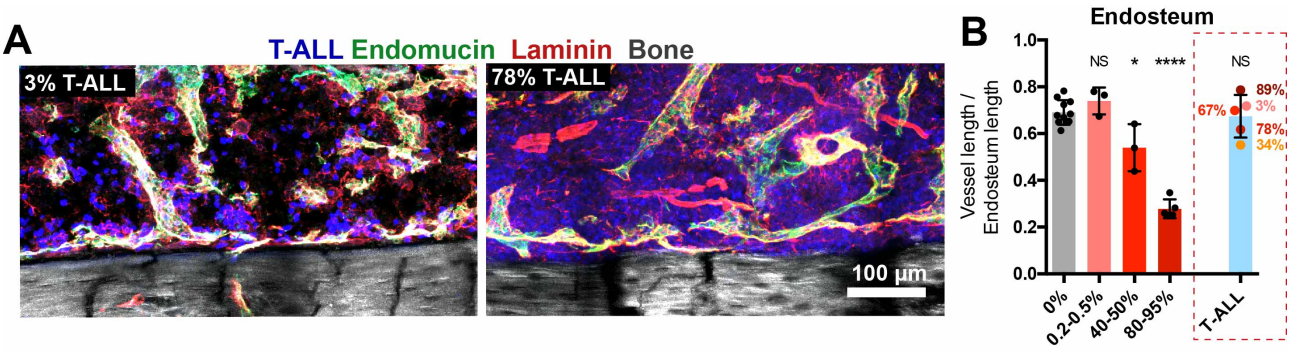

Figure 3.12 – Endosteal vessels are maintained in T-ALL. (A) Representative maximum intensity projections comparing endosteal vessels in poorly infiltrated (3%) and highly infiltrated (78%) mice with T-ALL. Grey: bone collagen SHG; green: endomucin$^+$ vessels; red: laminin$^+$ vessels and extracellular matrix; blue: T-ALL cells. **(B)** Quantification of endosteal vessels in mice with different levels of T-ALL (each dot represents a mouse). Control and AML samples are reproduced from Figure 3.10C. Error bars: mean ± SEM. Adapted from (Duarte et al., 2018a).

3.7 - AML creates a pro-inflammatory environment in the endosteum

Since I observed differential remodelling of the microenvironment in AML-burdened mice, I questioned whether they could be triggered by regional variations in leukaemia cells. To address this question, I performed RNA-seq analysis on sorted AML cells from trabecular-rich areas (crushed metaphysis) or central BM areas (flushed diaphysis) (Figure 3.13A). Jointly with Isabella Kong from the laboratory of Dr. Edwin Hawkins (The Walter and Elizabeth Institute of Medical Resarch, Melbourne, Australia), I compared the transcriptome of endosteal and central AML cells originating from three independent primary donors to non-transformed GMPs from the BM of healthy mice. Gene expression and multi-dimensional scale analyses illustrated that each AML batch had its own unique gene expression signature, consistent with clonal evolution of cancer cells, while control GMPs were extremely homogeneous (Figure 3.13B, C and D).

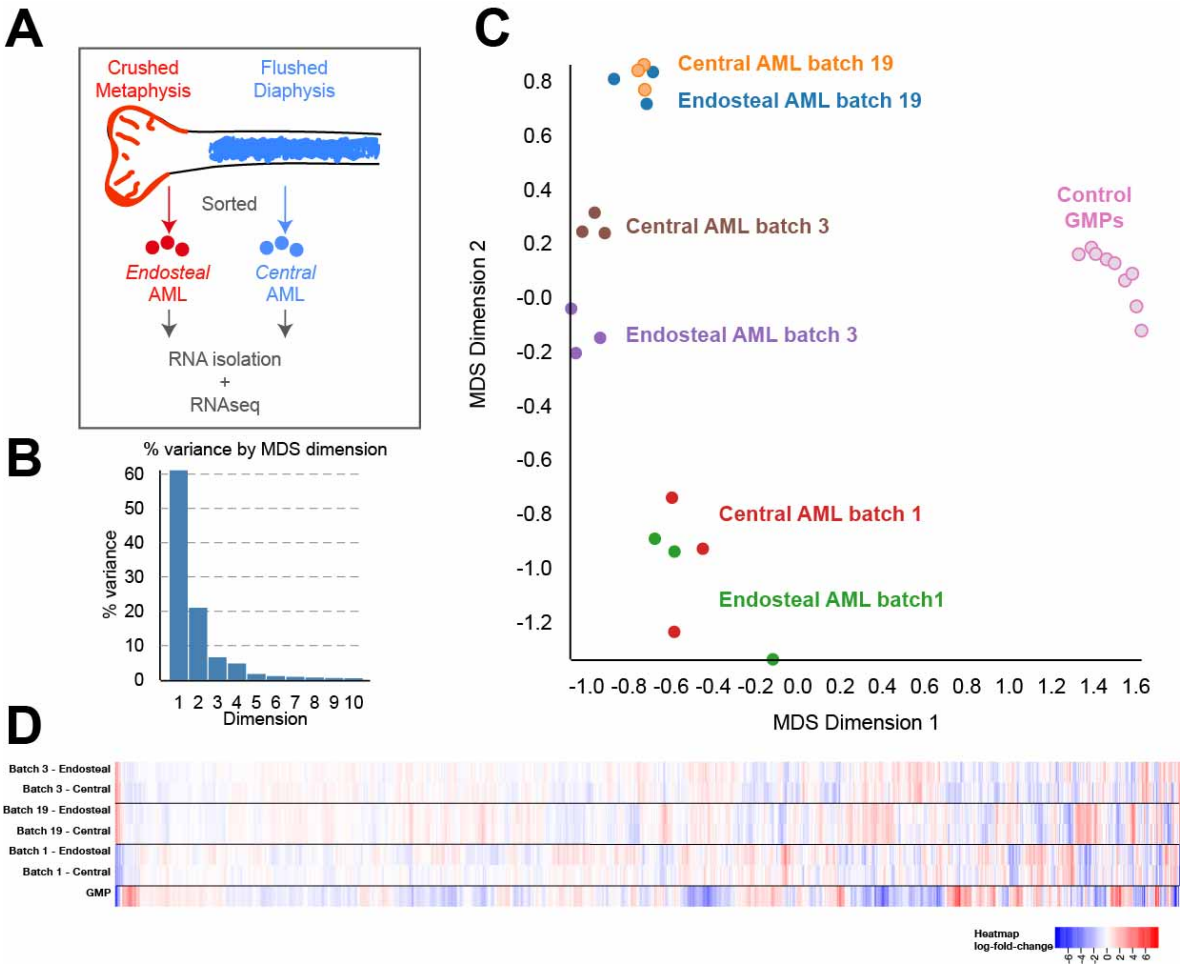

Figure 3.13 – RNA sequencing analysis of AML cells isolated from different BM areas. (A) Central and endosteal AML cells were isolated and analysed by RNAseq. **(B)** Most of the variance in the data is explained by MDS Dimensions 1 (60%) and 2 (21%). **(C)** Multidimensional scaling (MDS) plot of distances between gene expression profiles of AML cells and control GMPs. Each dot represents a sample. Data obtained from 3 AML batches, 3 biological replicates per batch and 9 control mice. **(D)** Heatmap of all the genes that are differentially regulated, with false detection rate (FDR) cut-off of 0.05. Gene expression is relative to GMP. Adapted from (Duarte et al., 2018a).

Despite the similarity in gene expression between endosteal and central AML cells, GSEA demonstrated endosteal AML cells were enriched for expression of genes involved in the inflammatory response (Figure 3.14A) and TNF signalling pathways (Figure 3.14B). Furthermore, the anti-angiogenic cytokine *Cxcl2* (also known as MIP-2α or chemokine gro-β; downstream of TNF (Tessier et al., 1997)) was significantly more expressed in endosteal AML cells (Figure 3.14C and D). ELISA analysis of TNF and CXCL2 levels in BM fluids confirmed that both cytokines were specifically and highly increased in endosteal areas of AML-burdened mice (Figure 3.14E and F). These results highlight the importance of inflammation in AML pathogenesis and support a role for CXCL2 and TNF in the remodelling of endosteal vessels.

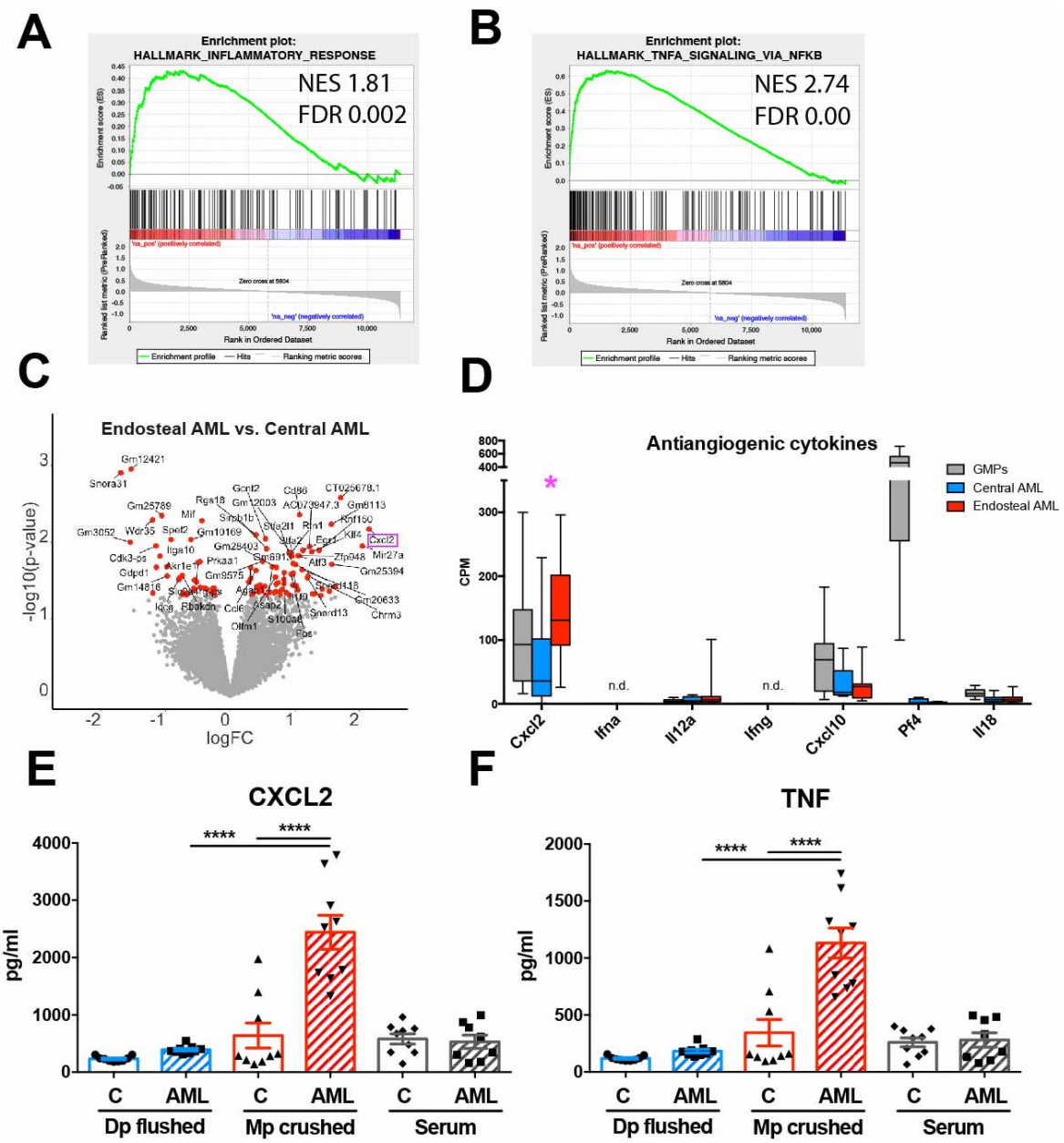

Figure 3.14 – AML creates an endosteal pro-inflammatory milieu. (A, B) Gene set enrichment analysis (GSEA) comparing AML cells isolated from central and endosteal BM areas for genes involved in (A) inflammatory response and in (B) the TNF signalling pathway. **(C)** Volcano plot showing genes that are differentially expressed in endosteal and central AML cells. Red dots represent individual genes that are differentially expressed with a p-value cut-off of 0.05. *Cxcl2* is highlighted and is overexpressed in endosteal AML cells. **(D)** Expression of genes encoding cytokines known to inhibit angiogenesis. **(E)** CXCL2 and **(F)** TNF levels in central and endosteal BM fluid fractions and in the serum of the same mice. Data obtained from 9 control and 9 AML-burdened mice. Adapted from (Duarte et al., 2018a).

3.8 - BM stroma is locally and progressively depleted in AML

Flow cytometry analysis (Figures 3.15A and B) demonstrated that although the proportion of ECs in surviving stroma was increased in AML-burdened mice (Figure 3.15C), the absolute number of ECs was not statistically significantly different (Figure 3.15D). However, phenotypically-defined endosteal ECs (CD31^{hi}Endomucin^{hi} or CD31^{+}Sca-1^{+}) were significantly reduced in diseased mice (Figure 3.15E and F).

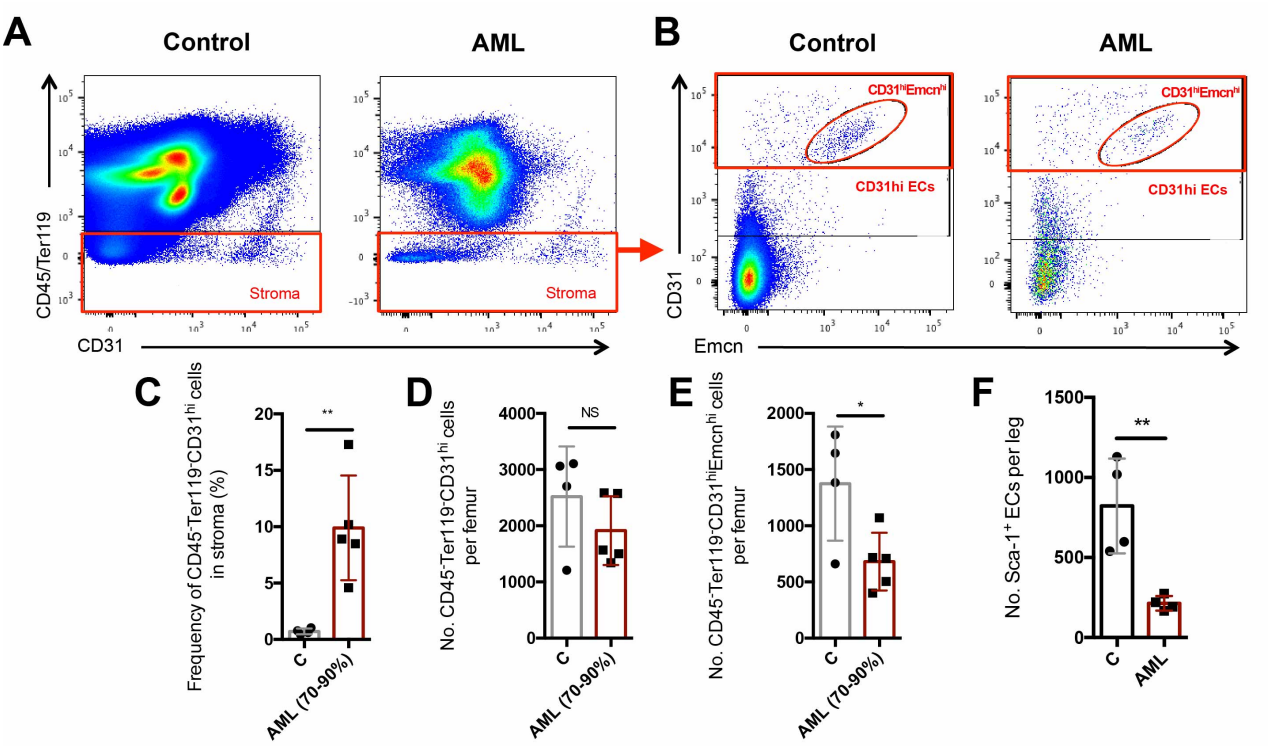

Figure 3.15 – Endosteal endothelial cells are decreased in AML. (A, B) Gating strategy used to quantify BM stroma cells **(A)** and ECs **(B)** by flow cytometry. Although the frequency **(C)** of ECs is increased, absolute EC numbers **(D)** are unaltered in AML-burdened mice. Absolute numbers of **(E)** CD31^{hi}Emcn^{hi} and **(F)** CD31^{+}Sca-1^{+} endosteal ECs are significantly decreased in fully infiltrated mice. Data obtained from 4 control and 5 leukaemic mice (A-E) and from 4 control and 4 leukaemic mice (F). Error bars: mean ± SEM. Adapted from (Duarte et al., 2018a).

To better understand how AML affects overall BM stroma, I imaged chimeric mice bearing membrane-bound Tomato^{+} stroma and wild-type, non-fluorescent haematopoietic cells, injected with YFP^{+}GFP^{+} double positive AML blasts. At >50% BM infiltration, I observed a dramatic reduction of overall stromal cells *in vivo*, including the stroma surrounding blood vessels and adjacent to bone (Figure 3.16A).

Consistent with this pattern, extensive IVM time-lapse (7 to 12 hours) of these mice revealed that blood vessels underwent abnormal oscillations, suggesting that their anchorage to the surrounding parenchyma had been lost (Figure 3.16B, Supplementary Video 3D, arrowheads). Extensive stroma loss was confirmed by flow cytometry analysis of non-chimeric mice, revealing a >10-fold reduction in the number of CD45^{-} Ter119^{-} cells in the BM of AML-burdened mice (Figure 3.16C). To better understand the process leading to such dramatic overhaul of BM stroma, we performed live imaging at earlier stages of disease (day 10-12 post-injection of leukaemia blasts, 5-15% infiltration). At these earlier time points, we could compare areas with low and high infiltration within the same mouse (Figure 3.16D). Here, perivascular and endosteal stroma were depleted in highly infiltrated areas (P2), while both components maintained a normal appearance in weakly infiltrated areas (P1), suggesting that AML cells remodel the stroma locally after reaching a certain threshold density.

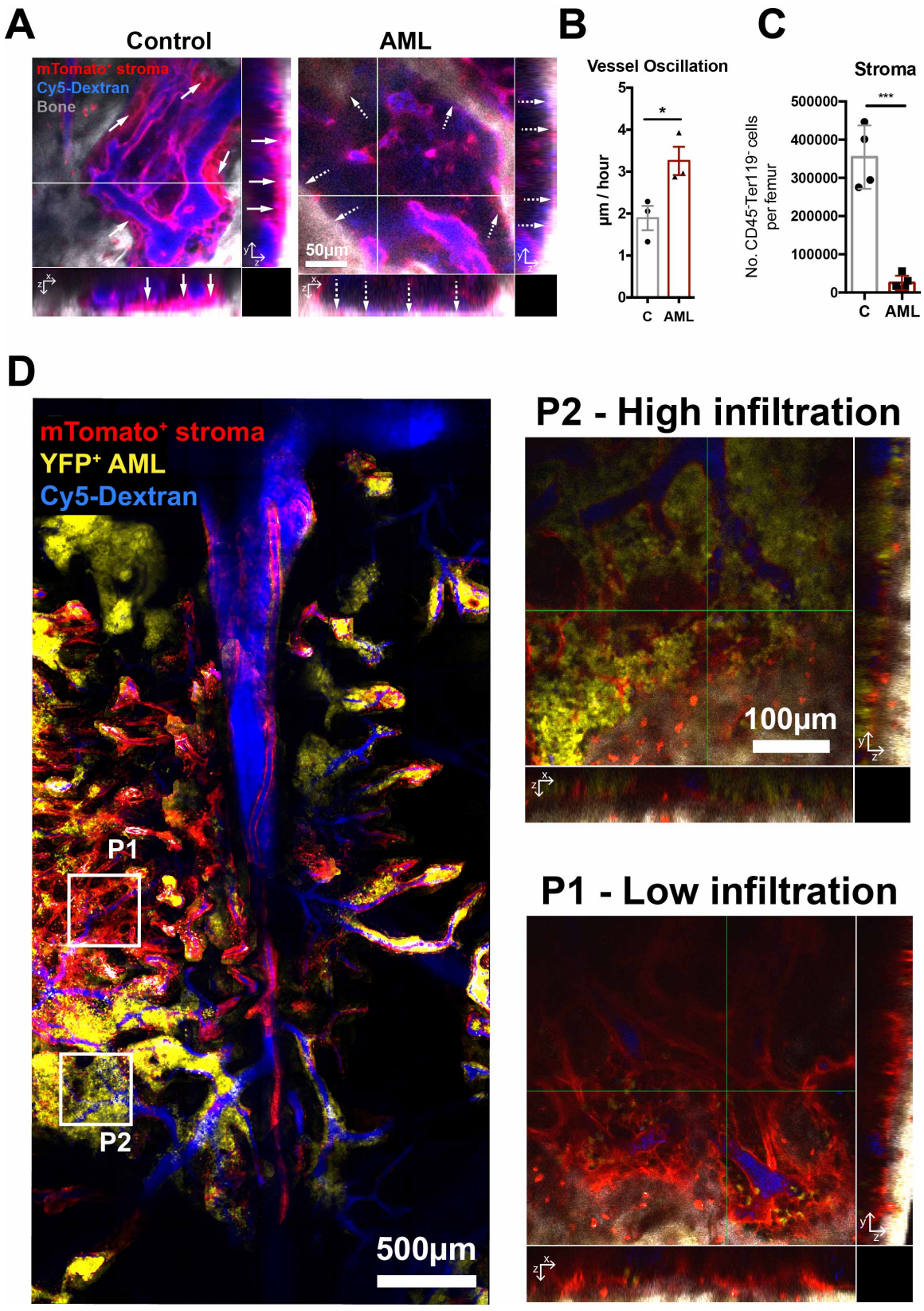

Figure 3.16 – Stroma is locally and progressively remodeled in AML. (A) Representative maximum intensity projections and orthogonal views of BM areas of mT/mG mice reconstituted with non-fluorescent wild-type BM (Control and AML) and transplanted with YFP^+GFP^+ leukaemia cells (AML, cells not shown). AML mice show depletion of $mTomato^+$ stromal cells (red) adjacent to

vessels (Cy-5 dextran; blue) and bone (SHG; grey). Arrows point at endosteal stroma in control mice. Dashed arrows evidence the loss of endosteal stroma in AML. Data is representative of 3 control and 3 leukaemic mice. YFP^+ AML cells not shown for clarity purposes. **(B)** Vascular oscillation is significantly increased in mice with AML, as shown in the Movie S4. Data pulled from a total of 2 BM positions per mouse, obtained from 3 control and 3 leukaemic mice. Error bars: mean ± SEM **(C)** Absolute numbers of overall $CD45^-Ter119^-$ stromal cells are significantly decreased in AML-burdened mice. Data obtained from non-chimeric 4 control and 5 leukaemic mice. *** $p<0.001$. Error bars: mean ± SD. **(D)** Representative tile scan and selected P1 and P2 areas showing AML cells (yellow) colonizing the calvarium in clusters and locally depleting $mTomato^+$ stromal cells (red) adjacent to blood vessels (Cy5 dextran; blue) and bone (SHG; grey). Data is representative of 3 mice. Adapted from (Duarte et al., 2018a).

3.9 - Osteoblastic cells are locally depleted in AML

Because the endosteal endothelium has been shown to locate next to and sustain osteoblasts (Kusumbe et al., 2014), I expanded my analysis of the endosteal microenvironment to include a focused investigation of osteoblastic cells (CFP^+ or GFP^+ cells in Col2.3-CFP/GFP reporter mice, respectively) during AML growth.

Together with Dr. Olufolake Akinduro, I performed IVM of the calvarium of Col2.3-GFP mice, which revealed that GFP^+ osteoblastic cells were significantly reduced in an infiltration-dependent manner (Figure 3.17A and B). IVM of chimeras containing CFP^+ osteoblastic cells, $mTomato^+$ healthy haematopoietic cells, and YFP^+GFP^+ leukaemia revealed that AML cells, as they remodel stroma and vessels locally, also outcompete healthy haematopoietic cells and eliminate osteoblastic cells (Figure 3.17C and D). This finding indicated that microenvironmental and haematopoietic changes induced by leukaemia evolve focally and in parallel. IVM of healthy and highly infiltrated double transgenic Flk1-GFP/Col2.3-CFP mice confirmed that osteoblasts and endosteal vessels were lost in the presence of AML, while central vessels were maintained (Figure 3.17E).

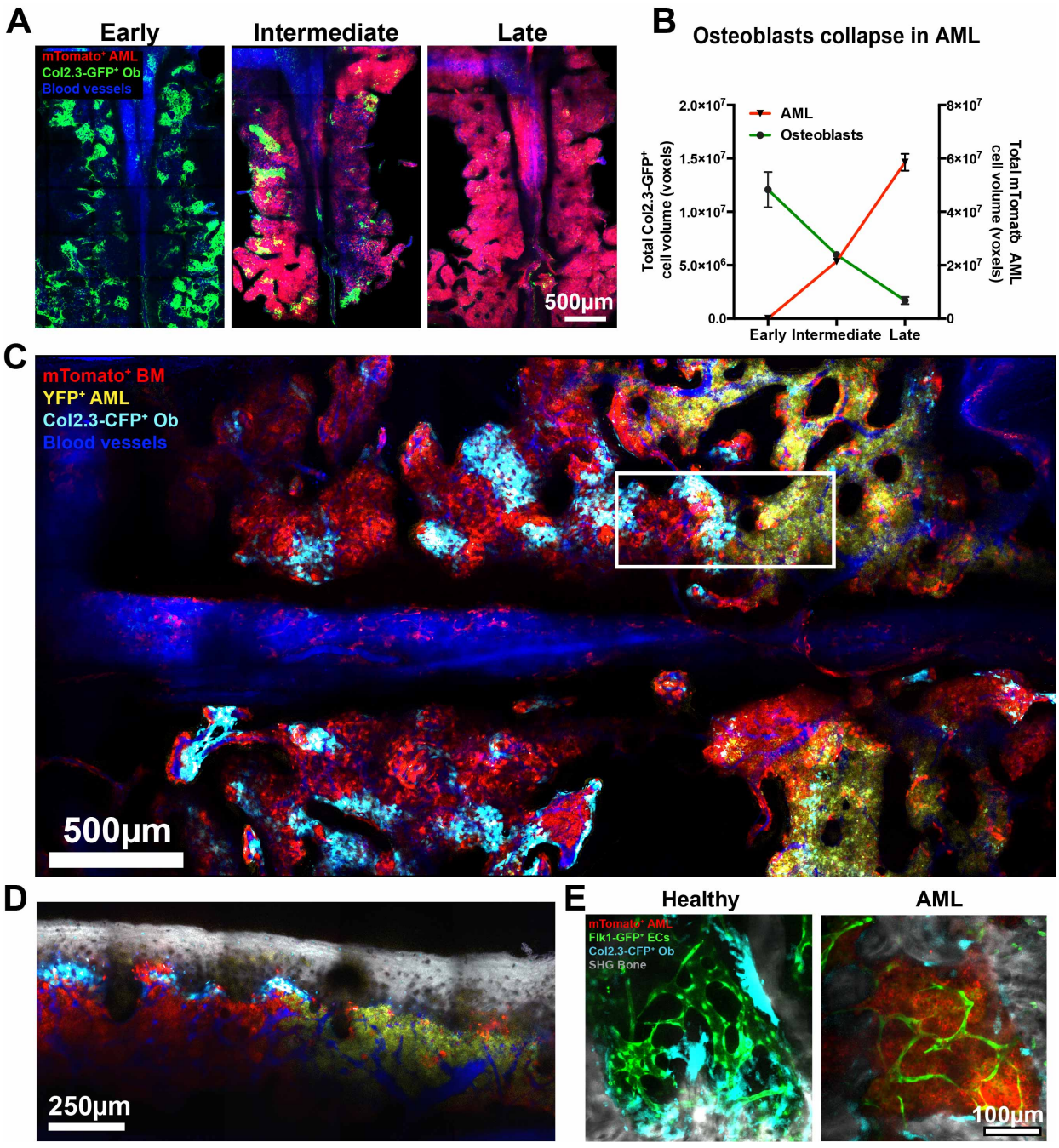

Figure 3.17 – AML remodels the endosteal niche and outcompetes normal haematopoiesis. (A) Representative tile scans of Col2.3-GFP mice transplanted with mTomato$^+$ leukaemia. Green: Col2.3-GFP$^+$ osteoblastic cells; red: mTomato$^+$ AML; blue: Cy5 Dextran$^+$ blood vessels. **(B)** Automatic segmentation and volume calculation (voxels) of osteoblast loss (green line) and leukaemia expansion (red line), over time. Data obtained from 17 mice, from 2 independent cohorts. Error bars: mean ± SEM. **(C)** Maximum intensity projection of a tile scan of a Col2.3-CFP recipient with mTomato$^+$ healthy haematopoietic cells and YFP$^+$GFP$^+$ AML blasts. Leukaemia cells (yellow) infiltrate the calvarium and deplete osteoblastic cells (cyan) and healthy haematopoietic cells (red) locally. **(D)** 2D slice from the area framed in (C) at a depth close to the calvarium surface, including the BM components from (C) and collagen bone SHG (grey). (C-D): Data obtained from 6 mice. **(E)** IVM

images of representative areas of the calvarium BM of control and AML-infiltrated Col2.3-CFP/Flk1-GFP double-transgenic mice. Cyan: Col2.3-GFP^{+} osteoblastic cells; green: Flk1-GFP^{+} ECs; red: mTomato^{+} AML cells; grey: bone. n: 3 mice. Adapted from (Duarte et al., 2018a).

To understand whether one microenvironment component may be lost first, I analysed long bone sections from mice at intermediate stages of disease (Figure 3.18A). Within the same bone, osteoblasts were significantly decreased only in areas with high levels of leukaemic infiltration (Figure 3.18B), while I could detect loss of endosteal vessels in areas with intermediate levels of infiltration (Figure 3.18C). These data suggest that endosteal vessels may be lost earlier than osteoblasts.

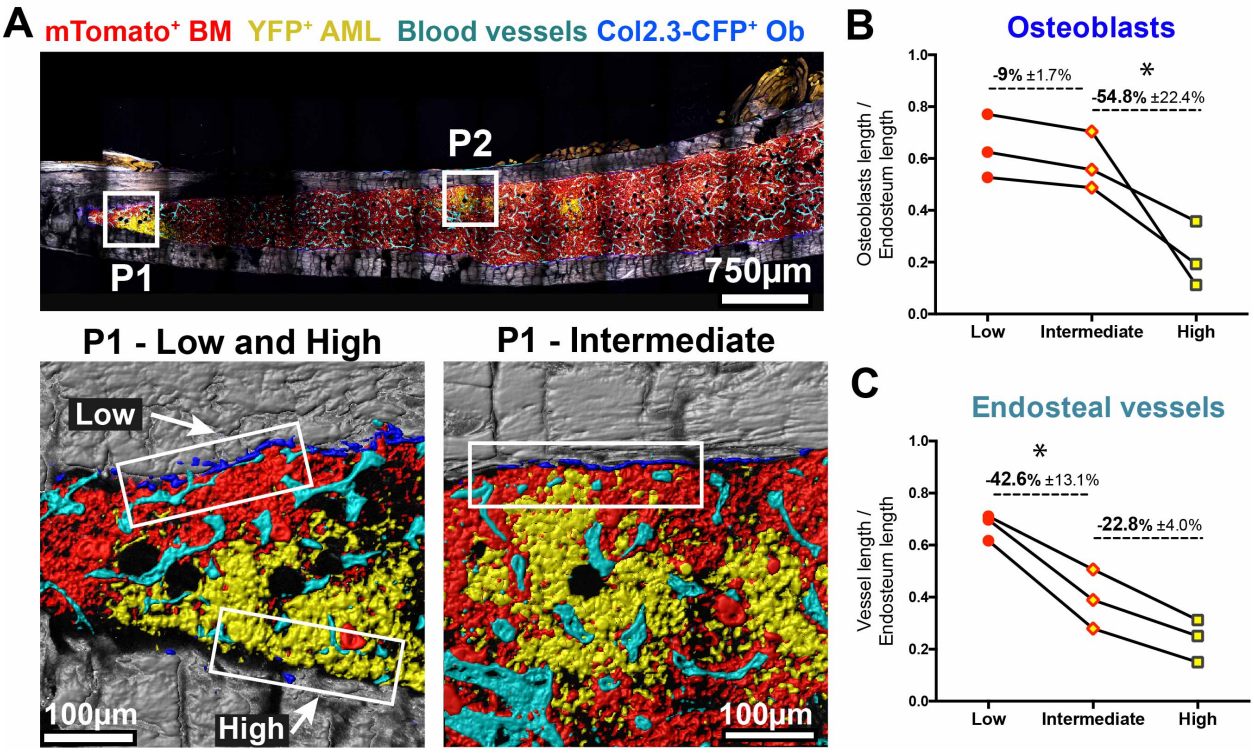

Figure 3.18 – Endosteal vessels are lost before osteoblasts. (A) Maximum intensity projection of a representative tile scan of undecalcified tibia sections from Col2.3-CFP recipients with mTomato^{+} healthy haematopoietic cells (red) and YFP^{+}GFP^{+} AML (yellow) blasts. Grey: bone; blue: osteoblasts; cyan: vessels (endomucin^{+}). Mice had intermediate levels of AML infiltration. Boxes in P1 and P2 higher magnification images illustrate examples of areas within the same bone with low, high and intermediate levels of infiltration, used to quantify stroma remodeling. **(B, C)** Quantification of osteoblasts and endosteal vessels. Data obtained from 3 mice. Adapted from (Duarte et al., 2018a).

3.10 - Loss of healthy haematopoiesis is temporally and spatially correlated with bone marrow and spleen vascular remodelling

I next investigated the haematopoietic changes associated with microenvironment remodelling. Flow cytometry analysis of non-chimeric mice with increasing AML infiltration showed a decrease of overall normal haematopoietic cells in the BM (Figure 3.1A) and a sharp and early decline of differentiated haematopoietic cells, as exemplified by neutrophils (Figure 3.19A). I also observed a progressive decrease of LKS progenitor cell and LKS $CD48^{-}$ $CD150^{+}$ HSC populations (Figures 3.19B). Importantly, HSCs in the BM were significantly reduced later than LKS progenitor, only at late stages of disease (Figure 3.19B), when endosteal and metaphyseal vessels, as well as osteoblastic cells, were all drastically reduced (Figure 3.10 and 3.17). Furthermore, while LKS cells were lost in areas both distant from (flushed diaphysis) and close to (crushed metaphysis) the bone (Figure 3.19C), HSCs were most dramatically lost in the bone-rich metaphysis (Figure 3.19D).

These observations suggest that the loss of HSCs is closely linked to the remodelling of the BM microenvironment both in time and space. This is consistent with previous observations that HSCs are relatively resistant to BM infiltration by leukaemic blasts, when compared to other haematopoietic cell populations (Cheng et al., 2015; Miraki-Moud et al., 2013). I also observed that, as disease progresses, there is extramedullary haematopoiesis (Figure 3.19E) and the number of HSCs in the spleen increases (Figures 3.19F and G). Notably, this haematopoietic elevation coincides with an increase of splenic ECs (Figure 3.19H).

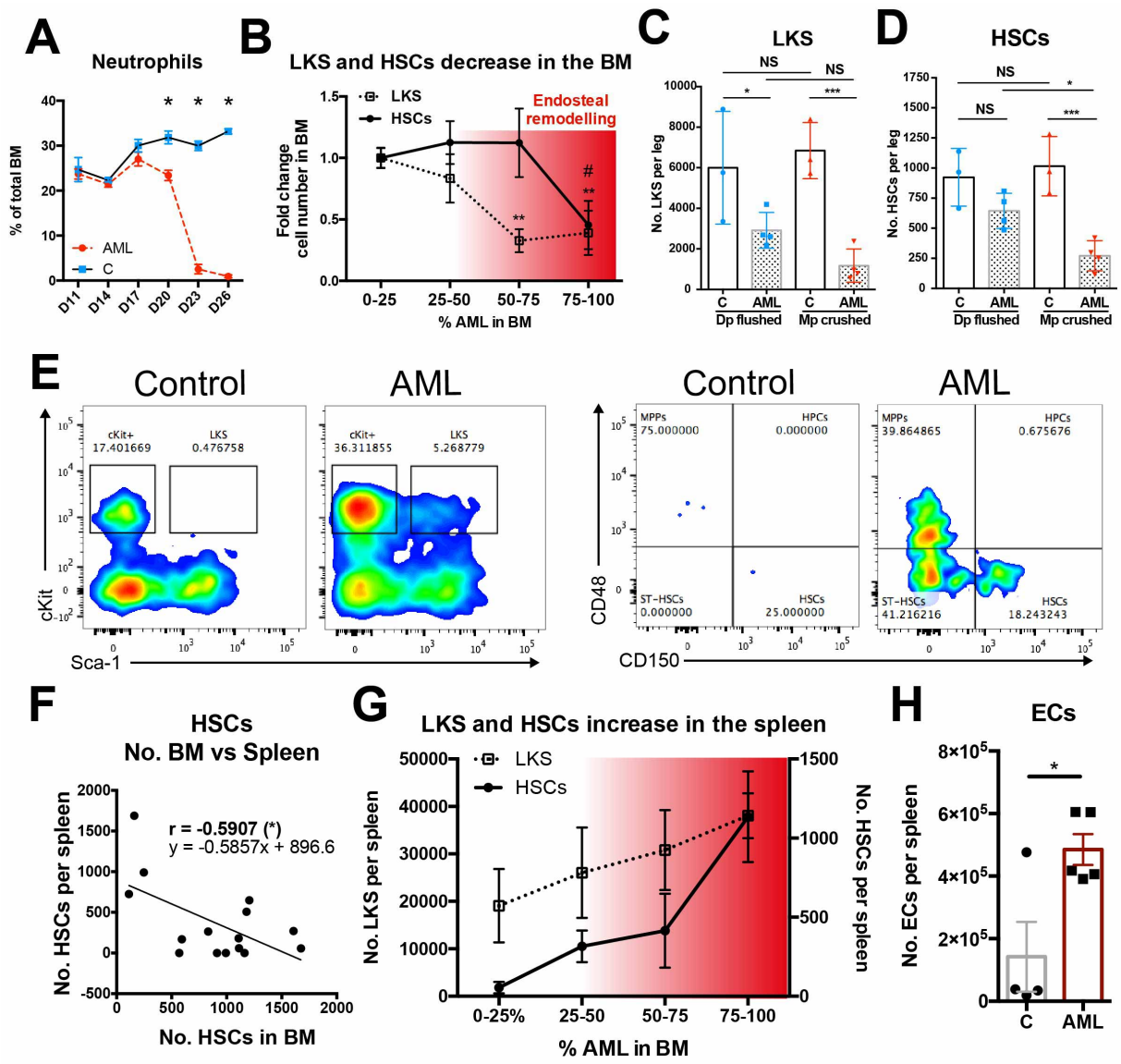

Figure 3.19 – HSC dynamics in BM and spleen. (A) Percentage of neutrophils in total BM. Data obtained from 5 leukaemic and 3 control mice per time-point from 2 cohorts. Error bars: mean ± SEM. **(B)** Fold change in LKS cells and HSCs with increasing AML infiltration. HSCs are only lost at late time points, when endosteal remodeling is more dramatic. Data obtained from 15 mice with 0-25%, 5 mice with 25-50%, 6 mice with 50-75% and 8 mice with 75-100% AML infiltration, from 2 independent cohorts. Error bars: mean ± SEM. **(C)** LKS cells are significantly decreased in both the diaphysis (Dp flushed) and in the trabecular bone-rich metaphysis (Mp crushed) of AML-burdened mice, with no differences between these two fractions. **(D)** HSCs are significantly lost in the metaphysis of AML-burdened mice. Data obtained from 3 control and 4 leukaemic mice. Error bars: mean ± SD. **(E)** Flow cytometry analysis reveals emergence of LKS and HSC populations in the leukaemic spleen. **(F)** Paired analysis shows a negative correlation between HSC numbers in spleen and BM (1 femur, 2 tibias, 2 ileac bones). **(G)** LKS cells and HSC numbers increase in the spleen during AML progression. Data obtained from 7 mice with 0-25%, 3 mice with 25-50%, 2 mice with

50-75% and 3 mice with 75-100% BM infiltration. Error bars: mean ± SEM. **(H)** Mice burdened with AML have significantly increased absolute cell numbers of $CD31^+$ ECs in the spleen. Data obtained from 4 control and 5 leukaemic mice. Error bars: mean ± SEM. Adapted from (Duarte et al., 2018a).

3.11 - AML disrupts the endosteal vascular niche function

An outstanding question is whether the niche function of BM blood vessels is affected by AML infiltration. Thus, I decided to investigate the expression of a panel of HSC maintenance genes (*Ang, Angpt1, Cxcl12, Kitlg, Vcam1, Vegfa, Opn*) by endothelial cells. I used flow cytometry to sort endothelial cells from the different areas (Central vs. Endosteal; Control vs. AML) and performed quantitative real-time polymerase chain reaction (qPCR) (Figure 3.20A). I observed a relocation of niche function to the central blood vessels (*Ang, Angpt1, Cxcl12, Kitlg, Opn*) and/or loss of niche function in the endosteal blood vessels (*Cxcl12, Vcam1, Vegfa*) (Figure 3.20B).

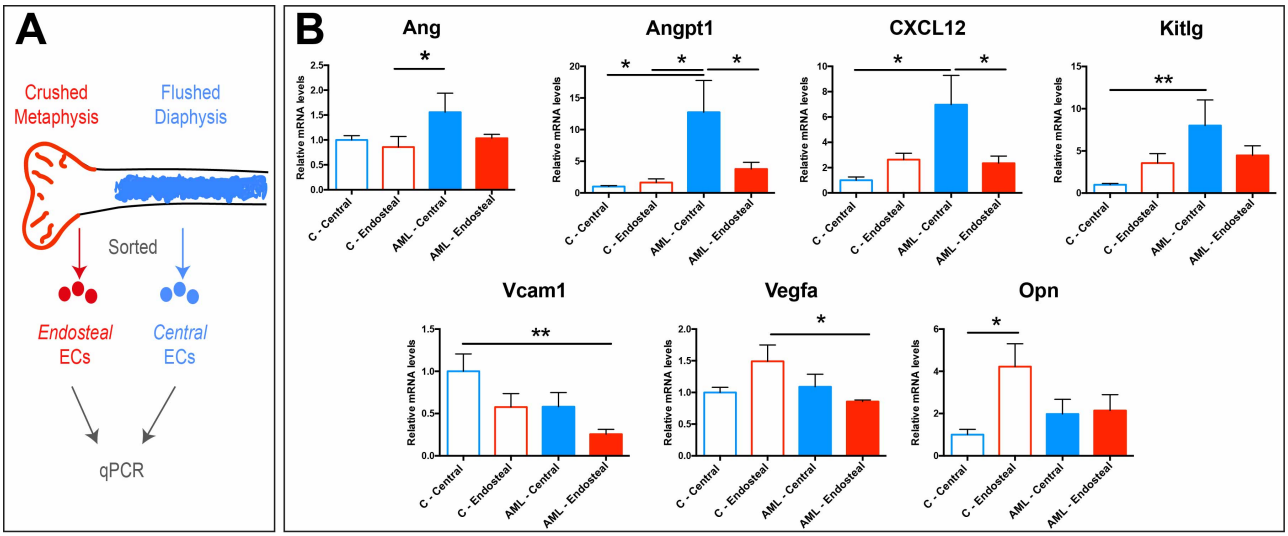

Figure 3.20 - Impaired vascular niche function in AML. (A) Collagenase-digested BM was split in crushed (*endosteal*) and flushed (*central*) fractions and DAPI$^-$CD45$^-$Ter119$^-$CD31$^+$ endothelial cells sort purified. RNA was extracted and processed for qPCR. **(B)** Gene expression analysis of HSC-maintenance genes. Abbreviations and full gene names: *Ang,* angiogenin; *Angpt1,* angiopoietin 1; *Cxcl12,* C-X-C motif chemokine 12 or stromal cell-derived factor 1; *Kitlg,* stem cell factor; *Opn,* osteopontin; *Vcam1,* vascular cell adhesion molecule 1; *Vegfa,* vascular endothelial growth factor a. Data obtained from 3 control and 4 AML-burdened mice. Error bars: mean ± SEM.

3.12 - Blood vessels in AML-infiltrated BM are more adhesive and cell permeable

To reconcile my initial observations on the morphological and structural changes in BM vessels of AML-infiltrated animals with the progressive loss of normal haematopoietic cells, I asked whether they could result in increased haematopoietic cell trafficking. I performed paired IVM of BM and spleen in the same AML-burdened and control mice (Figure 3.21A), and observed increased numbers of healthy haematopoietic cells adhering to (Figure 3.21B and C; Supplementary Video 3E) and transmigrating across (Figure 3.21D and E; Supplementary Video 3F) endothelial cells in leukaemic mice. This pattern of egress may contribute to the loss of BM haematopoiesis.

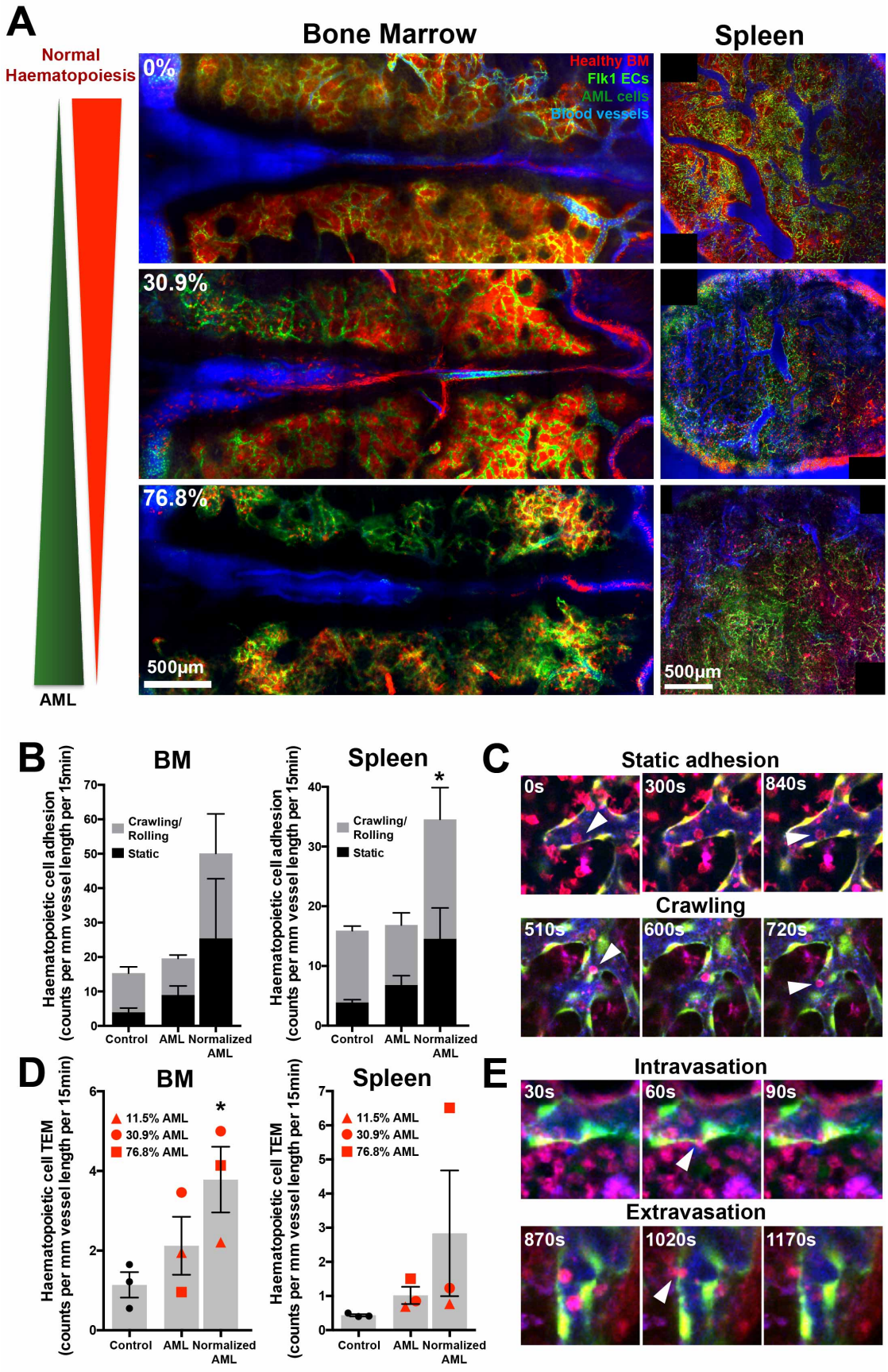

Figure 3.21 – Intravital imaging of haematopoietic cell trafficking in BM and spleen. (A) Maximum intensity projections of representative BM and spleen tile scans of Flk1-GFP mouse

chimeras reconstituted with mTomato^{+} haematopoietic cells and transplanted with GFP^{low} AML cells. mTomato^{+} haematopoietic cells are lost with increasing levels of AML infiltration. For each mouse, BM and spleen were imaged on the same day. To track single mTomato^{+} healthy haematopoietic cells in both the BM and spleen, we performed time-lapse imaging with high temporal resolution (30s acquisition interval). **(B)** Time-lapse *in vivo* imaging revealed that in AML-burdened mice, residual healthy mTomato^{+} cells had increased adhesion to the luminal endothelial surface, particularly in leukaemic spleens, when normalized by the frequency of surviving cells (e.g. once divided by 0.699 in a mouse with 30.1% blasts in the BM). **(C)** Examples of healthy tomato^{+} cells maintaining stable (static) or transient (crawling) adhesion to the splenic endothelium. **(D)** We observed a significant increase of healthy mTomato^{+} cells undergoing transendothelial migration (TEM) in the BM of AML-burdened mice, once normalized for the infiltration level. **(E)** Examples of cells migrating from the tissue to the vascular lumen (intravasation) and in the opposite direction (extravasation) are shown. (C and E): Green: Flk1-GFP^{+} ECs; red: mTomato^{+} healthy haematopoietic cells; blue: Cy5 Dextran. Data obtained from the analysis of 521 (BM) and 588 (spleen) tomato^{+} cells from 3 control and 3 leukaemic mice. * $p<0.05$. Error bars: mean ± SEM. Adapted from (Duarte et al., 2018a).

I also observed AML cell clusters that adhered to the endothelial cells on their intravascular surface and compromised blood flow (Figure 3.22A; Supplementary Video 3G), likely contributing to the observed functional alterations of the endothelium (Ramasamy et al., 2016). Analysis of surface molecules involved in cell adhesion revealed a higher expression of CD34 in the overall $CD45^{-}Ter119^{-}Flk1^{+}$ BM endothelium of AML-burdened mice (Figure 3.22B). CD34 is a well-known mediator of lymphocyte adhesion and TEM (Butcher and Picker, 1996). The expression of both intercellular adhesion molecule-1 (ICAM-1) and endomucin (Emcn), respectively involved in the attraction (Springer, 1994) and repulsion (Zahr et al., 2016) between leukocytes and endothelial cells was maintained in the endothelium of AML-burdened mice. Moreover, the expression of vascular endothelial cadherin (VECadh, VE-cadherin), which is an adhesion molecule involved in the stabilization of endothelial cell junctions (Vestweber et al., 2009), was also maintained in mice fully infiltrated with AML. These data suggest that the observed increased cell adhesion is, at least in part, mediated by CD34, which is involved in leukocyte-endothelial cell adhesion.

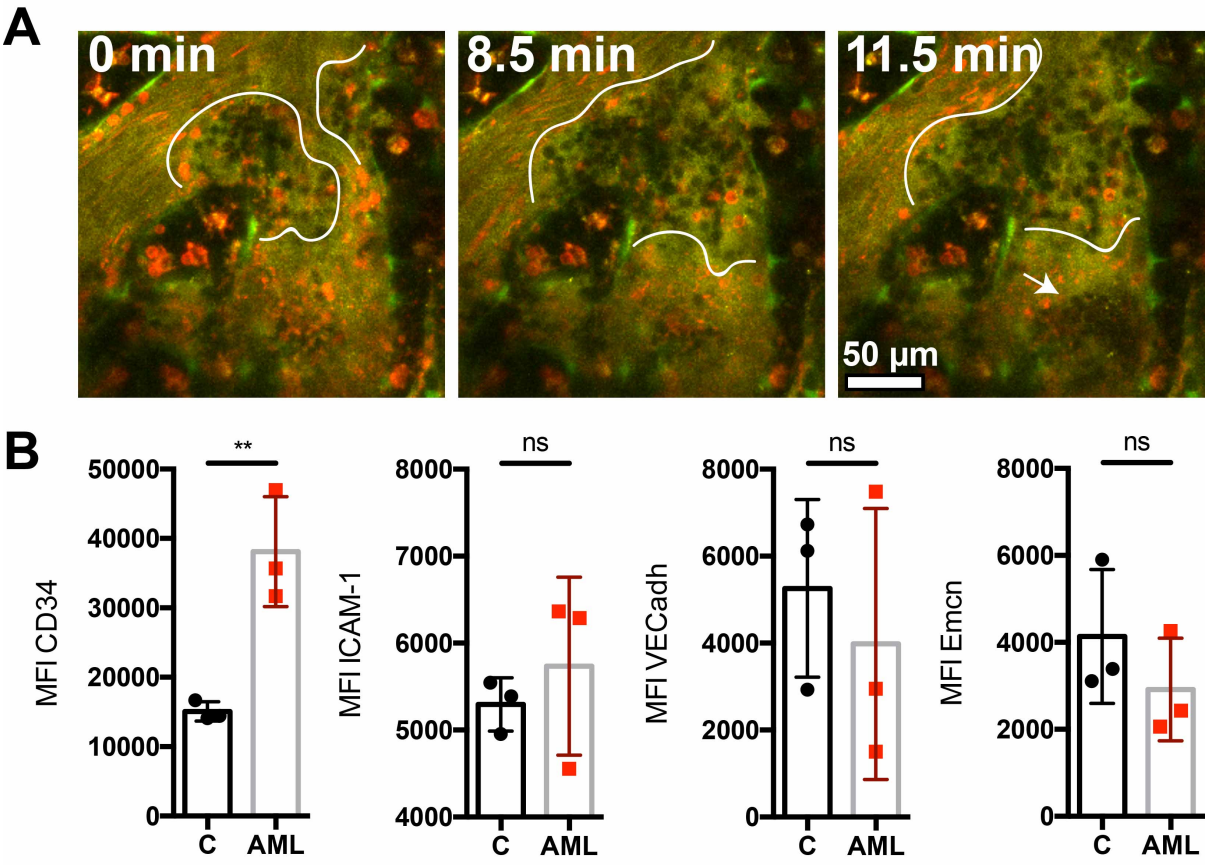

Figure 3.22 – Increased endothelial adhesion in AML-burdened mice. (A) Time-lapse of dark AML cells in a vessel bifurcation adhering to the endothelium, clumping together (white lines) and making the blood flow turbulent (white arrow). Representative Green: Flk1-GFP^{+} ECs; red: mTomato^{+} normal cells; blue/yellow: Cy5 dextran. **(B)** ECs were isolated from digested BM of Flk1-GFP mice, stained for adhesion molecules involved in leukocyte-endothelial adhesion and assessed by flow cytometry. Data are from 3 control and 3 leukaemic mice. Error bars: mean ± SD.

3.13 - AML-induced endosteal remodelling regulates HSC numbers

To confirm that HSC loss from the BM was due to the microenvironmental changes I observed rather than a direct effect of leukaemia cells on the stem cells, I asked whether the remodelled BM would still have the capacity to support homing of HSCs. To this end, I transplanted DiD-labelled HSCs into lethally irradiated control and leukaemic mice (Figure 3.23A). Two days after transplantation, significantly lower numbers of HSCs were found in the BM of leukaemic mice (Figure 3.23B). This observation suggests that AML leads to a specific collapse of HSC-supportive BM niches, as previously hypothesized for B-cell acute lymphoblastic leukaemia (Colmone et al., 2008).

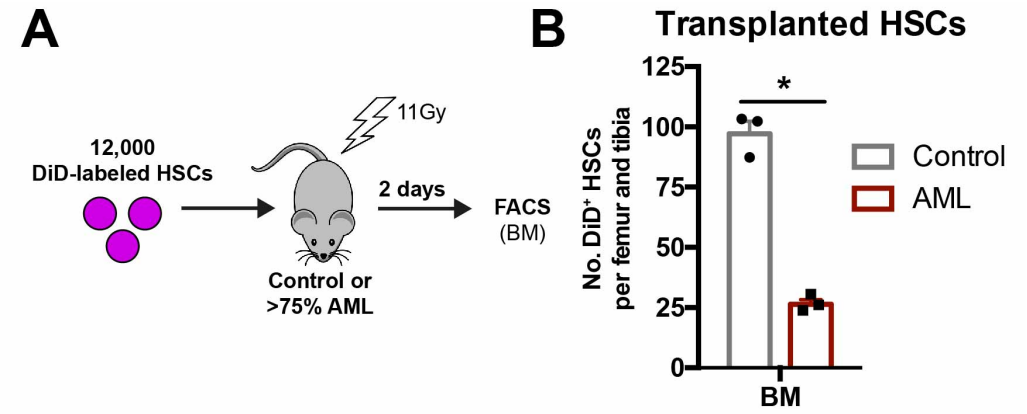

Figure 3.23 – The endosteal remodeling in AML impairs HSC homing. (A) 12,000 sort-purified HSCs were labelled with DiD and transplanted into irradiated control or AML recipient mice. 2 days after transplantation DiD^+ HSCs resident in the BM were quantified by flow cytometry. **(B)** Homing of transplanted DiD^+ HSCs was significantly impaired in the BM of AML-burdened mice. n= 3 control and 3 leukaemic mice. Adapted from (Duarte et al., 2018a).

To address if cell death could be playing a role in the loss of HSCs and progenitors, I performed Annexin V and DAPI staining on c-Kit enriched haematopoietic cells harvested from mice at advanced stages of AML progression. I observed that HSCs and MPPs isolated from AML-burdened mice had very low proportions of apoptotic and dead cells, comparable with healthy controls (Figure 3.24). In contrast, ST-HSCs from leukaemic mice had increased cell death levels. While it remains to be clarified why apoptosis is increased in ST-HSCs, these results reinforce the idea that HSC dynamics are tightly connected with their niches. These observations suggest that HSCs are probably lost through cell ousting from the BM upon the collapse of endosteal vessels at late stages of AML.

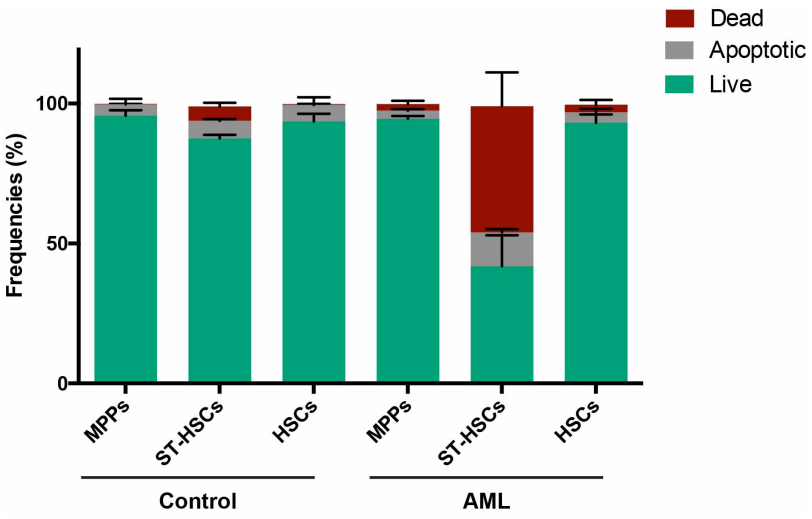

Figure 3.24 – Apoptosis of HSPC populations in AML. In AML, cell death is only significantly increased in ST-HSCs. Data representative from 3 control and 3 leukaemic mice. Error bars: mean ± SEM. Adapted from (Akinduro et al., 2018).

I then investigated whether maintenance of BM endosteal endothelium during AML growth would protect HSCs in endosteal areas. To address this, we treated leukaemic mice with deferoxamine (DFO), a clinically-approved prolyl-4-hydroxylase (PHD) inhibitor normally administered as an iron chelator, but also recently described to induce endosteal vessel expansion through enhancement of hypoxia-inducible factor 1α (Hif-1α) stability and activity (Kusumbe et al., 2014). DFO or control (PBS) treatment started 8 days post-injection of AML blasts and continued until day 22 post-transplantation, at which time point the BM was heavily infiltrated (Figure 3.25A). DFO-treated mice had similar numbers of AML cells in the BM (Figure 3.25C), and similar disease progression (Figure 3.25B and D) and survival (Figure 3.25E). Endosteal blood vessels were increased in DFO-treated mice (Figure 3.25F and G).

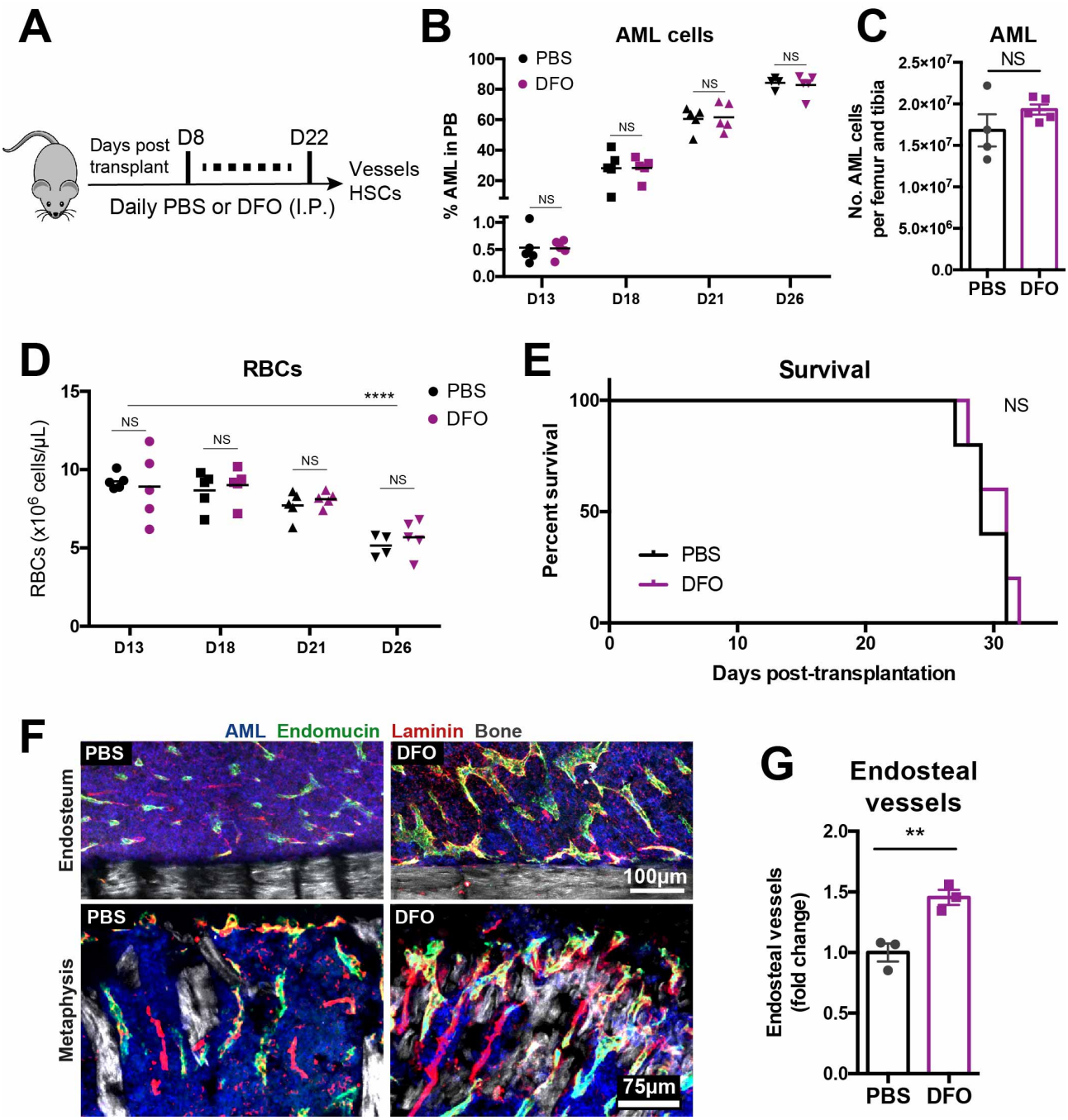

Figure 3.25 – DFO rescues endosteal vessels in AML. (A) Mice transplanted with AML were treated with either PBS or DFO from day 8 post-transplantation. **(B)** Percentage of mTomato^{+} blasts in the peripheral blood remained unaltered by DFO treatment. **(C)** DFO did not affect the total number of AML cells in the BM. **(D)** Percentage of red blood cell (RBC) counts and **(E)** survival of DFO- and PBS-treated mice shows similar disease progression between the two groups. Data obtained from 5 control (PBS) and 5 DFO-treated mice. **(F, G)** DFO increased the number of endosteal vessels. Grey: collage bone SHG; green: endomucin^{+} vessels; red: laminin^{+} vessels and extracellular matrix; blue: AML cells. Each dot represents a mouse. Error bars: mean ± SEM. Adapted from (Duarte et al., 2018a).

Consistent with the hypothesis that HSC numbers depend on endosteal vessels, I observed that leukaemic mice receiving DFO had significantly higher numbers of HSCs in the trabecular-rich metaphysis, but not in flushed diaphyseal BM (Figure 3.26A and B). A direct positive effect of DFO on HSC numbers was excluded through *in vitro* culture (Figure 3.26C-F). To further investigate the clinical utility of DFO, I investigated the homing of HSCs in mice infiltrated with AML and treated with DFO or vehicle (Figure 3.26G). In line with my hypothesis, DFO-treated mice supported HSC homing to the BM (Figure 3.26H). Altogether, these data suggested that rescue of endosteal vessels can support both HSC survival and homing despite AML growth.

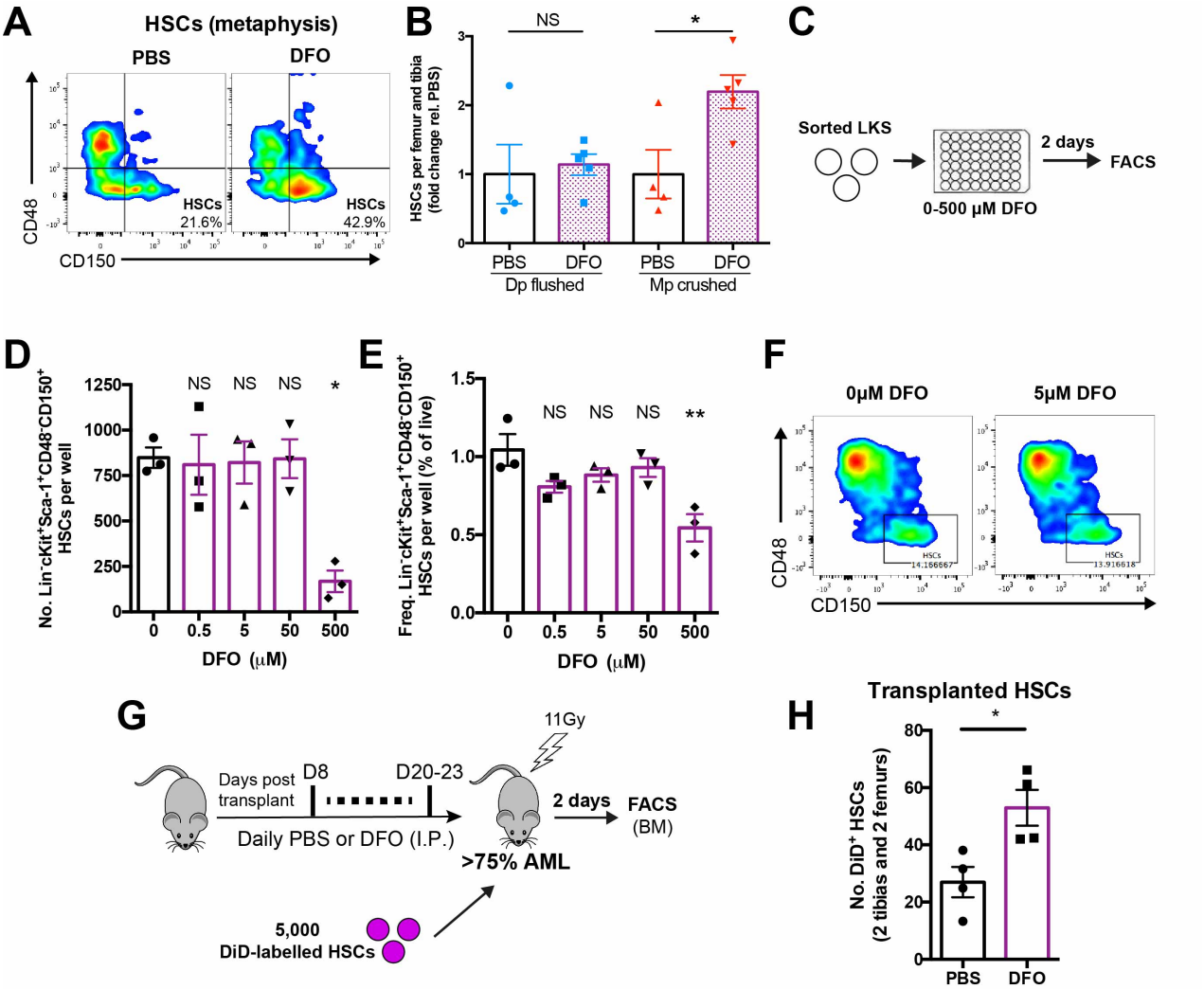

Figure 3.26 – DFO effect on HSCs *in vivo* and *in vitro*. (A, B) AML-burdened mice treated with DFO had similar numbers of HSCs in the diaphysis (Dp flushed) but a significant increase of HSCs remaining in the metaphysis (Mp crushed) in comparison to controls. Data obtained from 4 mice treated with PBS and 5 treated with DFO. **(C)** Live Lin$^-$c-Kit$^+$Sca-1$^+$ (LKS) cells were sorted, plated and incubated with increasing concentrations of DFO. 2 days later the **(D)** number and **(E, F)** frequency of Lin$^-$c-Kit$^+$Sca-1$^+$CD48$^-$CD150$^+$ HSCs were assessed by FACS. Experiment done in triplicate. **(G)** Mice transplanted with AML cells were treated with either PBS or DFO. At full infiltration, mice were lethally irradiated and transplanted with DiD-labeled HSCs that had not been exposed to DFO. **(H)** DFO improves the homing of transplanted DiD$^+$ HSCs in the BM of AML-burdened mice. Data obtained from 4 recipients treated with PBS and 4 recipients treated with DFO. (B-J). Error bars: mean ± SEM. Adapted from (Duarte et al., 2018a).

3.14 - Rescue of endosteal vessels improves chemotherapy efficiency

The observed remodelling of blood vessels in AML-burdened mice, and especially the loss of endosteal vessels led us to hypothesize that these changes could not only contribute to outcompeting healthy haematopoiesis, but also compromise delivery of chemotherapy. In a xenograft transplantation model of AML, chemoresistant leukaemia cells were previously shown to locate near the endosteum (Ishikawa et al., 2007). This suggests that localization of leukaemia cells in areas of BM stripped of their vasculature could provide them with a survival advantage. To investigate the impact of chemotherapy on AML cells *in vivo*, I treated mice with over 30% infiltration with drugs used for induction therapy in the clinical setting: cytarabine (Ara-C) and doxorubicin (Doxo). Following previous mouse studies (Wunderlich et al., 2013), I adapted the 7+3 regimen used in human patients to a 5+3, where Ara-C (100mg/kg, I.V.) is given daily for 5 days and Doxo (3mg/kg, I.V.) for 3 days (Figure 3.27A). Mice receiving chemotherapy had a significant reduction in AML cell numbers in BM (Figure 3.27B and C) and a significant reduction in spleen size (Figure 3.27D)

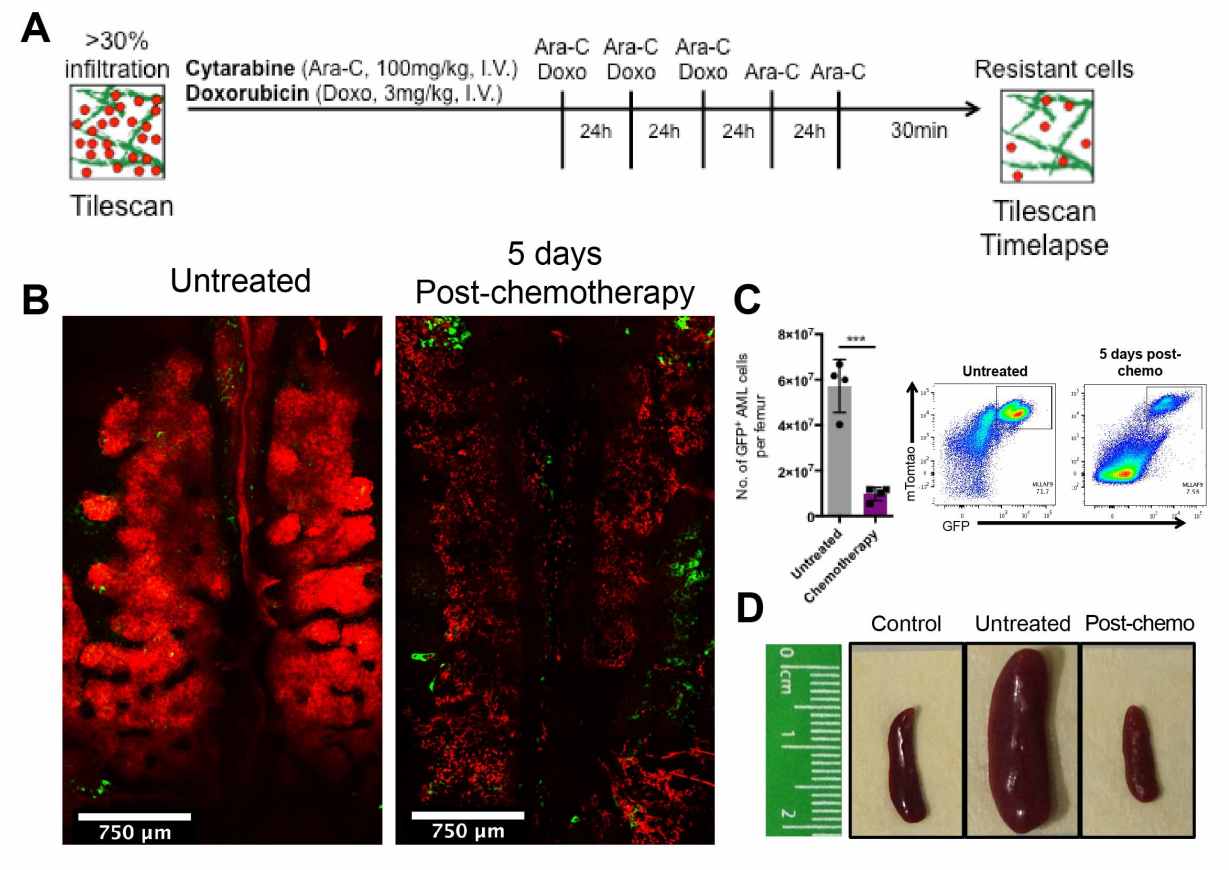

Figure 3.27 – Experimental model of AML induction chemotherapy. (A) Schematic representation of the schedule of cytarabine and doxorubicin administration and IVM. **(B)** Maximum projection tile scan of calvarium BM of Col2.3-GFP mice (green: osteoblastic cells) carrying mTomato^{+} AML cells (red) before and after chemotherapy (3 days of cytarabine and doxorubicin followed by 2 days of cytarabine alone). **(C)** Flow cytometry quantification of absolute numbers of AML cells in the BM. Data obtained from 4 control and 4 leukaemic mice. Error bars: mean ± S.D. **(D)** Appearance of spleens from control, untreated and 5 days-treated mice. Adapted from (Duarte et al., 2018a).

In our model, trabecular areas were enriched for AML cells both at early and late stages of infiltration and following induction chemotherapy (Figure 3.28).

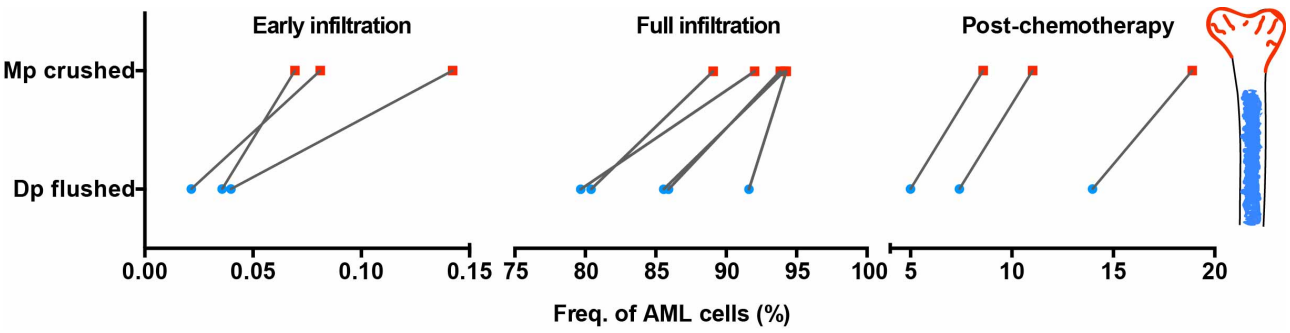

Figure 3.28 – Enrichment of AML cells in the endothelium. Paired comparison shows that leukemic cells are more frequent in crushed metaphysis (Mp) than in flushed diaphysis (Dp) at very early (3 mice) and late (5 mice) infiltration and post-chemotherapy (3 mice). Adapted from (Duarte et al., 2018a).

I hypothesized that by rescuing blood vessels in endosteal areas, I could increase chemotherapy delivery and therefore efficacy. To test this, I utilized Fbxw7$^{i\Delta EC}$ mutant mice, in which tamoxifen administration leads to increased-activation of Notch signalling specifically in ECs, thereby increasing the number of endosteal vessels and arterioles (Kusumbe et al., 2016; Ramasamy et al., 2014). Fully infiltrated Fbxw7$^{i\Delta EC}$ mutants had increased numbers of endosteal vessels (Figure 3.29A and B). At this point, I treated both Fbxw7$^{i\Delta EC}$ and control mice with the adapted form of clinical induction chemotherapy (Figures 3.29C and 3.27).

In agreement with a previous report (Hooper et al., 2009), I observed significant chemotherapy-induced damage to the BM vasculature, including endosteal vessels, in both control and mutant mice (Figure 3.29D). I observed that after treatment, the Fbxw7$^{i\Delta EC}$ mutants had reduced numbers of surviving AML cells in the BM (Figure 3.29E), delayed relapse (Figure 3.29F) and increased survival (Figure 3.29G). Altogether, these data suggest that the rescue of endosteal vessels before induction chemotherapy can improve its efficacy.

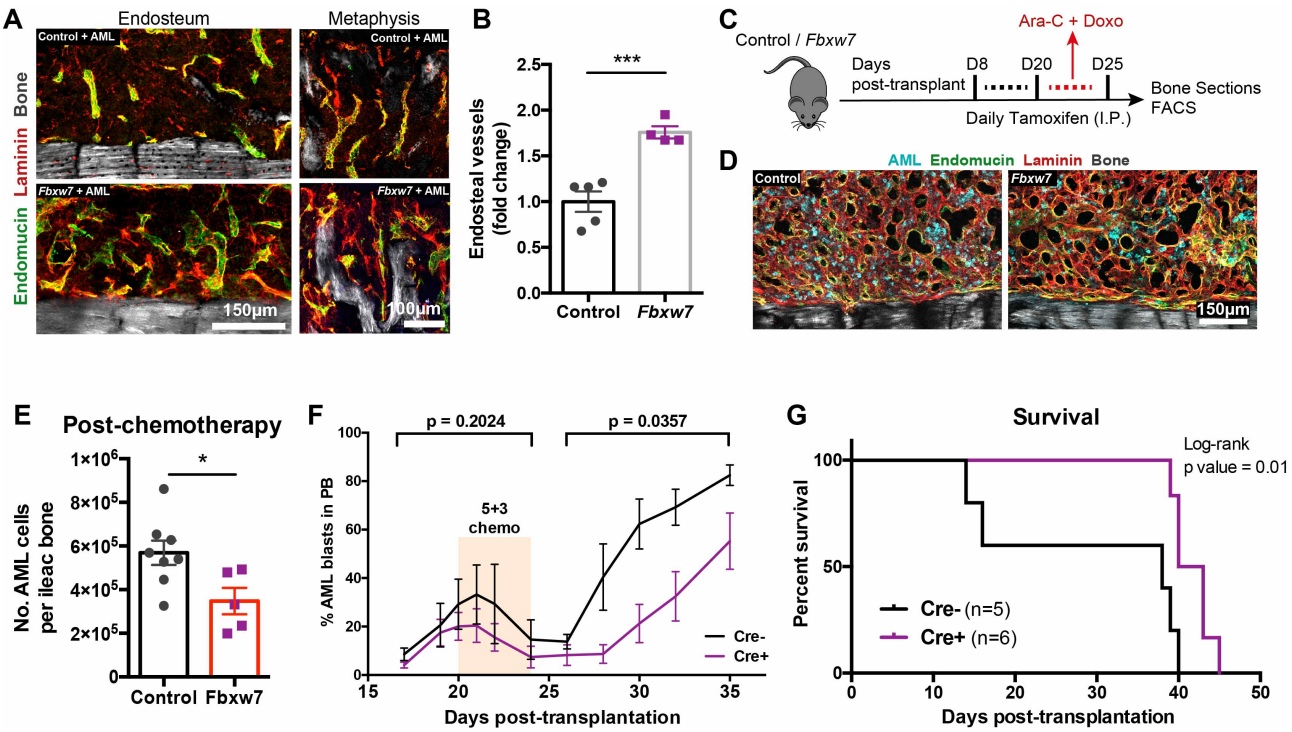

Figure 3.29 – Rescue of endosteal vessels increases induction chemotherapy efficiency. (A, B) Immunofluorescence staining of endosteal areas showing a significant increase of blood vessels in Fbxw7$^{i\Delta EC}$ mutants infiltrated with AML. Grey: bone collagen SHG; green: endomucin^{+} vessels; red: laminin^{+} vessels and extracellular matrix. Data obtained from 5 control mice and 4 Fbxw7$^{i\Delta EC}$ mice. **(C)** Scheme of treatment regimen used to delete Fbxw7 in ECs. **(D)** Maximum projections of immunofluorescence staining of representative endosteal areas showing dilated blood vessels (green: endomucin; red: laminin) after therapy in both control and mutant animals, as well as surviving AML cells (cyan) scattered through the tissue. Data representative of 3 control mice and 3 Fbxw7$^{i\Delta EC}$ mutants. **(E)** After chemotherapy, there was a significant decrease of surviving AML cells in Fbxw7$^{i\Delta EC}$ mutants, where the endosteal vessels had been rescued. Data obtained from 8 control mice and 5 Fbxw7$^{i\Delta EC}$ mutants. **(F)** Although disease progression before chemotherapy is similar, relapse is delayed in Fbxw7$^{i\Delta EC}$ mutants. n=3 Cre^{-} and 6 Cre^{+} mice. **(G)** Kaplan-Meyer curve showing improved survival in treated Fbxw7$^{i\Delta EC}$ mutants transplanted with AML. n=5 Cre^{-} and 6 Cre^{+} mice. (B-F) Error bars: mean ± SEM. Adapted from (Duarte et al., 2018a).

3.15 - Discussion

I have described how AML cells focally and progressively remodel BM vasculature to transform HSC niches into preferential leukaemia microenvironments. In particular, BM vasculature editing is anatomically diverse, with endosteal vessels being progressively obliterated, while central marrow vessels survive, albeit with compromised function. The two main consequences of this are HSC loss specifically from endosteal areas, and survival of leukaemia cells following chemotherapy treatment (Figure 3.30).

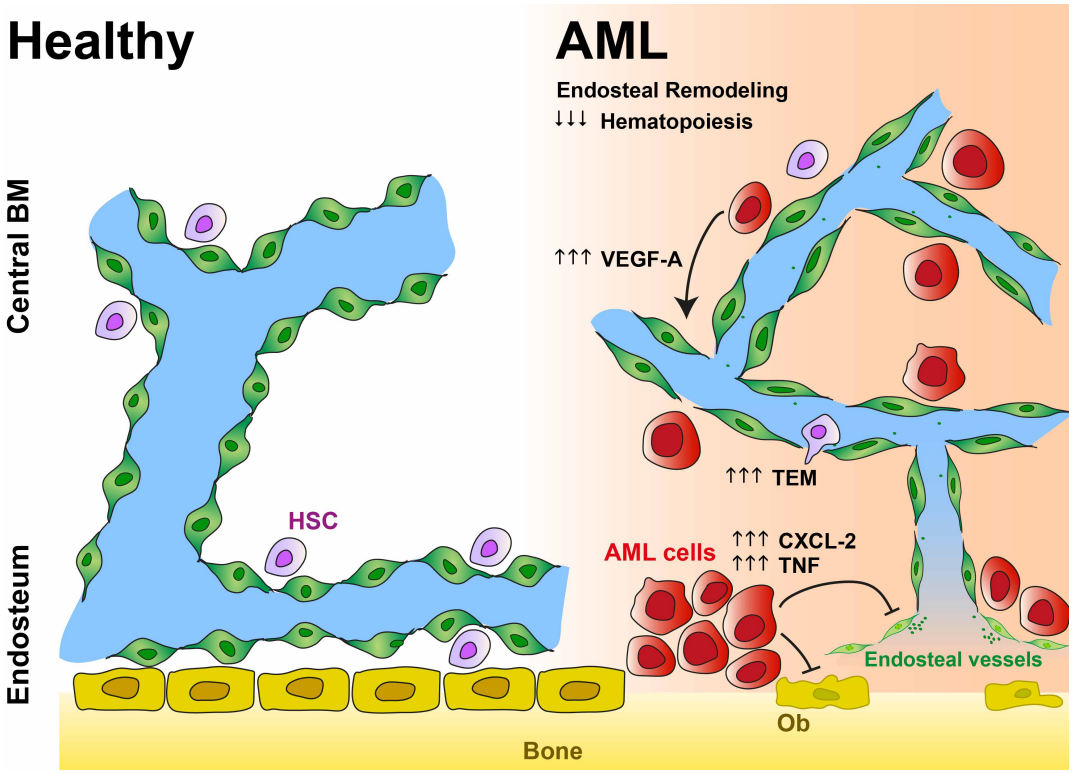

Figure 3.30 – Schematic representation of the selective osteo-vascular remodelling occurring in AML. In steady state, HSCs are regulated by different BM niches, including endosteal blood vessels. During AML progression there is remodelling of the BM microenvironment and loss of non-malignant haematopoiesis. The loss of HSCs is temporarily and spatially associated with the destruction of specialized endosteal microenvironments, namely osteoblastic cells (Ob) and endosteal vessels. AML cells secrete high levels of VEGF-A but the angiogenic stimuli is not effective. Endothelial cells are more permeable to transendothelial cell migration (TEM), which likely contributes to the loss of normal haematopoietic cells from the BM, as AML expands. Moreover, the increased levels of CXCL2 and TNF in the endosteum create a pro-inflammatory environment and likely contribute to the vascular remodelling occurring in this area. Adapted from (Duarte et al., 2018a).

IVM provided us with the unique opportunity to perform detailed, longitudinal analysis of progressive changes occurring across the entire vascular bed irrigating the calvarium BM. This approach identified dynamic and area-specific changes previously overlooked by studies of AML patient samples that focused on central BM areas or examined vasculature as a whole (Aguayo et al., 2000; Hanoun et al., 2014; Hussong et al., 2000; Padro et al., 2000). Consistent with initial reports of the angiogenic potential of AML cells (Fiedler et al., 1997), I observed increased levels of VEGF-A in leukaemic mice and endothelial cell dynamics resembling angiogenic sprouting (Gerhardt et al., 2003). However, these sprouts never gave rise to the formation of new vessels, which might be driven by VEGF-A-mediated tip cell competition (Jakobsson et al., 2010). This might explain the disappointing results of the clinical trials testing anti-angiogenic therapies for AML patients (Fiedler et al., 2003; Ossenkoppele et al., 2012; Zahiragic et al., 2007). Furthermore, the combination of high-resolution IVM and quantitative flow cytometry analysis of BM ECs showed that the apparent relative increase in ECs is a consequence of the overall loss of BM stroma. This finding contrasts with observations made in solid tumours, where most often accumulation of stroma and pro-fibrotic changes are reported adjacent to the cancerous cells (Quail and Joyce, 2013).

While central marrow vessels were maintained during AML infiltration, we observed dramatic remodelling of endosteal vessels. These vessels were initially remodelled in areas containing foci of disease, but eventually almost disappeared from the BM of heavily infiltrated animals. AML cells in endosteal areas were enriched in inflammatory signatures, including response to TNF, and expressed higher levels of CXCL2. Both TNF and CXCL2 levels were locally increased in endosteal areas. This is consistent with the recently described role of TNF in vascular destruction (Kammertoens et al., 2017). Furthermore, CXCL2 is an angiogenesis inhibitor (Cao et al., 1995) that has also been shown to mobilize HSCs from the BM (Fukuda et al., 2007) and to be associated with poor prognosis and reduced survival in AML (Katsumura et al., 2016). Overall my data support future investigation of the role of CXCL2 and TNF in the vascular remodelling and loss of HSCs induced by AML in endosteal regions.

In parallel with endosteal vessel remodelling, I also observed a similar pattern of osteoblastic cell loss. It was shown previously in a mouse model of myeloprofilerative neoplasia based on widespread induction of BCR-ABL that aberrant differentiation of mesenchymal progenitor cells led to an expansion of dysfunctional osteoblasts associated

with loss of HSC activity (Schepers et al., 2013). Here, I observed the depletion of not only osteoblasts but also endosteal vessels. This interpretation does not exclude "re-wiring" of mesenchymal progenitors, however, it highlights a dramatic imbalance between osteoblast generation and loss. Most importantly, my findings are consistent with studies that reported decreased numbers and activity of osteoblasts in patients with AML (Krevvata et al., 2014). Using a complementary experimental model, Hanoun and colleagues have shown that sympathetic neuropathy promotes the expansion of $Nestin^{+}$ MSCs but limits their differentiation into HSC-supportive $NG2^{+}$ cells in the arteriolar niche of mice with AML (Hanoun et al., 2014). These data, when combined with our results presented here, suggest that fast-growing AML depletes stroma with niche function.

By combining longitudinal IVM and immunoflourescence analyses with the study of mice with intermediate disease burden we obtained detailed temporal information on the progression of AML-induced BM remodelling. Our group has recently reported a similar collapse of the osteolineage at late stages of T-ALL (Hawkins et al., 2016). In contrast with AML, here I observed that endosteal vessels are not lost in T-ALL, highlighting the specificity of microenvironment remodelling in different types of leukaemia. Analysis of human AML samples revealed endosteal vessel remodelling in unrelated AML types. These findings, together with clinical evidence demonstrating that cytopenias are more common and severe in AML than in T-ALL, suggests that endosteal vessel remodelling may be the cause of dramatic cytopenias associated with AML.

Splenomegaly, though rare in AML patients, is present and accompanied by extramedullary haematopoiesis in experimental mouse models of acute leukaemia. In the model I studied, increased EC numbers in the spleen likely form *de novo* vascular niches able to support HSCs and extramedullary haematopoiesis, consistent with the recent discovery of a perisinusoidal niche in the spleen (Inra et al., 2015). Moreover, I was able to detect functional changes in endothelial cells allowing for greater adhesion and trans-endothelial migration of haematopoietic cells in diseased mice. This is consistent with a recent study highlighting increased vascular permeability in AML (Passaro et al., 2017). These changes likely contribute to the egress of healthy haematopoietic cells from the BM (Bixel et al., 2017; Itkin et al., 2016) and relocation to the spleen.

Consistent with previous studies indicating that HSCs are relatively resistant to AML invasion (Cheng et al., 2015; Miraki-Moud et al., 2013), I observed that HSC loss occurs at late stages of disease infiltration, when we show that endosteal remodelling is more evident.

Treatment with DFO significantly increased the number of endosteal blood vessels together with endosteal HSCs and improved the homing of HSCs to the BM of mice previously burdened with disease. DFO has been reported to limit leukaemic cell proliferation and to potentiate the effect of differentiation therapies in AML through iron chelation (Callens et al., 2010). Here, no significant changes in the number of AML cells or disease progression were observed in DFO-treated mice. This suggests that potential off target effects of DFO on AML proliferation did not play a major role in the protection of HSCs.

Apart from leading to HSC loss, elimination of endosteal vessels may favour AML cells during chemotherapy administration by providing them with a vessel-poor microenvironment where drug delivery would likely be challenged and/or inefficient, and therefore would foster chemoresistance. Consistent with our hypothesis, chemoresistant AML has been shown to initiate relapse from endosteal areas (Ishikawa et al., 2007). This genetic approach showed that endosteal vessels can be rescued in AML-burdened animals and, in doing so, the efficacy of chemotherapy treatment increases. This study suggests that induction of endosteal vessels and vascular normalization are promising avenues to both safeguard residual healthy haematopoiesis and improve chemotherapy treatment of AML patients.

Chapter 4

Chemoresistant T-cell acute lymphoblastic leukaemia is independent from specific bone marrow niches

4.1 - Introduction

How important are specific HSC niches to support the expansion and chemoresistance of leukaemic cells is a question that remains unanswered. T-ALL is a particularly aggressive type of leukaemia and once it relapses the prognosis is dismal (see section 1.3). It is therefore pivotal to understand better the physiopathology of T-ALL, including how T-ALL cells interact with surrounding BM microenvironments. Our understanding of these interactions has the potential to impact T-ALL therapy. In simple terms, we might conclude that particular niches (rather than the tissue as a whole) are key for T-ALL development and/or chemoresistance and in this way support the development of new strategies that target leukaemia-stroma communication in T-ALL. Alternatively, we might conclude that cell autonomous processes are overly important, that specific microenvironments are only accessory and turn our focus to therapies that target cell intrinsic mechanisms. Moreover, the development of new techniques and strategies that allow the direct and dynamic visualization of cell to cell interactions in the BM has the potential to contribute to future studies analysing other leukaemias, metastasis, HSCs and bone physiology.

Our group has previously used IVM to show that in the calvarium BM, seeding single T-ALL cells are first seen at day 10 post-transplantation, cell clusters at day 12-18 and full infiltration at day 18 post transplantation (Hawkins et al., 2016). Importantly, we concluded

that T-ALL is environment-agnostic by stochastically infiltrating the BM and that T-ALL remodels the endosteum by destroying osteoblastic cells (Hawkins et al., 2016).

Although previous studies have suggested that leukaemia depends on specific microenvironments to evade chemotherapy, *in vivo,* dynamic information is lacking to support these claims. For the present study, I applied IVM to ask if chemoresistant T-ALL is dependent on particular microenvironments.

T-ALL onset in primary recipients transplanted with Notch1-transduced foetal liver cells is highly variable (Sanda et al., 2010). Therefore, I transplanted blasts into secondary recipients, which develop disease in a well-defined manner both in time and space, colonizing first the BM and then spleen, lymph nodes and thymus (Hawkins et al., 2016). Using osteoblast (Col2.3-GFP and –CFP), perivascular mesenchymal stem/progenitor cell (Nestin-GFP) and endothelial cell (Flk1-GFP and vascular dyes) reporters it is possible to directly observe interactions between $DsRed^{+}$ T-ALL blasts and specific BM niche components (Figure 4.1). To measure leukaemia-to-stroma distances, I acquired tile scans that allow single cell resolution observation of the whole marrow tissue and applied an automated computational algorithm based on local heterogeneity segmentation (Khorshed et al., 2015). To record cell behaviour, I selected and time-lapsed specific areas for 3 hours or more (Figure 4.1).

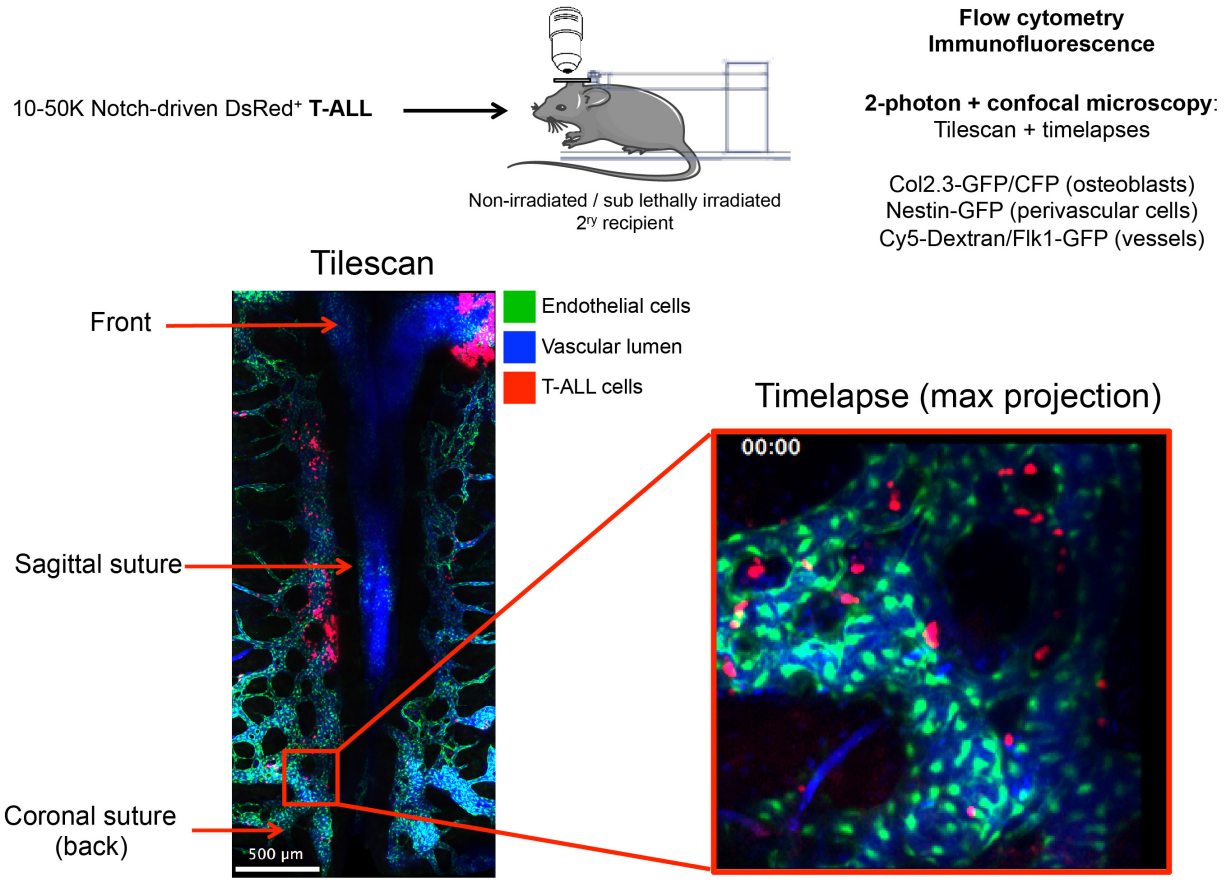

Figure 4.1 – Intravital imaging of T-ALL cells in heterogeneous BM microenvironments. Notch1 blasts were transplanted into secondary recipients and disease in BM was detected by IVM and flow cytometry. IVM of the calvarium was performed to evaluate interaction of leukaemia with BM niches, similarly to what is described in Chapter 3. In this case, for each typical imaging session, tile scans (which allow whole tissue analysis with single cell resolution) where acquired to analyse tissue T-ALL cell distribution in relation to specific niches (e.g. Col2.3^{+} osteoblastic cells). Areas of interest were then time-lapsed for 3 hours or more and T-ALL cell behaviour (e.g. cell migration) analysed.

4.2 - Dexamethasone treatment in experimental T-ALL

At day 18 post-transplantation, mice were tile scanned to confirm heavy BM infiltration, recovered and then treated with daily dexamethasone (15 mg/kg, I.V.) for 2 days (Figure 4.2). Importantly, tile scans and time-lapses were performed immediately after administration of the third dose of dexamethasone, to guarantee that captured cells were under the effect of high doses of the drug.

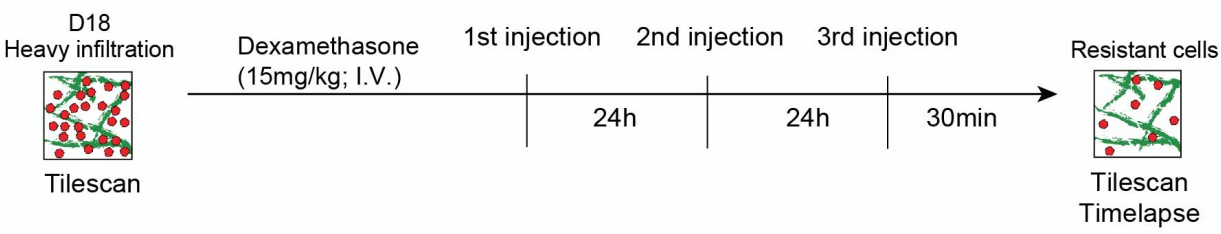

Figure 4.2 – Dexamethasone schedule. Schematic representation of the schedule of IVM and dexamethasone administration. Mice were imaged at day 18 post administration of primary blasts to confirm full infiltration and immediately afterwards received the first dose of dexamethasone. Two further doses were administered at 24 hours intervals, and 30 minutes following the third dose animals were imaged again.

4.2.1 – T-ALL cells surviving dexamethasone are chemoresistant

Upon maintenance of dexamethasone treatment for 7 days, I detected a progressive increase in T-ALL cell numbers both in peripheral blood and BM. Together with observations that after 7 days of continuous dexamethasone treatment leukaemia has regrown, this suggests that these blasts are truly chemoresistant (Figure 4.3A and B).

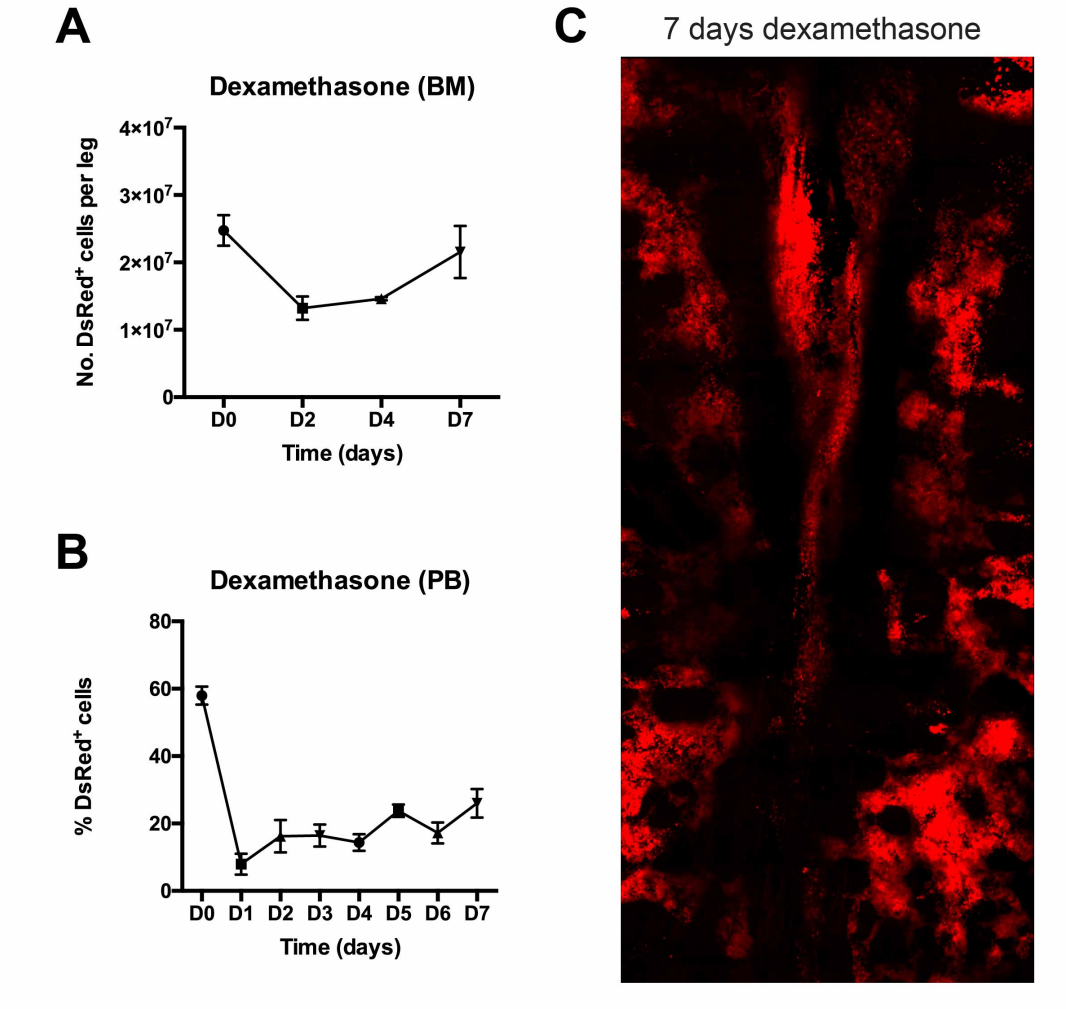

Figure 4.3 – T-ALL cells surviving dexamethasone treatment are chemoresistant. Continuous daily treatment with dexamethasone (15mg/kg) causes a dramatic loss of T-ALL cells initially but eventually leads to later resistance and regrowth of T-ALL cells in the BM **(A)** and re-emergence of blasts in the peripheral blood (PB) **(B)** after 7 days. **(C)** Representative maximum projection of calvarium BM of a mouse after 7 days of daily dexamethasone treatment (15mg/kg). Red: $DsRed^+$ T-ALL cells. Data are representative of 4 independent experiments using 4 independent T-ALL batches. Error bars = Mean ± S.E.M. Adapted from (Hawkins et al., 2016).

Moreover, to control for potential effects of dexamethasone and sub-lethal irradiation on the BM stroma, I measured the cell volume of osteoblasts and Nestin^{+} cells in healthy mice and observed no changes in BM stroma cellularity (Figure 4.4A and B).

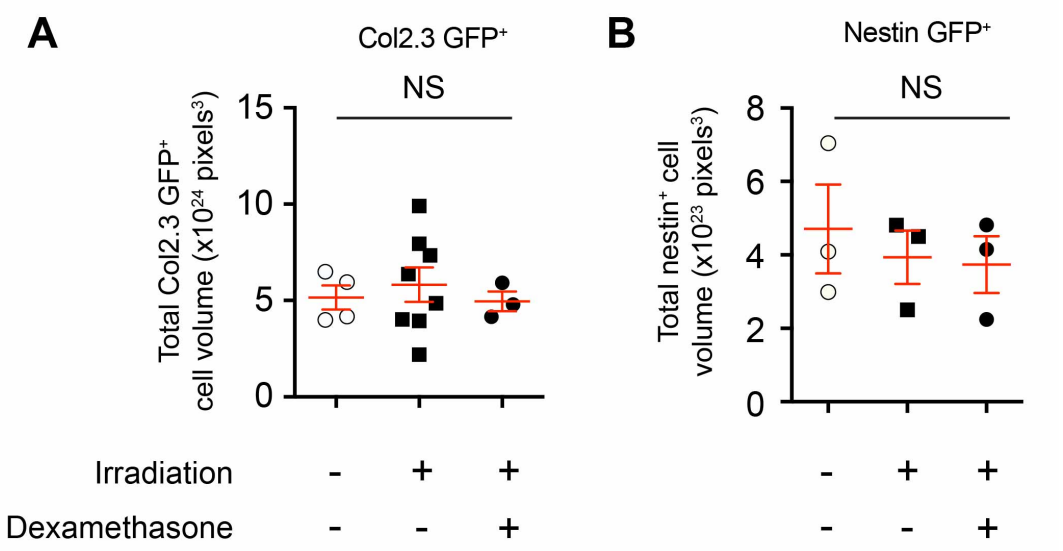

Figure 4.4 – Dexamethasone and sub-lethal irradiation do not affect stromal cellularity. (A) Col2.3-GFP or **(B)** Nestin-GFP mice were treated with combinations of sublethal irradiation (administered >18 days before measurement to reproduce the experimental timeframe) or dexamethasone treatment (administered greater than 2 days before treatment) as indicated. Then, using 3D image analysis, the total area of GFP^{+} was quantified. Groups were analysed using ANOVA with Bonferroni correction for multiple groups. Error bars = Mean ± S.D. Adapted from (Hawkins et al., 2016).

4.3 - Chemoresistant T-ALL is randomly distributed within the BM

Before initiating treatment, the BM cavity was fully infiltrated with T-ALL blasts (Figure 4.5A). Upon treatment completion, after 2 days, the marrow cavity was significantly emptied of leukaemic cells (Figure 4.5A) and only few surviving T-ALL cells were found scattered across the tissue (Figure 4.5B).

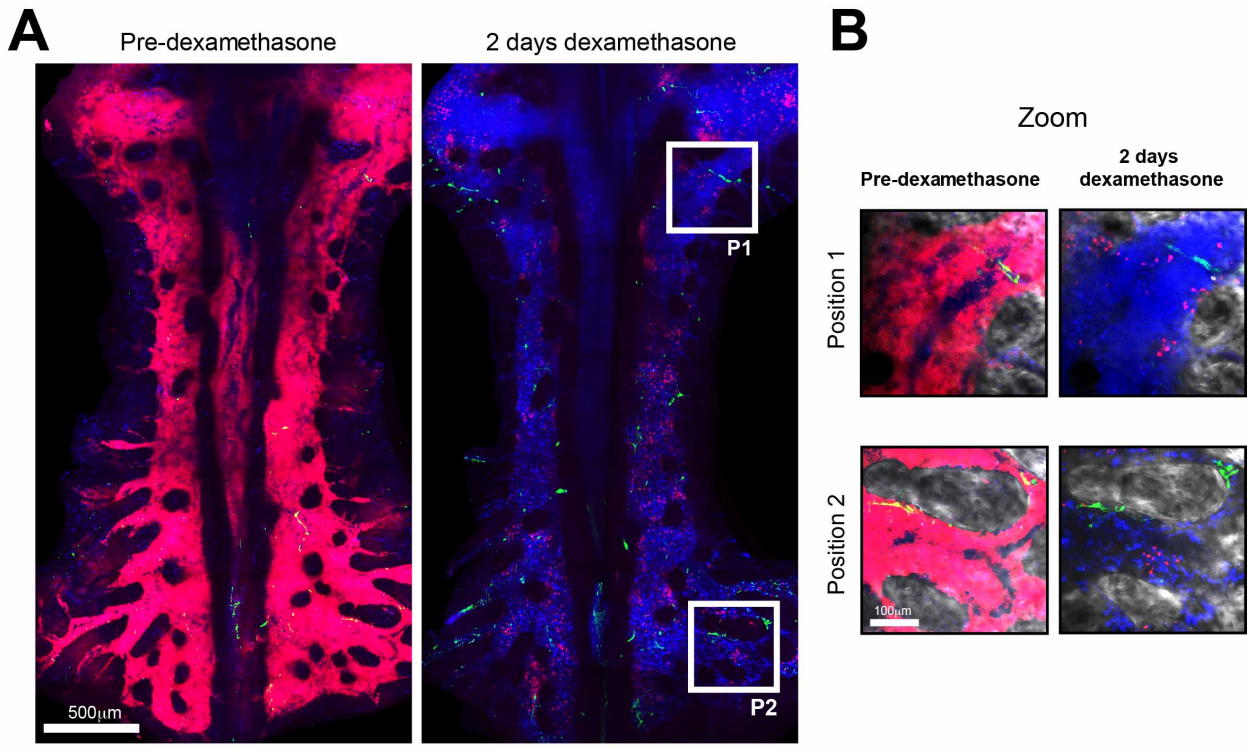

Figure 4.5 – IVM of dexamethasone-resistant T-ALL cells. (A) Representative Nestin–GFP mouse transplanted with T-ALL cells and imaged 18 days post-transplant to confirm complete BM infiltration (left). Tile scan imaging was repeated after 2 days of treatment with 15 mg/kg dexamethasone I.V. (right). **(B)** Magnified view of representative positions, framed in (A). Red: DsRed^{+} T-ALL cells; green: Nestin-GFP^{+} cells; blue: blood vessels (Cy5-Dextran); grey: bone (SHG). Adapted from (Hawkins et al., 2016).

At this point, the localisation of the leukaemic cells (real cells) was compared to randomly positioned dots (virtual data). A stochastic distribution of T-ALL cells relative to osteoblasts, Nestin^{+} cells and blood vessels was observed. This suggests that evasion from chemotherapy is not dependent on these microenvironment components (Figure 4.6).

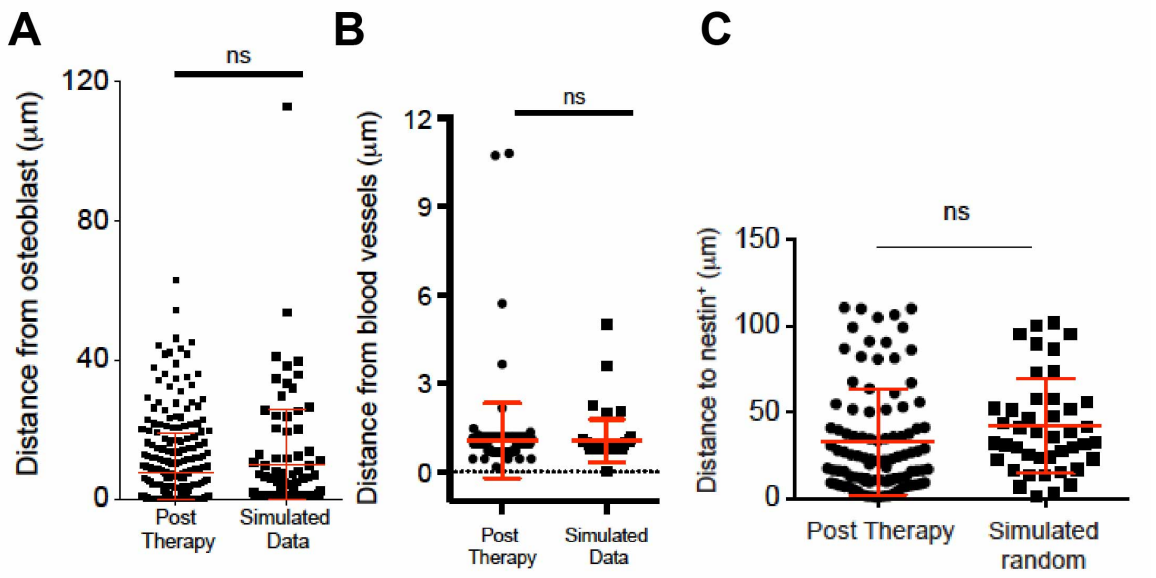

Figure 4.6 – Chemoresistant T-ALL cells are stochastically distributed. 3D measurement of the position of surviving cells and of artificial cells randomly positioned within the same 3D tile scans relative to the closest **(A)** Col2.3-GFP^{+} osteoblastic cell (*n*: 303 real and 91 artificial cells), **(B)** blood vessel (*n*: 143 real and 55 artificial cells) or **(C)** Nestin-GFP^{+} mesenchymal cell (*n*: 97 real and 43 artificial cells) Data shown are representative mice from five independent experiments using 2 independent T-ALL batches. Error bars: mean ± S.D. Adapted from (Hawkins et al., 2016).

To further explore any possible microenvironmental bias of chemoresistant T-ALL cells, I included the first day of treatment in the imaging schedule. Re-imaging of treated mice revealed a dramatic cell burden reduction after 1 day and very few resistant cells after 2 days of treatment (Figure 4.7A). During disease reduction, T-ALL distribution relative to osteoblasts and Nestin^{+} cells was maintained, providing evidence against a chemo-protective niche (Figure 4.7B).

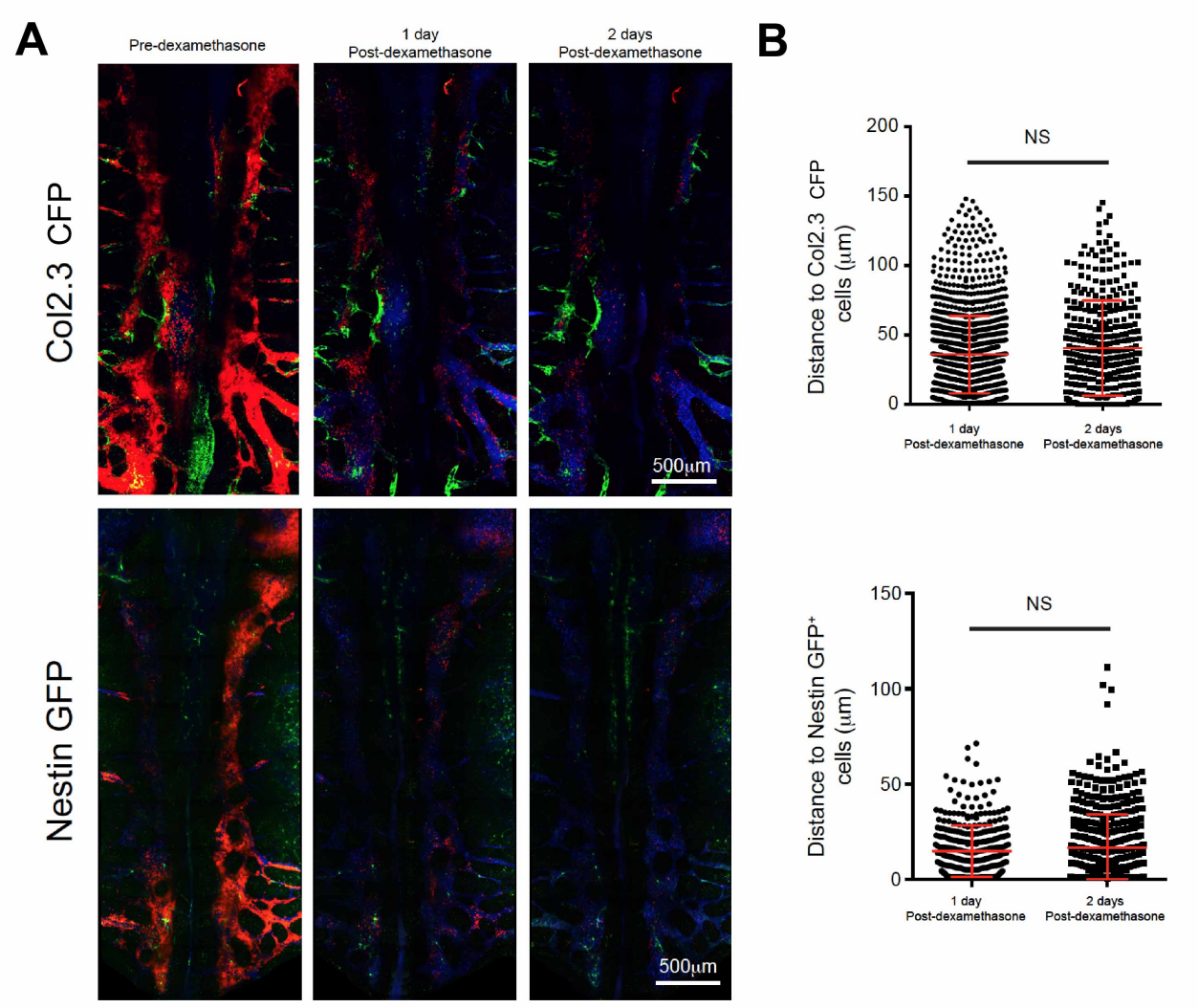

Figure 4.7 - Multi-day timecourse of response to chemotherapy. (A) Representative maximum projection of calvarium BM of Col2.3-CFP and Nestin-GFP mice 18 days post T-ALL transplant followed by 2 days of dexamethasone treatment (15mg/kg). **(B)** 3D measurement of the position of surviving cells in the same mice following 1 and 2 days of dexamethasone treatment relative to Col2.3-GFP^{+} osteoblastic cells (day 1 n: 1499 and day 2 n: 352) and Nestin-GFP^{+} cells (day 1 n: 363 and day 2 n: 496). Data is representative from 3 individual mice. Error bars in B: mean ± S.D. Adapted from (Hawkins et al., 2016).

4.4 - Chemoresistant T-ALL is highly migratory

Although the random distribution of chemoresistant T-ALL cells suggests independence from specific niches, there is the possibility that these surviving leukaemic cells may depend on long-lasting interactions with non-labelled surrounding stroma. To address this question, I performed time-lapse imaging of specific BM areas immediately after the third dose of dexamethasone was administered (Figure 4.8A). Importantly, residual T-ALL cells were still able to undergo division at the same time as cell death events were detected (Figure 4.8B, I and J and Supplementary Video 4A). When tracking single surviving T-ALL cells, I was able to observe that they were extremely migratory, fast moving and maintained only short-lived interactions with osteoblastic cells and Nestin^{+} MSCs (Figure 4.8B and C and Supplementary Video 4A). Notably, these cells migrated faster than seeding disease (Hawkins et al., 2016) (Figure 4.8H).

To explore whether increased migration was a dexamethasone-specific effect, I decided to test additional chemotherapy drugs used in T-ALL patients and analysed their effects using a combination of IVM to test for cell motility, and flow cytometry analysis to test for enrichment in quiescence, a known trait of chemo-resistant cells. I first tested vincristine (Figure 4.8A), which was more effective than dexamethasone in reducing T-ALL cells numbers (Figure 4.8I). After 3 doses of vincristine, I observed a higher enrichment for quiescent surviving T-ALL cells (Figure 4.8J), although some proliferation could still be detected (Figure 4.8D). Time-lapse imaging revealed that vincristine-resistant T-ALL cells were highly migratory (Figure 4.8E and Supplementary Video 4B) and, notably, faster that T-ALL cells surviving dexamethasone treatment (Figure 4.8H).

T-ALL patients are normally treated with combination therapy. To mimic the clinical setting, I combined dexamethasone, vincristine and L-asparaginase (DVA) (Figure 4.8A). This combination was the most effective at reducing the leukaemic burden, as evidenced by the low number of surviving blasts (Figure 4.8I), the majority of which were in G0 phase of the cell cycle (Figure 4.8J). Still, proliferation could be detected (Figure 4.8F). After 3 doses of combination DVA, I imaged the fastest cells recorded (Figure 4.8F and G and Supplementary Video 4C), when comparing to seeding, dexamethasone alone and vincristine alone treatments (Figure 4.8H).

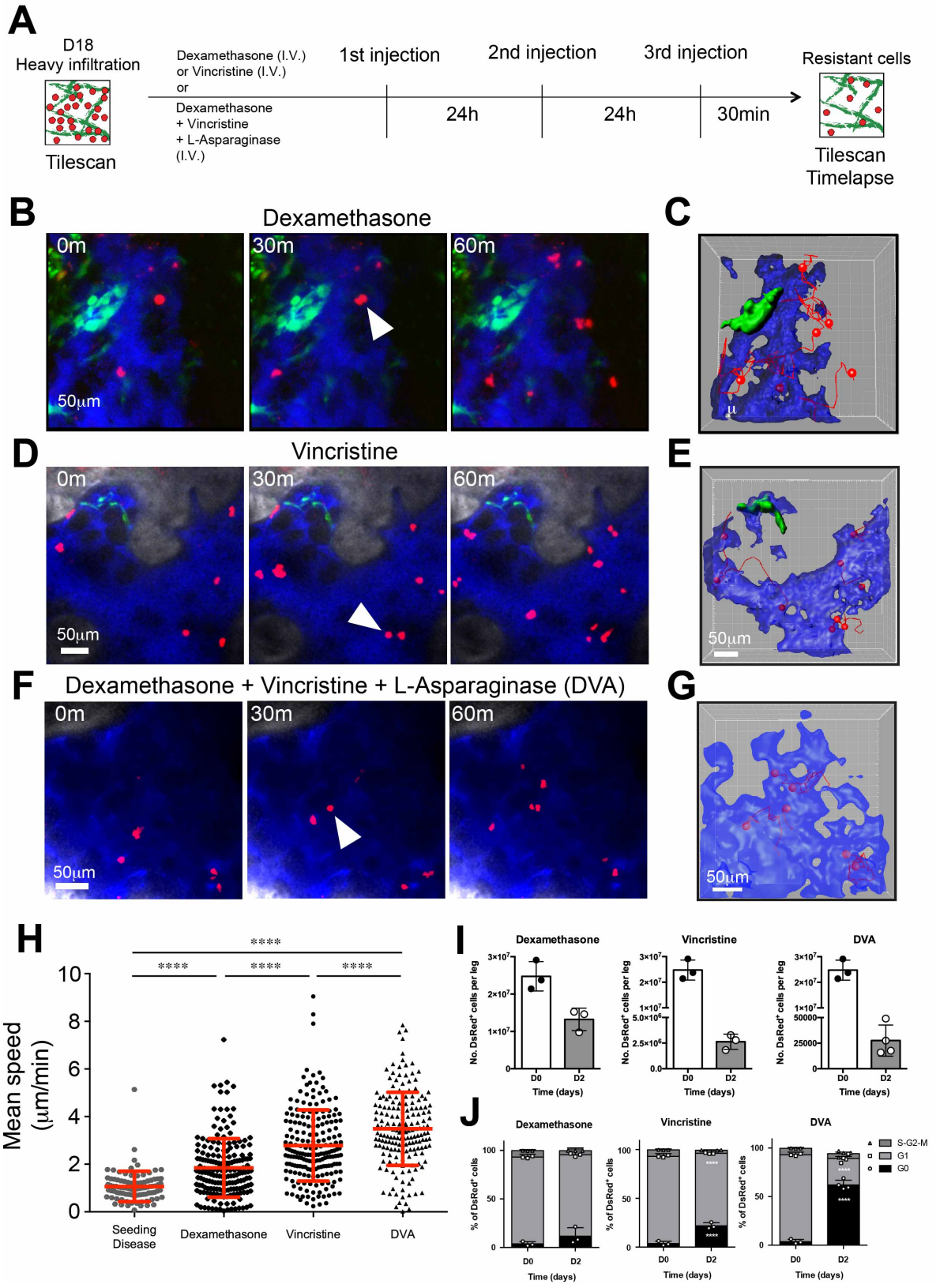

Figure 4.8 - Multi-day imaging of chemotherapy. (A) IVM and treatment schedule. I.V., intravenous. **(B, D, F)** Positions imaged at 3 min intervals for 3 h in mice treated with dexamethasone (B), vincristine (D) and dexamethasone, vincristine and l-asparaginase (DVA) (F). Arrows: mitosis; green: osteoblastic (B) or Nestin^{+} cells (D); blue: vasculature; red: T-ALL cells; grey: bone (D, F).

Corresponding cell tracks (red lines) for each treatment are in **(C)**, **(E)**, and **(G)**. **(H)** Mean speed of cells at early disease and with dexamethasone, vincristine or DVA treatment (n = 91, 184, 199 and 180 cell tracks, respectively). Data are pooled from seven early infiltrated, three dexamethasone-, five vincristine- and four DVA-treated mice (biological replicates) from eight independent experiments using T-ALL from two primary donors (early infiltration and dexamethasone treatment), one primary and two secondary donors (vincristine) and one secondary donor (DVA). **(I, J)** Cell number (I) and cell cycle analysis (J) before (day (D) 0) and after treatment (D2). Data are pooled from three mice (biological replicates) per time point, injected with T-ALL from one secondary donor. Error bars: mean ± S.D. NS, not significant. ****P ≤ 0.0001. Adapted from (Hawkins et al., 2016).

It is possible that the observed migratory behaviour of T-ALL cells is specific to cells that have overactivation of Notch1 and one might argue that T-ALL driven by alternative genetic alterations may have a different migratory phenotype. To address this problem, I injected non-irradiated recipients with murine TEL-JAK2-driven T-ALL blasts and performed IVM of the BM at different disease stages (Figure 4.9A). Similarly to Notch1-driven T-ALL, single TEL-JAK2 blasts were migratory at seeding early stages (Figure 4.9B). To visualize the behaviour of chemoresistant TEL-JAK2 blasts, I applied a dexamethasone regimen treatment analogous to what was described earlier for Notch1 T-ALL cells (Figure 4.2). Upon full BM colonization with TEL-JAK2 T-ALL cells, mice were treated with daily doses of dexamethasone (15 mg/kg) for 3 days and imaged on the third day (Figure 4.2). After 3 doses of dexamethasone I performed IVM of the BM to track dexamethasone-resistant TEL-JAK2 T-ALL cells (Figure 4.9A). Although no increase in cell migration was observed, motility was still a distinct feature of chemoresistant cells (Figure 4.9B and Supplementary Video 4D). Altogether, these observations challenge the hypothesis that chemoresistant T-ALL cells sit in specific BM hot spots.

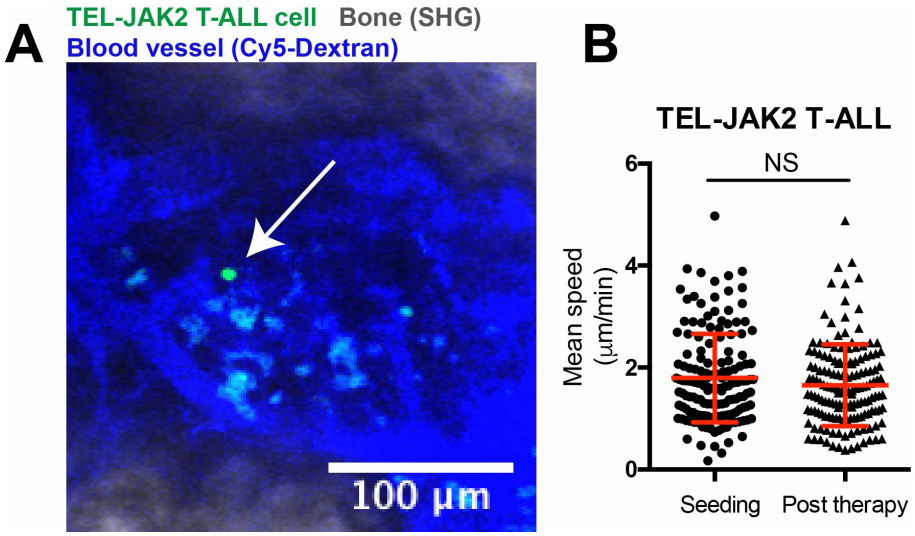

Figure 4.9 - Intravital imaging of TEL-JAK2 T-ALL cells in the BM during response to chemotherapy. (A) IVM was performed to track single TEL-JAK2 GFP^{+} T-ALL cells at early seeding stages and after dexamethasone treatment. **(B)** Quantification of the mean speed of T-ALL cells at early disease and after dexamethasone. n = 156 seeding and 153 post-therapy cell tracks. Data pooled from 4 mice at early disease (Seeding) and 4 mice after dexamethasone treatment (Post therapy). Error bars: mean ± S.D. NS, not significant.

4.5 - Human T-ALL is highly migratory

To expand the significance of these observations to the human disease, I used our IVM methods to study the migratory behaviour of xenotransplanted patient-derived T-ALL cells in NOD/SCID/γ recipient mice (Figure 4.10). I used a dexamethasone regimen adapted from (Chiu et al., 2010) that allowed the study of resistant human blasts.

Briefly, primary human T-ALL samples were obtained and injected into immunodeficient NOD/SCID/γ (NSG) recipient mice and retransplanted into secondary NSG recipients by our collaborators, Drs. John Gribben, Dominique Bonnet and Diana Passaro (Figure 4.10A). Upon early/intermediate infiltration of these mice, I performed *in vivo* labelling of the T-ALL blasts by injecting a PE-conjugated anti-human CD45 antibody. Thirty minutes after injection, these blasts can be imaged and tracked (Figure 4.10B and Supplementary Video 4E), using the IVM methods described earlier (Figure 4.1). This timepoint provided the opportunity to analyse the behaviour of single human T-ALL cells *in vivo,* before exposure to dexamethasone (Figure 4.10B). I was able to observe that these expanding blasts, contrarily to what has been previously suggested, are migratory, and not immotile (Figure 4.10B and E).

To gain insight into the effect of dexamethasone, I studied an additional group of mice that were treated with dexamethasone upon full infiltration. After 14 days of dexamethasone treatment, I observed a significant reduction in the number of blasts (Figure 4.10 C and D). Furthermore, double staining for human CD45 and Ki-67 of undecalcified bones from untreated and treated mice revealed no differences in leukaemia proliferation frequency, suggesting genuine chemoresistance (Figure 4.11). At this point, I was able to identify single surviving blasts that I then time-lapsed. Similarly to the murine Notch1-driven T-ALL, chemoresistant human T-ALL cells were faster and highly migratory (Figure 4.10E and Supplementary Video 4E). These data show that migration is associated with chemoresistance in T-ALL. Furthermore, T-ALL cells evading chemotherapy are not immotile, and instead maintain very transient interactions with their surrounding environment.

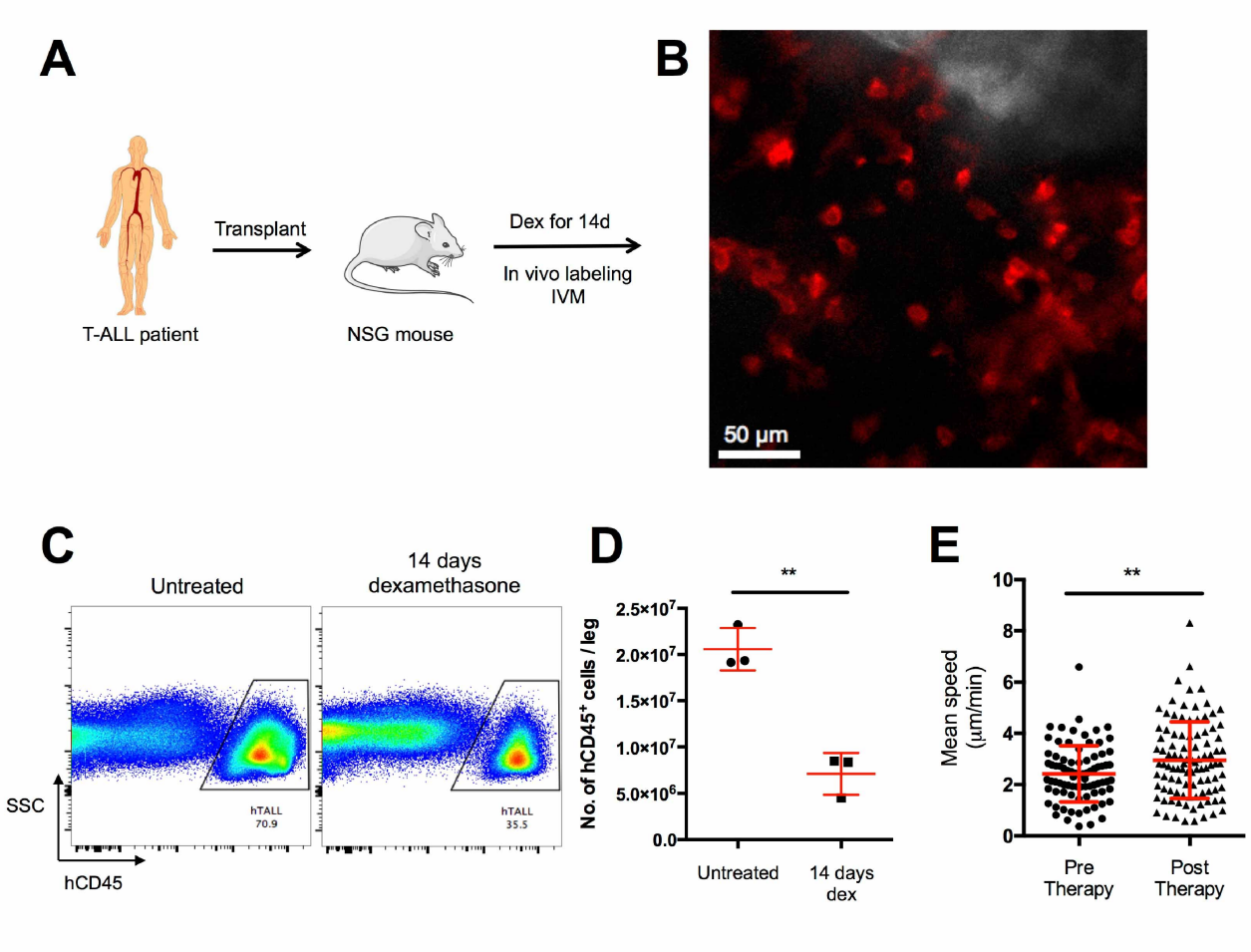

Figure 4.10 - Intravital imaging of human T-ALL during response to chemotherapy. (A) Human T-ALL samples were transplanted into NOD/SCID/γ mice and the response to dexamethasone measured. **(B)** For IVM, human T-ALL were labelled by injection of 10 µg anti-human CD45-PE 15 minutes before imaging. 18 days post-transplant, daily dexamethasone treatment at 15 mg/kg was initiated. 14 days later, the response was measured by flow cytometry **(C)** and **(D)**. Cells were imaged at 3 minute intervals for > 60 minutes and migration was measured by manual tracking of cells imaged either before or after dexamethasone treatment **(E)**. (pre-dex: n=82 cells from 2 independent mice, post-dex: n=100 from 3 independent mice). Error bars = mean +/- S.D. Patient information – Sample ID: JH; Sex: male; Age: 44; Cytogenetics: Del(6) (q12-13q21); Notch status: wild-type. Adapted from (Hawkins et al., 2016).

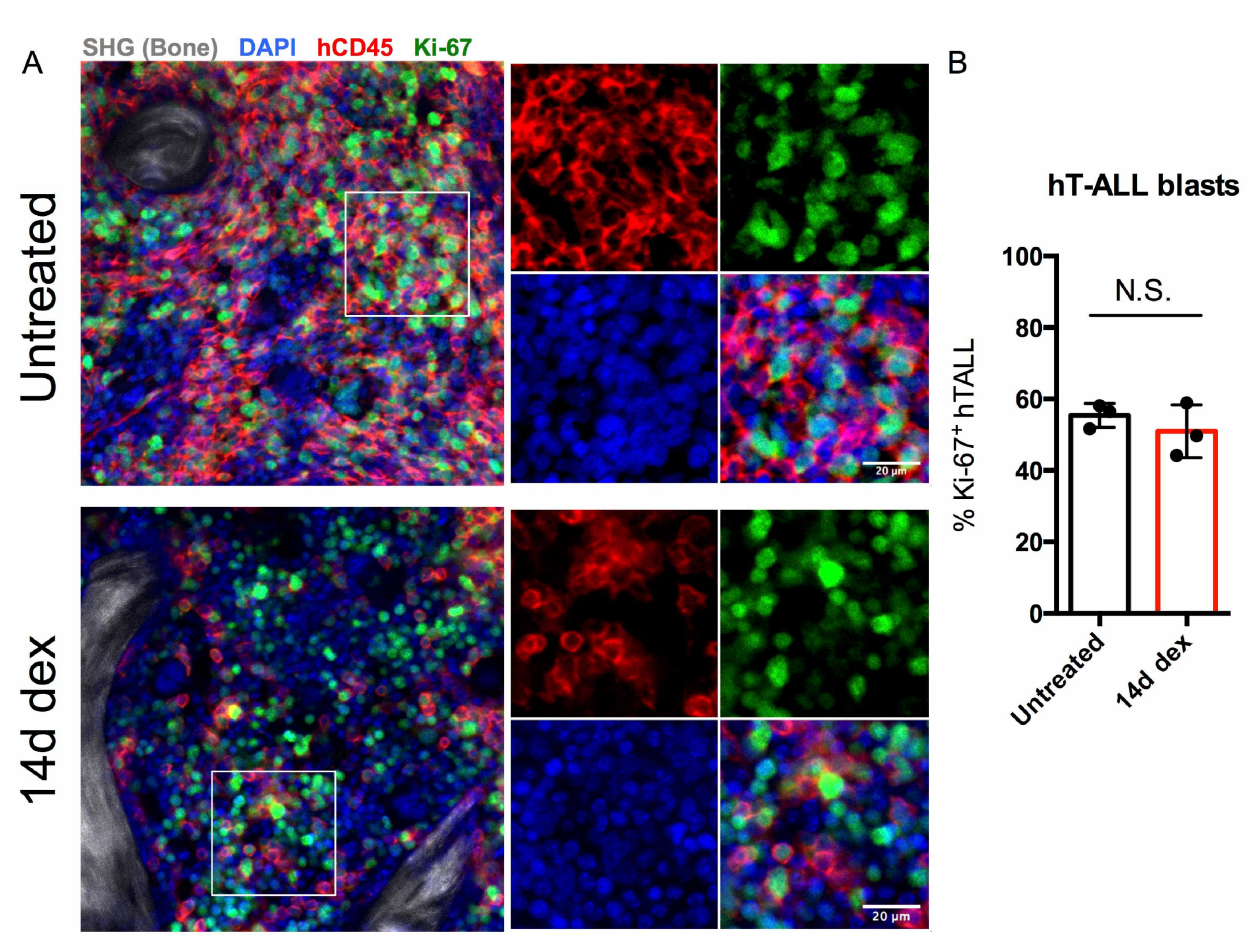

Figure 4.11 - Dexamethasone treatment does not enrich for quiescent/dormant T-ALL cells. NSG mice xenotransplanted with human T-ALL cells were either left untreated or received dexamethasone treatment for 14 days. At this point BM sections were stained for human CD45 (red) and Ki-67 (green). In addition, nuclei were visualized using DAPI (blue) and bone by means of second harmonic generation signal (grey). **(A)** BM areas in the white boxes are shown magnified and each channel separated. **(B)** Analysis of 2338 (untreated) and 1576 (dex) $hCD45^+$ cells in sections from 3 mice per condition reveals no change in the fraction of $Ki\text{-}67^+$ cells by the end of dexamethasone treatment. Error bars: mean ± S.D. Adapted from (Hawkins et al., 2016).

4.6 - T-ALL induces the apoptosis of osteoblasts

When analysing mice at late disease stages (after day 18 post-transplantation), at which time the BM was fully infiltrated by T-ALL, we observed a dramatic reduction in the number of osteoblasts (Hawkins et al., 2016). This was confirmed in trephine biopsies of human T-ALL patients, who also had lost bone-lining osteoblasts (Hawkins et al., 2016). Time-lapse recording of heavily infiltrated areas revealed blebbing of osteoblasts, a morphological hallmark of apoptosis (Hawkins et al., 2016). In order to understand the mechanisms underlying the observed cell loss, I performed TUNEL and cleaved caspase-3 histological staining, which confirmed that osteoblasts were undergoing apoptosis (Figure 4.12). I hypothesize that by targeting the osteoblastic remodelling observed in T-ALL it will be possible to ameliorate bone mass reduction and rescue healthy haematopoiesis.

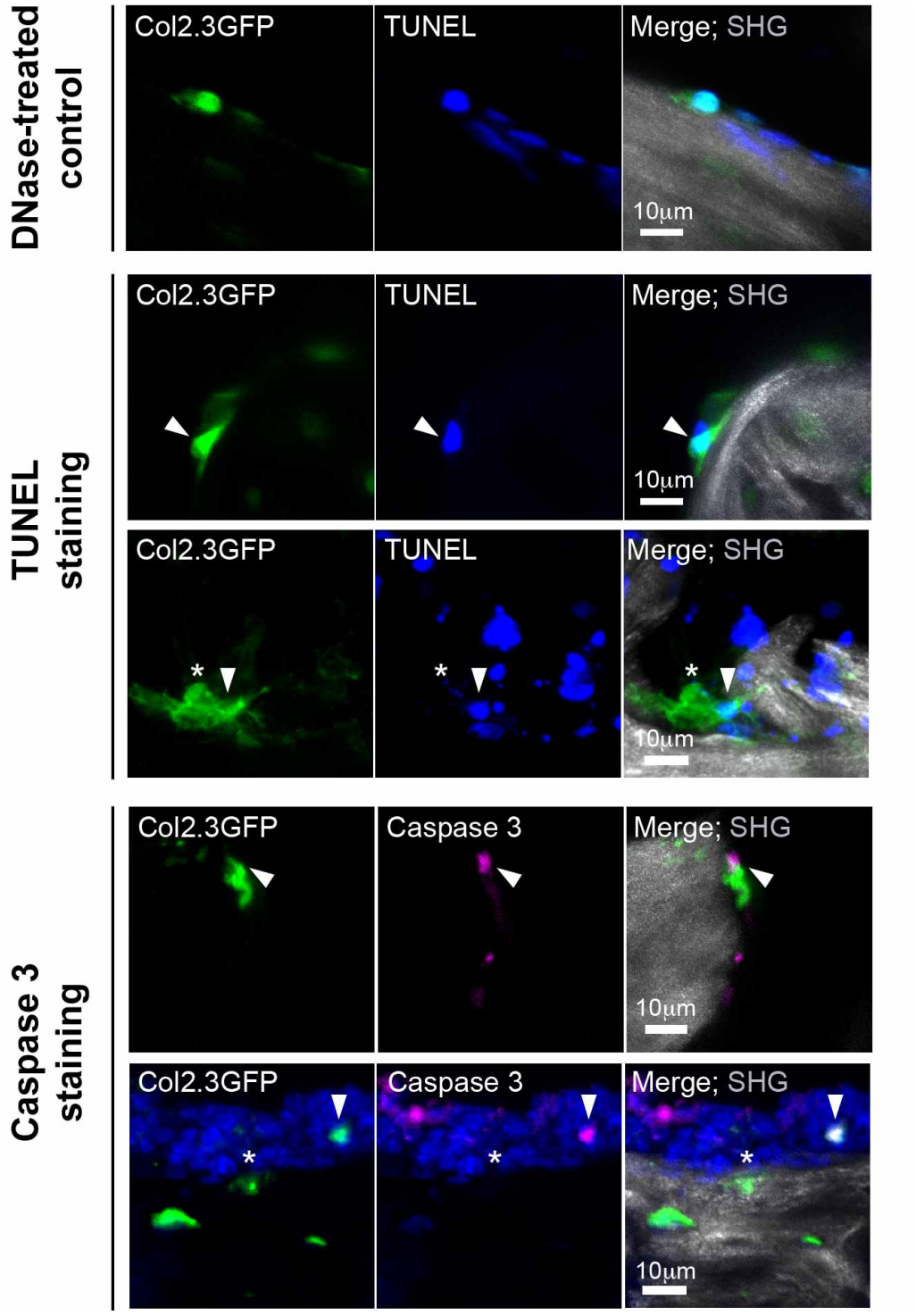

Figure 4.12 – Apoptosis of osteoblasts in T-ALL. Bone sections from Col2.3GFP mice stained for TUNEL or cleaved caspase-3. DNAse pre-treated sections (top) were TUNEL positive control. Grey: bone; green: GFP; blue: TUNEL/DAPI; purple: cleaved caspase-3; arrows: apoptotic osteoblasts; asterisks: surviving osteoblasts. Representative from three heavily infiltrated mice injected with T-ALL from two primary donors. Adapted from (Hawkins et al., 2016).

4.7 - Discussion

Previous work in the group had led to the conclusion that T-ALL seeding and onset is niche-agnostic (Hawkins et al., 2016). Using four-dimensional intravital imaging I directly measured the interactions of chemoresistant T-ALL with the surrounding BM microenvironments, namely osteoblasts, perivascular Nestin$^+$ MSCs and blood vessels. I chose these three stroma components because they have been shown to regulate HSC function in the BM (Calvi et al., 2003; Mendez-Ferrer et al., 2010; Nombela-Arrieta et al., 2013). Furthermore, Col2.3$^+$ osteoblasts were associated with the maintenance of lymphoid progenitors (Ding and Morrison, 2013; Greenbaum et al., 2013).

Using a combined approach of tile scan and time-lapse microscopy, followed by bespoke computational measurement of data (Khorshed et al., 2015), I made unbiased quantification of chemoresistant T-ALL cells' proximity to stroma as well as observations of T-ALL cell behaviour. I concluded that surviving T-ALL cells were extremely motile, maintaining transient interactions with their surroundings. This observation is in contrast with another study suggesting that immotile T-ALL cells reside in vascular sites (Pitt et al., 2015). However, this study is based on short-term (about 20 minutes) imaging sessions with variable temporal resolution, which I have highlighted to be insufficient to identify the migratory behaviour of T-ALL cells. Using 3 hour-long time-lapse imaging with constant Z stack (3 dimensional) acquisition every 3 minutes (temporal resolution), it was possible to generate cell tracks sufficiently long to demonstrate the migratory behaviour of T-ALL cells and to reveal the niche-agnostic characteristics of T-ALL cells. I also observed a stochastic distribution of resistant T-ALL relative to osteoblasts, Nestin$^+$ cells and blood vessels, which again supports the view that chemoresistant T-ALL is niche-independent.

To highlight the translational potential of these conclusions I also studied primary human T-ALL cells xenotransplanted into NSG mice. After dexamethasone treatment, surviving human cells in the BM space were highly migratory, corroborating the notion that chemoresistant T-ALL is not dependent on long-lived interactions with specific stromal cell types. Nevertheless, it is important to know whether the increased migration and active proliferation reported here are exclusive to dexamethasone resistance or a more general behaviour following chemotherapy. Since vincristine is another commonly used chemotherapy drug in T-ALL treatment but with a different mechanism of action, I also tested its effect of Notch1 T-ALL cell migration. I observed similar results to the ones obtained with dexamethasone. I expanded further the analysis of the effect of chemotherapy

on T-ALL motility by ultimately testing combination treatment of dexamethasone, vincristine and L-asparaginase. Surprisingly, T-ALL cells surviving this aggressive cocktail were the fastest I could record. These data suggest that cell migration may be directly correlated with chemoresistance in Notch-driven T-ALL. To test if non Notch-dependent T-ALL cells would display a similar phenotype, I further explored the migratory behaviour of T-ALL cells by timelapsing mice transplanted with TEL-JAK2 T-ALL cells both at seeding early disease and post-dexamethasone treatment. Similarly to Notch1-driven T-ALL, TEL-JAK2 cells were motile, although their speed did not increase upon dexamethasone treatment. Furthermore I did not test the additional therapies, namely the co-treatment with dexamethasone, vincristine and L-asparaginase. Such a stronger selective pressure could have led to the selection of faster chemoresistant T-ALL clones. Nevertheless, the maintained migratory behaviour of TEL-JAK2 T-ALL cells after dexamethasone therapy argues against the idea of specific BM niche maintaining stable, long-lived interactions with T-ALL cells. The mechanisms that explain the migratory behaviour of chemoresistant T-ALL cells is however unexplored.

Altogether, these findings have potential to influence the design of future therapies targeting clinical resistance to chemotherapy, highlighting the importance of leukaemic cell intrinsic mechanisms over extrinsic regulation by niches. Nevertheless, targeting stroma might be an important strategy to protect normal haematopoiesis during leukaemia. Indeed, our previous findings show a dramatic destruction of osteoblasts, cells that sit in the endosteum, participate in bone formation and regulate HSC function (Hawkins et al., 2016). Here, I show that the loss of osteoblasts happens through apoptosis. In the endosteum, a unique population of endosteal blood vessels is found regulating osteogenesis (Kusumbe et al., 2014) and HSCs (Kusumbe et al., 2016). Endosteal vessels are selectively lost in ageing (Kusumbe et al., 2016) and AML (Chapter 3). In Chapter 3, I reasoned that T-ALL could be changing this population as well. I observed, however, that endosteal vessels were maintained in T-ALL (Chapter 3). Altogether, I demonstrate that osteoblasts, but not endosteal blood vessels, are lost in T-ALL. Osteoblasts are responsible for bone production and associated with HSC maintenance, including in the context of leukaemia. Therefore, targeting the reported osteoblastic apoptosis may improve the reduced bone mass frequently observed in patients and survivors of T-ALL (Wilson and Ness, 2013) and contribute to maintain healthy haematopoiesis, commonly disrupted in leukaemia patients (Bowers et al., 2015).

It is not clear what are the specific signal transduction pathways involved in the apoptosis of osteoblasts (Hock et al., 2001). There are putative mechanisms that might lead to

programmed cell death of osteoblastic cells in T-ALL, namely an increase in the levels of TNF. TNF was previously shown to induce apoptosis of both murine and human osteoblasts (Jilka et al., 1998; Kitajima et al., 1996; Tsuboi et al., 1999). Furthermore, TNF contributes to bone turnover and loss (Kimble et al., 1997). Whether TNF is increased and leads to the observed loss of osteoblasts in mice burdened with T-ALL cells remains to be explored. Remodelling of the extracellular matrix (ECM) might also underlie the loss of osteoblasts. For example, fibronectin fragments, in contrast with full-length fibronectin, induce apoptosis of mature osteoblasts (Globus et al., 1998). Fibronectin is a fundamental ECM component and is cleaved by metalloproteinases (MMPs) (Zhao et al., 2004). Paediatric and adult ALL patients have increased expression of MMP-2 and MMP-9 (Kuittinen et al., 2001). It is possible that the increased levels of MMPs induce osteoblast apoptosis through fibronectin fragmentation. Future studies should therefore explore the factors involved in the apoptosis of osteoblasts in T-ALL and investigate targeted anti-apoptotic strategies to salvage the endosteal microenvironment.

Chapter 5

Impact of chemotherapy and CXCR4 inhibition on T-cell acute lymphoblastic leukaemia and acute myeloid leukaemia in vivo cell migration

5.1 - Introduction

The majority of AML patients (Dohner et al., 2015) and a significant number of relapsed T-ALL patients (Pui et al., 2008) have a bad prognosis with poor response to conventional chemotherapy. There is therefore a need for understanding drug resistance mechanisms in these diseases and a demand for new and more effective drugs. A popular theory is that leukaemic cells depend on nurturing and protective BM niches to expand and survive (Lane et al., 2009). Nalm-6 cells (an ALL cell line) were shown to home to specific vascular domains expressing E-selectin and CXCL12 (Sipkins et al., 2005). Furthermore, chemoresistant AML LSCs were shown to preferentially engraft and survive in osteoblastic-rich endosteal areas (Ishikawa et al., 2007). However, currently there is little information on the dynamics of leukaemia cells themselves *in vivo* to support the hypothesis that BM niches regulate the behaviour of leukaemia cells. Using IVM, our group has recently showed that Notch1-driven T-ALL is not dependent on specific microenvironments (Hawkins et al., 2016). Notably, in Chapter 4, I describe my observations that chemoresistant T-ALL cells are highly motile, maintaining only short-lived interactions with the surrounding stroma (Chapter 4 and (Hawkins et al., 2016)). An open question is how other types of leukaemic cells, including AML cells, migrate and respond to chemotherapy in their natural *in vivo* BM

environment. Additionally, the importance of leukaemia-microenvironment interactions and *in vivo* role of its mediators, such as CXCL12, in driving leukaemic cell motility is unknown.

CXCR4 is the main CXCL12 receptor, with major roles in cardiovascular development, neurogenesis and haematopoiesis (Sugiyama et al., 2006; Tachibana et al., 1998; Zou et al., 1998). CXCR4 is an essential component responsible for maintenance of HSCs (Sugiyama et al., 2006) and B cells (Beck et al., 2014) in the BM, and has been implicated in BM metastasis of breast cancer cells (Muller et al., 2001). A recent study has shown that CXCL12, a chemokine abundantly secreted in the BM, is key for T-ALL survival (Pitt et al., 2015). Similarly, small molecule antagonists of CXCR4, the principal CXCL12 receptor, were shown to promote mobilization and apoptosis of AML cells (Abraham et al., 2017; Nervi et al., 2009; Zeng et al., 2009). CXCR4 antagonists combined with existing treatment regimens are currently in clinical trials for relapsed or refractory AML, with positive results (Borthakur et al., 2014; Uy et al., 2012). These studies suggest that inhibiting CXCR4 might form an important arm of future therapeutic approaches for specific blood cancer lineages. Nevertheless, the direct effect of CXCR4 inhibition on either T-ALL or AML *in situ* is unknown. Understanding the specific biological response of leukaemia cells to CXCR4 inhibition will significantly aid in refining the use of CXCR4 antagonists to maximise therapeutic efficacy. CXCR4 is a known regulator of cell migration (Doitsidou et al., 2002). Our group previously showed that HSCs exposed to nematode infection become migratory in transplant recipients and express higher levels of CXCR4 than naïve HSCs (Rashidi et al., 2014). This raises the question whether CXCR4 modulation may affect leukaemia cell migration, as this may relate to disease outcome.

Thus, in this study I have combined IVM of calvarium BM with preclinical models of T-ALL (Notch1-driven T-ALL (Hawkins et al., 2016)) and AML (MLL-AF9-driven AML (Krivtsov et al., 2006)) to perform in depth characterization of (1) response of leukaemia cells to chemotherapy and (2) effect of CXCR4 inhibition on the migratory behaviour of T-ALL and AML *in situ*.

5.2 - Chemotherapy differentially affects T-ALL and AML cell migration *in situ*

Using time-lapse IVM, I analysed the motility of single leukaemic cells during disease establishment, when cells were either isolated or grouped in small clusters, and following treatment with clinically relevant chemotherapy regimens (Figure 5.1).

Figure 5.1 - Intravital imaging schedule. Mice carrying either T-ALL or AML blasts are imaged at early disease stages (day 10-14), when individual seeding cells could be tracked, and at later stages, after fully infiltrated mice were treated with disease-specific chemotherapy and single chemoresistant cells could be monitored.

Consistent with our previous studies (Hawkins et al., 2016), T-ALL cells were highly migratory (Figure 5.2). However, a previously unreported finding is that AML cells are also highly dynamic and indeed migrate faster than T-ALL cells in the BM at early stages of disease (Figure 5.2). Together, these findings suggest that migration is a conserved trait of malignant cells of both lymphoid and myeloid origin.

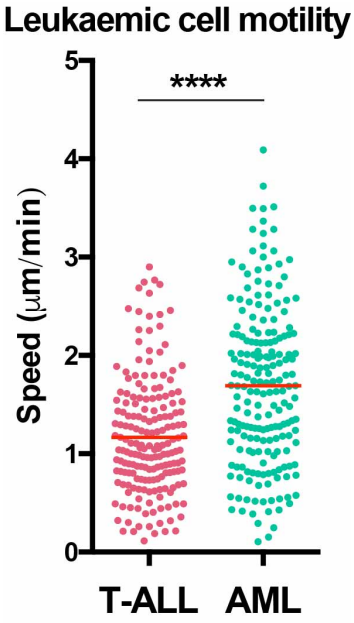

Figure 5.2 – AML cells are more motile than T-ALL cells. Mean speed of single blasts at early disease stages ("Seeding"). Data obtained from 3-4 mice per condition. Plotted data represent semi-automatic tracking of 187 seeding T-ALL cells and 198 seeding AML cells.

5.3 - Chemotherapy differentially affects T-ALL and AML *in vivo* cell migration

As described in Chapter 4 and (Hawkins et al., 2016), T-ALL cells resistant to combined dexamethasone, vincristine and L-asparaginase were consistently more migratory than untreated cells (Figure 5.3). In contrast, AML cells surviving cytarabine and doxorubicin induction chemotherapy were less migratory than seeding AML cells (Figure 5.3). This observation highlights previously unknown differences in cell migration between AML and T-ALL cells that survived chemotherapy. This is consistent with the hypothesis that, although dynamic, AML cells may depend on specific niches to survive (Lane et al., 2009). Furthermore, the increase in migration was specific to chemoresistant Notch1 T-ALL cells, not MLL-AF9 AML cells, suggesting that the observed phenotype is unlikely to be a consequence of BM space being emptied, but rather a unique, cell-intrinsic trait of chemoresistant T-ALL cells.

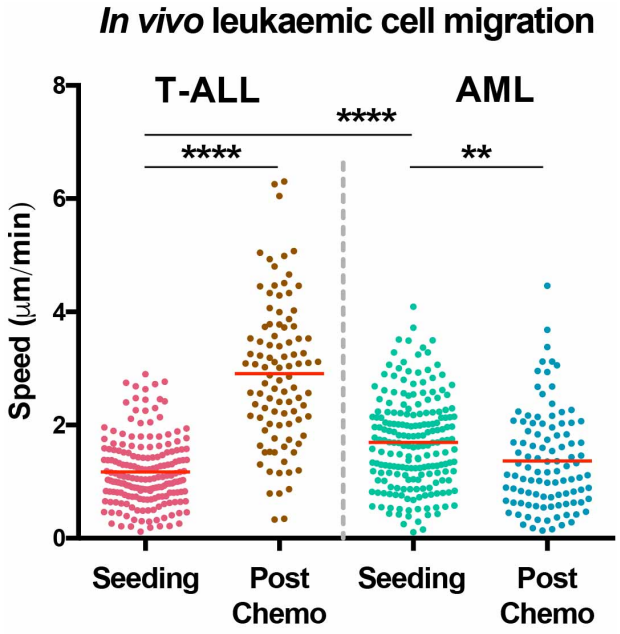

Figure 5.3 – Chemotherapy differentially affects T-ALL and AML cell migration. Mean speed of single blasts at early disease stages ("Seeding") (same data as in Figure 5.1) and after chemotherapy ("Post-chemo"). Data obtained from 3-4 mice per condition. Plotted data represent semi-automatic tracking of 187 seeding T-ALL cells, 97 post-chemo T-ALL cells, 198 seeding AML cells, 103 chemoresistant AML cells.

5.4 - CXCR4 expression in AML and T-ALL blasts

To investigate the role of CXCL12 in leukaemic cell motility, I first assessed the expression of CXCR4. T-ALL and AML blasts expressed higher amounts of CXCR4 compared to healthy lymphoid and myeloid counterparts (Figure 5.4A). Interestingly, the proportion of CXCR4$^+$ chemoresistant cells was variable in T-ALL, but increased in chemoresistant AML as compared to early disease (Figure 5.4B). This observation is consistent with the hypothesis that AML cells survive in CXC12-rich BM niches (Lane et al., 2009), but chemoresistant T-ALL cells' distribution is stochastic in nature (Hawkins et al., 2016).

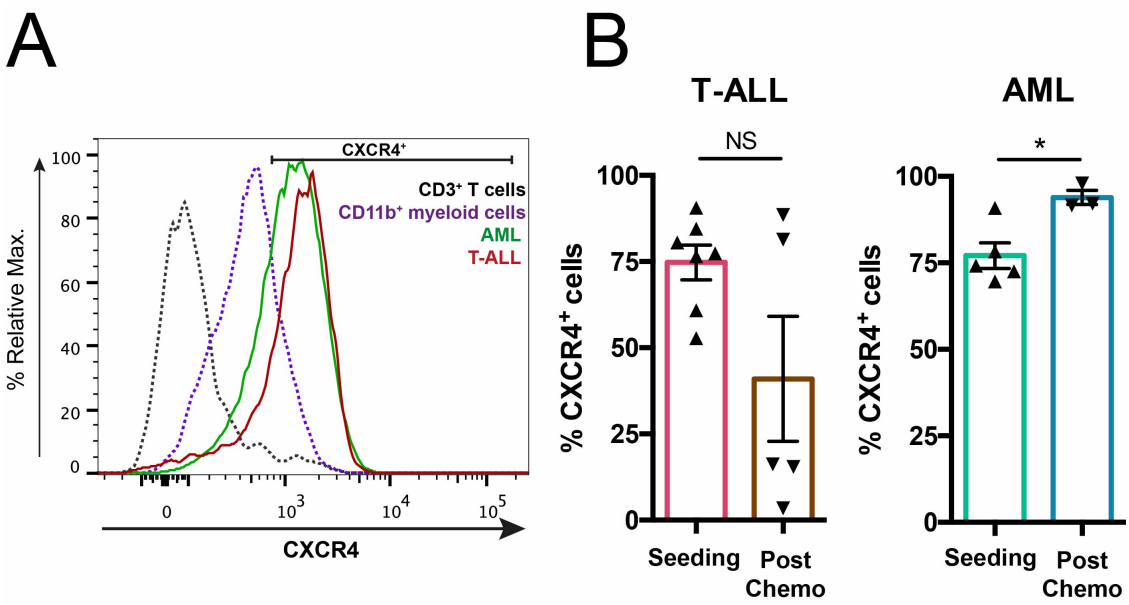

Figure 5.4 - CXCR4 expression in AML and T-ALL blasts. (A) Flow cytometry analysis of CXCR4 expression in AML, T-ALL, CD3$^+$ T and CD11b$^+$ myeloid cells. Plots are representative of 5 independent AML and 4 T-ALL batches, and BM from 3 control mice. **(B)** Frequency of CXCR4$^+$ AML (left) and T-ALL (right) cells before and after chemotherapy treatment, assessed by flow cytometry. Left panel (AML): data obtained from 5 mice burdened with AML (5 AML batches) untreated and 3 mice co-treated with cytarabine and doxorubicin (1 AML batch). Right panel (T-ALL): data obtained from 7 mice burdened with T-ALL, untreated, and 5 mice co-treated with dexamethasone, vincristine and L-asparaginase (1 T-ALL batch). Error bars: mean ± SEM.

5.5 - CXCR4 inhibition mobilizes AML and T-ALL blasts *in vivo*

To understand the short-term effect of CXCR4 inhibition, I performed time-lapse IVM (Figure 5.5A) of the same BM areas before and after administering AMD3100 (4mg/kg, I.V.). AMD3100 is a clinically approved CXCR4 antagonist (plerixafor) used to mobilize HSPCs for transplantation. The efficacy of AMD3100 was confirmed by visualization of T-ALL and AML cells' mobilization from the BM parenchyma into circulation (Figure 5.5B and C, Supplementary Videos 5A and 5B), a known effect of CXCR4 antagonism (Nervi et al., 2009; Pitt et al., 2015).

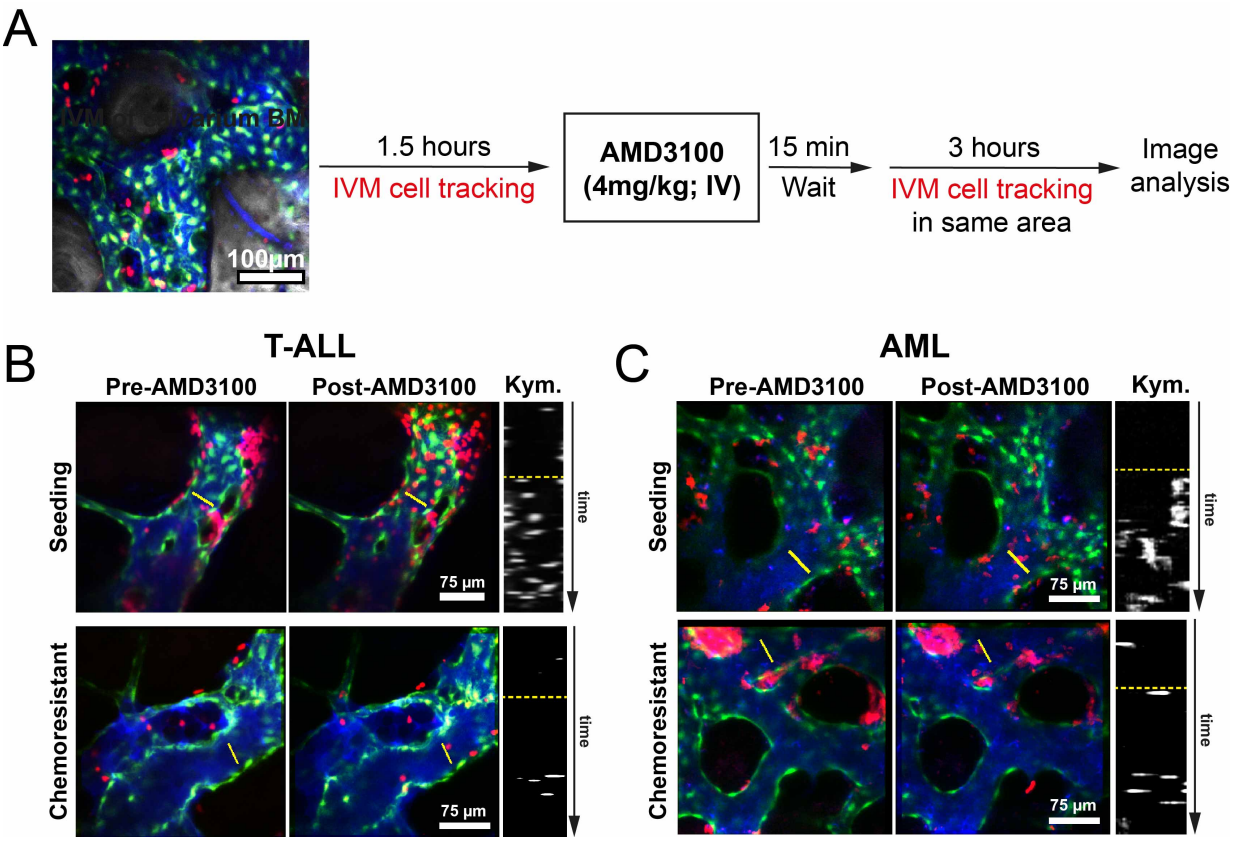

Figure 5.5 – AMD3100 mobilizes blasts from the BM. (A) In each imaging session, several positions within the BM space were selected and time-lapse recorded every 3 minutes, for 90 minutes. 15 minutes after injection of AMD3100, the same positions were timelapsed at the same rate for a further 3 hours. **(B, C)** Maximum intensity projections of representative BM areas showing seeding and chemoresistant T-ALL (B) and AML (C) cell mobilization upon AMD3100 injection. Left and middle panels: red, leukaemia cells; green, Flk1-GFP^{+} endothelial cells; blue, Cy5- labelled dextran inside blood vessels. Right panels are kymographs displaying a time projection of the vessel sections highlighted by the yellow lines in the left and middle panels. The dotted yellow lines separate time prior to (top) and following (below) AMD3100 administration.

5.6 - CXCR4 inhibition restrains T-ALL but not AML cell migration within the BM

I next investigated the effect of CXCR4 antagonism on non-mobilized, parenchymal T-ALL and AML cell migration. AMD3100 strikingly decreased T-ALL cell speed at both seeding and post-chemotherapy stages (Figure 5.6A-C, Supplementary Video 5C). In contrast, the speed of AML cells was not affected by AMD3100 (Figure 5.6A-C, Supplementary Video 5D). This was confirmed by the analysis of local displacement of T-ALL and AML blasts before and after AMD3100 treatment (Figure 5.6D). These observations are consistent with previous *in vitro* work showing that CXCR4-deficient T-ALL cells have decreased migration (Passaro et al., 2015).

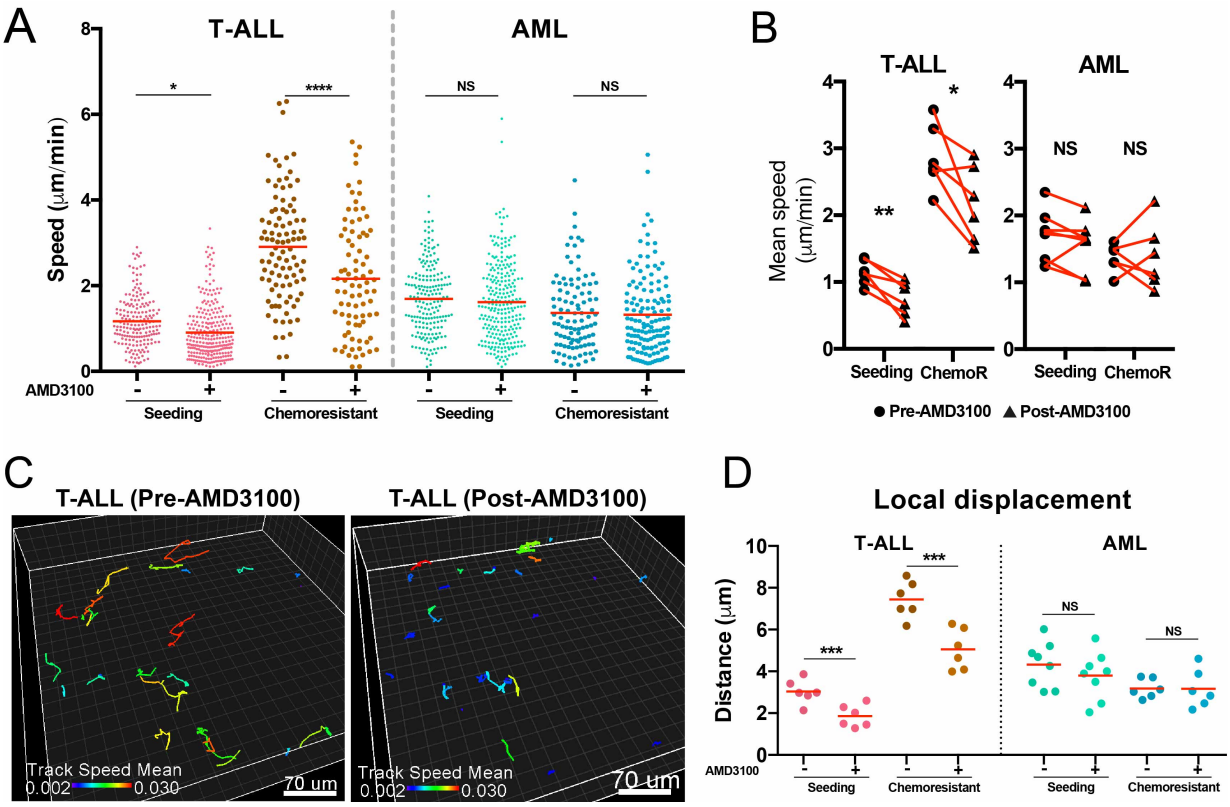

Figure 5.6 – The effect of AMD3100 on *in vivo* leukaemic cell migration. (A) Mean speed of single T-ALL and AML cells tracked before (-) (same data as in Figure 5.3) and after (+) exposure to AMD3100. Data obtained for T-ALL seeding: n=187 cells (-), n=265 cells (+) from 3 mice; T-ALL chemoresistant: n=97 cells (-), n=83 cells (+) from 3 mice; AML seeding: n=198 cells (-), n=262 (+) from 4 mice; AML chemoresistant: n=103 cells (-) and n=134 cells (+) from 3 mice. **(B)** Paired analysis of mean speed of tracks in the same areas before and after AMD3100 injection. Original tracking data obtained as in panel A; each dot represents average measures from one position. **(C)** Representative tracks of seeding T-ALL cells before (1.5 hours) and after (3 hours) exposure to AMD3100. **(D)** AMD3100 significantly diminishes the local cell displacement of seeding and chemoresistant T-ALL cells, but not of AML cells. Shown is the averaged local displacement measured in each of the positions shown in panel A.

5.7 – AML receives multiple chemokine signals

The data described in sections 5.6 suggest that while CXCL12 is key for chemoresistant T-ALL cell behaviour, this is not the case for AML cells. Therefore, these cells may rely on additional factors and more complex crosstalk with the BM microenvironment. This was supported by Gene Set Enrichment Analysis (GSEA) of Notch1 T-ALL cells (data generated by the Hawkins group - (Waibel et al., 2017)) and AML cells (Chapter 3) isolated from infiltrated mice. GSEA showed that AML cells are enriched for expression of genes involved in chemokine signalling pathways ("*chemokine mediated signalling pathway*" and "reactome peptide ligand binding receptor") and chemotaxis ("*regulation of chemotaxis*" and "*leukocyte chemotaxis*") (Figure 5.7). Together, these data suggest that redundancy in chemokine-mediated migration might be a specific feature of AML

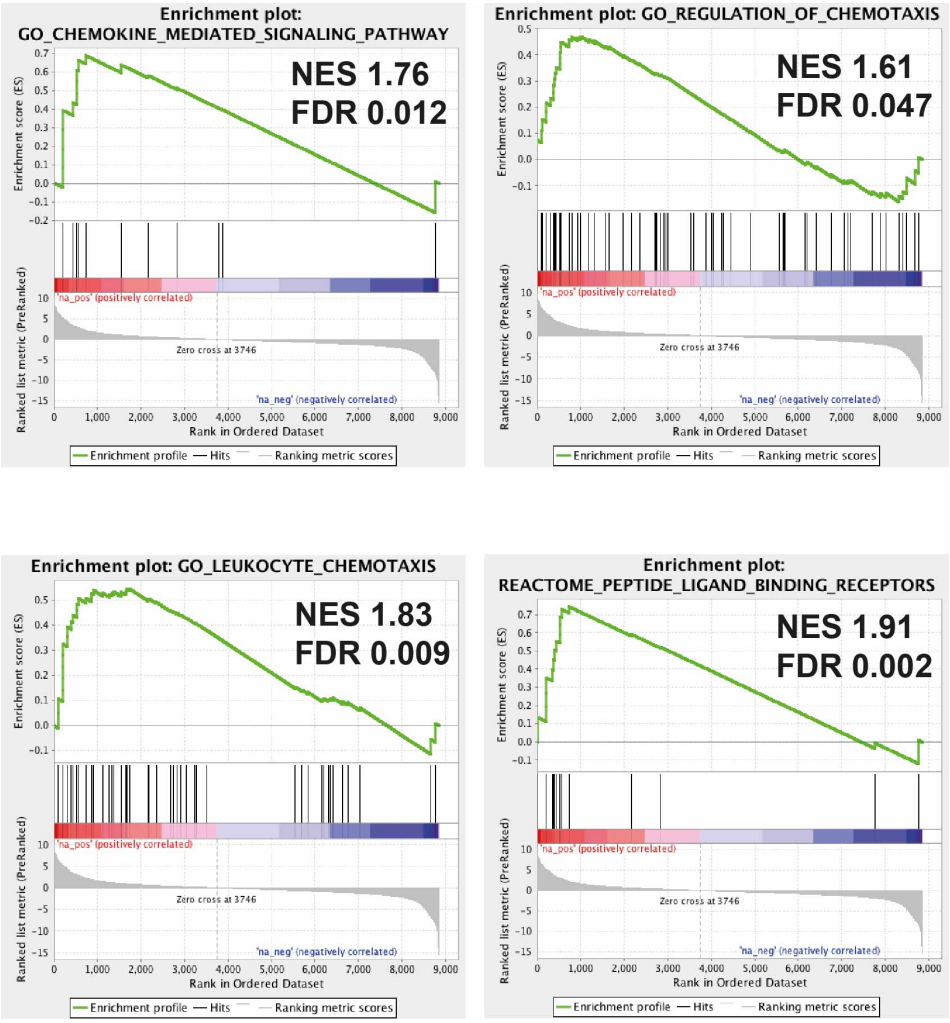

Figure 5.7 – RNA sequencing analysis of AML and T-ALL blasts. GSEA comparing AML and T-ALL cells isolated from fully infiltrated BM for genes involved in chemotaxis and chemokine signaling pathways. Data obtained from 6 mice (T-ALL) and 9 mice (AML).

5.8 - CXCR4 inhibition reduces T-ALL, but not AML cell clusters sizes

Interestingly, the size of T-ALL cell clusters diminished following AMD3100 treatment (Figure 5.7A and B, Supplementary Video 5E), as a result of combined intravasation and cell death. At this stage, cell death was qualitatively identified based on the phenotype of cells that stopped moving entirely and became increasingly smaller until they disappeared (Supplementary Video 5E).

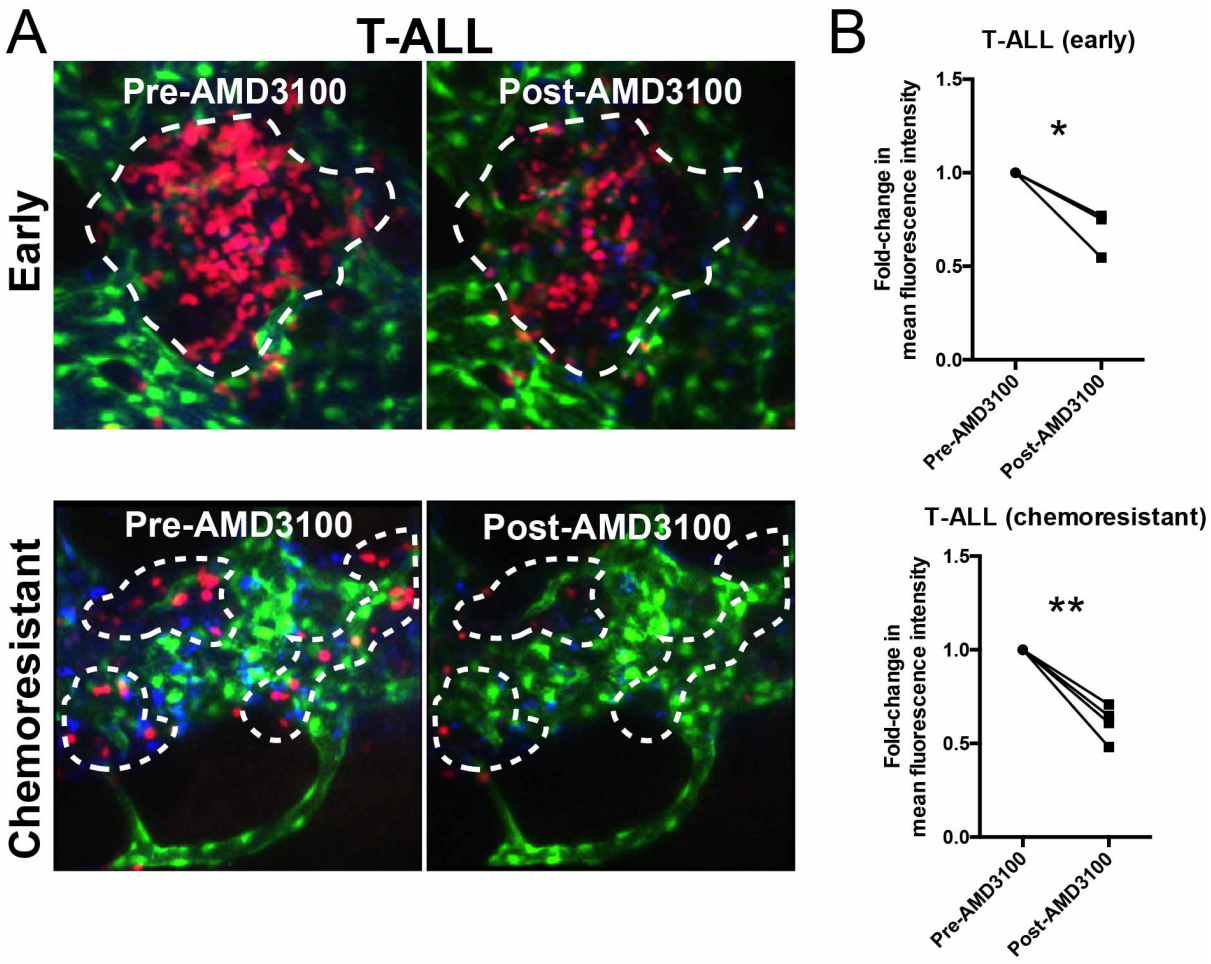

Figure 5.8 - AMD3100 effect on T-ALL cell clusters. (A) Representative maximum projections from IVM 3-dimensional stacks acquired prior to and 180 minutes following AMD3100 administration, showing the effect of the drug on T-ALL cell clusters. Red: T-ALL cells; green: Flk1-GFP^{+} endothelial cells; blue: Cy5-labelled blood vessels. **(B)** CXCR4 antagonism produced a significant reduction of early colonizing and chemoresistant T-ALL cell clusters as quantified by paired analysis of mean fluorescence intensity of the same areas before and 180 minutes after AMD3100 injection. Data obtained from 3 mice with early T-ALL infiltration and 4 mice with chemoresistant T-ALL.

In contrast, there was minimal AML cell death and a smaller reduction of AML cell cluster sizes after AMD3100 injection (Figure 5.9A and B, Supplementary Video 5F). This suggests that in contrast to T-ALL, the effect of CXCR4 inhibition on AML is mainly restricted to mobilization.

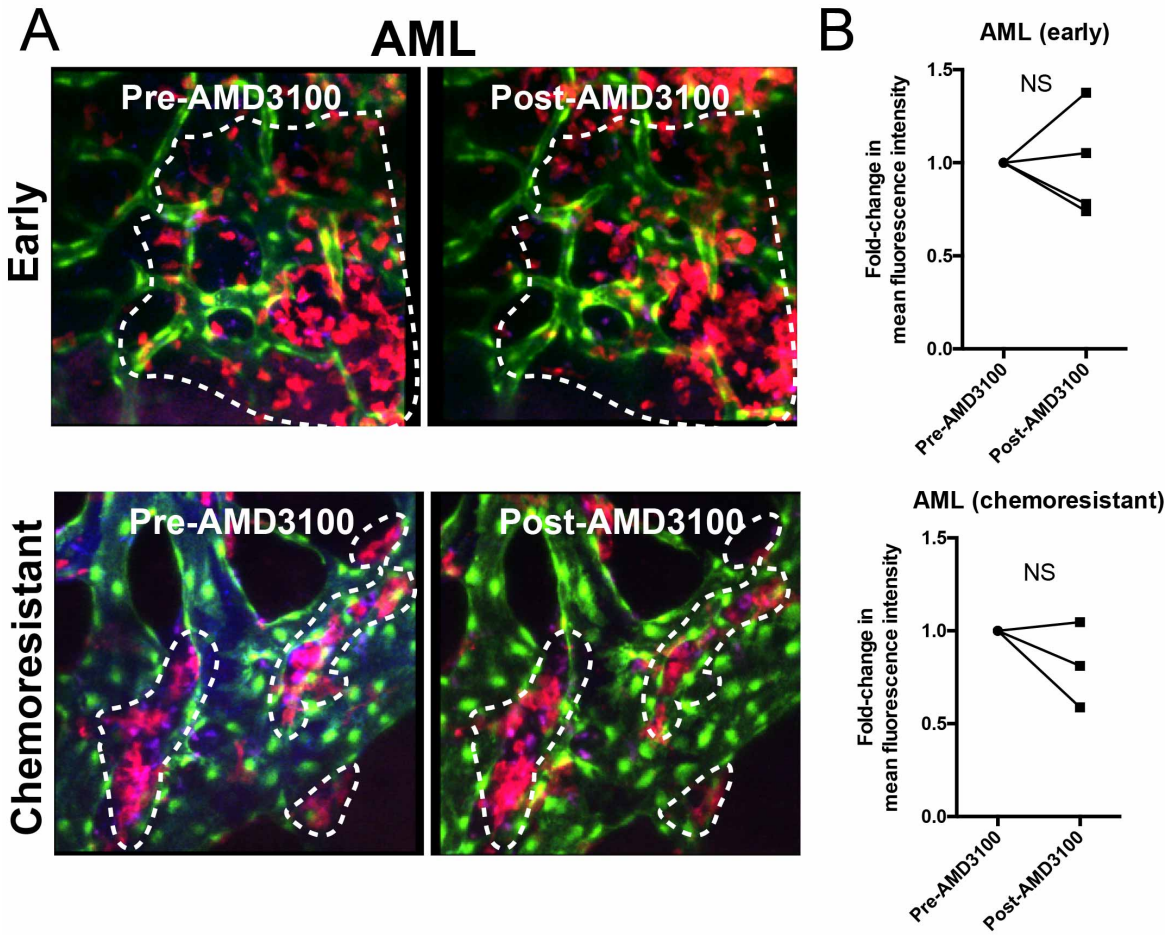

Figure 5.9 - AMD3100 effect on AML cell clusters. (A) Representative maximum projections from IVM 3-dimensional stacks acquired prior to and 180 minutes following AMD3100 administration, showing the effect of the drug on AML cell clusters. Red: T-ALL / AML cells; green: Flk1-GFP^{+} endothelial cells; blue: Cy5-labelled blood vessels. **(B)** CXCR4 antagonism produced minimal effect on AML cluster sizes as quantified by paired analysis of mean fluorescence intensity of the same areas before and 180 minutes after AMD3100 injection. Data obtained from 4 mice with early AML infiltration and 3 mice with chemoresistant AML.

5.9 - Discussion

Given the interest on a putative leukaemic niche that supports both early infiltration and chemoresistant cells, I aimed to unravel the role of conventional chemotherapy and of emerging anti-CXCR4 therapies in T-ALL and AML cell behaviour, in their natural BM context.

I showed that cell motility is a characteristic feature of both types of leukaemia. However, I demonstrate that in contrast with chemoresistant T-ALL, chemoresistant AML cells are less motile and more engaged with the microenvironment.

The importance of the CXCL12/CXCR4 axis in BM homing is illustrated by the clinical application of the CXCR4 antagonist AMD3100 to mobilise progenitors for HSC transplantation (Chen et al., 2006). The use of AMD3100 and related antagonists has been explored in AML (Nervi et al., 2009; Tavor et al., 2004; Zeng et al., 2009) and recently, in T-ALL (Pitt et al., 2015). It should be noted that in pre-clinical studies, despite the encouraging results, the response to CXCR4 antagonists is only partial and complete remission following CXCR4 antagonists alone is not achieved (Pitt et al., 2015). Importantly, it is not known what is the effect of these drugs on the *in vivo* behaviour of leukaemic cells. As recently acknowledged (Hawkins et al., 2016), understanding the mechanisms driving the movement of leukaemic cells might have therapeutic value.

Recently, Pitt et al. showed that T-ALL cells sit within $CXCL12^{high}$ areas and are partially killed by CXCR4 inhibition (Pitt et al., 2015). One might speculate that these inhibitors increase cell migration, which contradicts our observation of fast moving chemoresistant cells. Thus, I used our IVM system to investigate the effect of AMD3100 on both T-ALL and AML cells, to identify whether this inhibitor may trigger some shared responses between the two disease types. AMD3100 is also known as plerixafor and is a clinically approved CXCR4 inhibitor used for progenitor recruitment in case of G-CSF failure. Many studies looking at CXCR4 inhibition in leukaemia have used AMD3100, while others have used more recently developed inhibitors, such as AMD3465, with a longer half-life and higher potency (Pitt et al., 2015). Because the purpose of my study was to analyse the short-term effect of CXCR4 inhibition, I decided to use the broadly available AMD3100 administered via I.V. injection.

As expected, I detected high CXCR4 expression on AML and T-ALL blasts in the BM. Unexpectedly, chemotherapy seemed to select for a population of cells expressing higher

levels of CXCR4 in AML, while no differences in CXCR4 levels were found when comparing untreated and chemoresistant T-ALL cells.

When performing the IVM experiments, I observed a dramatic decrease of treatment-naïve and chemoresistant T-ALL cell migration following AMD3100 administration. These data suggest that CXCL12 regulates T-ALL residence and migration inside the BM. It also suggests that the high motility of chemoresistant cells might be targeted by CXCR4 inhibition.

In contrast with T-ALL, AML cell migration was not affected by AMD3100. Interestingly, AML cells express high levels of CXCR4 and have a significant enrichment for genes involved in chemokine-driven migration. It is possible that AML cells are more engaged with the surrounding microenvironment and receive additional and redundant niche signals, when compared to T-ALL. This would explain the lack of AML cell migration response to AMD3100.

In summary, in this chapter I show that CXCR4 regulates retention in the BM for both leukaemias, but that it is only fundamental for the exploratory behaviour of T-ALL cells (Figures 5.10). These results suggest that CXCR4 targeting might be particularly useful in relapsed or refractory T-ALL and support future investigations into the mechanisms underlying the observed migratory phenotypes of leukaemic cells.

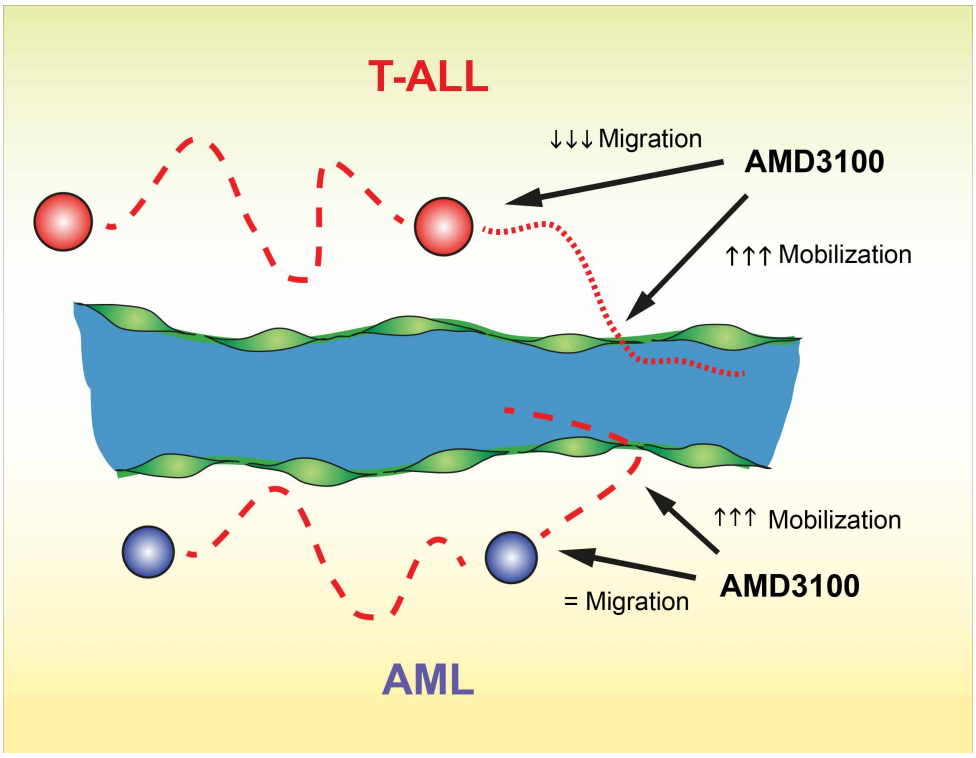

Figure 5.10 - Proposed model for the effect of CXCR4 inhibition on T-ALL and AML cells. CXCL12 is a crucial niche factor that binds CXCR4. Both T-ALL and AML cells express high levels of CXCR4 at the cell surface level. CXCR4 antagonism can be achieved through the use of the clinically available small molecule AMD3100 or plerixafor. Using IVM, I show that administration of AMD3100 promotes the *in vivo* ousting of both propagating and chemoresistant T-ALL and AML cells from the BM. This is consistent with the knowledge that CXCL12 is a key BM retention and homing signal. In contrast, the motility of leukaemia cells from different lineages is differentially impacted by CXCR4 antagonism. While AMD3100 significantly decreases the migration of both propagating and chemoresistant T-ALL cells, it does not affect the movement of AML cells.

Chapter 6

General Discussion and Conclusion

Tissue development and maintenance are determined by interactions between stem cells and the surrounding microenvironment or niche. BM perivascular niches maintain adult HSCs. Osteoblasts, endothelial cells and MSCs are key cell types that participate in the regulation of HSCs and influence healthy haematopoiesis.

Acute leukaemias, including T-ALL and AML, develop rapidly and are characterised by high relapse rates. Despite significant advances in our understanding of leukaemia genetics, our failure to detect disease at early stages, prevent leukaemia and chemotherapy-induced BM failure and the high resistance to chemotherapy have significantly affected improvement in patient survival. Because HSCs and leukaemia share dependence on stroma-derived factors such as CXCL12, an attractive hypothesis is that leukaemia resides in chemo-protective, quiescence-inducing BM niches, similar to the endosteal and vascular niches known to nurture HSCs (Lane et al., 2009; Morrison and Scadden, 2014). Alternatively, it has been proposed that leukaemia cells disrupt the microenvironment and in this way favour their own expansion (Arranz et al., 2014) and impair the maintenance of non-malignant haematopoiesis (Colmone et al., 2008; Hanoun et al., 2014; Schepers et al., 2013).

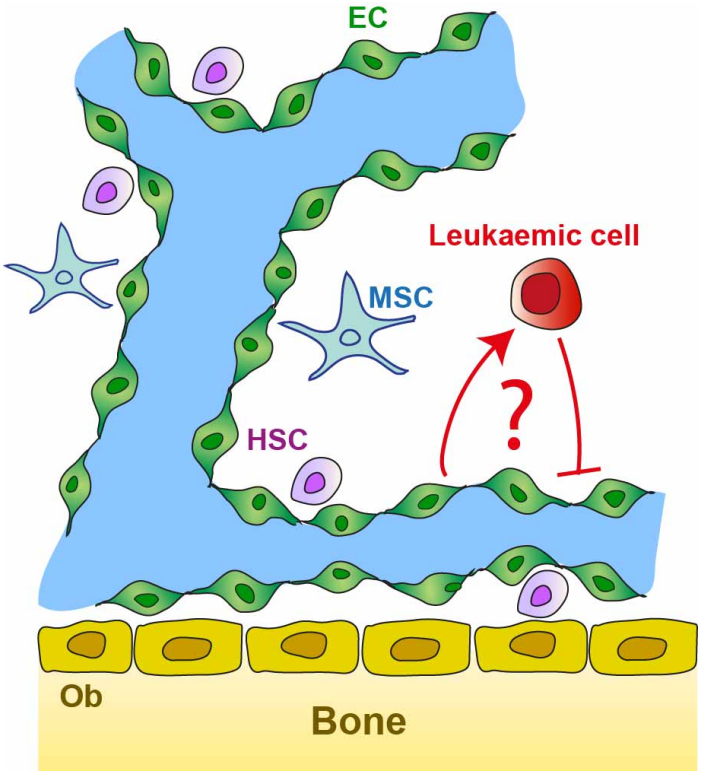

Figure 6.1 – The role of the BM microenvironment in leukaemia. It is currently not well understood whether the HSC-supportive niches are co-opted by leukaemia cells to favor their expansion and survival from chemotherapy. Inversely, leukaemic cells can also remodel the existing microenvironment and in this way negatively impact on healthy haematopoiesis.

In this work, I studied how AML cells remodel the HSC-supportive microenvironment *in vivo* (Chapter 3), whether a specific niche supports T-ALL chemoresistance *in vivo* (Chapter 4) and how chemotherapy and CXCR4 influence leukaemic cell behaviour *in vivo* (Chapter 5). To address these questions, I used pre-clinical mouse models of leukaemia and studied them using intravital confocal and 2-photon microscopy of the calvarium BM, complemented by immunofluorescence stainings of BM sections, gene expression and protein quantification assays (RNA-seq, qPCR, ELISA) and functional analyses.

In Chapter 3, I used a multi-modal microscopy strategy to monitor AML progression. It revealed a focal and progressive endosteal vessel remodelling, coupled to loss of osteoblastic cells and haematopoiesis. AML dramatically remodels endosteal stroma with osteoblastic cells and endosteal vessels, which are locally decreased at earlier disease stages and globally affected in advanced disease. The decrease of healthy haematopoietic cells was both temporally and spatially correlated with the endosteal remodelling. HSCs were lost from the BM when endosteal niches collapsed. Contrarily, HSCs increased in the spleen when splenic blood vessels expanded. *In vivo* cell tracking revealed increased vascular adhesion and transendothelial migration of healthy haematopoietic cells. This likely promotes the loss of healthy haematopoietic cells from the BM. To target the endosteal blood vessels I used the iron-chelator and HIF-1α stabilizer deferoxamine (Kusumbe et al., 2014). Deferoxamine administration partially rescued both vasculature and HSCs in endosteal areas. It has been shown that AML relapse is initiated in endosteal areas (Ishikawa et al., 2007). I therefore hypothesized that by inducing the endosteal endothelium it may be possible to increase chemotherapy delivery to these areas. Indeed, genetic induction of endosteal vessels in $Fbxw7^{i\Delta EC}$ mutant mice (Kusumbe et al., 2016; Ramasamy et al., 2014) enhanced the action of induction chemotherapy. Altogether, promotion of endosteal vessels rescued HSC loss and improved the efficacy of chemotherapy, demonstrating the therapeutic value of preserving endosteal vessels.

These results add endosteal transition blood vessels to the group of BM microenvironment components disrupted in AML, which include $Nestin^{+}$ MSCs and $NG2^{+}$ periarteriolar cells (Hanoun et al., 2014) and adipocytes (Boyd et al., 2017). The downstream consequences of haematopoiesis shutdown and cytopenias in AML include infection, anaemia and bleeding and can be fatal. A recent study has shown that AML patients with lower HSC frequency have lower disease-free survival (Wang et al., 2017). Furthermore,

mathematical modelling suggests that the loss of HSCs before AML relapse rely on the dislodgment of HSCs from their niches (Wang et al., 2017). The results presented in Chapter 3 suggest that the destruction of the endosteal vascular niche in AML may be a key event in the loss of HSCs. Future studies should explore the mechanisms underlying the remodelling of the endosteal vasculature. For example, it should be assessed whether the increased local levels of CCL2 and TNF act directly on the endothelium or contribute to the stromal remodelling indirectly, through the recruitment of inflammatory cells.

In Chapter 4, I built on our previous observations that T-ALL seeding and expansion was independent from known specific niche cell types (osteoblasts, blood vessels and Nes-GFP$^+$ MSCs) (Hawkins et al., 2016) to ask whether chemoresistant T-ALL cells were dependent on these microenvironments. I used IVM tile scans of the calvarium BM and automatic distance quantification as an unbiased strategy to measure the distribution of single chemoresistant T-ALL cells in the whole BM. I observed that individual T-ALL cells surviving dexamethasone were randomly distributed in relation to osteoblasts, blood vessels and Nes-GFP$^+$ MSCs. I then decided to track the behaviour of these cells. The assumption in the field is that cancer cells survive in specific tissue areas where they are mainly immotile and maintaining long-lasting interactions with surrounding stroma. Unexpectedly, I observed that chemoresistant (dexamethasone-, vincristine- and dexamethasone plus vincristine plus asparaginase-resistant) T-ALL cells were very motile. T-ALL cells surviving the more effective combination drug treatment were the fastest I could record. Furthermore, I observed that human T-ALL cells surviving dexamethasone were also more motile and that syngeneic murine TEL-JAK2 T-ALL cells were still migratory after dexamethasone treatment. Overall, these data argue against an important role of specific microenvironments in T-ALL and suggest that new therapies targeting migration should be explored against chemoresistant T-ALL. Further studies are needed to understand whether the observed migratory behaviour is driven by cell-intrinsic or cell-extrinsic changes. If cell-extrinsic, it might be the result of increased extracellular space to migrate, altered extracellular matrix or altered cytokine/growth factor milleu that promotes cell motility. If cell-intrinsic, it should be explored whether there are drug-induced changes in gene expression (e.g. because of new mutations) or whether the observed migration is a consequence of selection of faster clones.

I also investigated the mechanism driving the decay of osteoblasts in T-ALL. We had previously shown that osteoblasts were rapidly lost at late stages of T-ALL infiltration

(Hawkins et al., 2016). In Chapter 4, I used immunofluorescence to show that osteoblasts undergo apoptosis. Interestingly, I had observed that endosteal blood vessels were maintained in T-ALL (Chapter 3), while dramatically lost in AML. In comparison to AML, blood cytopenias are not as severe in T-ALL. This might be due to the coupled decay of endosteal blood vessels and osteoblasts in AML and single loss of osteoblasts in T-ALL.

In Chapter 5, I explored the cell migratory behaviour of not only T-ALL but also AML cells surviving chemotherapy. A major challenge in the treatment of patients with leukaemia is the effective targeting of chemoresistant leukaemic cells. I had observed that T-ALL surviving chemotherapy were characteristically more motile in the marrow space (Chapter 4). A question that remained open was whether this observation was specific for T-ALL cells or whether it was a more generalized trait of leukaemias, including leukaemias derived from alternative lineages, such as AML. To address this problem, I resorted to the previously described pre-clinical murine models of MLL-AF9 AML (Chapter 3) and Notch1-driven T-ALL (Chapter 4). The treatment of mice fully infiltrated with AML and T-ALL cells was carried out using the previously established regimens. Mice burdened with AML received three days of co-treatment with Ara-C and Doxo followed by two days of Ara-C alone (Chapter 3). Mice burdened with T-ALL were treated with three daily doses of dexamethasone plus vincristine plus L-asparaginase (Chapter 4). The application of these combination therapies is challenging because of the cumulative toxicity and narrow therapeutic window. Nevertheless, these treatment strategies have the great advantage of mimicking clinically relevant regimens used in patients with AML and T-ALL. A potential pitfall of this approach is the use of different drugs in AML and T-ALL. At the end of the treatment course, I used IVM to time-lapse single surviving leukaemic cells. In contrast to T-ALL, chemoresistant AML cells were less migratory than their treatment-naïve counterparts. This is consistent with the hypothesis that the BM microenvironment is important in the survival of AML cells.

The decreased mobility of chemoresistant AML cells suggests that these cells are more engaged with the surrounding tissue. The CXCR4/CXCL12 axis is one of the mediators of this crosstalk (Lane et al., 2009) and was recently shown to play a role both in AML and in T-ALL survival and propagation. Using AMD3100, a well-established CXCR4 antagonist, I showed that seeding and particularly chemoresistant T-ALL cells are highly dependent on CXCL12 to maintain their constant migration within the BM tissue. On the other hand, AML

cells do not respond to AMD3100, suggesting that additional signals and more complex crosstalk with the microenvironment might compensate for the loss of CXCL12 signals. This hypothesis was corroborated by the analysis of RNA-seq data (Chapter 3 and (Waibel et al., 2017)), which showed enrichment for genes involved in chemokine-driven motility in AML . Altogether this work shows that CXCR4 is key for the residence of both AML and T-ALL in the BM but that only T-ALL, and particularly chemoresistant T-ALL cell migration is effectively halted by CXCR4 inhibition *in vivo.* These results highlight differences between T-ALL and AML. Similarly to the observation that endosteal vessels are lost in AML bot not in T-ALL (Chapter 3), the migratory phenotype and response to CXCR4 antagonism is also leukaemia type-specific. Future studies should detail the specific components of the CXCR4 signalling pathway that are responsible for driving the migration of T-ALL cells. Furthermore, the factors that drive AML cell migration *in vivo* should be further explored.

In summary, in this thesis I aimed to study the interplay of acute leukaemic cells with their native BM microenvironment. To directly visualise this interplay *in vivo*, I studied well-established syngeneic mouse models of AML and T-ALL. A comprehensive imaging approach was applied by combining IVM with bone immunofluorescence. Using IVM, I was able to capture dynamic events (e.g. cell migration) and to analyse with high-resolution cellular events in their 3D natural *in vivo* marrow environment. Immunofluorescence was complementary because it allowed a more complex phenotypic analysis (e.g. the identification of Ki-67$^+$ proliferating cells, TUNEL$^+$ apoptotic cells) and the high-resolution study of stromal cell populations in long bones, which was not possible with IVM of the calvarium. Together, these imaging strategies have the advantage of providing spatial and tissue-context information, which is not assessable through flow cytometry. Nevertheless, flow cytometry was also frequently applied to provide quantitative power to the analyses and to obtain sensitive and extended phenotypic information. This approach allowed me to gain unique insight into previously unknown phenomena and biological behaviour in acute leukaemias, such as failed angiogenesis in central mattow and endosteal vascular remodelling in AML, apoptosis of osteoblasts in T-ALL, niche-independence and increased migration of chemoresistant T-ALL cells and a differential role of CXCR4 activity in T-ALL and AML cell migration.

I believe the data presented in this thesis contribute to the understanding of the physiopathology of T-ALL and AML and should be followed up by translational studies with the ultimate aim of improving the morbidity and mortality of leukaemia patients.

Bibliography

Abarrategi, A., Foster, K., Hamilton, A., Mian, S. A., Passaro, D., Gribben, J., Mufti, G., and Bonnet, D. (2017). Versatile humanized niche model enables study of normal and malignant human hematopoiesis. J Clin Invest *127*, 543-548.

Abraham, M., Klein, S., Bulvik, B., Wald, H., Weiss, I. D., Olam, D., Weiss, L., Beider, K., Eizenberg, O., Wald, O.*, et al.* (2017). The CXCR4 inhibitor BL-8040 induces the apoptosis of AML blasts by downregulating ERK, BCL-2, MCL-1 and cyclin-D1 via altered miR-15a/16-1 expression. Leukemia *31*, 2336-2346.

Acar, M., Kocherlakota, K. S., Murphy, M. M., Peyer, J. G., Oguro, H., Inra, C. N., Jaiyeola, C., Zhao, Z., Luby-Phelps, K., and Morrison, S. J. (2015). Deep imaging of bone marrow shows non-dividing stem cells are mainly perisinusoidal. Nature *526*, 126-130.

Aguayo, A., Kantarjian, H., Manshouri, T., Gidel, C., Estey, E., Thomas, D., Koller, C., Estrov, Z., O'Brien, S., Keating, M.*, et al.* (2000). Angiogenesis in acute and chronic leukemias and myelodysplastic syndromes. Blood *96*, 2240-2245.

Akashi, K., Traver, D., Miyamoto, T., and Weissman, I. L. (2000). A clonogenic common myeloid progenitor that gives rise to all myeloid lineages. Nature *404*, 193-197.

Akinduro, O., Weber, T. S., Ang, H., Haltalli, M. L. R., Ruivo, N., Duarte, D., Rashidi, N. M., Hawkins, E. D., Duffy, K. R., and Lo Celso, C. (2018). Proliferation dynamics of acute myeloid leukaemia and haematopoietic progenitors competing for bone marrow space. Nat Commun *9*, 519.

Al-Hajj, M., Wicha, M. S., Benito-Hernandez, A., Morrison, S. J., and Clarke, M. F. (2003). Prospective identification of tumorigenic breast cancer cells. Proc Natl Acad Sci U S A *100*, 3983-3988.

Antonelli, A., Noort, W. A., Jaques, J., de Boer, B., de Jong-Korlaar, R., Brouwers-Vos, A. Z., Lubbers-Aalders, L., van Velzen, J. F., Bloem, A. C., Yuan, H.*, et al.* (2016). Establishing human leukemia xenograft mouse models by implanting human bone marrow-like scaffold-based niches. Blood *128*, 2949-2959.

Arai, F., Hirao, A., Ohmura, M., Sato, H., Matsuoka, S., Takubo, K., Ito, K., Koh, G. Y., and Suda, T. (2004). Tie2/angiopoietin-1 signaling regulates hematopoietic stem cell quiescence in the bone marrow niche. Cell *118*, 149-161.

Arranz, L., Sanchez-Aguilera, A., Martin-Perez, D., Isern, J., Langa, X., Tzankov, A., Lundberg, P., Muntion, S., Tzeng, Y. S., Lai, D. M.*, et al.* (2014). Neuropathy of haematopoietic stem cell niche is essential for myeloproliferative neoplasms. Nature *512*, 78-81.

Asada, N., Kunisaki, Y., Pierce, H., Wang, Z., Fernandez, N. F., Birbrair, A., Ma'ayan, A., and Frenette, P. S. (2017). Differential cytokine contributions of perivascular haematopoietic stem cell niches. Nat Cell Biol *19*, 214-223.
Aster, J. C., Xu, L., Karnell, F. G., Patriub, V., Pui, J. C., and Pear, W. S. (2000). Essential roles for ankyrin repeat and transactivation domains in induction of T-cell leukemia by notch1. Mol Cell Biol *20*, 7505-7515.
Baryawno, N., Severe, N., and Scadden, D. T. (2017). Hematopoiesis: Reconciling Historic Controversies about the Niche. Cell Stem Cell *20*, 590-592.
Beck, T. C., Gomes, A. C., Cyster, J. G., and Pereira, J. P. (2014). CXCR4 and a cell-extrinsic mechanism control immature B lymphocyte egress from bone marrow. J Exp Med *211*, 2567-2581.
Becker, A. J., Mc, C. E., and Till, J. E. (1963). Cytological demonstration of the clonal nature of spleen colonies derived from transplanted mouse marrow cells. Nature *197*, 452-454.
Becker, K., Jahrling, N., Saghafi, S., and Dodt, H. U. (2013). Immunostaining, dehydration, and clearing of mouse embryos for ultramicroscopy. Cold Spring Harb Protoc *2013*, 743-744.
Beerman, I., Bhattacharya, D., Zandi, S., Sigvardsson, M., Weissman, I. L., Bryder, D., and Rossi, D. J. (2010). Functionally distinct hematopoietic stem cells modulate hematopoietic lineage potential during aging by a mechanism of clonal expansion. Proc Natl Acad Sci U S A *107*, 5465-5470.
Belver, L., and Ferrando, A. (2016). The genetics and mechanisms of T cell acute lymphoblastic leukaemia. Nat Rev Cancer *16*, 494-507.
Bixel, M. G., Kusumbe, A. P., Ramasamy, S. K., Sivaraj, K. K., Butz, S., Vestweber, D., and Adams, R. H. (2017). Flow Dynamics and HSPC Homing in Bone Marrow Microvessels. Cell Rep *18*, 1804-1816.
Bonnet, D., and Dick, J. E. (1997). Human acute myeloid leukemia is organized as a hierarchy that originates from a primitive hematopoietic cell. Nat Med *3*, 730-737.
Borthakur, G., Nagler, A., Ofran, Y., Rowe, J. M., Altman, J. K., Frankfurt, O., Tallman, M. S., Avivi, I., Peled, A., Pereg, Y.*, et al.* (2014). BL-8040, a Peptidic CXCR4 Antagonist, Induces Leukemia Cell Death and Specific Leukemia Cell Mobilization in Relapsed/Refractory Acute Myeloid Leukemia Patients in an Ongoing Phase IIa Clinical Trial. Blood *124*, 950.
Bowers, M., Zhang, B., Ho, Y., Agarwal, P., Chen, C. C., and Bhatia, R. (2015). Osteoblast ablation reduces normal long-term hematopoietic stem cell self-renewal but accelerates leukemia development. Blood *125*, 2678-2688.
Boyd, A. L., Campbell, C. J., Hopkins, C. I., Fiebig-Comyn, A., Russell, J., Ulemek, J., Foley, R., Leber, B., Xenocostas, A., Collins, T. J., and Bhatia, M. (2014). Niche displacement of human leukemic stem cells uniquely allows their competitive replacement with healthy HSPCs. J Exp Med *211*, 1925-1935.
Boyd, A. L., Reid, J. C., Salci, K. R., Aslostovar, L., Benoit, Y. D., Shapovalova, Z., Nakanishi, M., Porras, D. P., Almakadi, M., Campbell, C. J. V.*, et al.* (2017). Acute myeloid leukaemia disrupts endogenous myelo-erythropoiesis by compromising the adipocyte bone marrow niche. Nat Cell Biol *19*, 1336-1347.
Breart, B., Lemaitre, F., Celli, S., and Bousso, P. (2008). Two-photon imaging of intratumoral CD8+ T cell cytotoxic activity during adoptive T cell therapy in mice. J Clin Invest *118*, 1390-1397.
Broome, J. D. (1963). Evidence that the L-asparaginase of guinea pig serum is responsible for its antilymphoma effects. I. Properties of the L-asparaginase of guinea pig serum in relation to those of the antilymphoma substance. J Exp Med *118*, 99-120.

Broome, J. D. (1981). L-Asparaginase: discovery and development as a tumor-inhibitory agent. Cancer Treat Rep *65 Suppl 4*, 111-114.
Brown, S., and Greco, V. (2014). Stem cells in the wild: understanding the World of stem cells through intravital imaging. Cell Stem Cell *15*, 683-686.
Brunetti, L., Gundry, M. C., and Goodell, M. A. (2017). DNMT3A in Leukemia. Cold Spring Harb Perspect Med *7*.
Bruns, I., Lucas, D., Pinho, S., Ahmed, J., Lambert, M. P., Kunisaki, Y., Scheiermann, C., Schiff, L., Poncz, M., Bergman, A., and Frenette, P. S. (2014). Megakaryocytes regulate hematopoietic stem cell quiescence through CXCL4 secretion. Nat Med *20*, 1315-1320.
Bryder, D., Rossi, D. J., and Weissman, I. L. (2006). Hematopoietic stem cells: the paradigmatic tissue-specific stem cell. Am J Pathol *169*, 338-346.
Butcher, E. C., and Picker, L. J. (1996). Lymphocyte homing and homeostasis. Science *272*, 60-66.
Butler, J. M., Nolan, D. J., Vertes, E. L., Varnum-Finney, B., Kobayashi, H., Hooper, A. T., Seandel, M., Shido, K., White, I. A., Kobayashi, M.*, et al.* (2010). Endothelial cells are essential for the self-renewal and repopulation of Notch-dependent hematopoietic stem cells. Cell Stem Cell *6*, 251-264.
Cajal, S. R. (1911). Histologie du syste me nerveux de l'Homme et des verte be s. Maloine (Paris) *2*, 891-942.
Callens, C., Coulon, S., Naudin, J., Radford-Weiss, I., Boissel, N., Raffoux, E., Wang, P. H., Agarwal, S., Tamouza, H., Paubelle, E.*, et al.* (2010). Targeting iron homeostasis induces cellular differentiation and synergizes with differentiating agents in acute myeloid leukemia. J Exp Med *207*, 731-750.
Calvi, L. M., Adams, G. B., Weibrecht, K. W., Weber, J. M., Olson, D. P., Knight, M. C., Martin, R. P., Schipani, E., Divieti, P., Bringhurst, F. R.*, et al.* (2003). Osteoblastic cells regulate the haematopoietic stem cell niche. Nature *425*, 841-846.
Calvi, L. M., Sims, N. A., Hunzelman, J. L., Knight, M. C., Giovannetti, A., Saxton, J. M., Kronenberg, H. M., Baron, R., and Schipani, E. (2001). Activated parathyroid hormone/parathyroid hormone-related protein receptor in osteoblastic cells differentially affects cortical and trabecular bone. J Clin Invest *107*, 277-286.
Cao, Y., Chen, C., Weatherbee, J. A., Tsang, M., and Folkman, J. (1995). gro-beta, a -C-X-C- chemokine, is an angiogenesis inhibitor that suppresses the growth of Lewis lung carcinoma in mice. J Exp Med *182*, 2069-2077.
Cariappa, A., Mazo, I. B., Chase, C., Shi, H. N., Liu, H., Li, Q., Rose, H., Leung, H., Cherayil, B. J., Russell, P.*, et al.* (2005). Perisinusoidal B cells in the bone marrow participate in T-independent responses to blood-borne microbes. Immunity *23*, 397-407.
Carron, C., Cormier, F., Janin, A., Lacronique, V., Giovannini, M., Daniel, M. T., Bernard, O., and Ghysdael, J. (2000). TEL-JAK2 transgenic mice develop T-cell leukemia. Blood *95*, 3891-3899.
Cavanagh, L. L., Bonasio, R., Mazo, I. B., Halin, C., Cheng, G., van der Velden, A. W., Cariappa, A., Chase, C., Russell, P., Starnbach, M. N.*, et al.* (2005). Activation of bone marrow-resident memory T cells by circulating, antigen-bearing dendritic cells. Nat Immunol *6*, 1029-1037.
Challen, G. A., Sun, D., Jeong, M., Luo, M., Jelinek, J., Berg, J. S., Bock, C., Vasanthakumar, A., Gu, H., Xi, Y.*, et al.* (2011). Dnmt3a is essential for hematopoietic stem cell differentiation. Nat Genet *44*, 23-31.
Chen, J., Jette, C., Kanki, J. P., Aster, J. C., Look, A. T., and Griffin, J. D. (2007). NOTCH1-induced T-cell leukemia in transgenic zebrafish. Leukemia *21*, 462-471.

Chen, J., Larochelle, A., Fricker, S., Bridger, G., Dunbar, C. E., and Abkowitz, J. L. (2006). Mobilization as a preparative regimen for hematopoietic stem cell transplantation. Blood *107*, 3764-3771.
Chen, J. Y., Miyanishi, M., Wang, S. K., Yamazaki, S., Sinha, R., Kao, K. S., Seita, J., Sahoo, D., Nakauchi, H., and Weissman, I. L. (2016a). Hoxb5 marks long-term haematopoietic stem cells and reveals a homogenous perivascular niche. Nature *530*, 223-227.
Chen, W., Kumar, A. R., Hudson, W. A., Li, Q., Wu, B., Staggs, R. A., Lund, E. A., Sam, T. N., and Kersey, J. H. (2008). Malignant transformation initiated by Mll-AF9: gene dosage and critical target cells. Cancer Cell *13*, 432-440.
Chen, Y., Maeda, A., Bu, J., and DaCosta, R. (2016b). Femur Window Chamber Model for In Vivo Cell Tracking in the Murine Bone Marrow. J Vis Exp.
Cheng, H., Hao, S., Liu, Y., Pang, Y., Ma, S., Dong, F., Xu, J., Zheng, G., Li, S., Yuan, W., and Cheng, T. (2015). Leukemic marrow infiltration reveals a novel role for Egr3 as a potent inhibitor of normal hematopoietic stem cell proliferation. Blood *126*, 1302-1313.
Chiu, P. P., Jiang, H., and Dick, J. E. (2010). Leukemia-initiating cells in human T-lymphoblastic leukemia exhibit glucocorticoid resistance. Blood *116*, 5268-5279.
Chono, H., Yoshioka, H., Ueno, M., and Kato, I. (2001). Removal of inhibitory substances with recombinant fibronectin-CH-296 plates enhances the retroviral transduction efficiency of CD34(+)CD38(-) bone marrow cells. J Biochem *130*, 331-334.
Chung, K., Wallace, J., Kim, S. Y., Kalyanasundaram, S., Andalman, A. S., Davidson, T. J., Mirzabekov, J. J., Zalocusky, K. A., Mattis, J., Denisin, A. K., *et al.* (2013). Structural and molecular interrogation of intact biological systems. Nature *497*, 332-337.
Clarke, M. F., Dick, J. E., Dirks, P. B., Eaves, C. J., Jamieson, C. H., Jones, D. L., Visvader, J., Weissman, I. L., and Wahl, G. M. (2006). Cancer stem cells--perspectives on current status and future directions: AACR Workshop on cancer stem cells. Cancer Res *66*, 9339-9344.
Colmone, A., Amorim, M., Pontier, A. L., Wang, S., Jablonski, E., and Sipkins, D. A. (2008). Leukemic cells create bone marrow niches that disrupt the behavior of normal hematopoietic progenitor cells. Science *322*, 1861-1865.
Condeelis, J., and Segall, J. E. (2003). Intravital imaging of cell movement in tumours. Nat Rev Cancer *3*, 921-930.
Coutu, D. L., Kokkaliaris, K. D., Kunz, L., and Schroeder, T. (2018). Multicolor quantitative confocal imaging cytometry. Nat Methods *15*, 39-46.
Cozzio, A., Passegue, E., Ayton, P. M., Karsunky, H., Cleary, M. L., and Weissman, I. L. (2003). Similar MLL-associated leukemias arising from self-renewing stem cells and short-lived myeloid progenitors. Genes Dev *17*, 3029-3035.
Das, R., Strowig, T., Verma, R., Koduru, S., Hafemann, A., Hopf, S., Kocoglu, M. H., Borsotti, C., Zhang, L., Branagan, A., *et al.* (2016). Microenvironment-dependent growth of preneoplastic and malignant plasma cells in humanized mice. Nat Med *22*, 1351-1357.
DeGregori, J. (2017). Connecting Cancer to Its Causes Requires Incorporation of Effects on Tissue Microenvironments. Cancer Res *77*, 6065-6068.
Denk, W., Strickler, J. H., and Webb, W. W. (1990). Two-photon laser scanning fluorescence microscopy. Science *248*, 73-76.
Dexter, T. M., Allen, T. D., and Lajtha, L. G. (1977). Conditions controlling the proliferation of haemopoietic stem cells in vitro. J Cell Physiol *91*, 335-344.
Dick, J. E. (2008). Stem cell concepts renew cancer research. Blood *112*, 4793-4807.
Dick, J. E., Magli, M. C., Huszar, D., Phillips, R. A., and Bernstein, A. (1985). Introduction of a selectable gene into primitive stem cells capable of long-term reconstitution of the hemopoietic system of W/Wv mice. Cell *42*, 71-79.

Ding, L., Ley, T. J., Larson, D. E., Miller, C. A., Koboldt, D. C., Welch, J. S., Ritchey, J. K., Young, M. A., Lamprecht, T., McLellan, M. D*., et al.* (2012a). Clonal evolution in relapsed acute myeloid leukaemia revealed by whole-genome sequencing. Nature *481*, 506-510.
Ding, L., and Morrison, S. J. (2013). Haematopoietic stem cells and early lymphoid progenitors occupy distinct bone marrow niches. Nature *495*, 231-235.
Ding, L., Saunders, T. L., Enikolopov, G., and Morrison, S. J. (2012b). Endothelial and perivascular cells maintain haematopoietic stem cells. Nature *481*, 457-462.
Dohner, H., Estey, E. H., Amadori, S., Appelbaum, F. R., Buchner, T., Burnett, A. K., Dombret, H., Fenaux, P., Grimwade, D., Larson, R. A*., et al.* (2010). Diagnosis and management of acute myeloid leukemia in adults: recommendations from an international expert panel, on behalf of the European LeukemiaNet. Blood *115*, 453-474.
Dohner, H., Weisdorf, D. J., and Bloomfield, C. D. (2015). Acute Myeloid Leukemia. N Engl J Med *373*, 1136-1152.
Doitsidou, M., Reichman-Fried, M., Stebler, J., Koprunner, M., Dorries, J., Meyer, D., Esguerra, C. V., Leung, T., and Raz, E. (2002). Guidance of primordial germ cell migration by the chemokine SDF-1. Cell *111*, 647-659.
Dong, L., Yu, W. M., Zheng, H., Loh, M. L., Bunting, S. T., Pauly, M., Huang, G., Zhou, M., Broxmeyer, H. E., Scadden, D. T., and Qu, C. K. (2016). Leukaemogenic effects of Ptpn11 activating mutations in the stem cell microenvironment. Nature *539*, 304-308.
Doulatov, S., Notta, F., Laurenti, E., and Dick, J. E. (2012). Hematopoiesis: a human perspective. Cell Stem Cell *10*, 120-136.
Duan, C. W., Shi, J., Chen, J., Wang, B., Yu, Y. H., Qin, X., Zhou, X. C., Cai, Y. J., Li, Z. Q., Zhang, F*., et al.* (2014). Leukemia propagating cells rebuild an evolving niche in response to therapy. Cancer Cell *25*, 778-793.
Duarte, D., Hawkins, E. D., Akinduro, O., Ang, H., De Filippo, K., Kong, I. Y., Haltalli, M., Ruivo, N., Straszkowski, L., Vervoort, S. J*., et al.* (2018a). Inhibition of Endosteal Vascular Niche Remodeling Rescues Hematopoietic Stem Cell Loss in AML. Cell Stem Cell *22*, 64-77 e66.
Duarte, D., Hawkins, E. D., and Lo Celso, C. (2018b). The interplay of leukemia cells and the bone marrow microenvironment. Blood.
Dunne, J., Gascoyne, D. M., Lister, T. A., Brady, H. J., Heidenreich, O., and Young, B. D. (2010). AML1/ETO proteins control POU4F1/BRN3A expression and function in t(8;21) acute myeloid leukemia. Cancer Res *70*, 3985-3995.
Ellenbroek, S. I., and van Rheenen, J. (2014). Imaging hallmarks of cancer in living mice. Nat Rev Cancer *14*, 406-418.
Ellis, S. L., Grassinger, J., Jones, A., Borg, J., Camenisch, T., Haylock, D., Bertoncello, I., and Nilsson, S. K. (2011). The relationship between bone, hemopoietic stem cells, and vasculature. Blood *118*, 1516-1524.
Erturk, A., Becker, K., Jahrling, N., Mauch, C. P., Hojer, C. D., Egen, J. G., Hellal, F., Bradke, F., Sheng, M., and Dodt, H. U. (2012). Three-dimensional imaging of solvent-cleared organs using 3DISCO. Nat Protoc *7*, 1983-1995.
Farber, S., and Diamond, L. K. (1948). Temporary remissions in acute leukemia in children produced by folic acid antagonist, 4-aminopteroyl-glutamic acid. N Engl J Med *238*, 787-793.
Fiedler, W., Graeven, U., Ergun, S., Verago, S., Kilic, N., Stockschlader, M., and Hossfeld, D. K. (1997). Vascular endothelial growth factor, a possible paracrine growth factor in human acute myeloid leukemia. Blood *89*, 1870-1875.

Fiedler, W., Mesters, R., Tinnefeld, H., Loges, S., Staib, P., Duhrsen, U., Flasshove, M., Ottmann, O. G., Jung, W., Cavalli, F.*, et al.* (2003). A phase 2 clinical study of SU5416 in patients with refractory acute myeloid leukemia. Blood *102*, 2763-2767.
Fielding, A. K., Richards, S. M., Chopra, R., Lazarus, H. M., Litzow, M. R., Buck, G., Durrant, I. J., Luger, S. M., Marks, D. I., Franklin, I. M.*, et al.* (2007). Outcome of 609 adults after relapse of acute lymphoblastic leukemia (ALL); an MRC UKALL12/ECOG 2993 study. Blood *109*, 944-950.
Flex, E., Petrangeli, V., Stella, L., Chiaretti, S., Hornakova, T., Knoops, L., Ariola, C., Fodale, V., Clappier, E., Paoloni, F.*, et al.* (2008). Somatically acquired JAK1 mutations in adult acute lymphoblastic leukemia. J Exp Med *205*, 751-758.
Foster, K., Lassailly, F., Anjos-Afonso, F., Currie, E., Rouault-Pierre, K., and Bonnet, D. (2015). Different Motile Behaviors of Human Hematopoietic Stem versus Progenitor Cells at the Osteoblastic Niche. Stem Cell Reports *5*, 690-701.
Fujisaki, J., Wu, J., Carlson, A. L., Silberstein, L., Putheti, P., Larocca, R., Gao, W., Saito, T. I., Lo Celso, C., Tsuyuzaki, H.*, et al.* (2011). In vivo imaging of Treg cells providing immune privilege to the haematopoietic stem-cell niche. Nature *474*, 216-219.
Fukuda, S., Bian, H., King, A. G., and Pelus, L. M. (2007). The chemokine GRObeta mobilizes early hematopoietic stem cells characterized by enhanced homing and engraftment. Blood *110*, 860-869.
Gazit, R., Mandal, P. K., Ebina, W., Ben-Zvi, A., Nombela-Arrieta, C., Silberstein, L. E., and Rossi, D. J. (2014). Fgd5 identifies hematopoietic stem cells in the murine bone marrow. J Exp Med *211*, 1315-1331.
Genovese, G., Kahler, A. K., Handsaker, R. E., Lindberg, J., Rose, S. A., Bakhoum, S. F., Chambert, K., Mick, E., Neale, B. M., Fromer, M.*, et al.* (2014). Clonal hematopoiesis and blood-cancer risk inferred from blood DNA sequence. N Engl J Med *371*, 2477-2487.
Gerhardt, H., Golding, M., Fruttiger, M., Ruhrberg, C., Lundkvist, A., Abramsson, A., Jeltsch, M., Mitchell, C., Alitalo, K., Shima, D., and Betsholtz, C. (2003). VEGF guides angiogenic sprouting utilizing endothelial tip cell filopodia. J Cell Biol *161*, 1163-1177.
Globus, R. K., Doty, S. B., Lull, J. C., Holmuhamedov, E., Humphries, M. J., and Damsky, C. H. (1998). Fibronectin is a survival factor for differentiated osteoblasts. J Cell Sci *111 (Pt 10)*, 1385-1393.
Goncalves, K. A., Silberstein, L., Li, S., Severe, N., Hu, M. G., Yang, H., Scadden, D. T., and Hu, G. F. (2016). Angiogenin Promotes Hematopoietic Regeneration by Dichotomously Regulating Quiescence of Stem and Progenitor Cells. Cell *166*, 894-906.
Greenbaum, A., Hsu, Y. M., Day, R. B., Schuettpelz, L. G., Christopher, M. J., Borgerding, J. N., Nagasawa, T., and Link, D. C. (2013). CXCL12 in early mesenchymal progenitors is required for haematopoietic stem-cell maintenance. Nature *495*, 227-230.
Grove, C. S., and Vassiliou, G. S. (2014). Acute myeloid leukaemia: a paradigm for the clonal evolution of cancer? Dis Model Mech *7*, 941-951.
Guezguez, B., Campbell, C. J., Boyd, A. L., Karanu, F., Casado, F. L., Di Cresce, C., Collins, T. J., Shapovalova, Z., Xenocostas, A., and Bhatia, M. (2013). Regional localization within the bone marrow influences the functional capacity of human HSCs. Cell Stem Cell *13*, 175-189.
Halin, C., Mora, J. R., Sumen, C., and von Andrian, U. H. (2005). In vivo imaging of lymphocyte trafficking. Annu Rev Cell Dev Biol *21*, 581-603.
Hanahan, D., and Weinberg, R. A. (2011). Hallmarks of cancer: the next generation. Cell *144*, 646-674.
Hannon, G. J., Sun, P., Carnero, A., Xie, L. Y., Maestro, R., Conklin, D. S., and Beach, D. (1999). MaRX: an approach to genetics in mammalian cells. Science *283*, 1129-1130.

Hanoun, M., Zhang, D., Mizoguchi, T., Pinho, S., Pierce, H., Kunisaki, Y., Lacombe, J., Armstrong, S. A., Duhrsen, U., and Frenette, P. S. (2014). Acute myelogenous leukemia-induced sympathetic neuropathy promotes malignancy in an altered hematopoietic stem cell niche. Cell Stem Cell *15*, 365-375.
Harnett, M. M. (2007). Laser scanning cytometry: understanding the immune system in situ. Nat Rev Immunol *7*, 897-904.
Harrison, D. E. (1980). Competitive repopulation: a new assay for long-term stem cell functional capacity. Blood *55*, 77-81.
Hawkins, E. D., Duarte, D., Akinduro, O., Khorshed, R. A., Passaro, D., Nowicka, M., Straszkowski, L., Scott, M. K., Rothery, S., Ruivo, N.*, et al.* (2016). T-cell acute leukaemia exhibits dynamic interactions with bone marrow microenvironments. Nature *538*, 518-522.
Hawkins, E. D., Hommel, M., Turner, M. L., Battye, F. L., Markham, J. F., and Hodgkin, P. D. (2007). Measuring lymphocyte proliferation, survival and differentiation using CFSE time-series data. Nat Protoc *2*, 2057-2067.
Headley, M. B., Bins, A., Nip, A., Roberts, E. W., Looney, M. R., Gerard, A., and Krummel, M. F. (2016). Visualization of immediate immune responses to pioneer metastatic cells in the lung. Nature *531*, 513-517.
Helmchen, F., and Denk, W. (2005). Deep tissue two-photon microscopy. Nat Methods *2*, 932-940.
Herault, A., Binnewies, M., Leong, S., Calero-Nieto, F. J., Zhang, S. Y., Kang, Y. A., Wang, X., Pietras, E. M., Chu, S. H., Barry-Holson, K.*, et al.* (2017). Myeloid progenitor cluster formation drives emergency and leukaemic myelopoiesis. Nature *544*, 53-58.
Hills, D., Gribi, R., Ure, J., Buza-Vidas, N., Luc, S., Jacobsen, S. E., and Medvinsky, A. (2011). Hoxb4-YFP reporter mouse model: a novel tool for tracking HSC development and studying the role of Hoxb4 in hematopoiesis. Blood *117*, 3521-3528.
Hills, R. K., Castaigne, S., Appelbaum, F. R., Delaunay, J., Petersdorf, S., Othus, M., Estey, E. H., Dombret, H., Chevret, S., Ifrah, N.*, et al.* (2014). Addition of gemtuzumab ozogamicin to induction chemotherapy in adult patients with acute myeloid leukaemia: a meta-analysis of individual patient data from randomised controlled trials. Lancet Oncol *15*, 986-996.
Himburg, H. A., Harris, J. R., Ito, T., Daher, P., Russell, J. L., Quarmyne, M., Doan, P. L., Helms, K., Nakamura, M., Fixsen, E.*, et al.* (2012). Pleiotrophin regulates the retention and self-renewal of hematopoietic stem cells in the bone marrow vascular niche. Cell Rep *2*, 964-975.
Himburg, H. A., Muramoto, G. G., Daher, P., Meadows, S. K., Russell, J. L., Doan, P., Chi, J. T., Salter, A. B., Lento, W. E., Reya, T.*, et al.* (2010). Pleiotrophin regulates the expansion and regeneration of hematopoietic stem cells. Nat Med *16*, 475-482.
Hock, J. M., Krishnan, V., Onyia, J. E., Bidwell, J. P., Milas, J., and Stanislaus, D. (2001). Osteoblast apoptosis and bone turnover. J Bone Miner Res *16*, 975-984.
Hoffbrand, A., Catovsky , D., Tuddenham, E., and Green, A. (2010). Postgraduate Haematology, 6th Edition: Wiley-Blackwell).
Hooper, A. T., Butler, J. M., Nolan, D. J., Kranz, A., Iida, K., Kobayashi, M., Kopp, H. G., Shido, K., Petit, I., Yanger, K.*, et al.* (2009). Engraftment and reconstitution of hematopoiesis is dependent on VEGFR2-mediated regeneration of sinusoidal endothelial cells. Cell Stem Cell *4*, 263-274.
Hunger, S. P., and Mullighan, C. G. (2015). Acute Lymphoblastic Leukemia in Children. N Engl J Med *373*, 1541-1552.

Huntly, B. J., Shigematsu, H., Deguchi, K., Lee, B. H., Mizuno, S., Duclos, N., Rowan, R., Amaral, S., Curley, D., Williams, I. R.*, et al.* (2004). MOZ-TIF2, but not BCR-ABL, confers properties of leukemic stem cells to committed murine hematopoietic progenitors. Cancer Cell *6*, 587-596.
Hussong, J. W., Rodgers, G. M., and Shami, P. J. (2000). Evidence of increased angiogenesis in patients with acute myeloid leukemia. Blood *95*, 309-313.
Inra, C. N., Zhou, B. O., Acar, M., Murphy, M. M., Richardson, J., Zhao, Z., and Morrison, S. J. (2015). A perisinusoidal niche for extramedullary haematopoiesis in the spleen. Nature *527*, 466-471.
Ishikawa, F., Yoshida, S., Saito, Y., Hijikata, A., Kitamura, H., Tanaka, S., Nakamura, R., Tanaka, T., Tomiyama, H., Saito, N.*, et al.* (2007). Chemotherapy-resistant human AML stem cells home to and engraft within the bone-marrow endosteal region. Nat Biotechnol *25*, 1315-1321.
Itkin, T., Gur-Cohen, S., Spencer, J. A., Schajnovitz, A., Ramasamy, S. K., Kusumbe, A. P., Ledergor, G., Jung, Y., Milo, I., Poulos, M. G.*, et al.* (2016). Distinct bone marrow blood vessels differentially regulate haematopoiesis. Nature *532*, 323-328.
Ito, K., Turcotte, R., Cui, J., Zimmerman, S. E., Pinho, S., Mizoguchi, T., Arai, F., Runnels, J. M., Alt, C., Teruya-Feldstein, J.*, et al.* (2016). Self-renewal of a purified Tie2+ hematopoietic stem cell population relies on mitochondrial clearance. Science *354*, 1156-1160.
Jacamo, R., Chen, Y., Wang, Z., Ma, W., Zhang, M., Spaeth, E. L., Wang, Y., Battula, V. L., Mak, P. Y., Schallmoser, K.*, et al.* (2014). Reciprocal leukemia-stroma VCAM-1/VLA-4-dependent activation of NF-kappaB mediates chemoresistance. Blood *123*, 2691-2702.
Jaiswal, S., Fontanillas, P., Flannick, J., Manning, A., Grauman, P. V., Mar, B. G., Lindsley, R. C., Mermel, C. H., Burtt, N., Chavez, A.*, et al.* (2014). Age-related clonal hematopoiesis associated with adverse outcomes. N Engl J Med *371*, 2488-2498.
Jakobsson, L., Franco, C. A., Bentley, K., Collins, R. T., Ponsioen, B., Aspalter, I. M., Rosewell, I., Busse, M., Thurston, G., Medvinsky, A.*, et al.* (2010). Endothelial cells dynamically compete for the tip cell position during angiogenic sprouting. Nat Cell Biol *12*, 943-953.
Jeong, E. G., Kim, M. S., Nam, H. K., Min, C. K., Lee, S., Chung, Y. J., Yoo, N. J., and Lee, S. H. (2008). Somatic mutations of JAK1 and JAK3 in acute leukemias and solid cancers. Clin Cancer Res *14*, 3716-3721.
Jilka, R. L., Weinstein, R. S., Bellido, T., Parfitt, A. M., and Manolagas, S. C. (1998). Osteoblast programmed cell death (apoptosis): modulation by growth factors and cytokines. J Bone Miner Res *13*, 793-802.
Jin, L., Hope, K. J., Zhai, Q., Smadja-Joffe, F., and Dick, J. E. (2006). Targeting of CD44 eradicates human acute myeloid leukemic stem cells. Nat Med *12*, 1167-1174.
Joseph, C., Quach, J. M., Walkley, C. R., Lane, S. W., Lo Celso, C., and Purton, L. E. (2013). Deciphering hematopoietic stem cells in their niches: a critical appraisal of genetic models, lineage tracing, and imaging strategies. Cell Stem Cell *13*, 520-533.
Junt, T., Schulze, H., Chen, Z., Massberg, S., Goerge, T., Krueger, A., Wagner, D. D., Graf, T., Italiano, J. E., Jr., Shivdasani, R. A., and von Andrian, U. H. (2007). Dynamic visualization of thrombopoiesis within bone marrow. Science *317*, 1767-1770.
Kammertoens, T., Friese, C., Arina, A., Idel, C., Briesemeister, D., Rothe, M., Ivanov, A., Szymborska, A., Patone, G., Kunz, S.*, et al.* (2017). Tumour ischaemia by interferon-gamma resembles physiological blood vessel regression. Nature *545*, 98-102.

Katsumura, K. R., Ong, I. M., DeVilbiss, A. W., Sanalkumar, R., and Bresnick, E. H. (2016). GATA Factor-Dependent Positive-Feedback Circuit in Acute Myeloid Leukemia Cells. Cell Rep *16*, 2428-2441.
Keller, G., Paige, C., Gilboa, E., and Wagner, E. F. (1985). Expression of a foreign gene in myeloid and lymphoid cells derived from multipotent haematopoietic precursors. Nature *318*, 149-154.
Kelly, P. N., Dakic, A., Adams, J. M., Nutt, S. L., and Strasser, A. (2007). Tumor growth need not be driven by rare cancer stem cells. Science *317*, 337.
Khorshed, R. A., Hawkins, E. D., Duarte, D., Scott, M. K., Akinduro, O. A., Rashidi, N. M., Spitaler, M., and Lo Celso, C. (2015). Automated Identification and Localization of Hematopoietic Stem Cells in 3D Intravital Microscopy Data. Stem Cell Reports *5*, 139-153.
Kiel, M. J., Acar, M., Radice, G. L., and Morrison, S. J. (2009). Hematopoietic stem cells do not depend on N-cadherin to regulate their maintenance. Cell Stem Cell *4*, 170-179.
Kiel, M. J., Yilmaz, O. H., Iwashita, T., Yilmaz, O. H., Terhorst, C., and Morrison, S. J. (2005). SLAM family receptors distinguish hematopoietic stem and progenitor cells and reveal endothelial niches for stem cells. Cell *121*, 1109-1121.
Kim, J. A., Shim, J. S., Lee, G. Y., Yim, H. W., Kim, T. M., Kim, M., Leem, S. H., Lee, J. W., Min, C. K., and Oh, I. H. (2015). Microenvironmental remodeling as a parameter and prognostic factor of heterogeneous leukemogenesis in acute myelogenous leukemia. Cancer Res *75*, 2222-2231.
Kim, S., Lin, L., Brown, G. A., Hosaka, K., and Scott, E. W. (2016). Extended time-lapse in vivo imaging of tibia bone marrow to visualize dynamic hematopoietic stem cell engraftment. Leukemia.
Kim, Y. W., Koo, B. K., Jeong, H. W., Yoon, M. J., Song, R., Shin, J., Jeong, D. C., Kim, S. H., and Kong, Y. Y. (2008). Defective Notch activation in microenvironment leads to myeloproliferative disease. Blood *112*, 4628-4638.
Kimble, R. B., Bain, S., and Pacifici, R. (1997). The functional block of TNF but not of IL-6 prevents bone loss in ovariectomized mice. J Bone Miner Res *12*, 935-941.
Kirstetter, P., Anderson, K., Porse, B. T., Jacobsen, S. E., and Nerlov, C. (2006). Activation of the canonical Wnt pathway leads to loss of hematopoietic stem cell repopulation and multilineage differentiation block. Nat Immunol *7*, 1048-1056.
Kitajima, I., Soejima, Y., Takasaki, I., Beppu, H., Tokioka, T., and Maruyama, I. (1996). Ceramide-induced nuclear translocation of NF-kappa B is a potential mediator of the apoptotic response to TNF-alpha in murine clonal osteoblasts. Bone *19*, 263-270.
Kobayashi, H., Butler, J. M., O'Donnell, R., Kobayashi, M., Ding, B. S., Bonner, B., Chiu, V. K., Nolan, D. J., Shido, K., Benjamin, L., and Rafii, S. (2010). Angiocrine factors from Akt-activated endothelial cells balance self-renewal and differentiation of haematopoietic stem cells. Nat Cell Biol *12*, 1046-1056.
Kode, A., Manavalan, J. S., Mosialou, I., Bhagat, G., Rathinam, C. V., Luo, N., Khiabanian, H., Lee, A., Murty, V. V., Friedman, R.*, et al.* (2014). Leukaemogenesis induced by an activating beta-catenin mutation in osteoblasts. Nature *506*, 240-244.
Kohler, A., Schmithorst, V., Filippi, M. D., Ryan, M. A., Daria, D., Gunzer, M., and Geiger, H. (2009). Altered cellular dynamics and endosteal location of aged early hematopoietic progenitor cells revealed by time-lapse intravital imaging in long bones. Blood *114*, 290-298.
Kollet, O., Dar, A., Shivtiel, S., Kalinkovich, A., Lapid, K., Sztainberg, Y., Tesio, M., Samstein, R. M., Goichberg, P., Spiegel, A.*, et al.* (2006). Osteoclasts degrade endosteal components and promote mobilization of hematopoietic progenitor cells. Nat Med *12*, 657-664.

Kondo, M., Wagers, A. J., Manz, M. G., Prohaska, S. S., Scherer, D. C., Beilhack, G. F., Shizuru, J. A., and Weissman, I. L. (2003). Biology of hematopoietic stem cells and progenitors: implications for clinical application. Annu Rev Immunol *21*, 759-806.
Kondo, M., Weissman, I. L., and Akashi, K. (1997). Identification of clonogenic common lymphoid progenitors in mouse bone marrow. Cell *91*, 661-672.
Kothari, A., Hittelman, W. N., and Chambers, T. C. (2016). Cell Cycle-Dependent Mechanisms Underlie Vincristine-Induced Death of Primary Acute Lymphoblastic Leukemia Cells. Cancer Res *76*, 3553-3561.
Krause, D. S., Fulzele, K., Catic, A., Sun, C. C., Dombkowski, D., Hurley, M. P., Lezeau, S., Attar, E., Wu, J. Y., Lin, H. Y.*, et al.* (2013). Differential regulation of myeloid leukemias by the bone marrow microenvironment. Nat Med *19*, 1513-1517.
Krause, D. S., Lazarides, K., von Andrian, U. H., and Van Etten, R. A. (2006). Requirement for CD44 in homing and engraftment of BCR-ABL-expressing leukemic stem cells. Nat Med *12*, 1175-1180.
Krevvata, M., Silva, B. C., Manavalan, J. S., Galan-Diez, M., Kode, A., Matthews, B. G., Park, D., Zhang, C. A., Galili, N., Nickolas, T. L.*, et al.* (2014). Inhibition of leukemia cell engraftment and disease progression in mice by osteoblasts. Blood *124*, 2834-2846.
Krivtsov, A. V., and Armstrong, S. A. (2007). MLL translocations, histone modifications and leukaemia stem-cell development. Nat Rev Cancer *7*, 823-833.
Krivtsov, A. V., Figueroa, M. E., Sinha, A. U., Stubbs, M. C., Feng, Z., Valk, P. J., Delwel, R., Dohner, K., Bullinger, L., Kung, A. L.*, et al.* (2013). Cell of origin determines clinically relevant subtypes of MLL-rearranged AML. Leukemia *27*, 852-860.
Krivtsov, A. V., Twomey, D., Feng, Z., Stubbs, M. C., Wang, Y., Faber, J., Levine, J. E., Wang, J., Hahn, W. C., Gilliland, D. G.*, et al.* (2006). Transformation from committed progenitor to leukaemia stem cell initiated by MLL-AF9. Nature *442*, 818-822.
Kuittinen, O., Savolainen, E. R., Koistinen, P., Mottonen, M., and Turpeenniemi-Hujanen, T. (2001). MMP-2 and MMP-9 expression in adult and childhood acute lymphatic leukemia (ALL). Leuk Res *25*, 125-131.
Kumar, B., Garcia, M., Weng, L., Jung, X., Murakami, J. L., Hu, X., McDonald, T., Lin, A., Kumar, A. R., DiGiusto, D. L.*, et al.* (2017). Acute myeloid leukemia transforms the bone marrow niche into a leukemia-permissive microenvironment through exosome secretion. Leukemia.
Kunisaki, Y., Bruns, I., Scheiermann, C., Ahmed, J., Pinho, S., Zhang, D., Mizoguchi, T., Wei, Q., Lucas, D., Ito, K.*, et al.* (2013). Arteriolar niches maintain haematopoietic stem cell quiescence. Nature *502*, 637-643.
Kusumbe, A. P., Ramasamy, S. K., and Adams, R. H. (2014). Coupling of angiogenesis and osteogenesis by a specific vessel subtype in bone. Nature *507*, 323-328.
Kusumbe, A. P., Ramasamy, S. K., Itkin, T., Mae, M. A., Langen, U. H., Betsholtz, C., Lapidot, T., and Adams, R. H. (2016). Age-dependent modulation of vascular niches for haematopoietic stem cells. Nature *532*, 380-384.
Lacronique, V., Boureux, A., Monni, R., Dumon, S., Mauchauffe, M., Mayeux, P., Gouilleux, F., Berger, R., Gisselbrecht, S., Ghysdael, J., and Bernard, O. A. (2000). Transforming properties of chimeric TEL-JAK proteins in Ba/F3 cells. Blood *95*, 2076-2083.
Lacronique, V., Boureux, A., Valle, V. D., Poirel, H., Quang, C. T., Mauchauffe, M., Berthou, C., Lessard, M., Berger, R., Ghysdael, J., and Bernard, O. A. (1997). A TEL-JAK2 fusion protein with constitutive kinase activity in human leukemia. Science *278*, 1309-1312.
Lajtha, L. G., and Schofield, R. (1971). Regulation of stem cell renewal and differentiation: possible significance in aging. Adv Gerontol Res *3*, 131-146.

Lane, S. W., Scadden, D. T., and Gilliland, D. G. (2009). The leukemic stem cell niche: current concepts and therapeutic opportunities. Blood *114*, 1150-1157.
Lapidot, T., Dar, A., and Kollet, O. (2005). How do stem cells find their way home? Blood *106*, 1901-1910.
Lapidot, T., Sirard, C., Vormoor, J., Murdoch, B., Hoang, T., Caceres-Cortes, J., Minden, M., Paterson, B., Caligiuri, M. A., and Dick, J. E. (1994). A cell initiating human acute myeloid leukaemia after transplantation into SCID mice. Nature *367*, 645-648.
Lassailly, F., Foster, K., Lopez-Onieva, L., Currie, E., and Bonnet, D. (2013). Multimodal imaging reveals structural and functional heterogeneity in different bone marrow compartments: functional implications on hematopoietic stem cells. Blood *122*, 1730-1740.
Law, C. W., Chen, Y., Shi, W., and Smyth, G. K. (2014). voom: Precision weights unlock linear model analysis tools for RNA-seq read counts. Genome Biol *15*, R29.
Leewenhoeck, A. v. 1677 Observation, communicated to the publisher by Mr. Antony van Leewenhoeck, in a Dutch letter of the 9 Octob. 1676 here English'd: concerning little animals by him observed in rain-well-sea and snow water; as also in water wherein pepper had lain infused. Phil Trans *12*, 821-831.
Lemischka, I. R., Raulet, D. H., and Mulligan, R. C. (1986). Developmental potential and dynamic behavior of hematopoietic stem cells. Cell *45*, 917-927.
Lewandowski, D., Barroca, V., Duconge, F., Bayer, J., Van Nhieu, J. T., Pestourie, C., Fouchet, P., Tavitian, B., and Romeo, P. H. (2010). In vivo cellular imaging pinpoints the role of reactive oxygen species in the early steps of adult hematopoietic reconstitution. Blood *115*, 443-452.
Li, P., and Zon, L. I. (2010). Resolving the controversy about N-cadherin and hematopoietic stem cells. Cell Stem Cell *6*, 199-202.
Li, X., Gounari, F., Protopopov, A., Khazaie, K., and von Boehmer, H. (2008). Oncogenesis of T-ALL and nonmalignant consequences of overexpressing intracellular NOTCH1. J Exp Med *205*, 2851-2861.
Liao, Y., Smyth, G. K., and Shi, W. (2014). featureCounts: an efficient general purpose program for assigning sequence reads to genomic features. Bioinformatics *30*, 923-930.
Liberzon, A., Birger, C., Thorvaldsdottir, H., Ghandi, M., Mesirov, J. P., and Tamayo, P. (2015). The Molecular Signatures Database (MSigDB) hallmark gene set collection. Cell Syst *1*, 417-425.
Lo Celso, C., Fleming, H. E., Wu, J. W., Zhao, C. X., Miake-Lye, S., Fujisaki, J., Cote, D., Rowe, D. W., Lin, C. P., and Scadden, D. T. (2009). Live-animal tracking of individual haematopoietic stem/progenitor cells in their niche. Nature *457*, 92-96.
Lord, B. I., Testa, N. G., and Hendry, J. H. (1975). The relative spatial distributions of CFUs and CFUc in the normal mouse femur. Blood *46*, 65-72.
Mansour, A., Abou-Ezzi, G., Sitnicka, E., Jacobsen, S. E., Wakkach, A., and Blin-Wakkach, C. (2012). Osteoclasts promote the formation of hematopoietic stem cell niches in the bone marrow. J Exp Med *209*, 537-549.
Manz, M. G., Traver, D., Akashi, K., Merad, M., Miyamoto, T., Engleman, E. G., and Weissman, I. L. (2001). Dendritic cell development from common myeloid progenitors. Ann N Y Acad Sci *938*, 167-173; discussion 173-164.
Matsunaga, T., Takemoto, N., Sato, T., Takimoto, R., Tanaka, I., Fujimi, A., Akiyama, T., Kuroda, H., Kawano, Y., Kobune, M.*, et al.* (2003). Interaction between leukemic-cell VLA-4 and stromal fibronectin is a decisive factor for minimal residual disease of acute myelogenous leukemia. Nat Med *9*, 1158-1165.

Maximov, A. (1909). Untersuchungen über Blut und Bindegewebe. I. Die frühesten Entwicklungsstadien der Blut und Bindegewebszellen, etc., Arch. f. Mikr Anat, Bd *73*, 1916.
Mazo, I. B., Gutierrez-Ramos, J. C., Frenette, P. S., Hynes, R. O., Wagner, D. D., and von Andrian, U. H. (1998). Hematopoietic progenitor cell rolling in bone marrow microvessels: parallel contributions by endothelial selectins and vascular cell adhesion molecule 1. J Exp Med *188*, 465-474.
McClugage, S. G., Jr., McCuskey, R. S., and Meineke, H. A. (1971). Microscopy of living bone marrow in Situ. II. Influence of the microenvironment on hemopoiesis. Blood *38*, 96-107.
McCuskey, R. S., McClugage, S. G., and Younker, W. J. (1971). Microscopy of living bone marrow in situ. Blood *38*, 87-95.
McKerrell, T., Park, N., Moreno, T., Grove, C. S., Ponstingl, H., Stephens, J., Understanding Society Scientific, G., Crawley, C., Craig, J., Scott, M. A.*, et al.* (2015). Leukemia-associated somatic mutations drive distinct patterns of age-related clonal hemopoiesis. Cell Rep *10*, 1239-1245.
Mead, A. J., Neo, W. H., Barkas, N., Matsuoka, S., Giustacchini, A., Facchini, R., Thongjuea, S., Jamieson, L., Booth, C. A. G., Fordham, N.*, et al.* (2017). Niche-mediated depletion of the normal hematopoietic stem cell reservoir by Flt3-ITD-induced myeloproliferation. J Exp Med *214*, 2005-2021.
Mempel, T. R., Pittet, M. J., Khazaie, K., Weninger, W., Weissleder, R., von Boehmer, H., and von Andrian, U. H. (2006). Regulatory T cells reversibly suppress cytotoxic T cell function independent of effector differentiation. Immunity *25*, 129-141.
Mendez-Ferrer, S., Lucas, D., Battista, M., and Frenette, P. S. (2008). Haematopoietic stem cell release is regulated by circadian oscillations. Nature *452*, 442-447.
Mendez-Ferrer, S., Michurina, T. V., Ferraro, F., Mazloom, A. R., Macarthur, B. D., Lira, S. A., Scadden, D. T., Ma'ayan, A., Enikolopov, G. N., and Frenette, P. S. (2010). Mesenchymal and haematopoietic stem cells form a unique bone marrow niche. Nature *466*, 829-834.
Mignone, J. L., Kukekov, V., Chiang, A. S., Steindler, D., and Enikolopov, G. (2004). Neural stem and progenitor cells in nestin-GFP transgenic mice. J Comp Neurol *469*, 311-324.
Miraki-Moud, F., Anjos-Afonso, F., Hodby, K. A., Griessinger, E., Rosignoli, G., Lillington, D., Jia, L., Davies, J. K., Cavenagh, J., Smith, M.*, et al.* (2013). Acute myeloid leukemia does not deplete normal hematopoietic stem cells but induces cytopenias by impeding their differentiation. Proc Natl Acad Sci U S A *110*, 13576-13581.
Morrison, S. J., and Scadden, D. T. (2014). The bone marrow niche for haematopoietic stem cells. Nature *505*, 327-334.
Muller, A., Homey, B., Soto, H., Ge, N., Catron, D., Buchanan, M. E., McClanahan, T., Murphy, E., Yuan, W., Wagner, S. N.*, et al.* (2001). Involvement of chemokine receptors in breast cancer metastasis. Nature *410*, 50-56.
Muller-Sieburg, C. E., Sieburg, H. B., Bernitz, J. M., and Cattarossi, G. (2012). Stem cell heterogeneity: implications for aging and regenerative medicine. Blood *119*, 3900-3907.
Mullighan, C. G., Phillips, L. A., Su, X., Ma, J., Miller, C. B., Shurtleff, S. A., and Downing, J. R. (2008). Genomic analysis of the clonal origins of relapsed acute lymphoblastic leukemia. Science *322*, 1377-1380.
Munoz, L., Nomdedeu, J. F., Villamor, N., Guardia, R., Colomer, D., Ribera, J. M., Torres, J. P., Berlanga, J. J., Fernandez, C., Llorente, A.*, et al.* (2003). Acute myeloid leukemia with MLL rearrangements: clinicobiological features, prognostic impact and value of flow cytometry in the detection of residual leukemic cells. Leukemia *17*, 76-82.

Muzumdar, M. D., Tasic, B., Miyamichi, K., Li, L., and Luo, L. (2007). A global double-fluorescent Cre reporter mouse. Genesis *45*, 593-605.
Naveiras, O., Nardi, V., Wenzel, P. L., Hauschka, P. V., Fahey, F., and Daley, G. Q. (2009). Bone-marrow adipocytes as negative regulators of the haematopoietic microenvironment. Nature *460*, 259-263.
Nervi, B., Ramirez, P., Rettig, M. P., Uy, G. L., Holt, M. S., Ritchey, J. K., Prior, J. L., Piwnica-Worms, D., Bridger, G., Ley, T. J., and DiPersio, J. F. (2009). Chemosensitization of acute myeloid leukemia (AML) following mobilization by the CXCR4 antagonist AMD3100. Blood *113*, 6206-6214.
Nilsson, S. K., Johnston, H. M., Whitty, G. A., Williams, B., Webb, R. J., Denhardt, D. T., Bertoncello, I., Bendall, L. J., Simmons, P. J., and Haylock, D. N. (2005). Osteopontin, a key component of the hematopoietic stem cell niche and regulator of primitive hematopoietic progenitor cells. Blood *106*, 1232-1239.
Nombela-Arrieta, C., Pivarnik, G., Winkel, B., Canty, K. J., Harley, B., Mahoney, J. E., Park, S. Y., Lu, J., Protopopov, A., and Silberstein, L. E. (2013). Quantitative imaging of haematopoietic stem and progenitor cell localization and hypoxic status in the bone marrow microenvironment. Nat Cell Biol *15*, 533-543.
Notta, F., Doulatov, S., Laurenti, E., Poeppl, A., Jurisica, I., and Dick, J. E. (2011). Isolation of single human hematopoietic stem cells capable of long-term multilineage engraftment. Science *333*, 218-221.
Omatsu, Y., Sugiyama, T., Kohara, H., Kondoh, G., Fujii, N., Kohno, K., and Nagasawa, T. (2010). The essential functions of adipo-osteogenic progenitors as the hematopoietic stem and progenitor cell niche. Immunity *33*, 387-399.
Ossenkoppele, G. J., Stussi, G., Maertens, J., van Montfort, K., Biemond, B. J., Breems, D., Ferrant, A., Graux, C., de Greef, G. E., Halkes, C. J.*, et al.* (2012). Addition of bevacizumab to chemotherapy in acute myeloid leukemia at older age: a randomized phase 2 trial of the Dutch-Belgian Cooperative Trial Group for Hemato-Oncology (HOVON) and the Swiss Group for Clinical Cancer Research (SAKK). Blood *120*, 4706-4711.
Padro, T., Ruiz, S., Bieker, R., Burger, H., Steins, M., Kienast, J., Buchner, T., Berdel, W. E., and Mesters, R. M. (2000). Increased angiogenesis in the bone marrow of patients with acute myeloid leukemia. Blood *95*, 2637-2644.
Paic, F., Igwe, J. C., Nori, R., Kronenberg, M. S., Franceschetti, T., Harrington, P., Kuo, L., Shin, D. G., Rowe, D. W., Harris, S. E., and Kalajzic, I. (2009). Identification of differentially expressed genes between osteoblasts and osteocytes. Bone *45*, 682-692.
Paige, C. J., Kincade, P. W., Shinefeld, L. A., and Sato, V. L. (1981). Precursors of murine B lymphocytes. Physical and functional characterization, and distinctions from myeloid stem cells. J Exp Med *153*, 154-165.
Passaro, D., Di Tullio, A., Abarrategi, A., Rouault-Pierre, K., Foster, K., Ariza-McNaughton, L., Montaner, B., Chakravarty, P., Bhaw, L., Diana, G.*, et al.* (2017). Increased Vascular Permeability in the Bone Marrow Microenvironment Contributes to Disease Progression and Drug Response in Acute Myeloid Leukemia. Cancer Cell.
Passaro, D., Irigoyen, M., Catherinet, C., Gachet, S., Da Costa De Jesus, C., Lasgi, C., Tran Quang, C., and Ghysdael, J. (2015). CXCR4 Is Required for Leukemia-Initiating Cell Activity in T Cell Acute Lymphoblastic Leukemia. Cancer Cell *27*, 769-779.
Passegue, E., Wagner, E. F., and Weissman, I. L. (2004). JunB deficiency leads to a myeloproliferative disorder arising from hematopoietic stem cells. Cell *119*, 431-443.
Paul, F., Arkin, Y., Giladi, A., Jaitin, D. A., Kenigsberg, E., Keren-Shaul, H., Winter, D., Lara-Astiaso, D., Gury, M., Weiner, A.*, et al.* (2015). Transcriptional Heterogeneity and Lineage Commitment in Myeloid Progenitors. Cell *163*, 1663-1677.

Pear, W. S., Aster, J. C., Scott, M. L., Hasserjian, R. P., Soffer, B., Sklar, J., and Baltimore, D. (1996). Exclusive development of T cell neoplasms in mice transplanted with bone marrow expressing activated Notch alleles. J Exp Med *183*, 2283-2291.
Peeters, P., Raynaud, S. D., Cools, J., Wlodarska, I., Grosgeorge, J., Philip, P., Monpoux, F., Van Rompaey, L., Baens, M., Van den Berghe, H., and Marynen, P. (1997). Fusion of TEL, the ETS-variant gene 6 (ETV6), to the receptor-associated kinase JAK2 as a result of t(9;12) in a lymphoid and t(9;15;12) in a myeloid leukemia. Blood *90*, 2535-2540.
Perie, L., Duffy, K. R., Kok, L., de Boer, R. J., and Schumacher, T. N. (2015). The Branching Point in Erythro-Myeloid Differentiation. Cell *163*, 1655-1662.
Pinho, S., Lacombe, J., Hanoun, M., Mizoguchi, T., Bruns, I., Kunisaki, Y., and Frenette, P. S. (2013). PDGFRalpha and CD51 mark human nestin+ sphere-forming mesenchymal stem cells capable of hematopoietic progenitor cell expansion. J Exp Med *210*, 1351-1367.
Pitt, L. A., Tikhonova, A. N., Hu, H., Trimarchi, T., King, B., Gong, Y., Sanchez-Martin, M., Tsirigos, A., Littman, D. R., Ferrando, A. A.*, et al.* (2015). CXCL12-Producing Vascular Endothelial Niches Control Acute T Cell Leukemia Maintenance. Cancer Cell *27*, 755-768.
Preibisch, S., Saalfeld, S., Schindelin, J., and Tomancak, P. (2010). Software for bead-based registration of selective plane illumination microscopy data. Nat Methods *7*, 418-419.
Presson, R. G., Petrache, I., and Brown, M. B. (2014). Intravital Microscopy of the Lung. In Advances in Intravital Microscopy: From Basic to Clinical Research, R. Weigert, ed. (Dordrecht: Springer Netherlands), pp. 221-232.
Pui, C. H., Robison, L. L., and Look, A. T. (2008). Acute lymphoblastic leukaemia. Lancet *371*, 1030-1043.
Quail, D. F., and Joyce, J. A. (2013). Microenvironmental regulation of tumor progression and metastasis. Nat Med *19*, 1423-1437.
Raaijmakers, M. H., Mukherjee, S., Guo, S., Zhang, S., Kobayashi, T., Schoonmaker, J. A., Ebert, B. L., Al-Shahrour, F., Hasserjian, R. P., Scadden, E. O.*, et al.* (2010). Bone progenitor dysfunction induces myelodysplasia and secondary leukaemia. Nature *464*, 852-857.
Radtke, F., Wilson, A., Stark, G., Bauer, M., van Meerwijk, J., MacDonald, H. R., and Aguet, M. (1999). Deficient T cell fate specification in mice with an induced inactivation of Notch1. Immunity *10*, 547-558.
Rahmig, S., Kronstein-Wiedemann, R., Fohgrub, J., Kronstein, N., Nevmerzhitskaya, A., Bornhauser, M., Gassmann, M., Platz, A., Ordemann, R., Tonn, T., and Waskow, C. (2016). Improved Human Erythropoiesis and Platelet Formation in Humanized NSGW41 Mice. Stem Cell Reports *7*, 591-601.
Ramasamy, S. K., Kusumbe, A. P., Schiller, M., Zeuschner, D., Bixel, M. G., Milia, C., Gamrekelashvili, J., Limbourg, A., Medvinsky, A., Santoro, M. M.*, et al.* (2016). Blood flow controls bone vascular function and osteogenesis. Nat Commun *7*, 13601.
Ramasamy, S. K., Kusumbe, A. P., Wang, L., and Adams, R. H. (2014). Endothelial Notch activity promotes angiogenesis and osteogenesis in bone. Nature *507*, 376-380.
Rashidi, N. M., Scott, M. K., Scherf, N., Krinner, A., Kalchschmidt, J. S., Gounaris, K., Selkirk, M. E., Roeder, I., and Lo Celso, C. (2014). In vivo time-lapse imaging shows diverse niche engagement by quiescent and naturally activated hematopoietic stem cells. Blood *124*, 79-83.
Rauch, P. J., Ellegast, J. M., Widmer, C. C., Fritsch, K., Goede, J. S., Valk, P. J., Lowenberg, B., Takizawa, H., and Manz, M. G. (2016). MPL expression on AML blasts predicts peripheral blood neutropenia and thrombocytopenia. Blood *128*, 2253-2257.

Reinisch, A., Thomas, D., Corces, M. R., Zhang, X., Gratzinger, D., Hong, W. J., Schallmoser, K., Strunk, D., and Majeti, R. (2016). A humanized bone marrow ossicle xenotransplantation model enables improved engraftment of healthy and leukemic human hematopoietic cells. Nat Med *22*, 812-821.
Ritsma, L., Ellenbroek, S. I., Zomer, A., Snippert, H. J., de Sauvage, F. J., Simons, B. D., Clevers, H., and van Rheenen, J. (2014a). Intestinal crypt homeostasis revealed at single-stem-cell level by in vivo live imaging. Nature *507*, 362-365.
Ritsma, L., Ellenbroek, S. I. J., Zomer, A., Snippert, H. J., de Sauvage, F. J., Simons, B. D., Clevers, H., and van Rheenen, J. (2014b). Intestinal crypt homeostasis revealed at single-stem-cell level by in vivo live imaging. Nature *507*, 362-365.
Rodda, S. J., and McMahon, A. P. (2006). Distinct roles for Hedgehog and canonical Wnt signaling in specification, differentiation and maintenance of osteoblast progenitors. Development *133*, 3231-3244.
Rompolas, P., Deschene, E. R., Zito, G., Gonzalez, D. G., Saotome, I., Haberman, A. M., and Greco, V. (2012). Live imaging of stem cell and progeny behaviour in physiological hair-follicle regeneration. Nature *487*, 496-499.
Sacchetti, B., Funari, A., Michienzi, S., Di Cesare, S., Piersanti, S., Saggio, I., Tagliafico, E., Ferrari, S., Robey, P. G., Riminucci, M., and Bianco, P. (2007). Self-renewing osteoprogenitors in bone marrow sinusoids can organize a hematopoietic microenvironment. Cell *131*, 324-336.
Sanchez-Aguilera, A., and Mendez-Ferrer, S. (2017). The hematopoietic stem-cell niche in health and leukemia. Cell Mol Life Sci *74*, 579-590.
Sanda, T., Li, X., Gutierrez, A., Ahn, Y., Neuberg, D. S., O'Neil, J., Strack, P. R., Winter, C. G., Winter, S. S., Larson, R. S.*, et al.* (2010). Interconnecting molecular pathways in the pathogenesis and drug sensitivity of T-cell acute lymphoblastic leukemia. Blood *115*, 1735-1745.
Sanjuan-Pla, A., Macaulay, I. C., Jensen, C. T., Woll, P. S., Luis, T. C., Mead, A., Moore, S., Carella, C., Matsuoka, S., Bouriez Jones, T.*, et al.* (2013). Platelet-biased stem cells reside at the apex of the haematopoietic stem-cell hierarchy. Nature *502*, 232-236.
Sapoznikov, A., Pewzner-Jung, Y., Kalchenko, V., Krauthgamer, R., Shachar, I., and Jung, S. (2008). Perivascular clusters of dendritic cells provide critical survival signals to B cells in bone marrow niches. Nat Immunol *9*, 388-395.
Schepers, K., Pietras, E. M., Reynaud, D., Flach, J., Binnewies, M., Garg, T., Wagers, A. J., Hsiao, E. C., and Passegue, E. (2013). Myeloproliferative neoplasia remodels the endosteal bone marrow niche into a self-reinforcing leukemic niche. Cell Stem Cell *13*, 285-299.
Schmidt, S., Rainer, J., Ploner, C., Presul, E., Riml, S., and Kofler, R. (2004). Glucocorticoid-induced apoptosis and glucocorticoid resistance: molecular mechanisms and clinical relevance. Cell Death Differ *11 Suppl 1*, S45-55.
Schofield, R. (1978). The relationship between the spleen colony-forming cell and the haemopoietic stem cell. Blood Cells *4*, 7-25.
Schwaller, J., Frantsve, J., Aster, J., Williams, I. R., Tomasson, M. H., Ross, T. S., Peeters, P., Van Rompaey, L., Van Etten, R. A., Ilaria, R., Jr.*, et al.* (1998). Transformation of hematopoietic cell lines to growth-factor independence and induction of a fatal myelo- and lymphoproliferative disease in mice by retrovirally transduced TEL/JAK2 fusion genes. EMBO J *17*, 5321-5333.
Scott, M. K., Akinduro, O., and Lo Celso, C. (2014). In vivo 4-dimensional tracking of hematopoietic stem and progenitor cells in adult mouse calvarial bone marrow. J Vis Exp, e51683.

Shelton, J., Lu, X., Hollenbaugh, J. A., Cho, J. H., Amblard, F., and Schinazi, R. F. (2016). Metabolism, Biochemical Actions, and Chemical Synthesis of Anticancer Nucleosides, Nucleotides, and Base Analogs. Chem Rev *116*, 14379-14455.
Shlush, L. I., Mitchell, A., Heisler, L., Abelson, S., Ng, S. W. K., Trotman-Grant, A., Medeiros, J. J. F., Rao-Bhatia, A., Jaciw-Zurakowsky, I., Marke, R.*, et al.* (2017). Tracing the origins of relapse in acute myeloid leukaemia to stem cells. Nature *547*, 104-108.
Shlush, L. I., Zandi, S., Mitchell, A., Chen, W. C., Brandwein, J. M., Gupta, V., Kennedy, J. A., Schimmer, A. D., Schuh, A. C., Yee, K. W.*, et al.* (2014). Identification of pre-leukaemic haematopoietic stem cells in acute leukaemia. Nature *506*, 328-333.
Shultz, L. D., Lyons, B. L., Burzenski, L. M., Gott, B., Chen, X., Chaleff, S., Kotb, M., Gillies, S. D., King, M., Mangada, J.*, et al.* (2005). Human lymphoid and myeloid cell development in NOD/LtSz-scid IL2R gamma null mice engrafted with mobilized human hemopoietic stem cells. J Immunol *174*, 6477-6489.
Siminovitch, L., Till, J. E., and McCulloch, E. A. (1964). Decline in Colony-Forming Ability of Marrow Cells Subjected to Serial Transplantation into Irradiated Mice. J Cell Comp Physiol *64*, 23-31.
Singh, S. K., Hawkins, C., Clarke, I. D., Squire, J. A., Bayani, J., Hide, T., Henkelman, R. M., Cusimano, M. D., and Dirks, P. B. (2004). Identification of human brain tumour initiating cells. Nature *432*, 396-401.
Sipkins, D. A., Wei, X., Wu, J. W., Runnels, J. M., Cote, D., Means, T. K., Luster, A. D., Scadden, D. T., and Lin, C. P. (2005). In vivo imaging of specialized bone marrow endothelial microdomains for tumour engraftment. Nature *435*, 969-973.
Sirard, C., Lapidot, T., Vormoor, J., Cashman, J. D., Doedens, M., Murdoch, B., Jamal, N., Messner, H., Addey, L., Minden, M.*, et al.* (1996). Normal and leukemic SCID-repopulating cells (SRC) coexist in the bone marrow and peripheral blood from CML patients in chronic phase, whereas leukemic SRC are detected in blast crisis. Blood *87*, 1539-1548.
Skog, J., Wurdinger, T., van Rijn, S., Meijer, D. H., Gainche, L., Sena-Esteves, M., Curry, W. T., Jr., Carter, B. S., Krichevsky, A. M., and Breakefield, X. O. (2008). Glioblastoma microvesicles transport RNA and proteins that promote tumour growth and provide diagnostic biomarkers. Nat Cell Biol *10*, 1470-1476.
Somervaille, T. C., and Cleary, M. L. (2006). Identification and characterization of leukemia stem cells in murine MLL-AF9 acute myeloid leukemia. Cancer Cell *10*, 257-268.
Spangrude, G. J., Heimfeld, S., and Weissman, I. L. (1988). Purification and characterization of mouse hematopoietic stem cells. Science *241*, 58-62.
Spencer, J. A., Ferraro, F., Roussakis, E., Klein, A., Wu, J., Runnels, J. M., Zaher, W., Mortensen, L. J., Alt, C., Turcotte, R.*, et al.* (2014). Direct measurement of local oxygen concentration in the bone marrow of live animals. Nature *508*, 269-273.
Springer, T. A. (1994). Traffic signals for lymphocyte recirculation and leukocyte emigration: the multistep paradigm. Cell *76*, 301-314.
Stavropoulou, V., Kaspar, S., Brault, L., Sanders, M. A., Juge, S., Morettini, S., Tzankov, A., Iacovino, M., Lau, I. J., Milne, T. A.*, et al.* (2016). MLL-AF9 Expression in Hematopoietic Stem Cells Drives a Highly Invasive AML Expressing EMT-Related Genes Linked to Poor Outcome. Cancer Cell *30*, 43-58.
Stier, S., Ko, Y., Forkert, R., Lutz, C., Neuhaus, T., Grunewald, E., Cheng, T., Dombkowski, D., Calvi, L. M., Rittling, S. R., and Scadden, D. T. (2005). Osteopontin is a hematopoietic stem cell niche component that negatively regulates stem cell pool size. J Exp Med *201*, 1781-1791.

Stinchcombe, J. C., Bossi, G., Booth, S., and Griffiths, G. M. (2001). The immunological synapse of CTL contains a secretory domain and membrane bridges. Immunity *15*, 751-761.
Subramanian, A., Tamayo, P., Mootha, V. K., Mukherjee, S., Ebert, B. L., Gillette, M. A., Paulovich, A., Pomeroy, S. L., Golub, T. R., Lander, E. S., and Mesirov, J. P. (2005). Gene set enrichment analysis: a knowledge-based approach for interpreting genome-wide expression profiles. Proc Natl Acad Sci U S A *102*, 15545-15550.
Sugiyama, T., Kohara, H., Noda, M., and Nagasawa, T. (2006). Maintenance of the hematopoietic stem cell pool by CXCL12-CXCR4 chemokine signaling in bone marrow stromal cell niches. Immunity *25*, 977-988.
Sumen, C., Mempel, T. R., Mazo, I. B., and von Andrian, U. H. (2004). Intravital microscopy: visualizing immunity in context. Immunity *21*, 315-329.
Susaki, E. A., Tainaka, K., Perrin, D., Kishino, F., Tawara, T., Watanabe, T. M., Yokoyama, C., Onoe, H., Eguchi, M., Yamaguchi, S.*, et al.* (2014). Whole-brain imaging with single-cell resolution using chemical cocktails and computational analysis. Cell *157*, 726-739.
Swansbury, G. J., Slater, R., Bain, B. J., Moorman, A. V., and Secker-Walker, L. M. (1998). Hematological malignancies with t(9;11)(p21-22;q23)--a laboratory and clinical study of 125 cases. European 11q23 Workshop participants. Leukemia *12*, 792-800.
Swerdlow, S., Campo, E., Harris, N., Jaffe, E., Pileri, S., Stein, H., Thiele, J., and Vardiman, J. (2008). WHO Classification of Tumors of Hematopoietic and Lymphoid Tissues 4th Ed.(2008).
Szczepanski, T. (2007). Why and how to quantify minimal residual disease in acute lymphoblastic leukemia? Leukemia *21*, 622-626.
Tachibana, K., Hirota, S., Iizasa, H., Yoshida, H., Kawabata, K., Kataoka, Y., Kitamura, Y., Matsushima, K., Yoshida, N., Nishikawa, S.*, et al.* (1998). The chemokine receptor CXCR4 is essential for vascularization of the gastrointestinal tract. Nature *393*, 591-594.
Taichman, R. S., and Emerson, S. G. (1994). Human osteoblasts support hematopoiesis through the production of granulocyte colony-stimulating factor. J Exp Med *179*, 1677-1682.
Tamplin, O. J., Durand, E. M., Carr, L. A., Childs, S. J., Hagedorn, E. J., Li, P., Yzaguirre, A. D., Speck, N. A., and Zon, L. I. (2015). Hematopoietic stem cell arrival triggers dynamic remodeling of the perivascular niche. Cell *160*, 241-252.
Tauber, A. I. (2003). Metchnikoff and the phagocytosis theory. Nat Rev Mol Cell Biol *4*, 897-901.
Tavor, S., Petit, I., Porozov, S., Avigdor, A., Dar, A., Leider-Trejo, L., Shemtov, N., Deutsch, V., Naparstek, E., Nagler, A., and Lapidot, T. (2004). CXCR4 regulates migration and development of human acute myelogenous leukemia stem cells in transplanted NOD/SCID mice. Cancer Res *64*, 2817-2824.
Tessier, P. A., Naccache, P. H., Clark-Lewis, I., Gladue, R. P., Neote, K. S., and McColl, S. R. (1997). Chemokine networks in vivo: involvement of C-X-C and C-C chemokines in neutrophil extravasation in vivo in response to TNF-alpha. J Immunol *159*, 3595-3602.
Theocharides, A. P., Rongvaux, A., Fritsch, K., Flavell, R. A., and Manz, M. G. (2016). Humanized hemato-lymphoid system mice. Haematologica *101*, 5-19.
Till, J. E., and Mc, C. E. (1961). A direct measurement of the radiation sensitivity of normal mouse bone marrow cells. Radiat Res *14*, 213-222.
Tsuboi, M., Kawakami, A., Nakashima, T., Matsuoka, N., Urayama, S., Kawabe, Y., Fujiyama, K., Kiriyama, T., Aoyagi, T., Maeda, K., and Eguchi, K. (1999). Tumor necrosis factor-alpha and interleukin-1beta increase the Fas-mediated apoptosis of human osteoblasts. J Lab Clin Med *134*, 222-231.

Turcotte, R., Alt, C., Mortensen, L. J., and Lin, C. P. (2014). Characterization of multiphoton microscopy in the bone marrow following intravital laser osteotomy. Biomed Opt Express *5*, 3578-3588.
Uy, G. L., Rettig, M. P., Motabi, I. H., McFarland, K., Trinkaus, K. M., Hladnik, L. M., Kulkarni, S., Abboud, C. N., Cashen, A. F., Stockerl-Goldstein, K. E.*, et al.* (2012). A phase 1/2 study of chemosensitization with the CXCR4 antagonist plerixafor in relapsed or refractory acute myeloid leukemia. Blood *119*, 3917-3924.
Vas, V., Senger, K., Dorr, K., Niebel, A., and Geiger, H. (2012). Aging of the microenvironment influences clonality in hematopoiesis. PLoS One *7*, e42080.
Vestweber, D., Winderlich, M., Cagna, G., and Nottebaum, A. F. (2009). Cell adhesion dynamics at endothelial junctions: VE-cadherin as a major player. Trends Cell Biol *19*, 8-15.
Visnjic, D., Kalajzic, Z., Rowe, D. W., Katavic, V., Lorenzo, J., and Aguila, H. L. (2004). Hematopoiesis is severely altered in mice with an induced osteoblast deficiency. Blood *103*, 3258-3264.
Waibel, M., Vervoort, S. J., Kong, I. Y., Heinzel, S., Ramsbottom, K. M., Martin, B. P., Hawkins, E. D., and Johnstone, R. W. (2017). Epigenetic targeting of Notch1-driven transcription using the HDACi panobinostat is a potential therapy against T-cell acute lymphoblastic leukemia. Leukemia.
Walkley, C. R., Olsen, G. H., Dworkin, S., Fabb, S. A., Swann, J., McArthur, G. A., Westmoreland, S. V., Chambon, P., Scadden, D. T., and Purton, L. E. (2007). A microenvironment-induced myeloproliferative syndrome caused by retinoic acid receptor gamma deficiency. Cell *129*, 1097-1110.
Wang, L., Benedito, R., Bixel, M. G., Zeuschner, D., Stehling, M., Savendahl, L., Haigh, J. J., Snippert, H., Clevers, H., Breier, G.*, et al.* (2013). Identification of a clonally expanding haematopoietic compartment in bone marrow. EMBO J *32*, 219-230.
Wang, L., Zhang, H., Rodriguez, S., Cao, L., Parish, J., Mumaw, C., Zollman, A., Kamoka, M. M., Mu, J., Chen, D. Z.*, et al.* (2014). Notch-dependent repression of miR-155 in the bone marrow niche regulates hematopoiesis in an NF-kappaB-dependent manner. Cell Stem Cell *15*, 51-65.
Wang, W., Stiehl, T., Raffel, S., Hoang, V. T., Hoffmann, I., Poisa-Beiro, L., Saeed, B. R., Blume, R., Manta, L., Eckstein, V.*, et al.* (2017). Reduced hematopoietic stem cell frequency predicts outcome in acute myeloid leukemia. Haematologica *102*, 1567-1577.
Weng, A. P., Ferrando, A. A., Lee, W., Morris, J. P. t., Silverman, L. B., Sanchez-Irizarry, C., Blacklow, S. C., Look, A. T., and Aster, J. C. (2004). Activating mutations of NOTCH1 in human T cell acute lymphoblastic leukemia. Science *306*, 269-271.
Wiemels, J. L., Cazzaniga, G., Daniotti, M., Eden, O. B., Addison, G. M., Masera, G., Saha, V., Biondi, A., and Greaves, M. F. (1999). Prenatal origin of acute lymphoblastic leukaemia in children. Lancet *354*, 1499-1503.
Wilson, A., Murphy, M. J., Oskarsson, T., Kaloulis, K., Bettess, M. D., Oser, G. M., Pasche, A. C., Knabenhans, C., Macdonald, H. R., and Trumpp, A. (2004). c-Myc controls the balance between hematopoietic stem cell self-renewal and differentiation. Genes Dev *18*, 2747-2763.
Wilson, C. L., and Ness, K. K. (2013). Bone mineral density deficits and fractures in survivors of childhood cancer. Curr Osteoporos Rep *11*, 329-337.
Wiseman, D. H. (2011). Donor cell leukemia: a review. Biol Blood Marrow Transplant *17*, 771-789.

Wunderlich, M., Mizukawa, B., Chou, F. S., Sexton, C., Shrestha, M., Saunthararajah, Y., and Mulloy, J. C. (2013). AML cells are differentially sensitive to chemotherapy treatment in a human xenograft model. Blood *121*, e90-97.
Xie, M., Lu, C., Wang, J., McLellan, M. D., Johnson, K. J., Wendl, M. C., McMichael, J. F., Schmidt, H. K., Yellapantula, V., Miller, C. A.*, et al.* (2014). Age-related mutations associated with clonal hematopoietic expansion and malignancies. Nat Med *20*, 1472-1478.
Xie, T., and Spradling, A. C. (1998). decapentaplegic is essential for the maintenance and division of germline stem cells in the Drosophila ovary. Cell *94*, 251-260.
Xie, T., and Spradling, A. C. (2000). A niche maintaining germ line stem cells in the Drosophila ovary. Science *290*, 328-330.
Xie, Y., Yin, T., Wiegraebe, W., He, X. C., Miller, D., Stark, D., Perko, K., Alexander, R., Schwartz, J., Grindley, J. C.*, et al.* (2009). Detection of functional haematopoietic stem cell niche using real-time imaging. Nature *457*, 97-101.
Xu, Y., Yuan, L., Mak, J., Pardanaud, L., Caunt, M., Kasman, I., Larrivee, B., Del Toro, R., Suchting, S., Medvinsky, A.*, et al.* (2010). Neuropilin-2 mediates VEGF-C-induced lymphatic sprouting together with VEGFR3. J Cell Biol *188*, 115-130.
Yamazaki, S., Ema, H., Karlsson, G., Yamaguchi, T., Miyoshi, H., Shioda, S., Taketo, M. M., Karlsson, S., Iwama, A., and Nakauchi, H. (2011). Nonmyelinating Schwann cells maintain hematopoietic stem cell hibernation in the bone marrow niche. Cell *147*, 1146-1158.
Zahiragic, L., Schliemann, C., Bieker, R., Thoennissen, N. H., Burow, K., Kramer, C., Zuhlsdorf, M., Berdel, W. E., and Mesters, R. M. (2007). Bevacizumab reduces VEGF expression in patients with relapsed and refractory acute myeloid leukemia without clinical antileukemic activity. Leukemia *21*, 1310-1312.
Zahr, A., Alcaide, P., Yang, J., Jones, A., Gregory, M., dela Paz, N. G., Patel-Hett, S., Nevers, T., Koirala, A., Luscinskas, F. W.*, et al.* (2016). Endomucin prevents leukocyte-endothelial cell adhesion and has a critical role under resting and inflammatory conditions. Nat Commun *7*, 10363.
Zeng, Z., Shi, Y. X., Samudio, I. J., Wang, R. Y., Ling, X., Frolova, O., Levis, M., Rubin, J. B., Negrin, R. R., Estey, E. H.*, et al.* (2009). Targeting the leukemia microenvironment by CXCR4 inhibition overcomes resistance to kinase inhibitors and chemotherapy in AML. Blood *113*, 6215-6224.
Zhang, J., Niu, C., Ye, L., Huang, H., He, X., Tong, W. G., Ross, J., Haug, J., Johnson, T., Feng, J. Q.*, et al.* (2003). Identification of the haematopoietic stem cell niche and control of the niche size. Nature *425*, 836-841.
Zhao, M., Perry, J. M., Marshall, H., Venkatraman, A., Qian, P., He, X. C., Ahamed, J., and Li, L. (2014). Megakaryocytes maintain homeostatic quiescence and promote post-injury regeneration of hematopoietic stem cells. Nat Med *20*, 1321-1326.
Zhao, Y. G., Xiao, A. Z., Park, H. I., Newcomer, R. G., Yan, M., Man, Y. G., Heffelfinger, S. C., and Sang, Q. X. (2004). Endometase/matrilysin-2 in human breast ductal carcinoma in situ and its inhibition by tissue inhibitors of metalloproteinases-2 and -4: a putative role in the initiation of breast cancer invasion. Cancer Res *64*, 590-598.
Zhou, B. O., Ding, L., and Morrison, S. J. (2015). Hematopoietic stem and progenitor cells regulate the regeneration of their niche by secreting Angiopoietin-1. Elife *4*, e05521.
Zipfel, W. R., Williams, R. M., and Webb, W. W. (2003). Nonlinear magic: multiphoton microscopy in the biosciences. Nat Biotechnol *21*, 1369-1377.

Zou, Y. R., Kottmann, A. H., Kuroda, M., Taniuchi, I., and Littman, D. R. (1998). Function of the chemokine receptor CXCR4 in haematopoiesis and in cerebellar development. Nature *393*, 595-599.

Appendix A – Supplementary Video legends

Chapter 3

Supplementary Video 3A – Inefficient angiogenesis in AML-burdened mice.
Representative maximum projection of 3D time-lapse data (shown at 10 frames per second) of an area from a control (left) and leukemic (right) Flk1-GFP mouse collected every 90s for 90min (shown in figure 2G). Red arrowheads point to vascular sprouts that rapidly retract. Black: Flk1-GFP+ cells. Representative of 4 control and 3 leukemic mice. Adapted from (Duarte et al., 2018a).

Supplementary Video 3B – Blood vessel fragmentation in mice with AML.
Maximum projection of 3D time-lapse data (shown at 10 frames per second) of vascular disintegration (circled area; red arrows) in a leukemic Flk1-GFP mouse. Filmed every 90s for 90min. Black: Flk1-GFP$^+$ cells. Equivalent events were never observed in control mice. Adapted from (Duarte et al., 2018a).

Supplementary Video 3C – Circulating endothelial debris in BM vessels of AML-burdened mice.
Representative 2D time-lapse data collected every 156ms for 4min 24s (shown at 5 frames per second) from a Flk1-GFP mouse reconstituted with mTomato$^+$ healthy hematopoietic cells (left; Control) and a Flk1-GFP mouse infiltrated with mTomato$^+$ AML (right; AML). In control mice (left) no debris particles are detected in circulation but in leukemic mice (right) frequent endothelial debris is found inside the vascular lumen, sometimes adhering to the endothelium. Green: GFP signal; red: mTomato$^+$ healthy hematopoietic cells (left) or AML cells (right); blue: Cy5-Dextran. Arrowheads follow some of the debris observed in circulation. Representative of 3 control and 4 leukemic mice. Adapted from (Duarte et al., 2018a).

Supplementary Video 3D – Stroma dynamics in mice with AML.
Representative maximum projections of 3D time-lapse data (shown at 10 frames per second) collected at ten-minute intervals for 7h and 20min from a mT/mG control (left) chimera and a mT/mG chimera with high infiltration of GFP^+YFP^+ AML (right). AML cells not shown for clarity purposes. Red: $mTomato^+$ stromal cells; blue: Cy-5 $dextran^+$ blood vessels. Arrows follow oscillating vessels in AML-burdened mouse. Representative of 3 control and 3 leukemic mice. Adapted from (Duarte et al., 2018a).

Supplementary Video 3E – Cell adhesion to the splenic endothelium.
Representative maximum projections of time-lapse data (shown at 7 frames per second) of 2 areas scanned every 30s for 15min from the spleen of a leukemic Flk1-GFP mouse with $mTomato^+$ residual healthy hematopoietic cells. In area 1, the arrow points to a healthy hematopoietic cell adhering statically to the endothelium. In position 2, a cell adheres, crawls and detaches from the endothelium. Green: Flk^{1+} GFP ECs; red: $mTomato^+$ healthy hematopoietic cells; blue: Cy5-Dextran. Adapted from (Duarte et al., 2018a).

Supplementary Video 3F – Transendothelial migration in the bone marrow.
Representative maximum projections of time-lapse data (shown at 7 frames per second) of 2 areas scanned every 30s for 15min from the BM of a leukemic Flk1-GFP mouse with $mTomato^+$ residual healthy hematopoietic cells. In position 1, the arrow points to a normal hematopoietic cell intravasating and leaving the BM. In position 2, a cell adheres and extravasates towards the tissue. Green: $Flk1^+$ GFP ECs; red: $mTomato^+$ non-malignant hematopoietic cells; blue: Cy5-Dextran. Adapted from (Duarte et al., 2018a).

Supplementary Video 3G – Turbulent blood flow in vessels within AML infiltrated BM.
Representative maximum projection (shown at 7 frames per second) of a vascular bifurcation area collected every 30s for 15min from the spleen of a healthy (left) and a leukemic (right) Flk1-GFP mouse. Dark circles: AML cells form intravascular clusters that adhere to the endothelium and block blood flow; Green: $Flk1^+$ GFP ECs; Red: $mTomato^+$ non-malignant hematopoietic cells; Yellow: Cy5-Dextran. Adapted from (Duarte et al., 2018a).

Chapter 4

Supplementary Video 4A – T-ALL cell migration and mitosis in dexamethasone treated Nestin-GFP$^+$ mice.

Maximum projection of three-hour time-lapse data collected at three-minute intervals (15 frames per second) from mice after 2 days of treatment with 15mg/kg. Red: T-ALL cells; green: Nestin-GFP$^+$ cells; blue: blood vessels. Arrows in paused frames point at cells about to undergo mitosis. Adapted from (Hawkins et al., 2016).

Supplementary Video 4B - T-ALL cell migration and mitosis in vincristine treated Nestin-GFP$^+$ mice.

Maximum projection of three-hour time-lapse data collected at three-minute intervals (shown at 15 frames per second) from mice after 2 days of treatment with 0.15mg/kg. Red: T-ALL cells; green: Nestin-GFP$^+$ cells; blue: blood vessels. Arrow in paused frame point at a cell about to undergo mitosis. Bone and blood vessel signals of the first frame were maintained throughout the movie for clarity purposes. Adapted from (Hawkins et al., 2016).

Supplementary Video 4C - T-ALL cell migration and mitosis in DVA treated mice.

Maximum projection of three-hour time-lapse data collected at three-minute intervals (shown at 15 frames per second) from mice after 2 days of treatment with DVA combination therapy (dexamethasone 15 mg/kg, vincristine 0.15mg/kg, L-asparaginase 1000 IU/kg). Red: T-ALL cells; blue: blood vessels. Arrow in paused frame point at a cell about to undergo mitosis. Bone and blood vessel signals of the first frame were maintained throughout the movie for clarity purposes. Adapted from (Hawkins et al., 2016).

Supplementary Video 4D – Cell migration in TEL-JAK2 T-ALL disease burdened mice

Maximum projection time-lapse data collected at three-minute intervals (shown at 15 frames per second) from mice at early seeding stages and from mice treated with dexamethasone (15mg/kg) upon full intiltration. Green: GFP$^+$ TEL-JAK2 T-ALL blasts; blue: blood vessels; grey: bone SHG.

Supplementary Video 4E – Supplementary Video 2 - Human T-ALL cell migration in dexamethasone treated NOD/SCID/γ mice.

Maximum projection of time-lapse data collected at three-minute intervals (9 frames per second) from NOD/SCID/γ mice before, and after 14 days of treatment with 15mg/kg dexamethasone treatment. Red: human T-ALL cells labelled by I.V. injection of CD45-PE; grey: bone SHG. Adapted from (Hawkins et al., 2016).

Chapter 5

Supplementary Video 5A – Seeding and chemoresistant T-ALL cell mobilization.

Representative maximum projection of 3D time-lapse data (shown at 10 frames per second) of areas from Flk1-GFP mice acquired every 3min for 90 min prior and 180 min post-AMD3100 administration. Single cells at seeding (first part) and chemoresistant (second part) stages were tracked. Red: T-ALL cells; green: Flk1-GFP^{+} endothelial cells; blue: Cy5-labelled dextran inside blood vessels. The first frame of the blue channel was copied across the full movie to correct for cy5 signal bleaching. Upon CXCR4 inhibition, mobilized T-ALL cells are visible inside vessels.

Supplementary Video 5B – AMD3100 promotes intravasation of AML cells.

Representative maximum projection of 3D time-lapse data (shown at 10 frames per second) of areas from Flk1-GFP mice acquired every 3min for 90 min prior and 180 min post-AMD3100 administration. Single cells at seeding (first part) and chemoresistant (second part) stages were tracked. Red: AML cells; green: Flk1-GFP^{+} endothelial cells; blue: Cy5- labelled dextran inside blood vessels. The first frame of the blue channel was copied across the full movie to correct for cy5 signal bleaching. Upon CXCR4 inhibition, mobilized AML cells are visible inside vessels. Parenchymal cells maintain the same migratory behavior as prior to AMD3100 administration.

Supplementary Video 5C – AMD3100 affects *in situ* migration of parenchymal T-ALL cells.

Representative maximum projection of 3D time-lapse data (shown at 10 frames per second) of areas from Flk1-GFP mice acquired every 3min for 90 min prior and 180 min post-AMD3100 administration. Single cells at seeding (first part) and chemoresistant (second part) stages were tracked. Red: T-ALL cells; green: Flk1-GFP^{+} endothelial cells; blue: Cy5-labelled dextran inside blood vessels. The first frame of the blue channel was copied across the full movie to correct for cy5 signal bleaching. Upon CXCR4 inhibition, parenchymal T-ALL cells are significantly less migratory.

Supplementary Video 5D – AMD3100 does not affect *in situ* migration of parenchymal AML cells.

Representative maximum projection of 3D time-lapse data (shown at 10 frames per second) of areas from Flk1-GFP mice acquired every 3min for 90 min prior and 180 min post-AMD3100 administration. Single cells at seeding (first part) and chemoresistant (second part) stages were tracked. Red: AML cells; green: Flk1-GFP^{+} endothelial cells; blue: Cy5- labelled dextran inside blood vessels. The first frame of the blue channel was copied across the full movie to correct for cy5 signal bleaching. Upon CXCR4 inhibition, parenchymal cells maintain the same migratory behavior as prior to AMD3100 administration.

Supplementary Video 5E - AMD3100 induces T-ALL cell death, contributing to dramatic reduction in cell cluster sizes.

Representative maximum projection of 3D time-lapse data (shown at 10 frames per second) of areas from Flk1-GFP mice acquired every 3min for 90 min prior and 180 min post-AMD3100 administration. Single cells at seeding (first part) and chemoresistant (second part) stages were tracked. Red: T-ALL cells; green: Flk1-GFP^{+} endothelial cells; blue: Cy5-labelled dextran inside blood vessels. The first frame of the blue channel was copied across the full movie to correct for cy5 signal bleaching. Clusters of early colonizing (first part) and chemoresistant (second part) T-ALL cells are significantly reduced upon injection of AMD3100. Arrows point at intravasating cells. Cell death caused by AMD3100 is frequent and evidenced by reduction of the cell size and disappearance of fluorescent red signal over time (arrowheads and circles).

Supplementary Video 5F - AMD3100 induces little AML cell death and minimal impact on cell clusters.

Representative maximum projection of 3D time-lapse data (shown at 10 frames per second) of areas from Flk1-GFP mice acquired every 3min for 90 min prior and 180 min post-AMD3100 administration. Cell clusters at seeding (first part) and chemoresistant (second part) stages are marginally affected by AMD3100. Red: AML cells; green: Flk1-GFP^{+} endothelial cells; blue: Cy5-labelled dextran inside blood vessels. The first frame of the blue channel was copied across the full movie to correct for cy5 signal bleaching. Arrows point at intravasating cells.

Appendix B – Reproduction permissions

ELSEVIER LICENSE
TERMS AND CONDITIONS

Dec 21, 2017

This Agreement between Delfim Duarte ("You") and Elsevier ("Elsevier") consists of your license details and the terms and conditions provided by Elsevier and Copyright Clearance Center.

The publisher has provided special terms related to this request that can be found at the end of the Publisher's Terms and Conditions.

License Number	4253651271807
License date	Dec 21, 2017
Licensed Content Publisher	Elsevier
Licensed Content Publication	Elsevier Books
Licensed Content Title	Advances in Stem Cells and their Niches
Licensed Content Author	D. Duarte,C. Lo Celso
Licensed Content Date	Jan 1, 2017
Licensed Content Volume	1
Licensed Content Issue	n/a
Licensed Content Pages	25
Start Page	59
End Page	83
Type of Use	reuse in a thesis/dissertation
Portion	full chapter
Format	both print and electronic
Are you the author of this Elsevier chapter?	Yes
Will you be translating?	No
Title of your thesis/dissertation	In vivo imaging of the dynamic interactions of acute leukaemias with the bone marrow microenvironment.
Expected completion date	Mar 2018
Estimated size (number of pages)	200
Requestor Location	Delfim Duarte 27 Hamble St London, other United Kingdom Attn:
Publisher Tax ID	GB 494 6272 12
Billing Type	Invoice
Billing Address	Delfim Duarte 27 Hamble St

London, United Kingdom
Attn: Delfim Duarte

Total 0.00 USD

Terms and Conditions

INTRODUCTION

1. The publisher for this copyrighted material is Elsevier. By clicking "accept" in connection with completing this licensing transaction, you agree that the following terms and conditions apply to this transaction (along with the Billing and Payment terms and conditions established by Copyright Clearance Center, Inc. ("CCC"), at the time that you opened your Rightslink account and that are available at any time at http://myaccount.copyright.com).

GENERAL TERMS

2. Elsevier hereby grants you permission to reproduce the aforementioned material subject to the terms and conditions indicated.
3. Acknowledgement: If any part of the material to be used (for example, figures) has appeared in our publication with credit or acknowledgement to another source, permission must also be sought from that source. If such permission is not obtained then that material may not be included in your publication/copies. Suitable acknowledgement to the source must be made, either as a footnote or in a reference list at the end of your publication, as follows:
"Reprinted from Publication title, Vol /edition number, Author(s), Title of article / title of chapter, Pages No., Copyright (Year), with permission from Elsevier [OR APPLICABLE SOCIETY COPYRIGHT OWNER]." Also Lancet special credit - "Reprinted from The Lancet, Vol. number, Author(s), Title of article, Pages No., Copyright (Year), with permission from Elsevier."
4. Reproduction of this material is confined to the purpose and/or media for which permission is hereby given.
5. Altering/Modifying Material: Not Permitted. However figures and illustrations may be altered/adapted minimally to serve your work. Any other abbreviations, additions, deletions and/or any other alterations shall be made only with prior written authorization of Elsevier Ltd. (Please contact Elsevier at permissions@elsevier.com). No modifications can be made to any Lancet figures/tables and they must be reproduced in full.
6. If the permission fee for the requested use of our material is waived in this instance, please be advised that your future requests for Elsevier materials may attract a fee.
7. Reservation of Rights: Publisher reserves all rights not specifically granted in the combination of (i) the license details provided by you and accepted in the course of this licensing transaction, (ii) these terms and conditions and (iii) CCC's Billing and Payment terms and conditions.
8. License Contingent Upon Payment: While you may exercise the rights licensed immediately upon issuance of the license at the end of the licensing process for the transaction, provided that you have disclosed complete and accurate details of your proposed use, no license is finally effective unless and until full payment is received from you (either by publisher or by CCC) as provided in CCC's Billing and Payment terms and conditions. If full payment is not received on a timely basis, then any license preliminarily granted shall be deemed automatically revoked and shall be void as if never granted. Further, in the event that you breach any of these terms and conditions or any of CCC's Billing and Payment terms and conditions, the license is automatically revoked and shall be void as if never granted. Use of materials as described in a revoked license, as well as any use of the materials beyond the scope of an unrevoked license, may constitute copyright infringement and publisher reserves the right to take any and all action to protect its copyright in the materials.
9. Warranties: Publisher makes no representations or warranties with respect to the licensed material.

10. Indemnity: You hereby indemnify and agree to hold harmless publisher and CCC, and their respective officers, directors, employees and agents, from and against any and all claims arising out of your use of the licensed material other than as specifically authorized pursuant to this license.
11. No Transfer of License: This license is personal to you and may not be sublicensed, assigned, or transferred by you to any other person without publisher's written permission.
12. No Amendment Except in Writing: This license may not be amended except in a writing signed by both parties (or, in the case of publisher, by CCC on publisher's behalf).
13. Objection to Contrary Terms: Publisher hereby objects to any terms contained in any purchase order, acknowledgment, check endorsement or other writing prepared by you, which terms are inconsistent with these terms and conditions or CCC's Billing and Payment terms and conditions. These terms and conditions, together with CCC's Billing and Payment terms and conditions (which are incorporated herein), comprise the entire agreement between you and publisher (and CCC) concerning this licensing transaction. In the event of any conflict between your obligations established by these terms and conditions and those established by CCC's Billing and Payment terms and conditions, these terms and conditions shall control.
14. Revocation: Elsevier or Copyright Clearance Center may deny the permissions described in this License at their sole discretion, for any reason or no reason, with a full refund payable to you. Notice of such denial will be made using the contact information provided by you. Failure to receive such notice will not alter or invalidate the denial. In no event will Elsevier or Copyright Clearance Center be responsible or liable for any costs, expenses or damage incurred by you as a result of a denial of your permission request, other than a refund of the amount(s) paid by you to Elsevier and/or Copyright Clearance Center for denied permissions.

LIMITED LICENSE

The following terms and conditions apply only to specific license types:
15. **Translation**: This permission is granted for non-exclusive world **English** rights only unless your license was granted for translation rights. If you licensed translation rights you may only translate this content into the languages you requested. A professional translator must perform all translations and reproduce the content word for word preserving the integrity of the article.
16. **Posting licensed content on any Website**: The following terms and conditions apply as follows: Licensing material from an Elsevier journal: All content posted to the web site must maintain the copyright information line on the bottom of each image; A hyper-text must be included to the Homepage of the journal from which you are licensing at http://www.sciencedirect.com/science/journal/xxxxx or the Elsevier homepage for books at http://www.elsevier.com; Central Storage: This license does not include permission for a scanned version of the material to be stored in a central repository such as that provided by Heron/XanEdu.
Licensing material from an Elsevier book: A hyper-text link must be included to the Elsevier homepage at http://www.elsevier.com . All content posted to the web site must maintain the copyright information line on the bottom of each image.

Posting licensed content on Electronic reserve: In addition to the above the following clauses are applicable: The web site must be password-protected and made available only to bona fide students registered on a relevant course. This permission is granted for 1 year only. You may obtain a new license for future website posting.
17. **For journal authors:** the following clauses are applicable in addition to the above:
Preprints:
A preprint is an author's own write-up of research results and analysis, it has not been peer-reviewed, nor has it had any other value added to it by a publisher (such as formatting, copyright, technical enhancement etc.).
Authors can share their preprints anywhere at any time. Preprints should not be added to or

enhanced in any way in order to appear more like, or to substitute for, the final versions of articles however authors can update their preprints on arXiv or RePEc with their Accepted Author Manuscript (see below).
If accepted for publication, we encourage authors to link from the preprint to their formal publication via its DOI. Millions of researchers have access to the formal publications on ScienceDirect, and so links will help users to find, access, cite and use the best available version. Please note that Cell Press, The Lancet and some society-owned have different preprint policies. Information on these policies is available on the journal homepage.
Accepted Author Manuscripts: An accepted author manuscript is the manuscript of an article that has been accepted for publication and which typically includes author-incorporated changes suggested during submission, peer review and editor-author communications.
Authors can share their accepted author manuscript:

- immediately
    - via their non-commercial person homepage or blog
    - by updating a preprint in arXiv or RePEc with the accepted manuscript
    - via their research institute or institutional repository for internal institutional uses or as part of an invitation-only research collaboration work-group
    - directly by providing copies to their students or to research collaborators for their personal use
    - for private scholarly sharing as part of an invitation-only work group on commercial sites with which Elsevier has an agreement
- After the embargo period
    - via non-commercial hosting platforms such as their institutional repository
    - via commercial sites with which Elsevier has an agreement

In all cases accepted manuscripts should:

- link to the formal publication via its DOI
- bear a CC-BY-NC-ND license - this is easy to do
- if aggregated with other manuscripts, for example in a repository or other site, be shared in alignment with our hosting policy not be added to or enhanced in any way to appear more like, or to substitute for, the published journal article.

Published journal article (JPA): A published journal article (PJA) is the definitive final record of published research that appears or will appear in the journal and embodies all value-adding publishing activities including peer review co-ordination, copy-editing, formatting, (if relevant) pagination and online enrichment.
Policies for sharing publishing journal articles differ for subscription and gold open access articles:
Subscription Articles: If you are an author, please share a link to your article rather than the full-text. Millions of researchers have access to the formal publications on ScienceDirect, and so links will help your users to find, access, cite, and use the best available version.
Theses and dissertations which contain embedded PJAs as part of the formal submission can be posted publicly by the awarding institution with DOI links back to the formal publications on ScienceDirect.
If you are affiliated with a library that subscribes to ScienceDirect you have additional private sharing rights for others' research accessed under that agreement. This includes use for classroom teaching and internal training at the institution (including use in course packs and courseware programs), and inclusion of the article for grant funding purposes.
Gold Open Access Articles: May be shared according to the author-selected end-user license and should contain a CrossMark logo, the end user license, and a DOI link to the formal publication on ScienceDirect.

Please refer to Elsevier's posting policy for further information.
18. **For book authors** the following clauses are applicable in addition to the above: Authors are permitted to place a brief summary of their work online only. You are not allowed to download and post the published electronic version of your chapter, nor may you scan the printed edition to create an electronic version. **Posting to a repository:** Authors are permitted to post a summary of their chapter only in their institution's repository.
19. **Thesis/Dissertation**: If your license is for use in a thesis/dissertation your thesis may be submitted to your institution in either print or electronic form. Should your thesis be published commercially, please reapply for permission. These requirements include permission for the Library and Archives of Canada to supply single copies, on demand, of the complete thesis and include permission for Proquest/UMI to supply single copies, on demand, of the complete thesis. Should your thesis be published commercially, please reapply for permission. Theses and dissertations which contain embedded PJAs as part of the formal submission can be posted publicly by the awarding institution with DOI links back to the formal publications on ScienceDirect.

Elsevier Open Access Terms and Conditions
You can publish open access with Elsevier in hundreds of open access journals or in nearly 2000 established subscription journals that support open access publishing. Permitted third party re-use of these open access articles is defined by the author's choice of Creative Commons user license. See our open access license policy for more information.
Terms & Conditions applicable to all Open Access articles published with Elsevier:
Any reuse of the article must not represent the author as endorsing the adaptation of the article nor should the article be modified in such a way as to damage the author's honour or reputation. If any changes have been made, such changes must be clearly indicated.
The author(s) must be appropriately credited and we ask that you include the end user license and a DOI link to the formal publication on ScienceDirect.
If any part of the material to be used (for example, figures) has appeared in our publication with credit or acknowledgement to another source it is the responsibility of the user to ensure their reuse complies with the terms and conditions determined by the rights holder.
Additional Terms & Conditions applicable to each Creative Commons user license:
CC BY: The CC-BY license allows users to copy, to create extracts, abstracts and new works from the Article, to alter and revise the Article and to make commercial use of the Article (including reuse and/or resale of the Article by commercial entities), provided the user gives appropriate credit (with a link to the formal publication through the relevant DOI), provides a link to the license, indicates if changes were made and the licensor is not represented as endorsing the use made of the work. The full details of the license are available at http://creativecommons.org/licenses/by/4.0.
CC BY NC SA: The CC BY-NC-SA license allows users to copy, to create extracts, abstracts and new works from the Article, to alter and revise the Article, provided this is not done for commercial purposes, and that the user gives appropriate credit (with a link to the formal publication through the relevant DOI), provides a link to the license, indicates if changes were made and the licensor is not represented as endorsing the use made of the work. Further, any new works must be made available on the same conditions. The full details of the license are available at http://creativecommons.org/licenses/by-nc-sa/4.0.
CC BY NC ND: The CC BY-NC-ND license allows users to copy and distribute the Article, provided this is not done for commercial purposes and further does not permit distribution of the Article if it is changed or edited in any way, and provided the user gives appropriate credit (with a link to the formal publication through the relevant DOI), provides a link to the license, and that the licensor is not represented as endorsing the use made of the work. The full details of the license are available at http://creativecommons.org/licenses/by-nc-nd/4.0.
Any commercial reuse of Open Access articles published with a CC BY NC SA or CC BY NC ND license requires permission from Elsevier and will be subject to a fee.
Commercial reuse includes:

- Associating advertising with the full text of the Article
- Charging fees for document delivery or access
- Article aggregation
- Systematic distribution via e-mail lists or share buttons

Posting or linking by commercial companies for use by customers of those companies.

20. **Other Conditions**: Permission is granted to submit your article in print and electronic format. This license permits you to post this Elsevier article online on your Institution's website if the content is embedded within your thesis.

v1.9

Copyright Information

All material published in *Blood* represents the opinions of the authors and does not reflect the opinions of the American Society of Hematology, the Editors, or the institutions with which the authors are affiliated. Authors submitting manuscripts to *Blood* do so with the understanding that if a manuscript is accepted, the copyright in the article, including the right to reproduce the article in all forms and media, shall be assigned exclusively to The American Society of Hematology and that the corresponding author and all coauthors will be required to sign their copyright transfer using *Blood* Bench>Press. This can be done at any time following initial submission of a manuscript but must be completed before an accepted article is posted to First Edition or otherwise published in the journal.

Blood allows authors to retain a number of nonexclusive rights to their published article. Signatures for copyright transfer are collected online. The work of the authors who are U.S. Federal Government employees is not protected by the Copyright Act, and copyright ownership will not be transferred in these cases. The online form to sign on *Blood* Bench>Press allows authors to indicate their status as Federal Government employees.

Authors have permission to do the following after their article has been published in *Blood*, either in print or online as a First Edition Paper.

The Accepted, First Edition version of articles can be shared by authors:

- Privately with students or colleagues for their personal use in presentations and other educational endeavors.
- Privately on the authors' institutional repositories.
- On personal websites.

The Final or Print version of articles can be shared by authors:

- As listed above AND
- As a link to the article on the journal's website anywhere at any time.

After Embargo articles can be shared by authors:

- As listed above AND
- Publicly on non-commercial platforms.

Specific examples of acceptable author reuse and sharing include:

- Reprinting the article in print collections of the author's own writing.
- Reusing figures and tables created by the author in future works.
- Reproducing the article for use in courses the author is teaching. If the author is employed by an academic institution, that institution may also reproduce the article

Additional Links: Rights & Permissions | Public Access | Subscriptions

blood®

Leading the way in experimental and clinical research in hematology

American Society of Hematology
2021 L Street NW, Suite 900, Washington, DC 20036
Phone 202-776-0544 | Fax 202-776-0545

Current Issue
First Edition
Collections
All Issues
Abstracts
Video Library

About *Blood*
Subscriptions
Newsroom
Copyright
Public Access
Permissions

Submit to *Blood*
Blood App
Alerts
RSS
Contact Us
Order Reprints

Information for:
Authors
Subscribers
Institutions/Librarians
Advertising in *Blood*
Terms and Conditions

ASH Home | Research | Education | Advocacy | Meetings | Publications | ASH Store

Blood Journals

Privacy Policy | Terms of Service | Cont

Copyright Clearance Center

Note: Copyright.com supplies permissions but not the copyrighted content itself.

1 PAYMENT 2 REVIEW 3 CONFIRMATION

Step 3: Order Confirmation

Thank you for your order! A confirmation for your order will be sent to your account email address. If you have questions about your order, you can call us 24 hrs/day, M-F at +1.855.239.3415 Toll Free, or write to us at info@copyright.com. This is not an invoice.

Confirmation Number: 11697958
Order Date: 02/08/2018

If you paid by credit card, your order will be finalized and your card will be charged within 24 hours. If you choose to be invoiced, you can change or cancel your order until the invoice is generated.

Payment Information

Delfim Duarte
delfim.duarte14@imperial.ac.uk
+44 7446897799
Payment Method: n/a

Order Details

Cell stem cell

Order detail ID:	71006063
Order License Id:	4284421195739
ISSN:	1934-5909
Publication Type:	Journal
Volume:	
Issue:	
Start page:	
Publisher:	CELL PRESS
Author/Editor:	Cell Press

Permission Status: Granted

Permission type:	Republish or display content
Type of use:	Thesis/Dissertation

Requestor type	Academic institution
Format	Print, Electronic
Portion	chapter/article
Number of pages in chapter/article	33
The requesting person/organization	Delfim Duarte (author)
Title or numeric reference of the portion(s)	Full article
Title of the article or chapter the portion is from	Inhibition of Endosteal Vascular Niche Remodeling Rescues Hematopoietic Stem Cell Loss in AML
Editor of portion(s)	N/A
Author of portion(s)	Yes

Volume of serial or monograph	22
Issue, if republishing an article from a serial	1
Page range of portion	1-33
Publication date of portion	2018
Rights for	Main product and any product related to main product
Duration of use	Life of current edition
Creation of copies for the disabled	no
With minor editing privileges	yes
For distribution to	Worldwide
In the following language(s)	Original language of publication
With incidental promotional use	no
Lifetime unit quantity of new product	Up to 499
Title	In vivo imaging of the dynamic interactions of acute leukaemias with the bone marrow microenvironment.
Instructor name	n/a
Institution name	Imperial College London
Expected presentation date	Apr 2018
Attachment	

Note: This item will be invoiced or charged separately through CCC's **RightsLink** service. More info **$ 0.00**

Total order items: 1

This is not an invoice.

Order Total: 0.00 USD

Confirmation Number: 11697958

Special Rightsholder Terms & Conditions

The following terms & conditions apply to the specific publication under which they are listed

Cell stem cell
Permission type: Republish or display content
Type of use: Thesis/Dissertation

TERMS AND CONDITIONS

The following terms are individual to this publisher:

None

Other Terms and Conditions:

STANDARD TERMS AND CONDITIONS

1. Description of Service; Defined Terms. This Republication License enables the User to obtain licenses for republication of one or more copyrighted works as described in detail on the relevant Order Confirmation (the "Work(s)"). Copyright Clearance Center, Inc. ("CCC") grants licenses through the Service on behalf of the rightsholder identified on the Order Confirmation (the "Rightsholder"). "Republication", as used herein, generally means the inclusion of a Work, in whole or in part, in a new work or works, also as described on the Order Confirmation. "User", as used herein, means the person or entity making such republication.

2. The terms set forth in the relevant Order Confirmation, and any terms set by the Rightsholder with respect to a particular Work, govern the terms of use of Works in connection with the Service. By using the Service, the person transacting for a republication license on behalf of the User represents and warrants that he/she/it (a) has been duly authorized by the User to accept, and hereby does accept, all such terms and conditions on behalf of User, and (b) shall inform User of all such terms and conditions. In the event such person is a "freelancer" or other third party independent of User and CCC, such party shall be deemed jointly a "User" for purposes of these terms and conditions. In any event, User shall be deemed to have accepted and agreed to all such terms and conditions if User republishes the Work in any fashion.

3. Scope of License; Limitations and Obligations.

3.1 All Works and all rights therein, including copyright rights, remain the sole and exclusive property of the Rightsholder. The license created by the exchange of an Order Confirmation (and/or any invoice) and payment by User of the full amount set forth on that document includes only those rights expressly set forth in the Order Confirmation and in these terms and conditions, and conveys no other rights in the Work(s) to User. All rights not expressly granted are hereby reserved.

3.2 General Payment Terms: You may pay by credit card or through an account with us payable at the end of the month. If you and we agree that you may establish a standing account with CCC, then the following terms apply: Remit Payment to: Copyright Clearance Center, 29118 Network Place, Chicago, IL 60673-1291. Payments Due: Invoices are payable upon their delivery to you (or upon our notice to you that they are available to you for downloading). After 30 days, outstanding amounts will be subject to a service charge of 1-1/2% per month or, if less, the maximum rate allowed by applicable law. Unless otherwise specifically set forth in the Order Confirmation or in a separate written agreement signed by CCC, invoices are due and payable on "net 30" terms. While User may exercise the rights licensed immediately upon issuance of the Order Confirmation, the license is automatically revoked and is null and void, as if it had never been issued, if complete payment for the license is not received on a timely basis either from User directly or through a payment agent, such as a credit card company.

3.3 Unless otherwise provided in the Order Confirmation, any grant of rights to User (i) is "one-time" (including the editions and product family specified in the license), (ii) is non-exclusive and non-transferable and (iii) is subject to any and all limitations and restrictions (such as, but not limited to, limitations on duration of use or circulation) included in the Order Confirmation or invoice and/or in these terms and conditions. Upon completion of the licensed use, User shall either secure a new permission for further use of the Work(s) or immediately cease any new use of the Work(s) and shall render inaccessible (such as by deleting or by removing or severing links or other locators) any further copies of the Work (except for copies printed on paper in accordance with this license and still in User's stock at the end of such period).

3.4 In the event that the material for which a republication license is sought includes third party materials (such as photographs, illustrations, graphs, inserts and similar materials) which are identified in such material as having been used by permission, User is responsible for identifying, and seeking separate licenses (under this Service or otherwise) for, any of such third party materials; without a separate license, such third party materials may not be used.

3.5 Use of proper copyright notice for a Work is required as a condition of any license granted under the Service. Unless otherwise provided in the Order Confirmation, a proper copyright notice will read substantially as follows: "Republished with permission of [Rightsholder's name], from [Work's title, author, volume, edition number and year of copyright]; permission conveyed through Copyright Clearance Center, Inc. " Such notice must be provided in a reasonably legible font size and must be placed either immediately adjacent to the Work as used (for example, as part of a by-line or footnote but not as a separate electronic link) or in the place where substantially all other credits or notices for the new work containing the republished Work are located. Failure to include the required notice results in loss to the Rightsholder and CCC, and the User shall be liable to pay liquidated damages for each such failure equal to twice the use fee specified in the Order Confirmation, in addition to the use fee itself and any other fees and charges specified.

3.6 User may only make alterations to the Work if and as expressly set forth in the Order Confirmation. No Work may be used in any way that is defamatory, violates the rights of third parties (including such third parties' rights of copyright, privacy, publicity, or other tangible or intangible property), or is otherwise illegal, sexually explicit or obscene. In addition, User may not conjoin a Work with any other material that may result in damage to the reputation of the Rightsholder. User agrees to inform CCC if it becomes aware of any infringement of any rights in a Work and to cooperate with any reasonable request of CCC or the Rightsholder in connection therewith.

4. Indemnity. User hereby indemnifies and agrees to defend the Rightsholder and CCC, and their respective employees and directors, against all claims, liability, damages, costs and expenses, including legal fees and expenses, arising out of any use of a Work beyond the scope of the rights granted herein, or any use of a Work which has been altered in any unauthorized way by User, including claims of defamation or infringement of rights of copyright, publicity, privacy or other tangible or intangible property.

5. Limitation of Liability. UNDER NO CIRCUMSTANCES WILL CCC OR THE RIGHTSHOLDER BE LIABLE FOR ANY DIRECT, INDIRECT, CONSEQUENTIAL OR INCIDENTAL DAMAGES (INCLUDING WITHOUT LIMITATION DAMAGES FOR LOSS OF BUSINESS PROFITS OR INFORMATION, OR FOR BUSINESS INTERRUPTION) ARISING OUT OF THE USE OR INABILITY TO USE A WORK, EVEN IF ONE OF THEM HAS BEEN ADVISED OF THE POSSIBILITY OF SUCH DAMAGES. In any event, the total liability of the Rightsholder and CCC (including their respective employees and directors) shall not exceed the total amount actually paid by User for this license. User assumes full liability for the actions and omissions of its principals, employees, agents, affiliates, successors and assigns.

6. Limited Warranties. THE WORK(S) AND RIGHT(S) ARE PROVIDED "AS IS". CCC HAS THE RIGHT TO GRANT TO USER THE RIGHTS GRANTED IN THE ORDER CONFIRMATION DOCUMENT. CCC AND THE RIGHTSHOLDER DISCLAIM ALL OTHER WARRANTIES RELATING TO THE WORK(S) AND RIGHT(S), EITHER EXPRESS OR IMPLIED, INCLUDING WITHOUT LIMITATION IMPLIED WARRANTIES OF MERCHANTABILITY OR FITNESS FOR A PARTICULAR PURPOSE. ADDITIONAL RIGHTS MAY BE REQUIRED TO USE ILLUSTRATIONS, GRAPHS, PHOTOGRAPHS, ABSTRACTS, INSERTS OR OTHER PORTIONS OF THE WORK (AS OPPOSED TO THE ENTIRE WORK) IN A MANNER CONTEMPLATED BY USER; USER UNDERSTANDS AND AGREES THAT NEITHER CCC NOR THE RIGHTSHOLDER MAY HAVE SUCH ADDITIONAL RIGHTS TO GRANT.

7. Effect of Breach. Any failure by User to pay any amount when due, or any use by User of a Work beyond the scope of the license set forth in the Order Confirmation and/or these terms and conditions, shall be a material breach of the license created by the Order Confirmation and these terms and conditions. Any breach not cured within 30 days of written notice thereof shall result in immediate termination of such license without further notice. Any unauthorized (but licensable) use of a Work that is terminated immediately upon notice thereof may be liquidated by payment of the Rightsholder's ordinary license price therefor; any unauthorized (and unlicensable) use that is not terminated immediately for any reason (including, for example, because materials containing the Work cannot reasonably be recalled) will be subject to all remedies available at law or in equity, but in no event to a payment of less than three times the Rightsholder's ordinary license price for the most closely analogous licensable use plus Rightsholder's and/or CCC's costs and expenses incurred in collecting such payment.

8. **Miscellaneous.**

8.1 User acknowledges that CCC may, from time to time, make changes or additions to the Service or to these terms and conditions, and CCC reserves the right to send notice to the User by electronic mail or otherwise for the purposes of notifying User of such changes or additions; provided that any such changes or additions shall not apply to permissions already secured and paid for.

8.2 Use of User-related information collected through the Service is governed by CCC's privacy policy, available online here: http://www.copyright.com/content/cc3/en/tools/footer/privacypolicy.html.

8.3 The licensing transaction described in the Order Confirmation is personal to User. Therefore, User may not assign or transfer to any other person (whether a natural person or an organization of any kind) the license created by the Order Confirmation and these terms and conditions or any rights granted hereunder; provided, however, that User may assign such license in its entirety on written notice to CCC in the event of a transfer of all or substantially all of User's rights in the new material which includes the Work(s) licensed under this Service.

8.4 No amendment or waiver of any terms is binding unless set forth in writing and signed by the parties. The Rightsholder and CCC hereby object to any terms contained in any writing prepared by the User or its principals, employees, agents or affiliates and purporting to govern or otherwise relate to the licensing transaction described in the Order Confirmation, which terms are in any way inconsistent with any terms set forth in the Order Confirmation and/or in these terms and conditions or CCC's standard operating procedures, whether such writing is prepared prior to, simultaneously with or subsequent to the Order Confirmation, and whether such writing appears on a copy of the Order Confirmation or in a separate instrument.

8.5 The licensing transaction described in the Order Confirmation document shall be governed by and construed under the law of the State of New York, USA, without regard to the principles thereof of conflicts of law. Any case, controversy, suit, action, or proceeding arising out of, in connection with, or related to such licensing transaction shall be brought, at CCC's sole discretion, in any federal or state court located in the County of New York, State of New York, USA, or in any federal or state court whose geographical jurisdiction covers the location of the Rightsholder set forth in the Order Confirmation. The parties expressly submit to the personal jurisdiction and venue of each such federal or state court.If you have any comments or questions about the Service or Copyright Clearance Center, please contact us at 978-750-8400 or send an e-mail to info@copyright.com.

v 1.1

Close

Confirmation Number: 11697958

Citation Information

Order Detail ID: 71006063

Cell stem cell by Cell Press Reproduced with permission of CELL PRESS in the format Thesis/Dissertation via Copyright Clearance Center.

Close

Author Request

If you are the author of this content (or his/her designated agent) please read the following. If you are not the author of this content, please click the Back button and select no to the question "Are you the Author of this Springer Nature content?".
Ownership of copyright in original research articles remains with the Author, and provided that, when reproducing the contribution or extracts from it or from the Supplementary Information, the Author acknowledges first and reference publication in the Journal, the Author retains the following non-exclusive rights:
To reproduce the contribution in whole or in part in any printed volume (book or thesis) of which they are the author(s).
The author and any academic institution, where they work, at the time may reproduce the contribution for the purpose of course teaching.
To reuse figures or tables created by the Author and contained in the Contribution in oral presentations and other works created by them.
To post a copy of the contribution as accepted for publication after peer review (in locked Word processing file, of a PDF version thereof) on the Author's own web site, or the Author's institutional repository, or the Author's funding body's archive, six months after publication of the printed or online edition of the Journal, provided that they also link to the contribution on the publisher's website.
Authors wishing to use the published version of their article for promotional use or on a web site must request in the normal way.

If you require further assistance please read Springer Nature's online author reuse guidelines.

For full paper portion: Authors of original research papers published by Springer Nature are encouraged to submit the author's version of the accepted, peer-reviewed manuscript to their relevant funding body's archive, for release six months after publication. In addition, authors are encouraged to archive their version of the manuscript in their institution's repositories (as well as their personal Web sites), also six months after original publication.

v1.0

Copyright Clearance Center

Note: Copyright.com supplies permissions but not the copyrighted content itself.

1 PAYMENT 2 REVIEW 3 CONFIRMATION

Step 3: Order Confirmation

Thank you for your order! A confirmation for your order will be sent to your account email address. If you have questions about your order, you can call us 24 hrs/day, M-F at +1.855.239.3415 Toll Free, or write to us at info@copyright.com. This is not an invoice.

Confirmation Number: 11697954
Order Date: 02/08/2018

If you paid by credit card, your order will be finalized and your card will be charged within 24 hours. If you choose to be invoiced, you can change or cancel your order until the invoice is generated.

Payment Information

Delfim Duarte
delfim.duarte14@imperial.ac.uk
+44 7446897799
Payment Method: n/a

Order Details

Nature

Order detail ID:	71006052
Order License Id:	4284411239906
ISSN:	0028-0836
Publication Type:	Journal
Volume:	
Issue:	
Start page:	
Publisher:	Nature Publishing Group

Permission Status: Granted

Permission type: Republish or display content
Type of use: Thesis/Dissertation

Requestor type	Academic institution
Format	Print, Electronic
Portion	chapter/article
The requesting person/organization	Delfim Duarte (author)
Title or numeric reference of the portion(s)	Full article
Title of the article or chapter the portion is from	T-cell acute leukaemia exhibits dynamic interactions with bone marrow microenvironments
Editor of portion(s)	N/A
Author of portion(s)	Yes
Volume of serial or monograph	538

Page range of portion	
Publication date of portion	27 October 2016
Rights for	Main product and any product related to main product
Duration of use	Life of current edition
Creation of copies for the disabled	no
With minor editing privileges	yes
For distribution to	Worldwide
In the following language(s)	Original language of publication
With incidental promotional use	no
Lifetime unit quantity of new product	Up to 499
Title	In vivo imaging of the dynamic interactions of acute leukaemias with the bone marrow microenvironment.
Instructor name	n/a
Institution name	Imperial College London
Expected presentation date	Apr 2018
Attachment	

Note: This item will be invoiced or charged separately through CCC's **RightsLink** service. More info **$ 0.00**

Total order items: 1

This is not an invoice.

Order Total: 0.00 USD

Confirmation Number: 11697954

Special Rightsholder Terms & Conditions

The following terms & conditions apply to the specific publication under which they are listed

Nature
Permission type: Republish or display content
Type of use: Thesis/Dissertation

TERMS AND CONDITIONS

The following terms are individual to this publisher:

Nature Publishing Group hereby grants you a non-exclusive license to reproduce this material for this purpose, and for no other use, subject to the conditions below:

1. NPG warrants that it has, to the best of its knowledge, the rights to license reuse of this material. However, you should ensure that the material you are requesting is original to Nature Publishing Group and does not carry the copyright of another entity (as credited in the published version). If the credit line on any part of the material you have requested indicates that it was reprinted or adapted by NPG with permission from another source, then you should also seek permission from that source to reuse the material.

2. Permission granted free of charge for material in print is also usually granted for any electronic version of that work, provided that the material is incidental to the work as a whole and that the electronic version is essentially equivalent to, or substitutes for, the print version. Where print permission has been granted for a fee, separate permission must be obtained for any additional, electronic re-use (unless, as in the case of a full paper, this has already been accounted for during your initial request in the calculation of a print run).

3. Permission granted for a first edition does not apply to second and subsequent editions and for editions in other languages (except for signatories to the STM Permissions Guidelines, or where the first edition permission was granted for free).

4. Nature Publishing Group's permission must be acknowledged next to the figure, table or abstract in print. In electronic form, this acknowledgement must be visible at the same time as the figure/table/abstract, and must be hyperlinked to the journal's homepage.

5. The credit line should read:Reprinted by permission from Macmillan Publishers Ltd: [JOURNAL NAME] (reference citation), copyright (year of publication)For AOP papers, the credit line should read:Reprinted by permission from Macmillan Publishers Ltd: [JOURNAL NAME], advance online publication, day month year (doi: 10.1038/sj.[JOURNAL ACRONYM].XXXXX) Note: For republication from the British Journal of Cancer, the following credit lines apply.Reprinted by permission from Macmillan Publishers Ltd on behalf of Cancer Research UK: [JOURNAL NAME] (reference citation), copyright (year of publication) For AOP papers, the credit line should read:Reprinted by permission from Macmillan Publishers Ltd on behalf of Cancer Research UK: [JOURNAL NAME], advance online publication, day month year (doi: 10.1038/sj.[JOURNAL ACRONYM].XXXXX)

6. Adaptations of single figures do not require NPG approval. However, the adaptation should be credited as follows:Adapted by permission from Macmillan Publishers Ltd: [JOURNAL NAME] (reference citation), copyright (year of publication)Note: For adaptation from the British Journal of Cancer, the following credit line applies.Adapted by permission from Macmillan Publishers Ltd on behalf of Cancer Research UK: [JOURNAL NAME] (reference citation), copyright (year of publication)

7. Translations of 401 words up to a whole article require NPG approval. Please visit http://www.macmillanmedicalcommunications.com for more information. Translations of up to a 400 words do not require NPG approval. The translation should be credited as follows:Translated by permission from Macmillan Publishers Ltd: [JOURNAL NAME] (reference citation), copyright (year of publication).Note: For translation from the British Journal of Cancer, the following credit line applies.Translated by permission from Macmillan Publishers Ltd on behalf of Cancer Research UK: [JOURNAL NAME] (reference citation), copyright (year of publication)

We are certain that all parties will benefit from this agreement and wish you the best in the use of this material. Thank you.

Other Terms and Conditions:

STANDARD TERMS AND CONDITIONS

1. Description of Service; Defined Terms. This Republication License enables the User to obtain licenses for republication of one or more copyrighted works as described in detail on the relevant Order Confirmation (the "Work(s)"). Copyright Clearance Center, Inc. ("CCC") grants licenses through the Service on behalf of the rightsholder identified on the Order Confirmation (the "Rightsholder"). "Republication", as used herein, generally means the inclusion of a Work, in whole or in part, in a new work or works, also as described on the Order Confirmation. "User", as used herein, means the person or entity making such republication.

2. The terms set forth in the relevant Order Confirmation, and any terms set by the Rightsholder with respect to a particular Work, govern the terms of use of Works in connection with the Service. By using the Service, the person transacting for a republication license on behalf of the User represents and warrants that he/she/it (a) has been duly authorized by the User to accept, and hereby does accept, all such terms and conditions on behalf of User, and (b) shall

inform User of all such terms and conditions. In the event such person is a "freelancer" or other third party independent of User and CCC, such party shall be deemed jointly a "User" for purposes of these terms and conditions. In any event, User shall be deemed to have accepted and agreed to all such terms and conditions if User republishes the Work in any fashion.

3. Scope of License; Limitations and Obligations.

3.1 All Works and all rights therein, including copyright rights, remain the sole and exclusive property of the Rightsholder. The license created by the exchange of an Order Confirmation (and/or any invoice) and payment by User of the full amount set forth on that document includes only those rights expressly set forth in the Order Confirmation and in these terms and conditions, and conveys no other rights in the Work(s) to User. All rights not expressly granted are hereby reserved.

3.2 General Payment Terms: You may pay by credit card or through an account with us payable at the end of the month. If you and we agree that you may establish a standing account with CCC, then the following terms apply: Remit Payment to: Copyright Clearance Center, 29118 Network Place, Chicago, IL 60673-1291. Payments Due: Invoices are payable upon their delivery to you (or upon our notice to you that they are available to you for downloading). After 30 days, outstanding amounts will be subject to a service charge of 1-1/2% per month or, if less, the maximum rate allowed by applicable law. Unless otherwise specifically set forth in the Order Confirmation or in a separate written agreement signed by CCC, invoices are due and payable on "net 30" terms. While User may exercise the rights licensed immediately upon issuance of the Order Confirmation, the license is automatically revoked and is null and void, as if it had never been issued, if complete payment for the license is not received on a timely basis either from User directly or through a payment agent, such as a credit card company.

3.3 Unless otherwise provided in the Order Confirmation, any grant of rights to User (i) is "one-time" (including the editions and product family specified in the license), (ii) is non-exclusive and non-transferable and (iii) is subject to any and all limitations and restrictions (such as, but not limited to, limitations on duration of use or circulation) included in the Order Confirmation or invoice and/or in these terms and conditions. Upon completion of the licensed use, User shall either secure a new permission for further use of the Work(s) or immediately cease any new use of the Work(s) and shall render inaccessible (such as by deleting or by removing or severing links or other locators) any further copies of the Work (except for copies printed on paper in accordance with this license and still in User's stock at the end of such period).

3.4 In the event that the material for which a republication license is sought includes third party materials (such as photographs, illustrations, graphs, inserts and similar materials) which are identified in such material as having been used by permission, User is responsible for identifying, and seeking separate licenses (under this Service or otherwise) for, any of such third party materials; without a separate license, such third party materials may not be used.

3.5 Use of proper copyright notice for a Work is required as a condition of any license granted under the Service. Unless otherwise provided in the Order Confirmation, a proper copyright notice will read substantially as follows: "Republished with permission of [Rightsholder's name], from [Work's title, author, volume, edition number and year of copyright]; permission conveyed through Copyright Clearance Center, Inc. " Such notice must be provided in a reasonably legible font size and must be placed either immediately adjacent to the Work as used (for example, as part of a by-line or footnote but not as a separate electronic link) or in the place where substantially all other credits or notices for the new work containing the republished Work are located. Failure to include the required notice results in loss to the Rightsholder and CCC, and the User shall be liable to pay liquidated damages for each such failure equal to twice the use fee specified in the Order Confirmation, in addition to the use fee itself and any other fees and charges specified.

3.6 User may only make alterations to the Work if and as expressly set forth in the Order Confirmation. No Work may be used in any way that is defamatory, violates the rights of third parties (including such third parties' rights of copyright, privacy, publicity, or other tangible or intangible property), or is otherwise illegal, sexually explicit or obscene. In addition, User may not conjoin a Work with any other material that may result in damage to the reputation of the Rightsholder. User agrees to inform CCC if it becomes aware of any infringement of any rights in a Work and to cooperate with any reasonable request of CCC or the Rightsholder in connection therewith.

4. Indemnity. User hereby indemnifies and agrees to defend the Rightsholder and CCC, and their respective employees and directors, against all claims, liability, damages, costs and expenses, including legal fees and expenses, arising out of any use of a Work beyond the scope of the rights granted herein, or any use of a Work which has been altered in any unauthorized way by User, including claims of defamation or infringement of rights of copyright, publicity, privacy or other tangible or intangible property.

5. Limitation of Liability. UNDER NO CIRCUMSTANCES WILL CCC OR THE RIGHTSHOLDER BE LIABLE FOR ANY DIRECT, INDIRECT, CONSEQUENTIAL OR INCIDENTAL DAMAGES (INCLUDING WITHOUT LIMITATION DAMAGES FOR LOSS OF BUSINESS PROFITS OR INFORMATION, OR FOR BUSINESS INTERRUPTION) ARISING OUT OF THE USE OR INABILITY TO USE A WORK, EVEN IF ONE OF THEM HAS BEEN ADVISED OF THE POSSIBILITY OF SUCH DAMAGES. In any event, the total liability of the Rightsholder and CCC (including their respective employees and directors) shall not exceed the total amount actually paid by User for this license. User assumes full liability for the actions and omissions of its principals, employees, agents, affiliates, successors and assigns.

6. Limited Warranties. THE WORK(S) AND RIGHT(S) ARE PROVIDED "AS IS". CCC HAS THE RIGHT TO GRANT TO USER THE RIGHTS GRANTED IN THE ORDER CONFIRMATION DOCUMENT. CCC AND THE RIGHTSHOLDER DISCLAIM ALL OTHER WARRANTIES RELATING TO THE WORK(S) AND RIGHT(S), EITHER EXPRESS OR IMPLIED, INCLUDING WITHOUT LIMITATION IMPLIED WARRANTIES OF MERCHANTABILITY OR FITNESS FOR A PARTICULAR PURPOSE. ADDITIONAL RIGHTS MAY BE REQUIRED TO USE ILLUSTRATIONS, GRAPHS, PHOTOGRAPHS, ABSTRACTS, INSERTS OR OTHER PORTIONS OF THE WORK (AS OPPOSED TO THE ENTIRE WORK) IN A MANNER CONTEMPLATED BY USER; USER UNDERSTANDS AND AGREES THAT NEITHER CCC NOR THE RIGHTSHOLDER MAY HAVE SUCH ADDITIONAL RIGHTS TO GRANT.

7. Effect of Breach. Any failure by User to pay any amount when due, or any use by User of a Work beyond the scope of the license set forth in the Order Confirmation and/or these terms and conditions, shall be a material breach of the license created by the Order Confirmation and these terms and conditions. Any breach not cured within 30 days of written notice thereof shall result in immediate termination of such license without further notice. Any unauthorized (but licensable) use of a Work that is terminated immediately upon notice thereof may be liquidated by payment of the Rightsholder's ordinary license price therefor; any unauthorized (and unlicensable) use that is not terminated

immediately for any reason (including, for example, because materials containing the Work cannot reasonably be recalled) will be subject to all remedies available at law or in equity, but in no event to a payment of less than three times the Rightsholder's ordinary license price for the most closely analogous licensable use plus Rightsholder's and/or CCC's costs and expenses incurred in collecting such payment.

8. **Miscellaneous.**

8.1 User acknowledges that CCC may, from time to time, make changes or additions to the Service or to these terms and conditions, and CCC reserves the right to send notice to the User by electronic mail or otherwise for the purposes of notifying User of such changes or additions; provided that any such changes or additions shall not apply to permissions already secured and paid for.

8.2 Use of User-related information collected through the Service is governed by CCC's privacy policy, available online here: http://www.copyright.com/content/cc3/en/tools/footer/privacypolicy.html.

8.3 The licensing transaction described in the Order Confirmation is personal to User. Therefore, User may not assign or transfer to any other person (whether a natural person or an organization of any kind) the license created by the Order Confirmation and these terms and conditions or any rights granted hereunder; provided, however, that User may assign such license in its entirety on written notice to CCC in the event of a transfer of all or substantially all of User's rights in the new material which includes the Work(s) licensed under this Service.

8.4 No amendment or waiver of any terms is binding unless set forth in writing and signed by the parties. The Rightsholder and CCC hereby object to any terms contained in any writing prepared by the User or its principals, employees, agents or affiliates and purporting to govern or otherwise relate to the licensing transaction described in the Order Confirmation, which terms are in any way inconsistent with any terms set forth in the Order Confirmation and/or in these terms and conditions or CCC's standard operating procedures, whether such writing is prepared prior to, simultaneously with or subsequent to the Order Confirmation, and whether such writing appears on a copy of the Order Confirmation or in a separate instrument.

8.5 The licensing transaction described in the Order Confirmation document shall be governed by and construed under the law of the State of New York, USA, without regard to the principles thereof of conflicts of law. Any case, controversy, suit, action, or proceeding arising out of, in connection with, or related to such licensing transaction shall be brought, at CCC's sole discretion, in any federal or state court located in the County of New York, State of New York, USA, or in any federal or state court whose geographical jurisdiction covers the location of the Rightsholder set forth in the Order Confirmation. The parties expressly submit to the personal jurisdiction and venue of each such federal or state court.If you have any comments or questions about the Service or Copyright Clearance Center, please contact us at 978-750-8400 or send an e-mail to info@copyright.com.

v 1.1

Close

Confirmation Number: 11697954

Citation Information

Order Detail ID: 71006052

Nature by Nature Publishing Group. Reproduced with permission of Nature Publishing Group in the format Thesis/Dissertation via Copyright Clearance Center.

Close